Carlos Pedro Gonçalves Marques

Mestre em Ciência e Engenharia de Superfícies

MODIFICATION OF ALUMINIUM OXIDES THROUGH ION IMPLANTATION OF TRANSITION AND NOBLE METALS

Dissertação para obtenção do grau de Doutor em
Física Aplicada

Orientador: Eduardo Alves, Investigador Principal, ITN
Co-orientador: Rui Silva, Professor Auxiliar Convidado, FCT/UNL

Júri:

Presidente: Prof. Doutora Maria Adelaide de Almeida Pedro de Jesus
Arguente(s): Prof. Doutora Teresa Maria Fernandes Rodrigues Cabral Monteiro

Vogais: Prof. Doutor Luís Manuel Fernandes Rebouta
Prof. Doutor João Duarte Neves Cruz
Prof. Doutor Rui Manuel Coelho da Silva
Prof. Doutor Eduardo Jorge da Costa Alves

FACULDADE DE CIÊNCIAS E TECNOLOGIA
UNIVERSIDADE NOVA DE LISBOA

Dezembro 2009

Copyright

Programa Operacional Ciência e Inovação 2010

MINISTÉRIO DA CIÊNCIA, TECNOLOGIA E ENSINO SUPERIOR

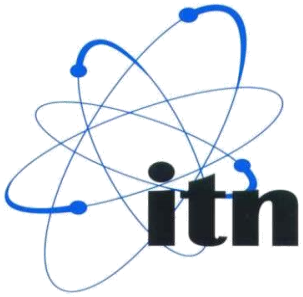

The work presented here was performed at **Instituto Tecnológico e Nuclear** and supported by **POCI 2010** through fellowship **SFRH/BD/14276/2003**.

To my Parents

Acknowledgments

I am particularly grateful to my exceptional advisors Eduardo Alves and Rui Coelho da Silva for the enthusiastic support, wise orientation and invaluable and patient guidance throughout this work.

I would like to express my deep gratitude to all my friends and colleagues at ITN, whose help eased this task. In particular, to Luis Cerqueira for the collaboration in the microbeam facility in IBIL experiments, Miguel Reis for PIXE measurements, Nuno Franco and Sérgio Magalhães for the important contribution in the X-ray diffraction experiments, Katharina Lorenz for the invaluable help with DICADA and FLUX codes, Alexandra Rodrigues for the expertise with CAD software, António Falcão and Miguel Carrapiço for the trial measurements of neutron diffraction, Vanya Darakchieva for the ellipsometry tests and Ana Rita Ramos, Carlos Jesus and Luís Prudêncio for the particularly fruitful discussions. Telma Silva for testing the IBIL operation manual, Nuno Pinhão for properly taming Linux code to run some simulation codes, Luísa Botelho for the use of the new spectrophotometer and Susana Gomes for the calibration sample used in the RBS experiments are also acknowledged. Thanks are also due to Sr. Manuel Cabaça for the proficiency on the fabrication of the metallic flanges and sample holders used in this work. To Jorge Rocha and Pedro Pereira many thanks for the ion implantations! To Helena Marcos and Carlos Canto e Castro thanks are due for providing software and hardware solutions. Guilherme Correia and Ulrich Wahl are also especially acknowledged for the possibility to work for a few weeks at CERN with emission channelling technique.

Precious collaboration in the scope of this project was made with Prof. Elvira Fortunato, Paulo Limão, André Wemans and Yuri Nunes (all from Universidade Nova de Lisboa) for the optical absorption and reflection measurements facilities, Professors Teresa Monteiro and Rosário Correia in the photoluminescence measurements at Universidade de Aveiro, Prof. Adrian Kozanecki for similar experiments at the Polish Academy of Sciences, Prof. Carl McHargue (University of Tennessee) and György Sáfrán (Hungarian Academy of Sciences) for the transmission electron microscopy measurements and Prof. Rogério Colaço for the atomic force microscopy expertise at IST.

Fátima Vicente and Maria Helena Rodrigues are deeply acknowledged for the kind administrative reminders and support and everlasting patience.

The free availability and kind support of software codes is also acknowledged: Nuno Barradas for NDF code, Philip Laven for MiePlot, Bruce Draine for DDSCAT, Peter Smulders for FLUX, Wolfgang Theiss for SCOUT, Konrad Gaertener for DICADA and J.F. Ziegler for SRIM.

Finally, acknowledgments are due to ITN for all the available facilities and to FCT for its support through the Ph. D. fellowship (SFRH/BD/14276/2003) and funding granted to attend several important conferences and to acquire research materials.

Modification of Aluminium Oxides through Ion Implantation of Transition and Noble Metals

Abstract

Sapphire (α-Al_2O_3) crystals were implanted at room temperature with *3d*- and *4f*-shell transition ions (Ni, Cu, Zn, Eu and Yb) and noble metal ions Ag and Au, with energies in the range of 100 keV to 300 keV. The implanted fluences varied from 1×10^{15} cm^{-2} to 1.8×10^{17} cm^{-2}, yielding up to 28 at. % concentration. Subsequent furnace annealings were performed up to 1573 K in vacuum (1×10^{-4} Pa) or in air for one hour. Rutherford backscattering spectrometry (RBS) and RBS under channelling conditions (RBS-C), X-Ray Diffraction (XRD), Optical Absorption (OA) and Ion Beam Induced Luminescence (IBIL) were used to characterize the as implanted state as well as the systems created after annealing on what concerns their composition, depth profiles, phases present and their structure, etc. The latter experimental technique was successfully established in our laboratory during this work and the experimental setup is described.

The implantation of high fluences allowed embedded metallic precipitates to form, epitaxially aligned with the matrix, and of 10 nm sized dimensions.

Thermal annealing in air promoted the crystalline recovery of the host sapphire and the formation of spinel oxide phases of the *3d* transition metals and sesquioxides of Eu and Yb. The band gaps of these compounds were estimated via Tauc plots. Silver and gold do not form compounds and tend to segregate to the surface, with the motion of the recrystallization front of sapphire.

Thermal annealings in vacuum promoted the alignment and growth of metallic phases, along the fast diffusion c-plane, while the crystalline recovery is limited. The exception is Zn in which case ZnO is observed after annealing at 1173 K. Low melting point metals (Cu and Zn) start to evaporate around 1073 K. The crystalline recovery of the matrix impel the highly mobile metallic ions to the surface where evaporation results in up to 90 % losses, which are higher on samples with c-plane directed to the surface (m- and r-cut samples).

The OA measurements in the UV region allowed inspecting the evolution of O vacancy defects (F-centres), while surface plasmon resonant (SPR) bands were measured mainly in the visible region. Detection of the SPR bands was used to probe the emergence (above a threshold fluence) of the precipitates and measure their sizes. This allows envisaging the possibility of using the SPR band to estimate the implanted fluences. Varying the processing conditions made possible changing the SPR band maximum by up to 80 nm.

The optical activation of Eu or Yb doped sapphire was measured with IBIL, the maximum luminescence reached after annealing in air at 1573 K.

Keywords: sapphire, ion implantation, transition metals, noble metals, nanoparticles, plasmons.

Modificação de Óxidos de Alumínio por Implantação Iónica de Metais Nobres e de Transição

Resumo

Neste trabalho procedeu-se ao estudo de safira (α-Al_2O_3) implantada com metais de transição dos períodos *3d* (Ni, Cu e Zn) e *4f* (Eu e Yb) e com metais nobres (Ag e Au). As alterações estruturais e ópticas resultantes da implantação e dos tratamentos térmicos subsequentes, realizados em vácuo (1×10^{-4} Pa) ou à atmosfera ambiente, até 1573 K, foram caracterizadas com as técnicas de espectrometria de retrodispersão de Rutherford (RBS), por RBS em combinação com canalização iónica (RBS-C), difracção de raios-X (XRD), absorção óptica (AO) e ionoluminescência (IBIL). Esta última foi implementada com sucesso no decurso deste trabalho, sendo aqui feita uma descrição detalhada da sua instalação e funcionamento.

As fluências implantadas variaram entre 1×10^{15} cm^{-2} e 1.8×10^{17} cm^{-2}, obtendo-se concentrações atómicas máximas de 28 %, a profundidades que atingem algumas dezenas de nanómetros.

A implantação das fluências mais elevadas permitiu a produção de dispersões de precipitados metálicos, alinhados epitaxialmente com a rede cristalina da safira, e com dimensões características de 10 nm.

Os recozimentos efectuados ao ar (atmosfera ambiente) resultam na formação de óxidos mistos, com estruturas de espinelas, no caso dos metais de transição *3d*, e sesquióxidos no caso das terras-raras. Estes óxidos crescem alinhados com a matriz. Os hiatos electrónicos destes óxidos foram estimados por meio de representações de Tauc. A Ag e o Au não formam compostos e tendem a segregar formando um filme metálico à superfície, que evapora à medida que a temperatura aumenta e a frente de recuperação cristalina avança.

Após o recozimento em vácuo a temperaturas elevadas observou-se o crescimento das dimensões médias dos precipitados obtidos após implantação, cristalizando alinhados com a matriz. No caso dos elementos com baixo ponto de fusão (Cu, Zn) ou elevada mobilidade (Ag e Au), a frente de recristalização da safira segrega-os para a superfície da amostra onde evaporam ou são facilmente removidos. Este processo depende da orientação cristalográfica da matriz, sendo mais eficaz nos cristais em que o plano de maior mobilidade (plano c) intersecta a superfície (e.g. amostras r e m). No caso do Zn observou-se a formação de ZnO em amostras do tipo m.

Através da técnica de AO foi possível analisar os defeitos criados pelo processo de implantação na subrede do oxigénio bem como observar a formação da banda de ressonância de plasma de superfície (SPR) associada a precipitados metálicos. A medição da banda SPR permitiu estimar fluências limite para a formação de precipitados metálicos opticamente activos bem como medir a fluência implantada. Variando as condições experimentais foi possível variar até 80 nm a posição do máximo de absorção da banda SPR.

A activação óptica da safira dopada com Eu e Yb foi verificada por IBIL, nomeadamente após os recozimentos ao ar a 1573 K.

Termos chave: safira, implantação iónica, metais de transição, metais nobres, nanopartículas, plasmões.

Table of contents

List of figures

List of tables

List of symbols

Symbol	Significance
a	screening length
a_0	Bohr radius
a_{TF}	Thomas-Fermi screening length
α	polarizability
α_{abs}	absorption coefficient
α_{ext}	extinction coefficient
α_{sca}	scattering coefficient
B	FWHM of XRD diffraction peak
c	speed of light
C_{abs}	absorption cross section
C_{ext}	extinction cross section
C_{sca}	scattering cross section
d	damage thickness
D	diffusivity
ΔR_p	straggle
e	electronic charge
E	energy
E_{cal}	channel to energy calibration
E_d	displacement energy
E_D	damage energy density
E_m	migration energy
ε	reduced energy
ε_0	electrical permittivity of vacuum
ε	electrical permittivity
ε_h	electrical permittivity of host material
ϵ	stopping cross section
F	implantation fluence
$F_A(\lambda,x)$	self-absorption factor
F_{esc}	fraction of the total light produced which escapes the surface of the sample
f_{sub}	substitutional fraction
F_t	threshold fluence for SPR
γ	attenuation factor
γ_0	bulk attenuation factor
ρ	reduced range
H	Hamiltonian
h	Planck's constant
k	extinction coefficient
k_B	Boltzmann's constant
K	kinematic factor
λ	wavelength
M	mass
m_e	electron mass
N_0	atomic density
N_a	number of target atoms per unit area

N_{disp}	number of displaced lattice atoms per incident ion
n_{dpa}	number of displacements per atom
N_e	electron density
n_F	F-centre concentration
$\Psi_{1/2}$	angular scan FWHM
ρ	reduced range
p	volume fraction
Q	total number of incident projectiles
Q_{abs}	absorption efficiency
Q_{ext}	extinction efficiency
Q_{sca}	scattering efficiency
R	reflection coefficient
$R(\lambda)$	combined efficiency of the detector and light collection system
R_C	capture radius
R_{eff}	effective radius
R_p	mean projected range
σ	average scattering cross section
θ_B	Bragg diffraction angle
T	absolute temperature
τ	mean collision time
u	lattice atom rms thermal vibration amplitude; maximum absorption coefficient
μ	magnetic permeability; reduced electron-hole mass
μ_0	magnetic permeability of vacuum
U	FWHM of the optical absorption band
ν	crystal field potential
V_A	vacancy of atom A
χ_{min}	channelling minimum yield
ω	angular frequency
ω_p	plasma angular frequency
ω_F	Frölich angular frequency
Z	atomic number
Ω	detector solid angle

Table of acronyms

Acronym	Definition
AFM	Atomic Force Microscopy
ATR	Attenuated Total Reflection
BC	Binary Collisions
bcc	body centred cube
BNC	Bayonet Neill Concelman
BSP	Both Sides Polished
CAD	Computed Aided Design
CCD	Charge-Coupled Device
CFT	Crystal Field Theory
CL	Cathodoluminescence
CVD	Chemical Vapour Deposition
CZ	Czochralsky
DDA	Discrete Dipole Approximation
EELS	Electron Energy Loss Spectrometry
EFG	Edge-defined Film-fed Growth
EMT	Effective Medium Theory
fcc	face centred cube
FED	Field Emission Display
FWHM	Full Width at Half Maximum
GMT	Generalized Mie Theory
hcp	hexagonal closed packing
HEM	Heat Exchange Method
HRTEM	High Resolution Transmission Electron Microscopy
IB	Interband
IBA	Ion Beam Analysis
IBIC	Ion Beam Induced Charge
IBIL	Ion Beam Induced Luminescence
IBM	International Business Machines
IL	Ionoluminescence (same as IBIL)
IR	Infrared
ITN	Instituto Tecnológico e Nuclear
LED	Light Emitting Diode
LO	Longitudinal Optical
MBE	Molecular Beam Epitaxy
MC	Monte-Carlo
MFM	Magnetic Force Microscopy
MOCVD	Metal Organic Chemical Vapour Deposition
NDF	Nuno's Data Furnace
NDP	Neutron Depth Profiling
NEP	Nuclear Encounter Probability
NIR	Near Infrared
NM	Noble Metal
NMR	Nuclear Magnetic Resonance
NRA	Nuclear Reaction Analysis
OA	Optical Absorption

OSP	One Side Polished
PDA	Photodiode Array
PDF	Powder Diffraction File
PIXE	Particle Induced X-Ray Emission
PL	Photoluminescence
PLD	Pulsed Laser Deposition
PMT	Photomultiplier Tube
RBS	Rutherford Backscattering Spectrometry
RBS-C	Rutherford Backscattering Spectrometry under Channelling conditions
RE	Rare Earth
RED	Radiation Enhanced Diffusion
rms	root mean square
RT	Room Temperature
RZ	Reflection Z-scan
SAED	Selected Area Electron Diffraction
SI	Système Internationale
SPP	Surface Plasmon Polariton
SPR	Surface Plasmon Resonance
SRIM	Stopping and Range of Ions in Matter
TEM	Transmission Electron Microscopy
TM	Transition Metal
TO	Transverse Optical
USB	Universal Serial Bus
UV	Ultra Violet
VGA	Van de Graaff Accelerator
XRD	X-Ray Diffraction
ZPL	Zero Phonon Line

1 Introduction

The need of new materials is a consequence of the increasing demand from technological development, e.g. of ultrafast and nanoscale devices. The production of materials with tailored physical properties for specific applications is one of today's major challenges in Solid State Physics, and particularly in Materials Science.

In this work, we aim at the production of embedded and surface nanophases in synthetic crystalline sapphire (α-Al_2O_3) through ion implantation of transition (*d* and *f*-shell) and noble metals (NM), studying also the concomitant lattice defect production, inherent to this processing method.

Amongst the various production techniques, ion implantation stands for the unique possibility it offers of controlled introduction of any ion at the surface region of any solid material, with the desired concentration profile. Since it is not an equilibrium process, this technique allows, unlike others, overcoming thermodynamic limitations, e.g. solid solubility limits of paramount importance for the formation of embedded metallic precipitates. Moreover, ion implantation offers high purity processing, even at the isotopic level, a major advantage over chemical routes. However, being a ballistic process, the implanted region is often damaged which, for most applications, namely optical, implies a subsequent treatment to promote the recovery of the surface damage.

The widespread use of the ion implantation technique, both in the diversity of applications and range of materials used, stresses the need of knowing the mechanisms that govern the inherent ion damage production, i.e. the creation, behaviour and evolution of defects as well as their interactions with other defects and matrix atoms, processes accompanying the formation of the envisaged systems. The site location of the implanted ions and the full characterization of its local environment are also fundamental to understand the properties displayed by the system at each experimental stage.

Sapphire is the main subject of this work and a relevant material in several key technological areas due to its outstanding physical and chemical properties. Nevertheless, these properties may be enhanced, or even new ones may be created, through ion implantation, e.g. novel specific and tuneable optical emission or absorption by selective doping. The most common applications of doped sapphire are the $Ti:Al_2O_3$ and $Cr:Al_2O_3$ lasers, where titanium or chromium are introduced to create energy levels in the band gap of sapphire, these levels being used for lasing in the red region of the visible spectrum.

The production of low-dimensional structures or nanoparticles embedded in insulators like sapphire, i.e. composite materials or cermets (ceramic-metallic), has been also pursued aiming at ultrafast (ps regimes) non-linear optical properties (arising from the interaction of high intensity light beams) for application in the next generation of computers. Being chemically inert and optically transparent, sapphire allows the fundamental study of optical properties of the embedded structures in several wavelength regions of technological interest, e.g. infrared (IR) for telecommunications, visible for displays and common lasers, and ultraviolet (UV) for high capacity data writing devices.

This work aims at creating new properties in sapphire by ion implantation through the formation of new surface phases, namely of embedded or surface metal or semiconductor nanoprecipitates. The study of the damage induced by the ion implantation and its interaction with the implantation species as well as its thermal evolution was also pursued.

The major objectives of this research are:

1. the systematic study of the effects of ion implantation of sapphire with transition metals (including f-shell or rare-earths) and NM, taking into account the chemical and physical nature of the implanted species as well as the implantation conditions;

2. the characterization of the defects and structures produced after implantation and after the annealing stages;

3. the application of optical absorption technique as a mean to analyse quantitatively not only the defect centres in sapphire but also, in the case metallic nanostructures, the surface plasmon resonance (SPR) absorption and interband characteristics, inferring its size or the implanted fluence, and, for oxide structures, the band-gap energies;

4. to understand and control the mechanism of reaction of the implanted elements with sapphire in order to tailor and target specific structures, morphologies or phases;

5. to install and implement an ion beam induced luminescence (IBIL) line on the microbeam and Rutherford backscattering spectrometry (RBS) experimental chambers.

To achieve these goals, specimens of synthetic sapphire, cut with three different crystallographic orientations (due to the anisotropy of this material), were implanted with several ions at room temperature (RT) in the energy range from 100 keV to 300 keV and with effective fluences up to 1.8×10^{17} cm^{-2}, allowing reaching implanted concentrations up to 28 at. % at depths of a few tens of nanometres. The samples were subsequently annealed up to 1573 K in vacuum (10^{-4} Pa) or at atmospheric pressure and examined by several experimental techniques. The thermal behaviour of the precipitates is particularly important, namely for applications in optical devices that are subject to laser irradiation.

It was found that upon implantation of low fluences (< 5×10^{15} cm^{-2}, resulting in low atomic concentrations, below 0.7 at. %) the implanted species are partially distributed in regular lattice sites of sapphire. As the fluence increases the damage extension and concentration builds-up and eventually amorphization is reached (< 1×10^{17} cm^{-2}). Highly reactive elements, such as Yb, formed oxides already at this stage.

At high fluence implantation, with atomic concentrations of about 10 at. %, metallic precipitates are often already present in the highly damaged surface region of sapphire, namely in c-cut samples. The first signature of these precipitates is the characteristic SPR absorption band. The analysis and simulation of the optical absorption spectra allowed estimating the size of the precipitates.

The dimensions of these precipitates increase after annealing in vacuum (for T > 1073 K), improving also their crystalline quality and epitaxial relation with the substrate in a solid state epitaxy reaction. The systems obtained are composite materials, a ceramic embedding metallic aggregates, that is a cermet material. A low fraction of oxides is also present after this annealing and it was possible to produce ZnO precipitates in the case of Zn implantation.

On the other hand, large quantities of oxides and mixed oxides, namely transition metal (TM) spinels or rare-earth (RE) sesquioxides, are formed after annealing in open atmosphere at T = 1273 K or T = 1573 K, respectively. The band gaps of these structures ranged from 3.8 eV in the case of $ZnAl_2O_4$ to 5.5 eV for Eu_2O_3.

At the end of this work it was possible to predict both the dimensions and stoichiometry of the phases present after implantation and after each annealing stage for each ion, annealing temperature, annealing atmosphere and crystallographic type of the implanted sample.

The new experimental technique of ion beam induced luminescence was successfully introduced at Unidade de Física e Aceleradores at Instituto Tecnológico e Nuclear (UFA – ITN). The selection of components and assembly of the custom designed setup for IBIL will be briefly described and the first results presented. This technique allowed the characterization of defect centres as well as following the behaviour of RE doped sapphire upon annealing, where the emission efficiency was found to increase more after annealing in air than after annealings in vacuum at the same temperature. This is a highly desirable feature as annealing in air is less stringent than annealing in vacuum. It was also possible to show the similarity of the spectra obtained with IBIL to those from photoluminescence (PL) measurements.

Regarding the outline of this thesis, this first chapter includes a brief introduction to this work, its main purposes and the results achieved. The second chapter contains a detailed description of the base material used, sapphire, and of the state of the art about the subject under study, i.e. production of TM and NM nanostructures in solid materials and RE doping by ion implantation, and IBIL applications and setups.

The third chapter is dedicated to the general theory underlying the experimental techniques (divided by structural and optical analysis) and the description of the corresponding experimental equipment. It starts with the description of the interaction of high energy (up to 2 MeV) charged particles with matter, and the applications of relevance to this work: ion implantation and RBS. Along with the description of ion implantation the concomitant radiation damage processes will be discussed. The ion channelling effect will be introduced in the chapter about RBS, presenting the RBS under channelling (RBS-C) technique. The optical analysis section encompasses IBIL, with particular emphasis on the custom made experimental setup assembled within the frame of this work. It is followed by a short introduction to the theory of scattering of light by small particles and effective medium theories, since it is at the heart of one of the main probing techniques for metallic nanoprecipitates: far-field optical absorption (OA). The final part of this chapter is dedicated to the presentation of all the experimental equipment used.

The fourth chapter is dedicated to the presentation of the most relevant experimental results and is divided into: *3d* transition metals (Zn, Cu and Ni), noble metals (Ag and Au) and *4f* transition metals (the rare-earths Eu and Yb). Each of these subchapters ends with a comprehensive discussion of the results, with a cumulative set of conclusions. SI units will be used except where alternatives, widespread for historical or practical reasons, are most frequent, e.g. cm^{-1} or eV for energy.

Finally, the general conclusions are presented in chapter five, where the whole set of results is discussed and summarized, and future trends are exposed. References are listed at the end of this last chapter and formatted according to Elsevier standards.

In the course of this work it was developed an operating manual of the IBIL line, which is available online at http://www.itn.pt/facilities/lfi/manual_ibil.pdf.

2 Materials

2.1 Sapphire

Sapphire is the only thermodynamically stable single crystalline form of aluminium oxide, with chemical formula Al_2O_3. It has a hexagonal lattice and is usually denoted by α-Al_2O_3.

In fact, aluminium oxide exists in several different polymorphs, several of which are metastable phases (ζ-Al_2O_3, γ-Al_2O_3, δ-Al_2O_3, θ-Al_2O_3, κ-Al_2O_3, η-Al_2O_3, ρ-Al_2O_3 and χ-Al_2O_3) and α-Al_2O_3 which is thermally stable [Wef87, Tro98, Bod08]. The latter is also known as corundum or, as previously mentioned, sapphire. The metastable phases (also known as transition phases since mediate the formation of sapphire) are intrinsically nanocrystalline [Bod08]. For example, the ζ, γ and δ-Al_2O_3 phases are considered to be a defective spinel (cubic) structure, i.e. a spinel structure with a deficit of cations, which evolve to monoclinic θ-Al_2O_3 upon annealing [Zho91]. The evolution from one form to another depends on the precursor (e.g. gibbsite, boehmite, diaspore, etc.) and treatment used (chemical vapour deposition – CVD –, direct oxidation of aluminium, Al_2O_3 powders for sintering or flame fusion as in Verneuil method, mechanical milling, etc.), and some intermediate phases may not form. *Figure 2.1* shows some processing routes leading to the formation of stable α-Al_2O_3 phase.

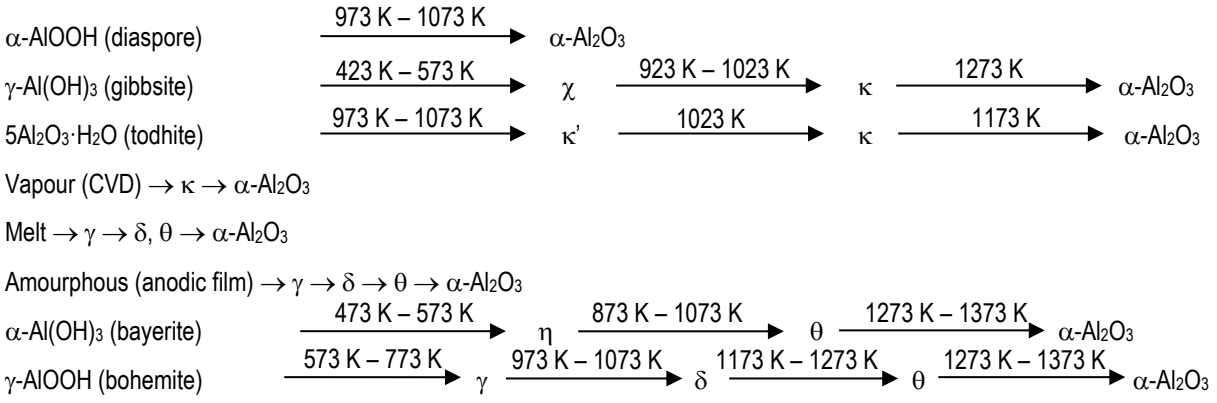

Figure 2.1 – Common processing routes resulting in the formation of different metastable Al_2O_3 structures and the sequences of phase transformations toward the stable α-Al_2O_3 phase [Tro98].

The ultimate, and monotropic, conversion is to α-Al_2O_3 and occurs at temperatures above 1273 K [Wef87]. In fact, this evolution is basically achieved by the reorganization of Al ions in an essentially fixed O lattice on the precursors. In the form of sapphire, all aluminium ions are in octahedral positions. Table 2.1 shows the distribution of the aluminium ions in several lattice positions for some aluminas.

Aluminium oxide may exist also as an amorphous material, i.e. amorphous alumina or a-Al_2O_3. In this phase it is considered the most important oxide ceramic material, with applications as microwave substrate, axles, sliding rings, pressure resistant parts, etc. The main advantages of single crystal sapphire over polycrystalline alumina are that it is transparent, non-porous and contains no grain boundaries. For instance, the use of single crystalline sapphire will eliminate corrosion along grain boundaries.

Table 2.1 – Aluminium coordination (%) in some the transition aluminas and sapphire [Zho91].

Form	Octahedral	Tetrahedral	Quasi-octahedral	Quasi-trihedral
η-alumina	51	36	0	13
γ-alumina	43	32	25	0
θ-alumina	50	50	0	0
α-alumina	100	0	0	0

The most stable phase is thus α-Al_2O_3 or sapphire, the form studied in this work. The main physical, optical, thermal, electrical and mechanical properties of sapphire are summarized in Table 2.2.

Table 2.2 – Main properties of sapphire at RT (mainly from references W1 or W2).

Chemical formula	α-Al_2O_3
Ion distances	Al – O, 0.198 nm ; 0.184 nm O – O, 0.272 nm ; 0.249 nm Al – Al, 0.280 nm ; 0.349 nm ; 0.376 nm
Molar mass	101.96 g mol^{-1}
Specific volume	3.985 g cm^{-3}
Atomic density	1.1768×10^{23} at. cm^{-3}
Symmetry and space group	$R\bar{3}c$, 167
Unit cell dimensions	a = b = 0.4748 nm; c = 1.2957 nm
Ionic radii	Al^{3+}: 0.039 nm; O^{2-}: 0.124 nm Al^{3+} : 0.053 nm; O^{2-} : 0.138 nm
Melting point	2326 K (2053 °C)
Boiling point	3253 K (2980 °C)
Thermal conductivity	40 W $(m\ K)^{-1}$
Debye temperature	1024 K (751 °C)
Speed of sound	~10^4 m s^{-1}
Thermal expansion coefficient	5.6×10^{-6} K^{-1} (parallel to *c*); 5.0×10^{-6} K^{-1} (normal to *c*)
Limit working temperature	2123 – 2193 K (1850 – 1920 °C)
Specific heat	750 J K^{-1}
Hardness (Mohs)	9 – 9.4
Hardness (Knoop)	2.1×10^9 kg m^{-2} (parallel to *c*); 1.8×10^9 kg m^{-2} (normal to *c*)
Friction coefficient	0.14 (against steel)
Young's module	400 GPa
Refraction index (at 598 nm)	1.760 (parallel to *c*); 1.768 (normal to *c*)
Birefringence	0.008
Optical transmission	0.17 to 6.5 μm (7.29 to 0.19 eV)
Electronic gap	8.5 – 9.5 eV
Electrical resistivity	10^{18} Ω m
Dielectric constant	9.4, normal to *c*; 11.6 parallel to *c*; (from 10 to 3×10^9 Hz)
Solubility	Insoluble in common acids and bases up to 1300 K; reacts only with HF and H_3PO_4 above 600 K
Chemical stability	Stable in contact with W, Mo and SiC (in the absence of O_2) up to the melting point
Enthalpy of formation	- 1676 kJ mol^{-1}
Phonons	LO_{ext} 0.064 eV (516 cm^{-1}); LO_{ord} 0.060 eV (484 cm^{-1})
Plasma energy	27.9 eV (free electron model); 21.6 eV (bulk)

It is important to notice that some of the values are not unique in the literature, e.g. reported energy gaps vary from 8.5 eV to 9.5 eV, the melting and boiling temperatures differ by some degrees, etc. The values presented are mainly taken from the datasheets of sapphire provided at the websites of some suppliers.

Sapphire is a light non-porous ceramic insulator, the hardest natural substance next to diamond, a chemically inert and an optically transparent material. It has unique physical, chemical and optical properties such as high surface hardness, excellent optical transmission, from the ultraviolet to the near infrared, high electrical resistance, very high melting temperature, high thermal conductivity (even better than copper when at cryogenic temperatures) and high dielectric constant.

Sapphire has a rhombohedral primitive cell, and belongs to the space group $R\bar{3}c$, as indicated in Table 2.2, with two formula units (z = 2) per cell. The lattice is better described as hexagonal by the association of three rhombohedral primitive cells (thus z = 6). The Bravais lattice of sapphire is hexagonal close-packed (*hcp*) with ABABAB structure and lattice constants of $a = b = 0.4748$ nm and $c = 1.2957$ nm. The O^{2-} anions are approximately hexagonally close-packed. The Al^{3+} cations are ordered occupying 2/3 of the available octahedral sites, the remaining 1/3 being vacant, i.e. in α-Al_2O_3 the oxygen ions create a *hcp* structure in which the aluminium ions are symmetrically placed in octahedral gaps between successive *hcp* layers of oxygen atoms, forming trigonally distorted AlO_6 octahedra (point symmetry C_3). The crystal structure of sapphire and the open octahedral sites between layers of close packed oxygen ions are shown in Figure 2.2a (in the c-plane) and Figure 2.2b (along the c-axis). The Al^{3+} ions and the vacant octahedral sites are arranged to achieve maximum separation of like charges and minimum separation of unlike charges, consistent with the necessary bonding between aluminium and oxygen, while maintaining overall electrical neutrality. The bonding is mainly ionic with some covalent character. Lagerlöf and co-workers suggest a partial charge for oxygen of -1.70 and thus +2.65 for aluminium [Lag98].

Even if the structure of sapphire may be described on the basis of close packing, there may be significant deviations from the ideal close-packed structure as a result of the electrostatic interactions between the ions.

Sapphire, being rhombohedral, exhibits anisotropy, i.e. it has different characteristic properties when measured along different axes, like hardness or refractive index (and thus has optical birefringence, cf. Table 2.2). This feature of single crystal sapphire implies that it must be produced with definite crystallographic directions. Sapphire crystals are commercialized with surfaces cut parallel to planes (0001) (c-cut samples), $(11\bar{2}0)$ (a-cut), $(10\bar{1}0)$ (m-cut), $(11\bar{2}3)$ (n-cut) or $(1\bar{1}02)$ (r-cut), or even without any specific orientation (cheaper material). Figure 2.2c and Figure 2.2d illustrates some of these crystallographic planes and directions. Out of the three major orientations, the c-axis is preferred for optical applications because it is the zero birefringence orientation.

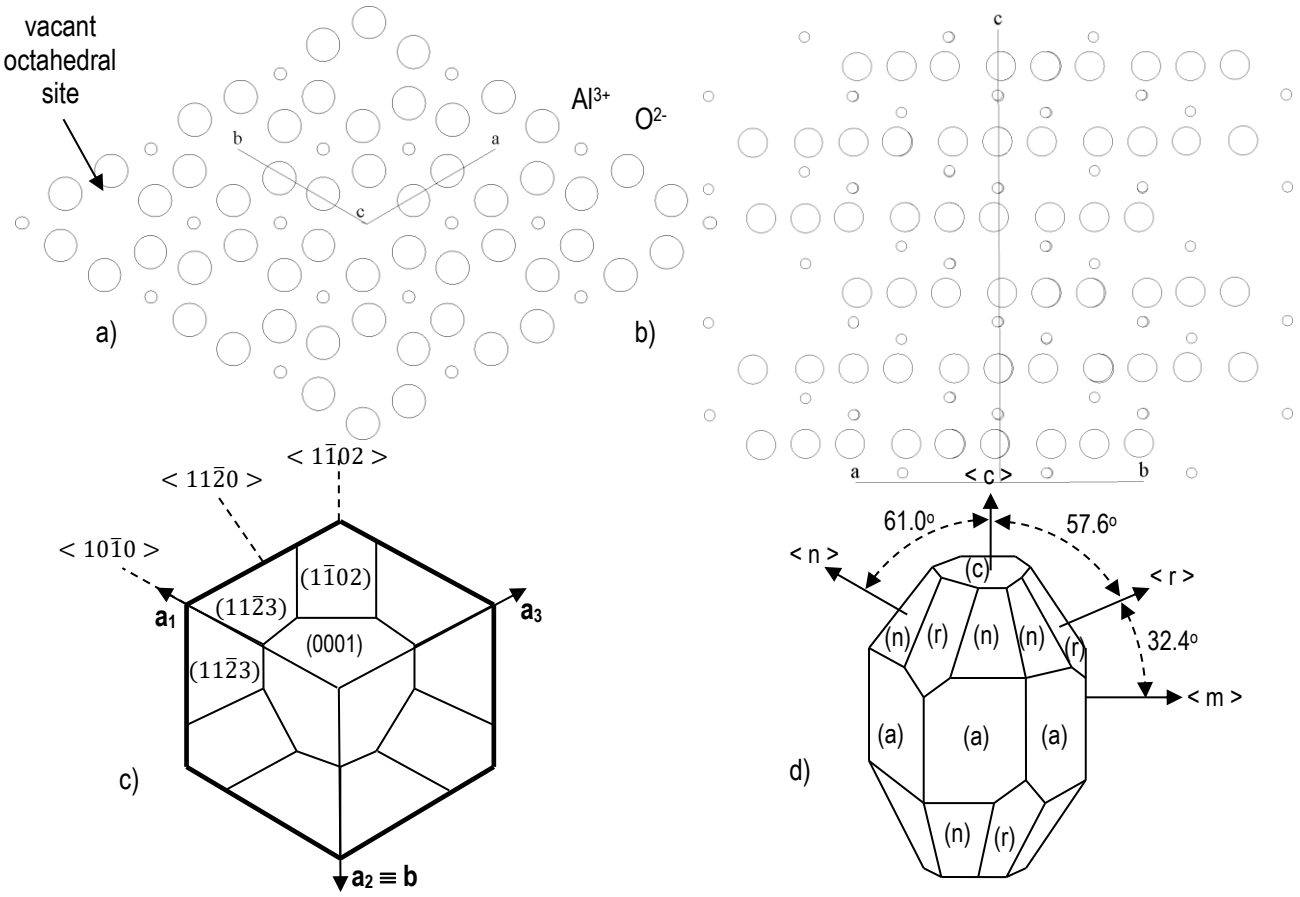

Figure 2.2 – Schematic representation of the crystalline structure of sapphire: a) along (0001) plane where it is visible the 2/3 occupation by Al^{3+}; b) Al^{3+} aligned along the c-axis (ABABAB packing); c) top view of the hexagonal cell resulting from three rhombohedral primitive cells with some of the major crystallographic planes and axis of sapphire and d) lateral view ditto [W1].

The base vector $\boldsymbol{a_1}$ (or $\boldsymbol{a}$), $\boldsymbol{a_2}$ (or $\boldsymbol{b}$), $\boldsymbol{a_3}$ and $\boldsymbol{c}$ belong to the 4 index Miller-Bravais notation used with hexagonal lattices. The conversion relations for the direction indices between the three axis notation [*h'k'w'*] and the four-axis notation [*hkiw*] are [Whi81]:

$$h = \frac{n}{3}(2h' - k') \quad [2.1]$$

$$k = \frac{n}{3}(2k' - h') \quad [2.2]$$

$$i = -(h' + k') \quad [2.3]$$

$$w = nw' \quad [2.4]$$

The variable *n* is chosen as to obtain whole numbers indices. In this work the four-index system will be used on hexagonal systems while cubic cells are identified with the standard three-axis indices.

2.2 Native defects in sapphire

Nearly all oxides exhibit large deviation from stoichiometry, but in α-Al_2O_3, any deviation from stoichiometry is too small to be detected. Therefore, while it is possible to substitute Al^{3+} for 3+ impurities (e.g. Cr^{3+} or Ti^{3+}, intrinsic impurities present in the μg/g range), it is impossible to incorporate impurities without creating charge-compensation defects. In fact, the previously mentioned vacant octahedral sites are structural vacancies and are ordered to maintain the electrostatic forces within the crystal.

The main point defects experimentally observed in α-Al_2O_3 are oxygen vacancies (F-type centres) containing trapped electrons: the F^+-centre (an oxygen vacancy with one electron) and the F-centre (an oxygen vacancy trapping two electrons). Oxygen divacancies, F_2-centres, are also observed, and there is some evidence for Al^{3+} interstitial-type defects in the form of Al pairs [Mor97]. No evidence for aluminium vacancies (V centres) exists according to some researchers [Mot86]. However, Valbis and co-workers assigned an absorption band in sapphire irradiated with UV radiation to V^- and V^{2-} centres (aluminium vacancies which have trapped two or one holes, respectively) [Val91]. Dislocations are also observed, as well as impurity-defect complexes.

The optical properties of sapphire are thus essentially sensitive to the presence of point defects and defects complexes in the oxygen sublattice. Table 2.3 lists the characteristics of the most common defect centres in sapphire [Eva94, Tow94 and references therein].

Table 2.3 – Optical characteristics of the most common defect centres found in sapphire.

Defect centre	Absorption nm (eV)	Emission nm (eV)	Transition	Number of vacancies	Number of trapped charges	Oscillator strength	Lifetime (s)
F	205 (6.05)	420 (2.95)	$^1S \rightarrow {}^1P$	1 (O)	2 (e)	1.3	0.034
F^+	203 (6.11) 225 (5.51) 258 (4.81)	325 (3.82)	$1A \rightarrow 2B$ $1A \rightarrow 2A$ $1A \rightarrow 1B$	1 (O)	1 (e)	0.66	3×10^{-9}
F_2	300 (4.14) 329 (3.77) 352 (3.52) 374 (3.32)	322 (3.85)	-	2 (O)	4 (e)	-	-
F_2^+	355 (3.49)	379 (3.27)	-	2 (O)	3 (e)	-	-
F_2^{2+}	455 (2.73)	550 (2.25)	-	2 (O)	2 (e)	-	-
V			-	1 (Al)	3 (h)	-	-
V^-	410 (3.02)		-	1 (Al)	2 (h)	-	-
V^{2-}	410 (3.02)		-	1 (Al)	1 (h)	-	-
Cr^{3+}	409 (3.03)	694.5 (1.785) 693.0 (1.789)	$^2E \rightarrow {}^4A_2$ $^4A_2 \rightarrow {}^4T_2$ $^4A_2 \rightarrow {}^4T_1$	-	-	-	0.002
Ti^{3+}	230 (5.39)	414 (3.00) 790 (1.57)	$^2T_2 \rightarrow {}^2E$	-	-	-	-

The F-centre excited state is very close to the conduction band and hence it is possible to an electron in this state to be easily promoted to the conduction band, being later trapped in an impurity level created by a defect centre or impurity. This is shown in the diagram of the energy level scheme for absorption and emission of F and F^+ centres in sapphire presented in Figure 2.3.

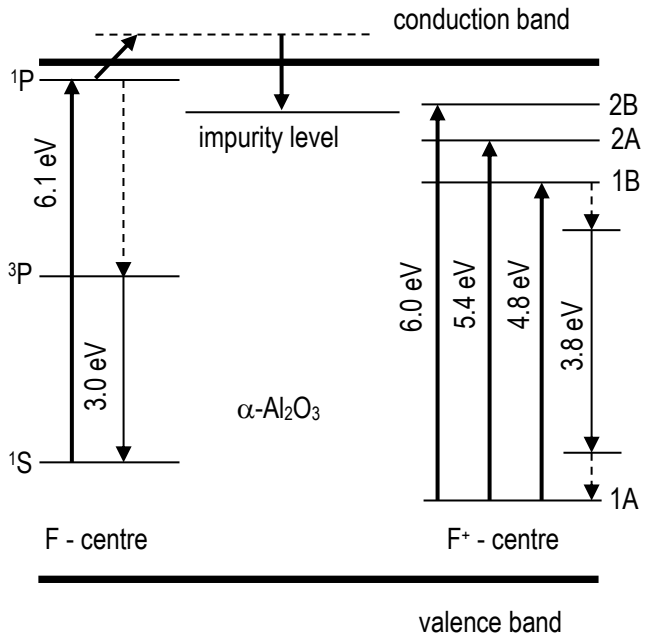

Figure 2.3 – Diagram of the energy level scheme for absorption and emission processes associated with F and F$^+$ centres in sapphire, where the dotted arrows represent non radiative paths (adapted from [Eva78]).

The F$^+$-centre has C_2 symmetry which causes the *2p* state to split into *1B*, *2A* and *2B* states [Eva78]. The emission and absorption wavelengths of F-type centres are not exact values and it is possible to find slightly different values in the literature, e.g. recently Zhou and co-workers attributed the values of 5.344 eV and 4.881 eV for the absorption of F$^+$-centres [Zho06]. Moreover, in this work a 6.078 eV absorption is ascribed exclusively to F-centre absorption, which may be incorrect since it should comprise the *1A* → *2B* of the F$^+$-centre absorption.

F-type centre studies begun with alkali halides, for which models are established for F-type centre production during irradiation with high energy particles. One of these models has been applied to radioluminescence measurements in pure sapphire by Moroño and co-workers [Mor02]. In this model, radiation produces Frenkel pairs which will interact with pre-existing F-centres. The proposed model is sketched in Figure 2.4.

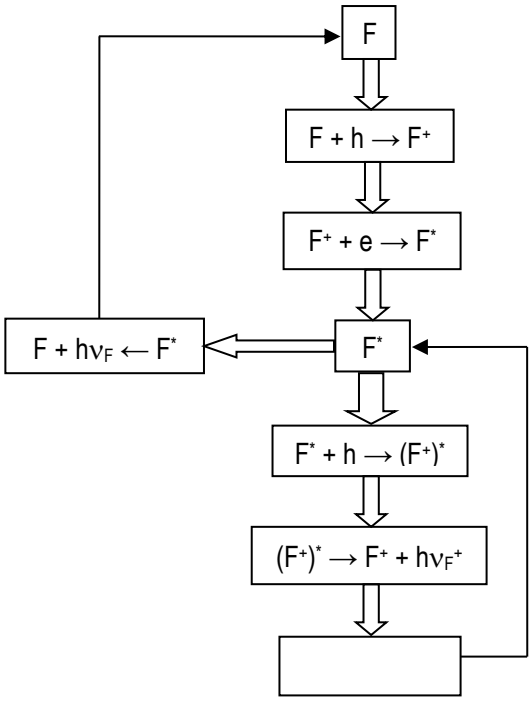

Figure 2.4 – Flow diagram for the F and F$^+$ centres luminescence processes [Mor97].

The pre-existing F-centre captures a hole (*h*) and an F$^+$-centre is created. This centre rapidly captures an electron and an excited F-centre (F*) is obtained. This decays to an F-centre by emitting a 3.0 eV photon, thus recovering an F-centre. However, this is a slow process (a few milliseconds) since it is a strongly forbidden triplet to singlet transition (cf. Figure 2.3). Therefore, it is possible for this F* state to capture a hole and become an F$^+$-centre in an excited state. The deexcitation is fast (ns regime), for it's an allowed transition, emitting a 3.8 eV photon. The F$^+$-centre then captures an electron and an F* state is restored.

This group applied a generally accepted model for the evolution of F-centre concentration during irradiation time (F-colouring curves) of alkali halides to sapphire [Mor02]. This model describes the growth of F-centre concentration (N_F) by:

$$N_F = \sum_{i=1}^{m} A_i(1 - e^{-a_i t}) \qquad [2.5]$$

where:

$$a_i = \sigma_i \phi + \frac{1}{\tau_i} \qquad [2.6]$$

$$A_i = \frac{(\sigma_i \phi N_{0i})}{\sigma_i \phi + \frac{1}{\tau_i}} \qquad [2.7]$$

and N_{0i} is the concentration of trap i, σ_i is the cross section for capture of interstitials by these traps, τ_i the lifetime of the interstitial in trap type i and ϕ is the flux of interstitials during irradiation. Assuming that $\sigma_i \phi \ll \frac{1}{\tau_i}$ then:

$$a_i \approx \frac{1}{\tau_i} \qquad [2.8]$$

Two different trap types or components are used to better fit the F couloring curves. Despite this model being used in radioluminescence experiments (1.8 MeV electrons) we will explore it with IBIL in chapter 4.5.

When using ion implantation to dope sapphire several defect types are produced. In this respect, simulations obtained with computer codes like SRIM (Stopping and Range of Ions in Matter) [Zie09] give information on the production of vacancies in each sublattice, considering only the binding energies involved in an amorphous material. Table 2.4 lists the threshold displacement energies (E_d) of several ceramics. In this work the values obtained from Caulfield and co-workers will be used [Cau93].

However, many vacancies recombine with an interstitial of the same kind during the "cool-down" period (10^{-9} s). It is the surviving defects that are of interest. Attempts to determine the surviving fraction of defects in the oxygen sublattice by comparing the number of F and F^+-centres present in ion implanted sapphire with the number obtained by calculations have been reported by Agnew [Agn92] and Pells [Pel79a]. Agnew's results for implantations and measurements made at RT indicate surviving fractions of 0.08 to 0.17 for implantation of B, N, Ar and Kr with fluences of 1×10^{12} cm^{-2} to 5×10^{12} cm^{-2}. The low fluences were used in an attempt to avoid the displacements cascades. The measurements did not include defects that may have formed clusters. It is important to note that the surviving fraction was higher for the lighter B than for the other species.

The observations of Ren [Ren95] for as implanted specimens showed F^+- centres to be favoured at the expense of F-centres in the regions of high defect density generation by all ions but hydrogen or helium. These researchers found that F-centre production was favoured in implantation of lighter ions that did not produce dense cascades along their tracks. They also observed additional optical absorption peaks that they attributed to clusters of defects involving the oxygen sublattice.

Table 2.4 – Threshold displacement energies in ceramics [Zin97].

Material	Threshold displacement energy, E_d (eV)
α-Al_2O_3	E_d (Al) ≈ 20; E_d (O) = 50 E_d (Al) = 31; E_d (O) = 51 [Cau93]
MgO	E_d (Mg) = 55; E_d (O) = 55
$MgAl_2O_4$	E_d (O) = 60
ZnO	E_d (Zn) ≈ 50; E_d (O) = 55
BeO	E_d (Be) ≈ 25; E_d (O) = 70
UO_2	E_d (U) = 40; E_d (O) = 20
SiC	E_d (Si) ≈ 40; E_d (O) = 20
Graphite	E_d (C) = 30
Diamond	E_d (C) = 40

The nature of the residual damage resulting from displacements in the Al sublattice is poorly characterized and understood. Crawford [Cra84] noted that any enhancement of the V-type absorption band expected to be associated with cation vacancies has not been observed. Pells and co-workers [Pel79b, Pel79c, Sta83] observed features in sapphire subjected to electron irradiation at 873 K and above in a electron microscope, suggesting to be stoichiometric interstitial dislocation loops (loops composed of aluminium and oxygen interstitial ions in the ratio of 2:3) and Al colloidal particles. It was proposed that the features identified as Al colloids arose from the aggregation of Al interstitials. Moreover, Hunt and co-workers [Hun97] reported the presence of 12 nm – 13 nm crystals of Al containing a small amount of highly stable yttria in the amorphous region of a sample of sapphire implanted with 5×10^{16} cm^{-2} Y of 150 keV, at RT. No attempt was made to ascertain the disposition of the vacancies left in the Al sublattice.

The asymmetry in the formation of vacancies is due to the different energy of formation: 3.5 eV for O^{2-} and 9.1 eV for Al^{3+} [Die75]. Other researchers found 5.17 eV for the energy of formation of Schottky defects and 4.87 eV and 6.59 eV required for oxygen and aluminium Frenkel pairs, respectively [Lag98].

Despite all this work, there are a lot of open questions about the process of damage production, namely the influence of the implanted ion or of the specific implantation parameters (temperature, current density, etc.).

2.3 Applications and state-of-the-art

The combination of all the properties listed in Table 2.2 in sapphire allows this material to withstand the high temperature, high pressure, thermal shock, abrasion and erosion of harsh environments, such as those needed to meet the stringent demands of recent advances in key technological areas such as in optics and laser systems, semiconductors manufacturing equipment, optoelectronics, medical instruments and surgical devices, military and aerospace components. In fact it finds extensive use as a substrate for catalytic materials, nuclear storage compartments, spacecraft windows, substrate for materials engineering, transparent dome in high speed missile systems and satellites or glass melting operations.

For example, during the “Star Wars” program (particularly in the Strategic Defence Initiative), sapphire infrared windows were a key component for the High Endoatmosphere Defense Interceptor. The windows were required to withstand very high launch stresses and to protect the infrared sensors from raindrops, dust and other debris at speeds as high as Mach 15. As part of that program, McHargue and Snyder [McH93] demonstrated that

an improved polishing technique followed by implantation of chromium greatly increased the resistance to fracture. The design stress for high reliability, i.e., probability of failure less than 0.1 %, could be increased by a factor of 100 over that allowed by conventional fabrication processes even if the transmission was decreased by 1 % in the IR region of interest. The increase in fracture strength was attributed to the elimination of surface flaws created by the polishing process and to the introduction of a high residual compressive stress by the implantation. The residual compressive stress was measured to be greater than 1 GPa [McH89, Spe92].

The exceptional chemical stability, even at high temperatures in corrosive environments, makes sapphire a widely used substrate in thin film growth processes. Combined with the hexagonal structure, this makes it the top choice as substrates for materials with hexagonal type structures such as ZnO, GaN, AlN, YBaCO, etc. The high chemical stability can effectively reduce the interface reaction between the thin film and sapphire substrate so that thin films can be grown with high crystalline quality. Moreover, the large band gap of sapphire allows optical characterization of the thin films developed on it to be carried out without significant disturbance in the 200 nm to 6500 nm wavelength range.

It has the lowest acoustic loss of any material and such small thermal vibrations that it may be used in laser interferometry for gravitational wave detection, as that performed at the Laser Interferometer Gravitational Wave Observatory, accurately measuring position with a precision of 10^{-17} m.

Sapphire is produced by several methods, namely Czochralsky (CZ), Bridgman, Verneuil, EFG (edge-defined film-fed growth) or HEM (Heat Exchanger Method), with crystals reaching up to ($250 \times 250 \times 30$) mm^3 [Con90]. The production of larger crystals is sought mainly for space and military applications. Commercial crystals have high purity (less than 10 μg/g of elements like Si, P, Cl, K, Ca, Ti, V, Cr or Fe) and excellent transparency in the wavelength range from 0.2 μm to 6 μm. Nevertheless, the presence of intrinsic defects (essentially F-type centres) produces well known absorption bands (see Table 2.3).

In the following sections the state-of-the-art of the systems studied in this work will be presented.

2.3.1 α-Al_2O_3:TM

Metallic nanoparticles embedded in dielectric matrices (composite materials or cermets) are of great interest, both from the theoretical and application points of view. The formation of metal nanoclusters in transparent materials is of high technological interest due to the optical resonances in the visible spectrum, related to plasmon resonance of the metal/alloy considered.

The optical response of clusters is a function of their electronic structure, which strongly depends on their shape and dimension and also on the properties of the host material. The control of the clusters morphology allows designing and tuning the optical absorption characteristics of the system. These linear and also other arising nonlinear effects have long been used to colorize glasses and can also be used in all sorts of optical applications, like switches, real time holography, waveguiding or diffraction devices. The non optical applications include paramagnetic particles for magnetic resonance contrast imaging and metal particles for thermal probing of specific biomolecular interactions [Tan02].

The key issue is that with plasmon-based structures light can be confined to and manipulated on a scale smaller than the wavelength of light (one sixth of a few hundred nanometres), i.e. smaller than would be possible by conventional (far-field) optics [Bar03]. A striking example of this phenomenon is the high transmission efficiency of light through sub-wavelength holes in a thick metal screen [Ebb98, Din05]. The enhanced field intensity close to surface corrugations (like the holes in the metal film) is currently being investigated for use in near-field optical lithography and near-field optical storage heads [Din05, Lin05].

Exploiting the interfacial nature of the surface plasmons, thin metal films can replace dielectric waveguides in optical devices, as the electromagnetic energy (confined to the metal-dielectric interface) can be guided over distances of tens to hundreds of micrometers for visible and infrared wavelengths [Dio05, Atw05]. Very tight lateral confinement of light can be achieved by use of linear arrays of metal nanoparticles, along which electromagnetic energy can propagate over a micrometer distance [Qui98, Bro00]. Furthermore, the high local field enhancements close to the metal particles can be exploited for molecular sensors and spectroscopy and nonlinear optical elements [Xu00, McF03, Whi05]. Applications of SPR features, namely SPR propagation, e.g. surface plasmon polaritons (SPP) are presented in [Bar03].

Small particles of different sizes and shapes have been shown to be suitable markers, contrast agents (e.g. in optical coherence tomography) or therapeutic agents for biomedical applications [Fuj03, Hir06]. For these applications it is advantageous to be able to tune the particle plasmon resonance to the near-infrared region between 650 nm and 900 nm, where water and haemoglobin have their lowest absorption coefficient [Jin01, Kel03]. On the other hand, for such applications as Blu-Ray (successor of DVD for data storage), wavelengths around 400 nm are required. This tuneability is provided by engineering the size, shape, composition and geometry of the particles as well as their local environment. The field of plasmonics has an excellent reference book with special focus on technological applications in [Mai07].

Third period transition metal ion dopants have a strong interaction with the crystal field due to the relatively large radius of the *3d* orbitals and the fact that they are unshielded by outer shells. In crystalline materials the crystal field splits the *3d* states and the strong coupling to phonons broadens these states into continuous vibronic bands. This gives rise to continuous absorption and emission bands. As the concentration of dopant increases metallic aggregates develop and metallic like behaviour is observed, e.g. plasma oscillations.

Regarding the ions used in this work, Ni-Al-O systems have been widely studied mainly from the point of view of catalytic applications (e.g. in the metane-steam reforming process) [Bol95, Jun99, Kim03, Mat04], usually starting from the unwanted spinel phase ($NiAl_2O_4$) and reducing it through thermal annealings to metallic Ni, the active catalyst, and crystalline aluminium oxide [Bol93], or in Ni-Al containing alloys operating at high temperatures in ambient atmosphere where oxide formation compromises performance [Lee99, Abe04, Sal04]. The reduction method has also been used to produce composite materials, a process that is somewhat the inverse of ion implantation and annealing [Ust00, Iso07]. This body of work allowed understanding the thermodynamics of the solid state reaction between these components, with the essential aid of the phase diagrams of Elrefaie and co-workers [Elr81] and the spinels studies of J.S. Armijo [Arm69]. Extensive research has also been performed on cermets of $Ni:Al_2O_3$ as resistor materials for applications such as gas flow sensors [Chi06a].

Ion implantation of Ni in sapphire was initially experimented in an extensive study of the mechanical changes induced by ion implantation [Hio86], where a 30 % volume increase was measured in the radiation amorphized region. Electrical studies in a similar system were later performed by Kobayashi and co-workers [Kob96]. The specific production of embedded pure Ni precipitates in oxides by this method for magnetic and optical studies followed and, in particular, has recently been studied in sapphire [Xia04a, Xia05] and also in silica [Gon99, Ame04]. The main issue with ion implantation is the control of the size distribution and, to a lesser extent, of the composition of the precipitates. In these works the SPR and intra-band absorption bands are inferred, thoroughly using the first optical studies of transition metals of W.E. Spicer [Spi66] and Müller and co-workers [Mül66]. Several other works have also been performed in other host materials, namely $CdCsBr_3$ [Vir92], yttria-stabilized zirconia [Xia04b] or ZnO [Ull03].

About copper, the study of nanoparticles of this element follows that of the other noble metals (completely full *d* shell: Ag and Au), taking advantage of its low reactivity as well as of its electronic characteristics. Cu implantation in oxides has been reported mainly to produce composite materials of metallic or oxides particles embedded in insulator or semiconductor matrices. Amekura and co-workers have reported the production of CuO and metallic Cu by ion implantation into SiO_2, having also measured the SPR band of Cu nanoparticles in this material to be centred at 2.15 eV [Ame04, Ame05]. Oxide particles were also produced by high energy co-implantation of Cu and O in sapphire [Nak02]. Kishimoto and co-workers reported Cu metallic clusters formed by ion implantation in a-SiO_2, MgO·2.4(Al_2O_3), MgO·1.0(Al_2O_3), $SrTiO_3$ and $LiNbO_3$, studying the optical properties of these systems [Lee02, Tak02, Kis02, Kis03]. In particular, Kishimoto and co-workers used laser irradiation during Cu implantation in a-SiO_2 to process the morphology of the systems created since this particular annealing method allows defining the treated volume to the surface layers [Kis02].

Some of the studies involving nanoparticles of copper are dedicated to investigate the non-linear optical properties of these phases, namely the third order susceptibility [Fal98, Ser01, Ste05a, Yes07]. In this context Stepanov and co-workers have studied shelled nanoparticles, with a Cu core involved by an oxide (CuO or Cu_2O) shell, after Cu (40 keV) implantation in sapphire, followed by laser annealing [Ste02]. In this work the implantation current density is shown to affect the depth distribution of copper, with the enlargement of the implanted profile with increasing current and hence, with a higher deviation from computer codes predictions, as those of SRIM. This affects also the optical response, with a small red shift of the SPR band with increasing current. A review of these effects was later published by the same author [Ste05b]. Similar energy implantation was recently also used to produce composite layers for optoelectronics materials, where copper particles would act as an optical switcher in waveguides [Mir07]. Townsend and co-workers measured the luminescence of copper in silica and alumina and the results were inconclusive about the interpretation of the interaction of copper with these substrates [Tow01, Wu02], a conclusion we also drew from trial experiments with photoluminescence. Garces and co-workers followed the influence of copper oxidation state in the green luminescence of copper doped ZnO [Gar02]. The study of this system was later complemented with ion implantation of copper into the same host matrix [Kar05].

The production of nanoparticles also involves chemical methods as the case of the work of Liu and co-workers where mesoporous silica is soaked in copper nitrate and dried, followed by thermal reduction at 973 K. The SPR band was investigated and the authors found a red shift on the SPR band related to the oxidation of the

outer layer of the nanoparticles [Liu02]. Yeshshenko and co-workers studied recently the morphology of the SPR band with temperature and diameter of nanoparticles embedded in silica by the sol-gel method [Yes07]. The effect of temperature revealed, according to these authors, a strong electron-phonon interaction. The size of the particles ranged from 2 nm to 65 nm and was controlled by the annealing atmosphere. Luminescence measurements were also performed in this work and an increase on the luminescence efficiency was reported with decreasing particle size, a process related to photon-plasmon coupling. Finally, aqueous colloid solutions with metallic and oxidised copper nanoprecipitates were also achieved by Paradies and co-workers [Par00].

The interest of Zn systems is mainly directed to the production of zinc oxide structures. ZnO is currently the focus of considerable research since it is a wide band-gap semiconductor (3.3 eV), with a large free exciton binding energy of 60 meV (as compared with 26 meV for GaN or 20 meV for ZnSe), which stabilizes excitons even at RT (where $kT \approx 26$ meV). This large exciton binding energy of ZnO allows excitonic recombination and optically pumped laser oscillations at RT. In the nanometre range the size of the particles affects and determines the band-gap in semiconductors, becoming thus possible to tailor the electronic properties of the material (band gap engineering).

Several methods have been used to produce ZnO structures, from films to nanoprecipitates, namely MBE [Mur05, Sha05, Kum06], CVD [Ata96], MOCVD [Chi06b], PLD [Cho99] or ion implantation [Xia06a, Ame07], aiming at optimizing the crystalline quality and controlling (and narrowing) the size distribution, the latter as a means to control the band gap of the precipitates.

Since the passivation of the Zn phases in contact with air affects the efficiency of the desired optical behaviour encapsulated structures are preferred. In this context, ion implantation surpasses other techniques and zinc has been implanted in several oxide hosts, from SiO_2 [Che98, Liu02, Ame05, Ame07] to MgO [Hui04] or sapphire [Xia06a, Xia06b], in attempts to produce embedded semiconductor ZnO aggregates, with Zn metallic precipitates also reported. In sapphire, these metallic precipitates have SPR absorption bands in the UV region [Xia06a]. Only recently the production of ZnO by Zn implantation into c-cut Al_2O_3 has been reported using fluences of 1×10^{17} cm^{-2} and implantation energy of 48 keV followed by annealing in O_2-flow in the range 873 K – 1073 K [Xia06a]. Unfortunately this temperature range limits the crystalline recovery of the host matrix that is essential to preserve the optical properties of the phases formed, since implantation defects act as non-radiative paths for de-excitation and thus compromise the optical performance of the system. The production of ZnO precipitates was also achieved in silica glass namely by Amekura and co-workers using 60 keV Zn ions followed by oxidation at 973 K [Ame05].

Colloidal zinc and zinc oxide were recently produced by laser ablation in aqueous solution by Singh and co-workers, who reported the SPR bands of ellipsoidal Zn nanoparticles in the UV and blue region of the spectra [Sin07].

Zn and O sequential implantation have also been reported as a means to produce ZnO particles in amorphous SiO_2 [Lee05].

Moreover, the studies concerning zinc aluminate spinel present important information on the interaction of the elements present in our system (Al, O and Zn or ZnO and Al_2O_3) and a significant amount of work is found in [Sam98, Yoo02, Kum06] namely regarding the catalytic properties of this semiconducting (E_g = 3.8 eV) material.

2.3.2 α-Al2O3:NM

The definition of a noble metal (NM) is not unique. In this work we use that which requires NM ions to have totally filled *d*-bands and that they don't cross the Fermi level. Noble metals (Cu, Ag and Au) have similar electronic structure, with an outer *s* band with one electron, after a completely filled d band. The *s* bands approximate reasonably well to free electron states and these elements share some properties, such as excellent thermal and electrical conductivity. The main difference between these NM is the energy gap between the *d*-bands and the Fermi level, with interband (IB) transition energies of 2.2 eV for copper, 4 eV for silver and 2.3 eV for gold, which give these elements their different optical properties. Several reference studies encompass the optical properties of two or even all of these ions [Lin00, Xu02, Kli03, Gan05, Mit06, Bla07].

These metals are often preferred for their low reactivity allowing easier formation of pure metal particles. In fact, plasmonic structures are often made of noble metals such as copper, silver and gold, because these metals are stable under ambient conditions and show strong surface plasmon resonances. Moreover, they are compatible to biological systems, and the binding of proteins, oligonucleotides and other biologically relevant systems to the metal surface is well established [Tat02]. In the latter case, the SPR band is affected by the presence of organic compounds and a novel spectroscopy based on the changes in the SPR band has been developed recently [Fuj06]. Several host materials have been used to produce nanoprecipitates of noble metals: $LiNbO_3$ [Sar98, Wil99], Bi_2TeO_5 [Kli01], glass [Woo93, Hof03], polymers [Hei99, You02, Pro07], aqueous solutions [Pri04], silicon [Mer04], YSZ [Sai03], MgO and $SrTiO_3$ [Tak99], quartz and sapphire [Piv02], using processing methods such as electron beam lithography [Got96], ion implantation [Tak06], pulsed laser deposition (PLD) [Mar07] or ion exchange [Arn96]. As in the case of TM, the main challenges are to control the size and morphology of the precipitates, as well as its composition, parameters that allow tuning the SPR band shape and absorption maximum. In this context Zhao and co-workers used pulsed laser to convert silver nanoprisms to spheres [Zha04]. A comprehensive description of the shape and size dependence of optical properties of gold nanocrystals can be found in [Lin00].

2.3.3 α-Al_2O_3:RE

In the context of this work RE elements are taken as the *4f* transition elements. RE ions are formed when the outermost *6s* electrons are removed, leaving the optically active (unfilled) *4f* orbitals inside the filled *5s* and *5p* shells. This means that *4f* orbitals are partially shielded from external fields and thus crystal field effects are weak in RE systems. In fact, the RE intra *4f* transitions luminescence depends very little on the nature of the host and the ambient temperature. On the other hand, spin-orbit coupling is quite large (it varies with Z^4) and splitting of the electronic structure of free atoms into fine structure terms is expected. It will be these sublevels that will eventually suffer further splitting from the local crystal field. This is the opposite of the *3d* TM, as previously described.

RE doped materials are very attractive mainly due to their potential optoelectronic applications since intra *4f* transitions produce luminescence in several technological key wavelengths, from near infrared (e.g. 1.54 μm for Er^{3+}) to visible (lasers, LEDs, etc.) and UV (short wavelength lasers for more compact data storage), applied in optical-circuit technology. RE systems are developed to be used in optical amplifiers, in display phosphors or in

microlasers with a submicron dimension. This requires that the RE-based materials be synthesized and integrated with functional substrates, such as single crystals, ceramic microspheres, and nanofibers.

RE ions, such as Nd, Er and Eu, are found in a range of important optoelectronic applications, including solid state lasers and phosphors, presenting very sharp optical emissions with energies largely independent of the host material. For example, doping with europium, erbium and thulium, respectively, can generate red, green and blue emissions. Factors associated with stability, ease of synthesis, and environmental safety often make them significantly superior to other phosphors such as sulphur-based materials that tend to degrade rapidly under the high current densities such as those needed for field emission display (FED) technology. Besides they do not contaminate the electron emitters in FEDs and are chemically inert to plasmas commonly used in plasma operated flat panel displays. As for the host materials for RE doped systems, a wide range has been used, namely ZnS [Qu02], AlN [Jad01, Per06], SiO_2 [Hay99, Can96], CaO [Voo92], CaF_2 [Aon98], $CsCdBr_3$ [Gol97], GaN [Jad03, Saw05], polymers [Sos03] or Al_2O_3 [Wrz02] while the production methods include sol-gel techniques [Eil95, Hay99], gas phase condensation with continuous wave-CO_2 laser heating [Eil96], sonochemical synthesis and deposition [Ged00], co-precipitation [Esp02], molecular beam epitaxy (MBE) [Jad01], metal organic chemical vapour deposition (MOCVD) [Mck00] and ion implantation [Can96, Nak03, Per06]. Among oxide-based phosphors, aluminium oxide is an important material due to its application as a dielectric layer on different types of microelectronic devices and as gate oxides in metal-oxide–semiconductor structures such as passivation layers or dielectric films in chemical sensors. Sapphire is also an interesting material for waveguides, its relatively high refractive index, contrasting to that of SiO_2, cladding layers allows confining light very well in the waveguide, and makes small devices feasible.

Eu ions have tremendous potential, due to its strong characteristic red emission, for applications in phosphors, electroluminescent devices, optical amplifiers or lasers, and high density optical storage. There is nowadays a considerable interest in the development of Eu-based phosphors for applications in advanced display technologies including plasma, field emission, and electroluminescent displays. The emission spectrum of Eu^{3+} shows emission lines extending from visible to the near IR with a relatively simple energy level structure, especially the $^5D_0 \rightarrow {}^7F_J$ (J = 0, 1, 2, 3, 4) manifold transitions which enables one to ascertain the microscopic symmetry around the site, making it an ideal experimental probe of the crystalline environment [Ozu04].

On the other hand, with the emergence of high-power InGaAs laser diode as pump sources between 900 nm and 980 nm, trivalent ytterbium-doped hosts have emerged as impressive solid state lasers emitting in the near-IR around 1 µm. Yb^{3+} has important advantages in comparison with the widely used Nd^{3+} laser ion. The energy-level scheme of Yb^{3+} is simple and contains two multiple manifolds: the $^2F_{7/2}$ ground state and the excited state $^2F_{5/2}$, separated by about 1.24 eV (10000 cm^{-1}), with only seven Stark levels distributed in the two manifolds and labelled from 1 to 4 in the ground state and from 5 to 7 in the excited state, from the lowest to the highest energy. The absence of high-lying energy levels avoids the detrimental effects of luminescence quenching due to high concentration, up-conversion losses and excited-state absorption that exist in Nd laser media. Moreover, the broad emission band characteristic of Yb^{3+} is very favourable for tuneable or ultra-fast lasers. Additionally, the Yb^{3+}-doped materials also have longer radiative lifetimes than their Nd^{3+}-doped counterparts (four times greater), giving improved energy storage. Lastly, the low Stokes loss (due to near spectral neighbouring of the Yb^{3+} absorption and

emission bands) leads to a low thermal load (11 % vs. up to 40 % in the case of Nd^{3+}), which is also an advantage [Kir02, Yos03]. The host materials doped with Yb vary from $CsCdBr_3$ [Gol97], GGG [Kir02], GaN [Jad03], YAG [Bou03], sesquioxides Yb_2O_3, Lu_2O_3 or Sc_2O_3 [Kuz07, Pet08], tunsgstates $NaY(WO_4)_2$ or $NaGd(WO_4)_2$ [Cor07, Cas06] and Al_2O_3 [Kre01], aiming usually at crystallographic compatibility to enhance the lasing properties of the system. The doping processes include ion implantation [Jad03], PLD [Kuz07], doping during CZ growth [Kir02, Cor07] or laser heated pedestal growth technique for fibres [Kre01].

2.3.4 IBIL

Ion beam irradiation of insulators and semiconductors is usually accompanied by light emission, a standard observation during ion implantation or ion beam analysis (IBA) processes. In 1993-1994 this light starts to be used as a probing tool to characterize the irradiated material, namely in minerals, in conjunction with other IBA techniques.

Ion beam induced luminescence (IBIL) is thus the analysis of luminescence produced by solid samples during irradiation with energetic charged particles. In contrast to processes leading to the production of X-rays, in which the inner atomic shells are involved, the luminescence process is related to the transitions of the outermost electrons involved in chemical bonds of atoms or in lattice defects. For this reason, IBIL is sensitive to the local chemical environment of compounds and trace substitutes and to the microstructure of the network. The electronic optical transitions are induced by the secondary electrons scattered into the track by the impinging ion. Hence, IBIL as an analytical technique is in principle similar to cathodoluminescence (CL), which is a routinely used for the analysis of minerals and semiconductors. This similarity allows the use of the CL spectra databases for the analysis of IBIL features arising from different compounds.

In 1993-1994 IBIL experiments were performed for the first time with a focused nuclear microprobe at Lund, Sweden [Yan96, Hom94a], and in Melbourne, Australia [Bet94]. The IBIL systems developed at these two laboratories allowed for IBIL imaging to be performed in conjunction with traditional nuclear microprobe techniques, such as particle induced X-ray emission (PIXE) and RBS, on samples with spatial variation. The systems were capable of both imaging and spectroscopy. In this pilot study, Yang illustrated the IBIL technique by applying it to the study of a broad range of samples. Panchromatic imaging was used to study a zircon grain and a rat incisor tooth. The spectroscopic system was used to measure spectra from a sample of willemite activated with Mn, and a thin film which contained Eu. It was suggested that IBIL could be used to perform rapid imaging analysis because of the high IBIL count rate relative to PIXE. A number of improvements to the early system were proposed which included the addition of cold stage to cool samples, and the inclusion of a charge-coupled device (CCD) array for spectroscopy. The prototype Lund IBIL system was updated in 1994 with the introduction of a new photomultiplier tube (PMT) which was more appropriate for single photon counting [Yan94]. The new system was used to characterise zircon mineral grains by combining IBIL imaging and spectroscopy with PIXE analysis. Elemental maps measured with PIXE were correlated with monochromatic IBIL images. Homman and co-workers [Hom94b] combined quantitative PIXE analysis with IBIL in order to estimate the trace sensitivity of the IBIL technique. IBIL spectra were measured on a number of synthetic zircon and calcite samples doped with a single RE element, and

an apatite standard which contained several rare earth impurities. From a detailed analysis of the IBIL spectra, and by careful comparison with PIXE results, a detection limit of μg/g was estimated for the Lund grating scanning mode system, and 0.1 μg/g for the CCD system. A number of subsequent studies on the IBIL analysis of geological samples using the Lund system have been published by Yang [Yan95, Yan97a, Yan97b]. In 1997, Manfredotti and co-workers included panchromatic IBIL images in a paper which applied ion beam induced charge (IBIC) to study Norton CVD diamond detectors [Man97a]. The IBIL images were only used for comparing the crystal morphology of the detectors, which were imaged in an orientation perpendicular to the electrical contacts. The IBIL detection system utilised two PMT mounted directly inside the sample chamber 1 cm from the sample at angles of 135° and 225° to the beam direction. A coincidence technique was used to effectively reduce the background count rate of the uncooled PMT system to less than 1 count per second. In a subsequent study, Manfredotti and co-workers showed that the maps obtained by IBIC and panchromatic-IBIL were complementary [Man97b]. The columnar structure observed in both the IBIL and IBIC images was related to the structure of the CVD sample. The light emission was most likely the A-band, which was found to be insensitive to damage for proton fluences up to 10^{16} cm^{-2}. This complementarity was elaborated on in a later paper which suggested that only the ratio of the IBIL/IBIC signal is inversely proportional to the radiative recombination lifetime [Man98]. Regions of non-complementarity in IBIL and IBIC images were also found. In these regions, both IBIC and IBIL signals were absent. It is clear that combining IBIL analysis with other nuclear microprobe imaging techniques like PIXE, in the case of geological samples, and IBIC, in the case of semiconductor materials, greatly enhances the information which can be gained.

Regarding technological materials, Skuratov and co-workers presented in 1996 the luminescence spectra associated with F-type centres of sapphire upon irradiation with 1 MeV / amu [Sku96]. This group later extended the analysis to ruby and LiF [Sku06]. The lifetime of several phosphors was studied with single ion luminescence by F.C. McDaniel and co-workers [McD02]. IBIL measurements in YAG were performed by Huddle and co-workers [Hud07]. Rare-earth doped $LiNbO_3$ has also been studied in recent times [Cas08].

Recently several laboratories have developed IBIL setups, namely in external beam facilities to characterize cultural artefacts [Qua06, Qua07, Ruv08]. Reviews of the latest developments of this technique may be found in [Bro02, Qua05, Tow07].

3 Experimental techniques and equipment

3.1 Introduction

This chapter is dedicated to the theoretical and practical description of the experimental techniques used in this work for the production of surface structures and for their optical and structural characterization, namely ion implantation, Rutherford backscattering spectrometry (RBS), RBS with ion channelling (RBS-C), ion beam induced luminescence (IBIL) and optical absorption (OA), along with some examples of the analysis carried in chapter 4.

The experimental techniques will be presented in the next two sections, the first dealing with surface modification (ion implantation and thermal annealings), the second with analysis (RBS, RBS-C, IBIL and OA, subdivided in structural and optical analysis, following the scheme also used for the presentation of the experimental results). The experimental equipment is described in a third section, with particular emphasis on the IBIL setup assembled within the scope of this work.

The main references used throughout this chapter are [Chu78] for RBS and RBS-C, [Tow94] for ion implantation and [Mai07, Fox04, Boh98] for the optical theories while solid state physics and classical electrodynamics notions may be found in [Oma93] and [Jac98], respectively.

3.2 Ion implantation and radiation defects

Ion beams were extensively used in this work not only to produce the desired surface features and properties but also as an analysing tool to probe the resultant surface composition, structure and optical properties. This section starts by addressing the physics behind the interactions of high energy ($E \leq 2.0$ MeV) positively charged particles (hereon simply referred to as ions) with matter, namely crystalline solids, from ion implantation and radiation induced defects to RBS or IBIL.

The nature of the interaction between the incident ions and the target material depends on many parameters such as ion energy (i.e. velocity), charge and mass and also target composition, structure and temperature. These parameters will determine the type of interactions that will dominate along the path followed by the ions inside the target as well as its final outcome, namely where the impinging ion will come to rest and the effects produced in the target.

As an energetic ion penetrates a solid material (hereafter assuming a moving ion and all target atoms in thermal rest) it will loose energy, essentially in a large number of small energy transfer collisions with electrons (causing mainly ionization and excitation), slowing down with essentially no deviation from its original direction. Eventually the ions will undergo major interactions such as large angle scattering (even backscattering) from a target nucleus that is set in motion. This leads to a cascade of atomic displacements, substrate sputtering or nuclear reactions, the number of such events increasing as the energy decreases. Figure 3.1 illustrates these processes. Most of the ions will finally stop at random positions around a definite depth in the host material.

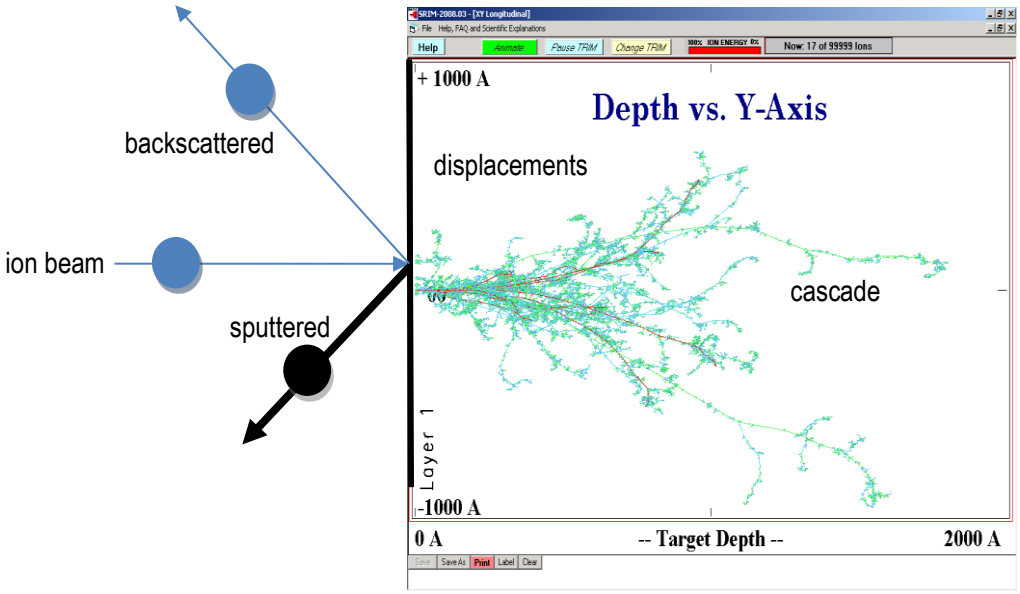

Figure 3.1 – Schematic diagram depicting different processes occurring with an energetic ion interacting with a target and a SRIM code simulation of the paths of the impinging ion (red) and of the displaced ions (blue for O and green for Al).

High energy light ions will penetrate deeply (a few micrometers) into the sample with occasional major interactions before they are stopped. In these conditions, electronic stopping (i.e. energy losses to the electrons) dominates. A technique in which high energy light ions (H^+ or He^+) are used is, for example, RBS. This technique is based on the fact that (very) few ions (about 1 out of 10000) undergo elastic nuclear collisions that get them scattered out of the sample (a comprehensive description of RBS can be found in section 3.3). On the other hand, low energy heavy ions, such as those used in ion implantation, will penetrate only tens to a couple of hundreds of atomic layers before they are stopped mainly by nuclear stopping (i.e. a nuclear interaction with significant energy transfer and atomic displacement).

A general classification of the different effects which occur during bombardment of materials with energetic ions can be made as follows:

1. Inelastic collisions with electrons of the target material. These occur when the energy of the ion equals the characteristic energy of atomic energy levels. The energy is lost in the excitation or ionization of the atom. However, the effect on the incident ion is limited: it suffers only a very small energy loss (less than 0.2 % of its energy) and negligible change in direction.

2. Inelastic collisions with nuclei. These interactions are the least common since they require very high energies, energies high enough to overcome the Coulomb barrier. Inelastic nuclear collisions cause bremsstrahlung (stopping radiation), nuclear excitation or nuclear reactions.

3. Elastic collisions with bound electrons, which are only important for very low energies (< 1 keV, depending on the ion and target masses).

4. Elastic collisions with nuclei or atoms. For small impact parameters, the incident ion undergoes a major change in direction and part of its kinetic energy is transferred to the target atom involved in the collision, which will recoil or even be displaced from its original position.

It becomes clear that in our experimental conditions, among these, inelastic collisions with electrons and elastic nuclear collisions are the dominant processes of slowing down the incoming ions. The energy dependence of both contributions to the stopping power is depicted in Figure 3.2 for some of the experimental conditions used in this work, where typical values are a few keV per nm. The slowing down process is thus essentially governed by these two mechanisms, electronic and nuclear stopping, and is measured by the (total) stopping power, $\frac{dE}{dx}$ the energy loss per unit distance travelled. This quantity is discussed in the framework of RBS in section 3.3.

Knowing $\frac{dE}{dx}$ the average path length R_t of ions with energy E_1 can then be calculated through:

$$R_t = \int_0^{E_1} \left(\frac{dE}{dx}\right)^{-1} dE \qquad [3.1]$$

However, this is not very useful since frequent collisions cause a departure from linearity of the ion trajectory and give rise to a statistical distribution in path lengths. The projection of each path lengths on the original ion direction is known as the projected range and its mean value R_p is most useful in practice.

Fluctuations in the shape of the ion trajectories affect the ratio of projected range to path length and introduce distributions in both projected range and lateral displacement. For low fluences the ion distributions as a function of depth are typically described by Gaussian shape characterised by two quantities: its central value, the mean projected range R_p, and its standard deviation, the straggling ΔR_p.

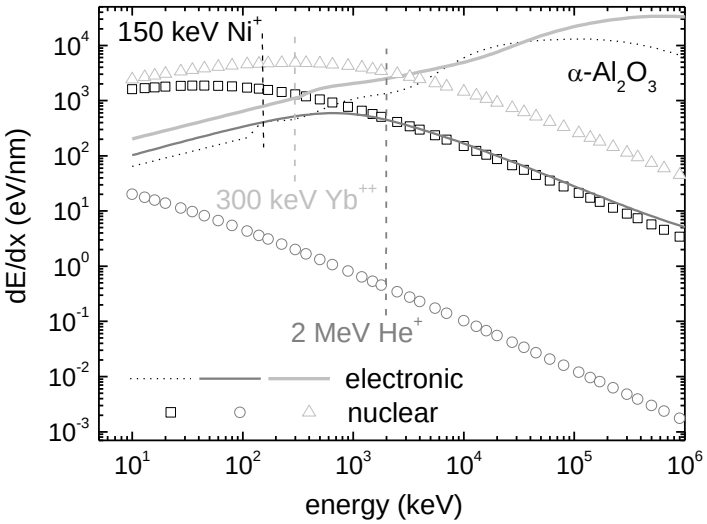

Figure 3.2 – Typical electronic and nuclear energy loss as a function of energy (up to 1 GeV), for Ni and Yb implanted in sapphire as well as He^+ used in RBS analysis (dashed lines represent the energies used in this work).

Assuming this type of distribution, from the parameters R_p and ΔR_p and knowing the implantation fluence F, the depth distribution $N(z)$ of the implanted ions is thus written as [Chu78]:

$$N(z) = \frac{F}{\sqrt{2\pi}\Delta R_p} e^{-\frac{(z-R_p)^2}{2\Delta R_p^2}} \qquad [3.2]$$

Although this theoretical approach assumes a Gaussian shape for the depth distribution of the implanted ions, experimental results show that significant deviations from this model may occur, in particular if there is radiation enhanced diffusion (RED) or ion channelling (the measured range is then higher than predicted), surface recoil or ion loss through sputtering, self-annealing in the case of high beam current densities or poor thermal contact with the sample holder, etc. However, the Gaussian shape is still adequate as a first approximation for most practical purposes. And in practice an alternative method is also used to compute range distributions. A computer code based on the Monte-Carlo method, named SRIM (the Stopping and Range of Ions in Matter), is typically used to calculate ion-atom interactions and predict ion distributions [Zie09]. SRIM is actually a group of programs which calculate the stopping and range of ions (up to 10 GeV/amu) in matter using a quantum mechanical treatment of ion-atom collisions. This calculation is made very efficient by the use of statistical algorithms which allow the ion to make jumps between calculated collisions and then averaging the collision results over the intervening gap. During the collisions, the ion and atom have a screened Coulomb collision, including exchange and correlation interactions between the overlapping electron shells. The ion has long range interactions creating electron excitations and plasmons in the target. These are accounted for by including a description of the target's collective electronic structure and interatomic bond structure when the calculation is setup (tables of nominal values are supplied). The charge state of the ion within the target is described using the concept of effective charge, which includes a velocity dependent charge state and long range screening due to the collective electron sea of the target. As a drawback, this code only considers amorphous target materials and thus may not fully describe ion interactions in crystals.

As previously mentioned, ion beams impinging on a solid will suffer many collisions with electrons and substrate ions. The electronic excitations mainly serve as an energy-loss mechanism which slows down the ion, but do not create significant structural damage. More important are the elastic collisions with the lattice atoms that lead to defect production. A recoiling lattice atom can be removed from its lattice site to become permanently displaced within the solid if the atom receives energy in excess of a minimum value, called the displacement energy, E_d (cf. Table 2.4). The exact magnitude of the displacement energy not only depends on the solid in question, but also on the recoil direction in the crystal, i.e. ions can be displaced more easily in certain directions.

During implantation, ions eventually come to rest at random positions in the crystal lattice. In the energy transfer process many different types of radiation damage are produced by nuclear collisions and collision cascades, even leading to the formation of amorphous regions in the target material, depending on several factors such as ion energy, substrate temperature, etc.

By a crystalline defect one generally means any region where the microscopic arrangement of atoms differs from that of a perfect crystal. Defects are labelled as volume, surface, line or point defects, according to the dimensionality of the defect. In this paragraph a brief overview of the types of radiation-induced defects, their migration and agglomeration is given. For a more detailed survey, refer to [Tow94] and references therein.

The simplest defects in solids are point defects. These can be vacancies, i.e. a missing atom A (V_A), substitutional ions, i.e. impurity ions B replacing lattice atoms A (B_A) or interstitials, i.e. impurity ions or lattice atoms C occupying interstitial sites (I_C). Moreover, various interstitial formations are possible depending on the lattice position and the number of atoms involved. Combinations of these three kinds of defects are also possible and, among them, Frenkel pairs, i.e. are V_A-I_A complexes formed by an atom displaced from a lattice site to a nearby

interstitials site are of most frequent occurrence during irradiation of crystalline solids. Frenkel pairs can either recombine spontaneously or become stable when the interstitial-vacancy separation exceeds a critical distance, the recombination or capture radius R_C. A typical value of the capture radius in Si is 0.233 nm [Kle92]. Hence, recombination occurs when interstitials and vacancies are within a distance R_C. The recombination radius of such a V_A-I_A pair in a crystal, however, is often anisotropic and displays maxima along close-packed directions. Through the operation of replacement collision sequences, the separation of interstitial and vacancy is aligned predominantly along close-packed directions. Single point defects disappear either by annihilation with a point defect of opposite nature or form clusters by aggregation with defects of the same nature. Furthermore, point defects can disappear at sinks such as the surface of the crystal or extended crystallographic defects. The defect evolution is governed by the mobility of interstitials and vacancies which depend on the temperature. The temperature dependence of the diffusivity D of a vacancy or an interstitial follows an Arrhenius type law [Tow94]:

$$D = D_0 e^{-\frac{E_m}{k_B T}} \qquad [3.3]$$

where D_0 is the pre-exponential factor (containing the migration entropy), E_m is the migration energy, k_B is Boltzmann's constant and T is the absolute temperature. Generally, the mobility of interstitials is larger than the mobility of vacancies, hence, they become mobile at lower temperatures. The development of the defect concentrations can be calculated by a set of diffusion equations or by applying reaction rate theory. Under continuous irradiation, already existing defects will accumulate and new defects form clusters or recombine with existing defects. Thus, the damage rate decreases when new defects are generated within the recombination volume of an already existing defect or cluster with opposite nature. Interstitials or vacancies have a tendency to aggregate into clusters to reduce their free energy, which can lead to extended defects. For example, the clustering of interstitials leads to dislocation loops on close-packed planes. Such extended defects will hinder the migration of point defects and are stable up to higher temperatures. Simple defects usually survive only at low fluence and energy implantation in targets at RT or below. In these cases, the defects consist of vacancies from knocked-on ions of the host matrix, populated by several loose electrons. Moreover, phase transitions may potentiate the diffusion process: the Hedval effect.

Knowing the threshold energy needed to displace a substrate atom, it is possible to estimate the total number of displacements per atom (n_{dpa}) with the Kinchin-Pease formula [Kin55]:

$$n_{dpa} = \frac{0.8F\left(\frac{dE}{dx}\right)_n}{2E_d N_0} \qquad [3.4]$$

where N_0 denotes the host matrix atom density (4.712×10^{22} cm^{-3} for Al^{3+} and 7.068×10^{22} cm^{-3} for O^{2-}), F the implanted fluence and E_d the displacement energy. Another way of finding n_{dpa} is:

$$n_{dpa} = \frac{FN_{disp}}{N_0} \qquad [3.5]$$

where N_{disp} (which contains the stopping power and displacement energy) is the number of ions displaced per incident ion taken from SRIM code.

Another practical measure of the damage produced is the damage energy density, E_D. This parameter integrates the implantation energy E_{imp} and F, averaging the result over the damage layer thickness d as follows:

$$E_D = \frac{FE_{imp}}{d} \qquad [3.6]$$

The threshold for amorphization in sapphire implanted at RT occurs at $E_D \cong 3\times10^{23}$ keV cm^{-3} [Mou87]. This parameter ignores any chemical or physical effect related to the nature of the implanted species as well as important implantation parameters such as current density or implantation temperature. Still, it allows for an estimate of the degree of damage.

The displaced atoms themselves can also displace other atoms, in collision cascades, leading to the accumulation of vacancies and interstitial atoms but also to complex lattice defects along the ion path. An illustration of an impinging ion creating several collision cascades is presented in Figure 3.1. A collision cascade can be divided into three phases [Bol94]. The initial stage, during which atoms collide, is called the collision phase, and typically lasts about 1 ps. As a result of the collisions, one can assume that all atoms near the impact point are in thermal motion at high temperatures. A high temperature front will spread and the temperature decrease in the crystal by heat conduction. This stage is called the thermal spike, and lasts roughly 1 ns. When the thermal spike has cooled down, a large quantity of defects will usually remain in the crystal. If the lattice temperature is high enough, many of these defects will relax by thermally activated migration. This is the so called relaxation phase of the collision cascade. The remaining defects can range from vacancies and interstitial atoms to complex interstitial-dislocation loops and volume defects, as mentioned above.

3.3 Rutherford backscattering spectrometry

In Rutherford backscattering spectrometry (RBS) an ion beam is directed onto a target and the ions backscattered by atomic nuclei in the near surface region of the sample are collected, counted and their energy measured, usually with solid state Si surface barrier detectors. It is worth noting that a (nuclear) backscattering event has around 0.01 % probability. Application of the conservation laws for momentum and energy translates this measured energy into information about the nature of the scattering nucleus. Together with knowledge of the energy losses in the incoming and outgoing paths allows calculating its location relative to the surface of the sample.

The backscattering process is illustrated in

Figure *3.3*. The ratio between the backscattered and the impinging energy is defined as the kinematic factor *K* and since we are dealing with elastic collisions the conservation of momentum and energy in the laboratory framework translates as:

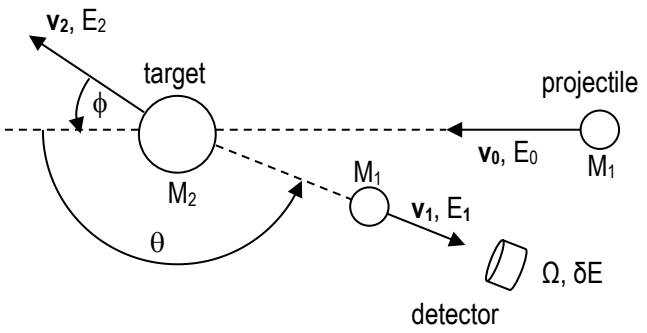

Figure 3.3 – Diagram of a backscattering event with the pertaining quantities involved (vector quantities in bold).

$$K \equiv \frac{E_1}{E_0} = \left[\frac{\frac{M_1}{M_2}\cos\theta + \sqrt{1-\frac{M_1^2}{M_2^2}\sin^2\theta}}{1+\frac{M_1}{M_2}}\right]^2 \qquad [3.7]$$

The projectile's mass (M_1) and energy (E_0) and the angle between the beam direction and the detector (θ) are determined by the experimental conditions, while the backscattered energy E_1 is measured to give M_2. Thus the kinematic factor K allows identifying the composition of the target material, M_2. Equation 3.7 is plotted in Figure 3.4.

From Figure 3.4 it is evident that for $M > 30$ the kinematic factor is almost constant and hence it is difficult to discriminate between neighbouring masses with RBS in this mass ratio range, i.e. the mass resolution decreases. Thus, if heavy atoms with slightly different masses have to be well identified, the mass of the scattered ions has to be increased. Mass resolution is quantifiable by differentiating equation 3.7, which yields (for $\theta = 180^o$ and $M_1 << M_2$, a typical set of experimental conditions):

$$\partial M_2 \approx \frac{\partial E_1}{E_0}\frac{M_2^2}{M_1} \qquad [3.8]$$

Thus, the mass resolution strongly decreases (i.e. ∂M_2 increases) with increasing M_2.

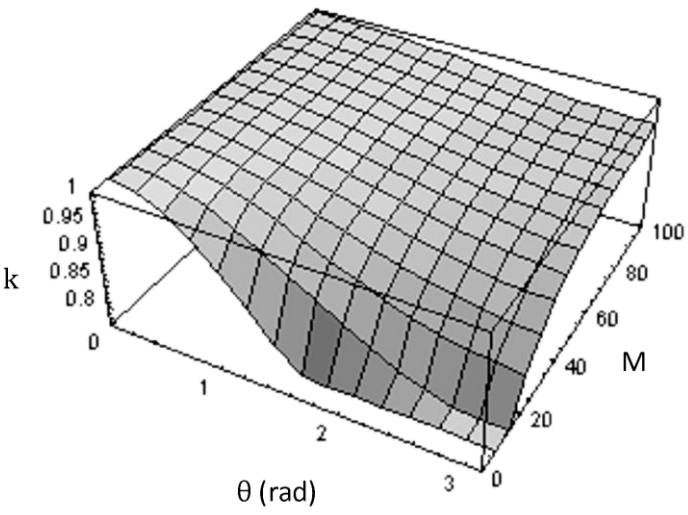

Figure 3.4 – Plot of K(θ,M), with $M = \frac{M_1}{M_2}$.

To circumvent this one may increase the projectile mass, as previously mentioned, or its energy which, on the other hand, result in poor depth resolution or may lead to nuclear reactions, respectively, the latter inducing changes on the scattering probability.

After passing through a target the beam will not only loose energy, it will spread in energy, increasing δE_1 and again degrading mass

resolution. This effect increases with higher target atom masses since it is affected by the number of electrons of the material traversed.

Most of the ions are not directly backscattered by the first layer of surface atoms but deeper inside the sample. In fact, typical experimental RBS setups probe a few micrometers deep and the backscattered ion looses energy in its way in and out of the target. This is depicted in Figure 3.5.

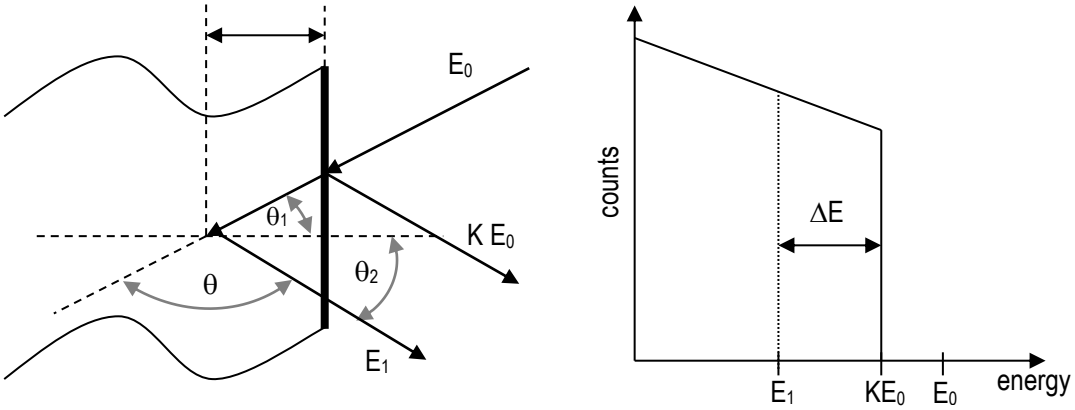

Figure 3.5 – Schematic representation of surface and subsurface backscattering events.

Considering that the incoming and outgoing paths are $\Delta x/\cos\theta_1$ and $\Delta x/\cos\theta_2$, respectively, and such a small Δx that the energy losses per unit length traversed $(dE/dx)_{in}$ and $(dE/dx)_{out}$ may be considered as constant, the energy of the ion is:

- before the collision at Δx $$E = E_0 - \frac{\Delta x}{cos\theta_1}\left(\frac{dE}{dx}\right)_{in} \quad [3.9]$$
- after the collision at Δx $$E' = KE \quad [3.10]$$
- at the detector $$E_1 = E' - \frac{\Delta x}{cos\theta_2}\left(\frac{dE}{dx}\right)_{out} \quad [3.11]$$

In the surface approximation we get:

$$E_1 = KE_0 - \Delta x\left[\frac{K}{cos\theta_1}\left|\frac{dE}{dx}\right|_{in} + \frac{1}{cos\theta_2}\left|\frac{dE}{dx}\right|_{out}\right] \quad [3.12]$$

The maximum energy detectable for a given element is KE_0, when the element is at the surface ($\Delta x = 0$). The energy loss per length traversed per atomic density N of the medium traversed is defined as the stopping cross section ε:

$$\varepsilon = -\frac{1}{N}\left(\frac{dE}{dx}\right) \quad [3.13]$$

The stopping power is:

$$[\varepsilon] = \frac{K}{cos\theta_1}\varepsilon(E_0) + \frac{1}{cos\theta_2}\varepsilon(KE_0) \qquad [3.14]$$

The energy loss factor *[S]* is given by:

$$[S] = N[\varepsilon] \qquad [3.15]$$

The collision depth may thus be determined by:

$$\Delta x = \frac{\Delta E}{N[\varepsilon]} = \frac{\Delta E}{[S]} \qquad [3.16]$$

The knowledge of the amount of energy lost per unit length, i.e. the stopping power $\frac{dE}{dx}$ mentioned in section 3.2, is fundamental to determine the depth distribution of the elements, and its values are tabulated for light ions (H^+ and He^+) in simple elemental materials [And77, Zie77]. For compounds Bragg's rule is applied, that is for a A_mB_n compound:

$$\left(\frac{dE}{dx}\right)^{A_mB_n} = m\left(\frac{dE}{dx}\right)^{A} + n\left(\frac{dE}{dx}\right)^{B} \qquad [3.17]$$

A typical energy loss for 2 MeV $^4He^+$ ion beam is between 100 eV nm^{-1} and 800 eV nm^{-1}, depending on the target material (cf. Figure 3.2).

Detailed theoretical predictions of the stopping power are complex and mostly inaccurate, so that in simulations usually empirical data is used [May77].

The total amount *T* of particles detected at a given depth z is naturally proportional to the total number of incident projectiles *Q*, to the detector solid angle Ω (cf.

Figure *3.3*), to the number N_a of target atoms per unit area in that region, and also to the average scattering probability, i.e. the average scattering cross section σ (angular and energy - thus depth - dependent):

$$T(z) = Q\Omega N_a(z)\sigma(\theta, E(z)) \qquad [3.18]$$

However, the energy of the backscattered ion is measured not in discrete values but in small energy intervals (or channels) of width ΔE, the width of each channel being determined by the experimental conditions. In the experimental data, i.e. the histogram displaying the number of backscattered particles per channel – the spectrum – this means that what we actually measure is an area *A* of a single channel, i.e. a given energy interval or at a given thickness of the target at a particular depth, and thus use:

$$A(z) = Q\Omega N_a(z)\sigma(\theta, E(z))dz \qquad [3.19]$$

For the typical energies involved in RBS experiments ($E \leq 2.0$ MeV) effects like electronic screening to the nuclear Coulomb field or nuclear forces may be discarded, as previously mentioned, and the interaction between ions and nuclei are essentially elastic collisions with probabilities well described by the Rutherford differential scattering cross section [Chu78]:

$$\frac{d\sigma}{d\Omega} = \left(\frac{1}{4\pi\varepsilon_0}\frac{Z_1 Z_2 e^2}{4E_0}\right)^2 \frac{4}{sin^4\theta} \frac{\left\{\left[1-\left(\frac{M_1}{M_2}sin\theta\right)^2\right]^{\frac{1}{2}}+cos\theta\right\}^2}{\left[1-\left(\frac{M_1}{M_2}sin\theta\right)^2\right]^{\frac{1}{2}}} \qquad [3.20]$$

where the symbols have their usual meaning. As the scattering cross section is proportional to the square of the nuclear charge $(Z_2e)^2$ of the target ions, RBS is particularly sensitive to the presence of heavy elements.

In practice a computer code (XRUMP [Doo85] or NDF [Bar97]) is used to quantify the composition of the samples by fitting a simulated spectrum to the experimental data. In particular, NDF analyses RBS, ERDA (elastic recoil detection analysis), non-resonant NRA (nuclear reaction analysis), and NDP (neutron depth profiling) data using the Simulated Annealing algorithm to fit automatically to the data. NDF determines the depth profile that leads to the best fit. These codes have an extensive database of scattering cross-sections as well as stopping powers, the usual input being the experimental conditions used and information about the chemical elements present in the target, whose amount will be adjusted to give the best fit of the experimental data.

With the experimental data and the tabulated values of energy loss and scattering σ cross sections it is possible to calculate the relative concentration *C* of implanted ion *i* relative to matrix atom *m* with:

$$C_i = \frac{N_i}{N_m} = \frac{T_i}{T_m}\frac{\sigma_m(E_0,\theta)}{\sigma_i(E_0,\theta)}\frac{[\varepsilon]_i}{[\varepsilon]_m} \qquad [3.21]$$

where $[\varepsilon]_i$ is the stopping cross section of atom *i*. The implanted fluence is given by:

$$F = \frac{A_i}{T_m}\frac{\sigma_m(E_0,\theta)}{\sigma_i(E_0,\theta)}\frac{\delta E}{[\varepsilon]_m} \qquad [3.22]$$

As an example of application, a typical RBS spectrum is shown in Figure 3.6 for a calibration sample. This sample is used to calibrate the RBS spectra in order to convert channel number to energy (the operational quantity) and it is usually the first spectrum taken. The arrows point to the surface position of the elements – the element edge position – and the corresponding channel numbers are also shown. This calibration sample has known homogeneous composition (C, O, Si, Zr and Hf). The calculus of *K* (equation 3.7) for each of the elements present in the sample for a given experimental geometry and beam particle and energy translates the indicated surface channels into energy (e.g. channel 200, attributed to C, with $K = 0.2501$ for this experimental conditions, is assigned the energy $E = 0.5002$ MeV). The more elements and the more spaced they are the better and a regression analysis

of all E_oK allows obtaining the energy calibration of the spectra. It is possible now to translate channels to energy. In the example an energy calibration of E_{cal} = 2.361 keV/channel + 32 keV is obtained. An energy scale can thus be inserted on the graph (top x axis in the graph of Figure 3.6, in the results section it will always be the abscissa).

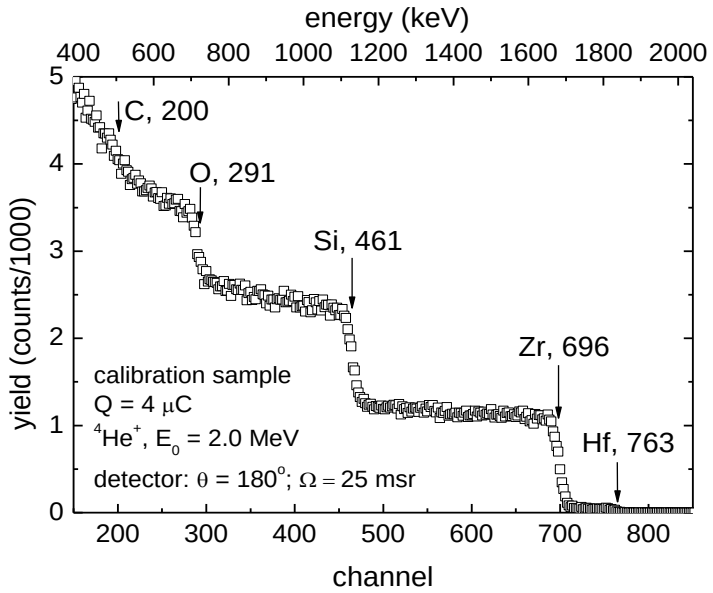

Figure 3.6 – Typical RBS spectrum of a calibration sample, with the main parameters for the calibration procedure.

This energy translation will be input on the analysis of the RBS spectra of interest. Moreover, a depth to channel conversion D per element e is then possible with:

$$D_e = \frac{E_{cal}}{N_a[\varepsilon]_e^m} \qquad [3.23]$$

valid for the surface region, where N_a is the atomic concentration of the target and $[\varepsilon]_e^m$ is the stopping cross section of element e in the matrix m.

3.4 Ion channelling

In a single crystalline material, charged particles travelling along an atom row or plane experience a steering force induced by the regular crystal structure. As the atomic rows and planes of a crystal form channels and this steering phenomenon tends to keep the moving ions confined to these channels, it is thereby called channelling. Due to the steering potential, the flux of charged particles travelling along a channel in the lattice is not homogeneous and therefore the nuclear encounter probability between the incoming particles and the atoms in the host lattice depends strongly on the incoming angle of the particles [Gem74]. This is represented in Figure 3.7.

By channelling experiments with few MeV energy ions, the yields of close-encounter processes recorded in some predefined direction as a function of the angle between the incoming, well-collimated, ion beam and an axial or planar direction of the crystal can be measured. This contains information on the crystal structure, namely irregularities such as structural defects, in the surface layer, to approximately one micrometre depth.

The notation used to identify an axial channel corresponds to the direction indices of that crystal direction. Concomitantly, a planar channel is identified by the corresponding Miller indices of the planes. As an example of the steering effect on the flux, the backscattering yield of a beam of light ions incident along a main axial channel in a sapphire single crystal is about 2-3 % of the yield recorded for amorphous alumina or in non-channelling directions (cf. Figure 3.9). The incident ions will channel along the main axial or planar directions if they enter the crystal within a critical angle for channelling. Analytic models for ion channelling date back to the 1960's [Rob63]. Since then, several models have been published in the literature [Gem74, Lin65].

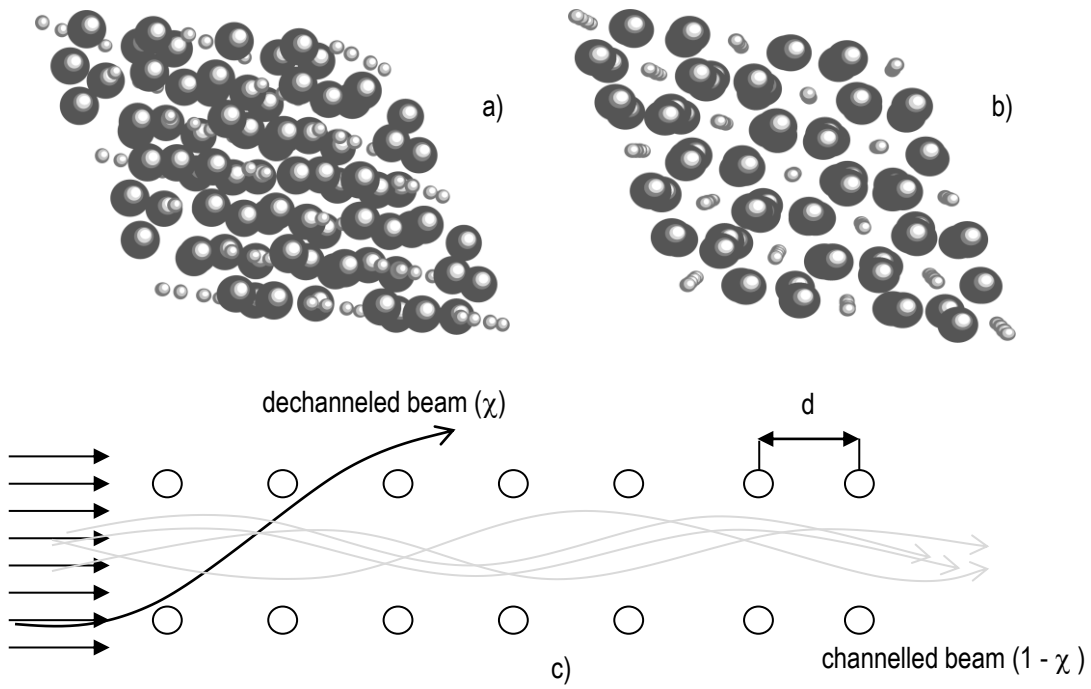

Figure 3.7 – Schematic representation of the channelling effect: a) random oriented sapphire lattice; b) sapphire lattice aligned with c-axis and c) channelling effect in an axial direction.

In these models formulas for calculating critical angles and minimum yields for axial and planar channels have been presented. The most well known formula derives from Lindhard's model [Lin65]. Lindhard presented the following equation for the critical angle for axial channelling:

$$\Psi_1 = \left(\frac{2Z_1 Z_2 e^2}{Ed}\right)^{\frac{1}{2}} \qquad [3.24]$$

where Z_1 and Z_2 are the atomic numbers of the bombarding ion and the host atom, e is the electronic unit charge, E is the energy of the ion and d distance between atomic rows projected on to the plane perpendicular to the channel direction. The critical angle for channelling 2.0 MeV $^4He^+$ ions along the <100> axial channel in silicon is about 0.5°. The backscattering yield detected when the ions impinge along channelling directions is due to dechanneled ions, i.e. ions scattered away from the channelling direction. The factors affecting the dechanneling rate will be discussed in the next section. The use of channelling to detect crystalline imperfections is based on dechanneling of the probing particles caused by the defects in the crystal. The channelling phenomenon has been combined with various ion beam analysis methods, e.g. RBS, PIXE, NRA [Ras94, Mey95], ERDA [Nol98] and charged particle activation analysis [Sch94]. It has also been used together with implanted radioactive isotopes by detecting the channelling and blocking patterns of emitted particles (alpha or beta particles) coming out of the crystal. This technique is called emission channelling [Hof91, Hof96].

In this work, channelling of $^4He^+$ ions is studied combining the effect with RBS. RBS channelling (RBS-C) is applied to probe the lattice sites occupied by impurity atoms and implantation-induced damage distributions, as well. In ion channelling experiments, typical quantities describing how well ions channel in a crystal are the

channelling minimum yield χ_{min} and the FWHM of angular scan curve (Figure 3.8b). An angular scan curve displays the detected yield as a function of the angle of the incoming beam with respect to an axial or planar direction. In practice, a collection of RBS spectra is recorded for several angles, chosen to vary symmetrically around some crystallographic direction (usually θ varies ± 2°). From these spectra some regions of interest are chosen (cf. Figure 3.8a). The integral of counts in these regions is then displayed as a function of the angle. The minimum yield is the yield along the channelled direction (θ = 0°), normalised to the yield obtained in a random (i.e. non-channelled) direction, e.g. the yield obtained from a non-crystalline or amorphous material. It is commonly agreed to determine the random yield for crystalline materials as an average yield of a few points of an azimuthal scan to better cancel planar channelling effects [Dyg94a, Dyg94b]. Because of inevitable feeding effects [App67], the random yield from a crystalline sample does not fully correspond to the yield from an amorphous material. The FWHM of an angular scan is related to the critical angle for channelling [Bar76]. Barrett [Bar71] has derived the following equation for $\Psi_{\frac{1}{2}}$ for axial channelling using Monte Carlo simulations:

$$\Psi_{\frac{1}{2}}(u_1) = 0.83\Psi_1 \left\{ ln \left[\left(\frac{Ca}{u_1} \right)^2 + 1 \right] \right\}^{\frac{1}{2}} \qquad [3.25]$$

In this equation, the minimum distance of approach of the ions to the atom rows is approximated to be equal to the root mean square (rms) amplitude of thermal vibration u_1 of the lattice atoms. The factor C is a function of the angular divergence of the incoming ion beam and a is one screening length. The equation for the channelling minimum yield based on Barrett's Monte Carlo simulations [Bar71] is:

$$\chi_{min} = 18.8 N_a d u_1^2 (1 + \xi^{-2})^{\frac{1}{2}} \qquad [3.26]$$

where

$$\xi = 126 \frac{u_1}{\Psi_{\frac{1}{2}} d} \qquad [3.27]$$

and N_a is the atomic density. An increase of χ_{min} and a decrease of $\Psi_{\frac{1}{2}}$ indicate increasing ion dechanneling. Factors affecting dechanneling rate are:

- energy and atomic number of the incoming ion;
- angular divergence of the incoming ion beam and amorphous layers or other surface imperfections; particularly all crystal imperfections like point defects, dislocations or strain fields, affect the dechanneling rate.
- temperature;
- atomic number and mass of host atoms;
- atom positions in the unit cell and the distance between atoms in rows or spacing between planes.

By comparing the minimum yield for a given dopant species i with the minimum yield in the corresponding region of the host matrix m it is possible to estimate the apparent substitutional fraction of the dopant ions, f_{sub}:

$$f_{sub} = \frac{1 - \chi_{min}^{i}}{1 - \chi_{min}^{m}} \qquad [3.28]$$

In the example below, f_{sub} of Ti in sapphire is close to 50 % measured in the $< 0001 >$ direction.

The behaviour of the minimum yield, i.e. dechanneling rate, as a function of the incoming ion energy, is different for each type of defect, which can be employed in identifying crystal defects [Fel82].

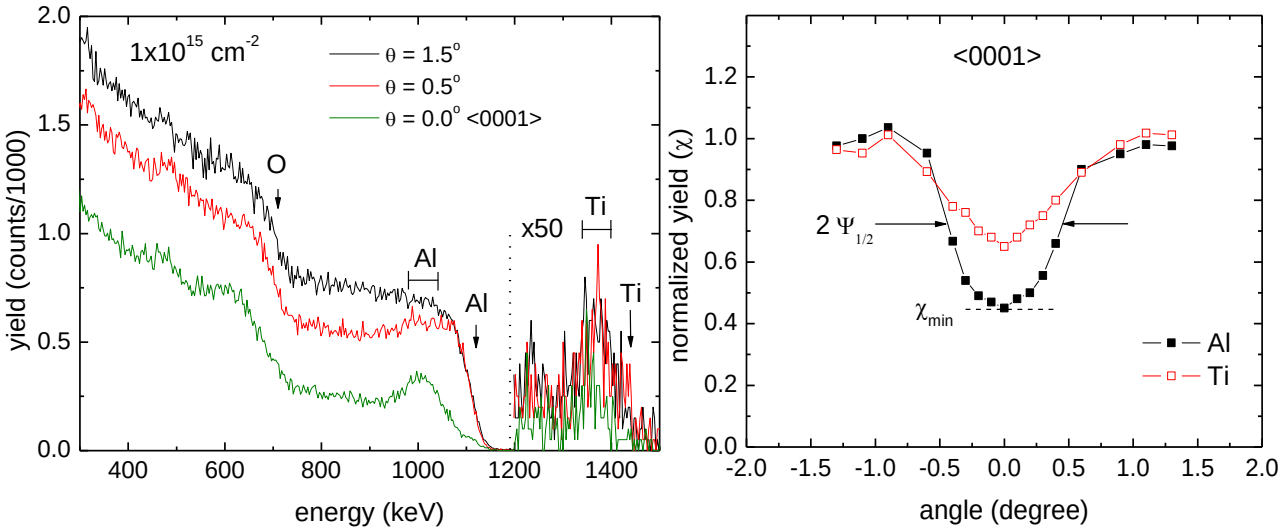

Figure 3.8 – Angular scan performed on sapphire implanted with Ti⁺, with the most common parameters used to characterise angular scans: minimum yield χ_{min} and FWHM $\Psi_{1/2}$.

We will now consider a typical example of application to implanted sapphire. Figure 3.9 shows the RBS-C spectra of a sample of α-Al_2O_3 implanted at RT with 180 keV 2×10^{17} $^{55}Mn^+$. The spectrum of a virgin sample is also presented for comparison. The quantities of interest that can be taken directly from the spectra are: integral *I* of the implanted species (22600 counts), height *T* of barrier of a particular element (T_{Al} = 425 counts), ratio between the aligned and random spectra at a given energy or depth for a given element (χ_{min} or, if measured in an element of the host lattice, the damage concentration: χ_{min} = 100 % for the as implanted sample - and this region is thus said to be amorphous as seen through RBS-C -, and χ_{min} = 2 % for the pristine sample), channel where the maximum of counts of the implanted species occurs (591, to estimate R_p, value to be compared with SRIM code prediction), position of the half height of the edge of the elements present (the first scattering from this element, i.e. its surface position).

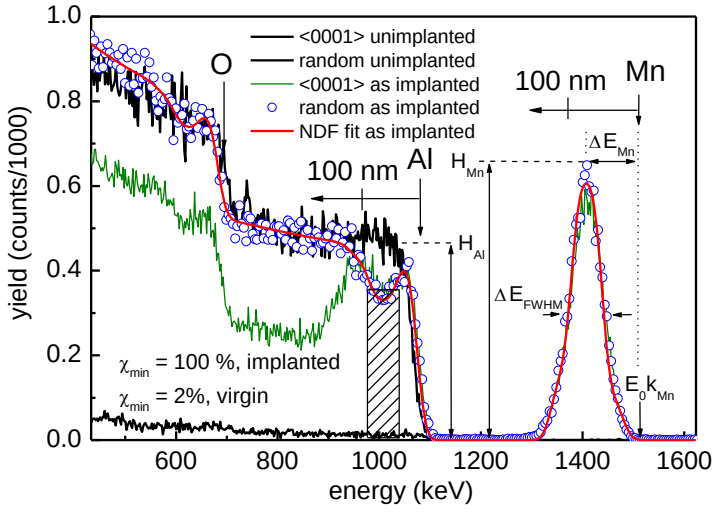

Figure 3.9 – RBS-C spectra of a virgin α-Al_2O_3 sample as well as after implantation at RT of 180 keV 2×10^{17} cm^{-2} $^{55}Mn^+$.

For this particular case these values allow calculating the following:

- the conversion to depth scales, performed with equation 3.16: 3.0 nm/ch for Al and 2.9 nm/ch for Mn, allowing attaching a depth scale to each element.

- from the energy calibration, channel 450 corresponds to 1100 keV and thus $K = 0.55$ which, from equation 3.7, yields $M_2 = 27$, that is Al.
- similarly, beam particles backscattered at the surface by Mn atoms ($M_2 = 55$) are expected with 1494 MeV or at channel 619 and since the maximum counts is at channel 591 the measured R_p is 85 nm, in good agreement with SRIM prediction (90 nm).
- the implanted fluence, calculated with equation 3.15: $F = 2\times10^{17}$ cm^{-2}.
- the maximum concentration of Mn, calculated with equation 3.13, is 14 at. % in Al_2O_3.

It is worth noting that the depression in the Al signal around 1000 keV (or 80 nm) is where Mn has maximum concentration, i.e. the relative concentration of Al is lower in this region. With the depth scale it is possible now to estimate the extension of damage (180 nm) and thus the damage energy density (2×10^{24} keV cm^{-3}) and the FWHM of the implantation profile (60 nm, thus well inside the disordered layer) is in good agreement with the straggling predicted by SRIM (28 nm corresponding to a FWHM of 66 nm). However, the experimental $FWHM_{exp}$ is affected by factors such as the energy resolution (δE_{sist}) and energy dispersion (δE_{disp}). The first is related to geometrical factors of the experimental setup (essentially the beam dimension or the angle of acceptance of the detector) and the energy resolution of the detector (typically about 15 keV), while the latter depends mainly on the target and incident ions nature but is independent of the energy. It is determined by:

$$\delta E_{disp} = [(8ln2)4\pi e^4 Z_1^2 Z_2 N x]^{\frac{1}{2}} \qquad [3.29]$$

To account for these effects, in Gaussian distributions, the real FWHM is given by:

$$FWHM = (FWHM_{exp}^2 - \delta E_{sist}^2 - \delta E_{disp}^2)^{\frac{1}{2}} \qquad [3.30]$$

The thickness of the implanted species (index i) is then given by:

$$\Delta R_p^i = \frac{FWHM}{N_m[\varepsilon]_i^m} \qquad [3.31]$$

A simulation with NDF code is often performed on the random spectra to obtain the composition of the samples but also to validate some of the above calculations, as the maximum concentration, fluence and thicknesses.

3.5 Ion beam induced luminescence

In the scope of this thesis an ion beam induced luminescence experimental line was assembled at ITN. This technique allows probing the optical properties, namely of RE doped systems, extending our ion beam based analysis capabilities.

This chapter aims at introducing the framework needed to assign energy levels to luminescence peaks and bands, as found in the scope of this work, e.g. due to radiation induced defects, and the incorporation of rare-earths atoms.

Luminescence is sometimes classified according to the method used to excite the emission of light. The excitation source can be energetic particles like electrons (cathodoluminescence, CL, also known as radioluminescence, RL) or ions (ion beam induced luminescence, IBIL, or ionoluminescence, IL), heat (thermoluminescence, TL), external electric fields (electroluminescence, EL) or even photons from laser or X-ray sources (photoluminescence, PL). Although a number of different names have been proposed in the literature for this light emission [Suc97, Ziv76a, Ziv76b] the term ion beam induced luminescence and its acronym IBIL will be used hereafter to describe the light emission which emanates from materials irradiated with ion beams.

There are numerous excitation mechanisms that lead to light emission during ion beam irradiation. Normally, a distinction is made between the luminescence emanating from the bulk material and that which emanates from atoms, ions and molecules sputtered from the surface. For some samples, a significant proportion of the light detected during keV ion beam excitation comes from excited sputtered particles. IBIL produced with keV ion beams accounts for a large proportion of the published work on the subject but much of the information therein is still useful for MeV ion work, in particular in relation with damage behaviour. In contrast to keV ion beam luminescence, MeV ion beam irradiation produces light which comes from the bulk and is more indicative of the chemical properties of the bulk material. Since the photon energies reflect the electron distribution in the atom and the energy levels of the electron shells are affected by the chemical bonding, the IBIL method can in principle provide some information about the chemical form of the elements (speciation), which cannot be obtained by other ion beam analytical methods (e.g. RBS, PIGE or standard PIXE).

In Materials Sciences the IBIL method can be applied to study the influence of ion beam modification (e.g. production of intrinsic defects) in the properties of solids. Most of the literature published for MeV ion beam induced luminescence deals with the study of scintillator materials for applications in nuclear and particle physics, and the monitoring of materials modification during ion implantation.

The production of luminescence via radiative recombination requires the use of an excitation source. This energy is then transferred to the irradiated material, the electronic deexcitation processes giving rise to luminescence. The processes which occur after excitation, namely energy transfer and recombination, depend on the nature of the system and are discussed with the aid of a number of theoretical models which encompass the characteristic behaviour of defect centres, and incorporation of transition and rare-earth elements.

The theoretical models which describe the transfer of charge and radiative recombination in materials are important for gaining an understanding of the mechanisms which lead to luminescence, and for assigning peaks in IBIL spectra. The interpretation of luminescence data is incomplete without an understanding of the charge carrier generation process. Determining the luminescence generation volume for an energetic ion has important

implications for imaging using the IBIL technique, and for determining how the ion beam modifies the acquired spectrum.

To determine the spatial distribution of the luminescence produced by the ion-solid interaction involves a detailed look at the process of electronic stopping and the production of delta rays. A delta ray consists of very fast electrons produced in quantity by fast energetic charged particles knocking orbiting electrons out of atoms. Collectively, these electrons are defined as delta radiation when they have sufficient energy to ionize further atoms through subsequent interactions on their own. In this work the samples are tilted more than 45° relative to the H^+ 1.0 MeV beam direction and the interaction volume is thus confined to a few micrometers, containing the entire implanted layer as well as some bulk information. In fact, the spatial extent of the luminescence signal produced by an energetic ion is an important consideration when trying to compare the data obtained from complementary ion beam analytical techniques.

The quantification of the total IBIL yield in a given spatial distribution is obtained by considering equation 3.32 written for a given radiative recombination centre C per incident ion [Yan96].

$$Y_C(\lambda) = N_c R(\lambda) F_{esc} \int_0^{\Delta x} F_A(\lambda, x) B_c \left[\left(\frac{dE}{dx}\right)_e + f_n \left(\frac{dE}{dx}\right)_n \right] dx \qquad [3.32]$$

In equation 3.32, N_C is the total number of radiative recombination centres of type *C*. The term $R(\lambda)$ represents the combined efficiency of the detector and light collection system. The measurement of this factor is quite difficult in practice as it involves a careful calibration of the absolute intensity every time an experiment is performed. Usually all that is required is a relative efficiency calibration for correcting spectra. The calibration procedure used for the IBIL data in this thesis is discussed in a later section. The term F_{esc}, represents the fraction of the total light produced that escapes the surface of the sample. The evaluation of this term depends on the refractive index of the sample. A fraction of the light produced inside the sample will be lost due to self-absorption. The self-absorption factor, $F_A(\lambda,x)$, is both wavelength and depth dependent, and is proportional to $e^{-\alpha x}$, where α is the absorption coefficient at wavelength λ. Not all of the electron-hole pairs generated by an ion will produce light; B_C represents the fraction recombining radiatively at centre *C*. B_C cannot be easily determined as it depends on the interaction of centre C with the other defects and centres present in the sample. An important characteristic of a recombination centre is its lifetime. In this work this quantity will not be measured.

The luminescence yield primarily depends on the electronic energy loss $(dE/dx)_e$ of the ion in the given material. A small fraction f_n of the nuclear energy loss $(dE/dx)_n$ will also contribute to the luminescence yield since the atomic cascades from ion-nuclear collisions may also produce delta rays. This term is difficult to calculate but can be usually ignored for light ions because the nuclear energy loss term is small. Both of the electronic and nuclear stopping power terms are well understood and can be either calculated or determined from Monte Carlo simulations, as discussed in a previous section. It should be noted that both ion beam damage and temperature can alter the values of some of the parameters in equation 3.32. The damage caused by the ion beam changes the value of B_C by introducing new radiative and non-radiative recombination centres. The number of recombination centres, N_C, can also change with ion irradiation. The index of refraction can change resulting in a variation in F_{esc},

and new absorption bands can be introduced resulting in a new value of F_A. The optical effects of ion implantation are reviewed in detail by Townsend and co-workers [Tow87, Tow94]. Sample temperature will not only alter damage effects by either freezing in damage or enabling self-annealing to occur, but it also directly affects the value of B_C. Temperature effects are not considered in this work.

Figure 3.10 illustrates the ionoluminescence process.

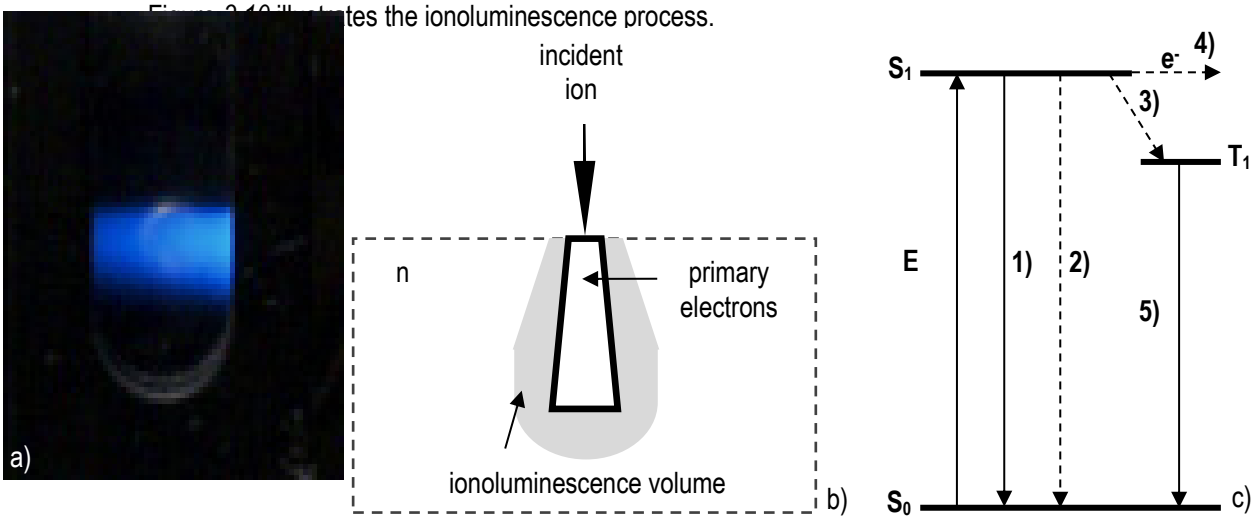

Figure 3.10 – a) photography of a sapphire sample during irradiation with 1.0 MeV H^+; b) schematic representation of the ionoluminescence process and c) Jablonski scheme for photon absorption E followed by: 1) fluorescence; 2) radiationless decay; 3) intersystem crossing (singlet to triplet); 4) electron transfer and 5) phosphorescence.

Since this is one of the objectives of this thesis, a brief discussion of the luminescence of RE and TM is presented.

Rare earth impurities are usually found in either the 2+ or 3+ oxidation states, the 3+ state being the most common.

Trivalent RE activated luminescence spectra are due to transitions across the unfilled 4f electron energy levels. Transitions of this kind in free ions are forbidden for electric dipole radiation by the parity selection rule. However, due to crystal field interactions the actual terms are a mixture of states with different parities, luminescence is observed. Magnetic dipole transitions are not forbidden but are much weaker than the electric dipole transitions.

A typical spectrum for trivalent RE consists of groups of sharp spectral lines separated by approximately 1.2 eV (10000 cm^{-1}) which result from transitions across Russell-Saunders free ion like levels. Figure 3.11 shows the Russell-Saunders energy levels calculated for trivalent RE. The data for Figure 3.11 was derived from calculations performed by Carnall and co-workers [Car68a,b,c,d] on trivalent RE ions in aqueous solution. In a crystal, a slight shift in position and splitting of the levels will occur depending on the symmetry of the impurity environment. Despite these effects, Figure 3.11 is still a useful starting point for the assignment of peaks. This type of figure is used in later sections to assist in assigning transitions to the peaks observed in RE spectra.

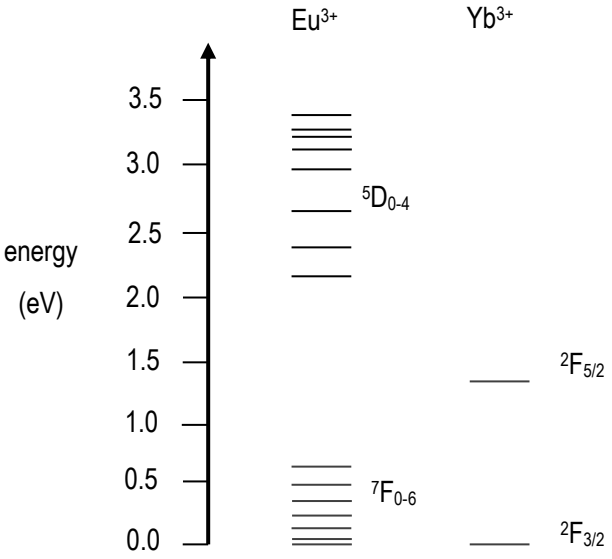

Figure 3.11 – Russell-Saunders energy levels calculated for trivalent Eu and Yb.

The crystal field splits the free ion states into a number of levels which can be determined by knowledge of the point group describing the impurity site. Furthermore, group theory can be used to derive selection rules for radiative transitions between the crystal field levels. Table 3.1 shows the number of levels that result from the crystal field splitting of terms with total angular momentum *J*. Schönflies notation is used for the 32 point groups.

Trivalent RE spectra can be further complicated by the interaction of phonons with the crystal field levels, and the presence of other impurities in the crystal structure. Phonon assisted transitions, which are typically broader than their zero-phonon counterparts, result in temperature dependent lines being observed on the low energy side of the spectrum. The presence of impurity ions can cause a localized distortion of the crystal field resulting in slightly different energy levels.

For example, if we consider Eu^{3+} in sapphire it will occupy a site which has a point symmetry described by the C_6 group. The Russel-Saunders free ion level of the ground state of Eu^{3+} is $^7F_0$. This level has spin $S = 3$ and momentum $L = 3$ giving a total angular momentum $J = 0$. Following the rules outlined in Table 3.1 for determining the level splitting, $J = 0$ in a C_6 symmetry splits into a total of 1 singlet levels and 1 doublet levels.

Regarding the first row transition metals, in a crystal, the partially filled *3d* orbital of a TM element penetrates the outer filled *4s* orbital. This results in the exposure of the *3d* orbital to the influence of the crystal field. Generally, transitions that occur in TM are influenced by the valence state and coordination of the impurity in the crystal. The energy levels of a TM in a crystal cannot be assigned according to the free ion states. The energy levels correspond to the irreducible representations of the point symmetry group of the TM environment.

Table 3.1 – Splitting of the RE elements 3+ terms in crystal with various point symmetries [Fic57]. The brackets [ ] indicate that in case of a non-integer number the next small integer should be taken.

symmetry		J	0	1	2	3	4	5	…J	p	J	$\frac{1}{2}$	$\frac{3}{2}$	$\frac{5}{2}$	$\frac{7}{2}$	$\frac{9}{2}$	$\frac{11}{2}$	…J	p
triclinic	C_1, C_i		1	3	5	7	9	11	2J + 1	1									
monoclinic	C_s, C_2, C_{2h}																		
rhombic	C_{2v}, D_2, D_{2h}																		
trigonal	C_3, C_{3i}, C_{3v}, D_3, D_{3d}		1	1	1	3	3	3	2[J/3] +1	1		1	2	3	4	5	6	J + (1/2)	2
hexagonal	C_{3h}, C_6, C_{6h}, D_{3h}, C_{6v}, D_6, D_{6h}		0	1	2	2	3	4	[(2J - 1)/3] + 1	2									
tetragonal	S_4, C_4, C_{4h}, D_{2d}, C_{4v}, D_4, D_{4h}		1	1	3	3	5	5	2[J/2] +1	1									
			0	1	1	2	2	3	[(J²+1)/2]	2									
cubic	T, T_h, T_d, O, O_h		1	0	0	1	1	0	ϕ_1(x) + [J/6]	1		1	0	1	2	1	2	ϕ(y) + [J/3]	2
			0	0	1	0	1	1	ϕ_2(x) + [J/6]	2		0	1	1	1	2	2	[(J + (3/2))/3]	4
			0	1	1	2	2	3	[(J + 1)/2]	3									

p is the degeneracy of the level and the functions ϕ_1(x), ϕ_2(x) and ϕ(y) are given by:

x	0	1	2	3	4	5
ϕ_1(x)	1	0	0	1	1	0
ϕ_2(x)	0	0	1	0	1	1

y	$\frac{1}{2}$	$\frac{3}{2}$	$\frac{5}{2}$
ϕ(y)	1	0	1

where x and y are calculated for a given J by:

$J = x + 6\lambda$

$J = y + 3\lambda$

for $\lambda = 0, 1, 2, 3, \ldots$

3.6 Optical absorption

3.6.1 Introduction

To study the properties of solids we need a variety of experimental probes, among which techniques using electromagnetic radiation are the most fruitful ones. The widely used methods of optical characterization include optical absorption (from infrared to ultraviolet), photoluminescence and Raman spectroscopy. In this work mainly far-field optical absorption was used. The shortcomings of this technique are essentially the absence of spatial resolution as well as the difficulty to resolve below 10^{-3} absorption. In the next discussion we will start from the experimental point of view while focussing all the argument on the optical behaviour on the wavelength region of our analysis setup, from 190 nm to 1100 nm. We also assume here non-magnetic materials (e.g. $\mu = \mu_0$).

From the optical absorption spectrum we seek to extract the absorption coefficient α. This is the operational parameter, independent of the thickness of the sample, a fundamental input e.g. in the Smakula formula, which allows quantifying the amount of absorption centres related to a given absorption band [Dex56] or in the determination of the band gap via Tauc plots [Fox04].

The response of a material to the exposure of electromagnetic radiation is usually given by its dielectric constant ε. This dielectric constant is a complex number, $\varepsilon = \varepsilon_1 + i\varepsilon_2$, related to the complex refraction index $N = n + ik$ by:

$$\varepsilon_1 = n^2\text{-}k^2 \qquad [3.33]$$

$$\varepsilon_2 = 2nk \qquad [3.34]$$

where *k* is the extinction coefficient and *n* is the real part of the refractive index. The extinction coefficient *k* determines the attenuation of electromagnetic waves propagating through the medium while the refractive index *n* quantifies the loss of the phase velocity of the propagating waves due to polarization of the materials. All of these quantities vary with the wavelength of the propagating electromagnetic wave, e.g. are frequency dependent. The dielectric constants of a material can be obtained by reflection and/or transmission measurements on clean surfaces. For a dielectric medium like sapphire, the real part of the refractive index for optical frequencies is nearly constant and equals 1.76. Its imaginary part, related to extinction, is negligible, sapphire, therefore, is transparent in the optical wavelengths range [Tro98].

When an incident light beam reaches a medium with different refraction index, part of the beam will be reflected by the medium, part of the beam will be transmitted through the medium in a given direction, and the rest of the beam will be extinct by absorption and scattering.

The amount of reflection when light travels from a non absorbing medium 1 (with refractive index n_1) and impinges perpendicularly on a slab of a medium with refractive index n_2 and extinction coefficient *k* is given by:

$$R = \frac{(n_2 - n_1)^2 + k^2}{(n_2 + n_1)^2 + k^2} \qquad [3.35]$$

Figure 3.12 shows the diagram of the optical absorption experiments performed in this work. The case of unimplanted samples is diagrammed in Figure 3.12a, where light impinges perpendicularly a slab of homogeneous material (index 2). In the particular case of ion implanted samples (Figure 3.12b), the analysis may be simplified by considering two slabs of material, an implanted layer (index 3) on top of the unchanged matrix (index 2).

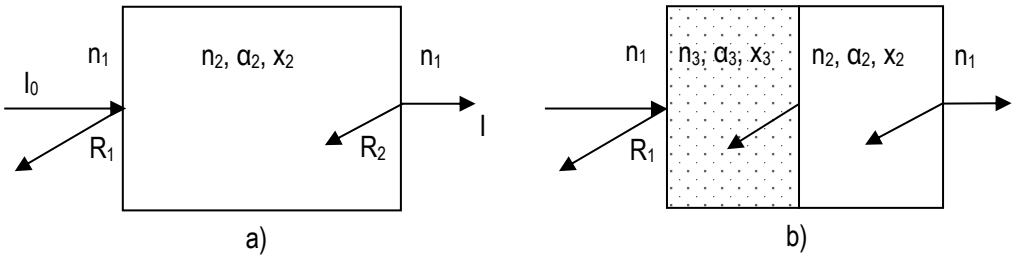

Figure 3.12 – Diagrams of the basic optical phenomena occurring in optical absorption measurements in: a) a slab of pristine material and b) two joined slabs of optically different materials (ion implanted layer on top of the pristine substrate).

In the case depicted in Figure 3.12a of a pristine sapphire sample (which has *k* close to 0 in the visible range), when light travels from air (n_1 = 1), as is the case of most optical absorption measurements, the reflection coefficient ($R = R_1 = R_2$) is given by:

$$R(\lambda) = \frac{(n_2(\lambda) - 1)^2}{(n_2(\lambda) + 1)^2} \qquad [3.36]$$

Assuming that the scattering effects are minimum (as is the case of a sample with both sides polished) and neglecting multiple reflections (valid for systems with low reflection coefficients, like the air/sapphire interface), the transmitted intensity *I* through the two interfaces is given by Beer's law:

$$I(\lambda) = I_0(1 - R(\lambda))^2 e^{-\alpha_2(\lambda)x_2} \quad [3.37]$$

Thus, knowing the tabulated values of $n(\lambda)$ and measuring x_2 it is possible to extract $\alpha_2(\lambda)$, the absorption coefficient of material 2, from the experimental optical absorption spectra, which yields $f(\lambda) = log\ (I_0/I(\lambda))$. The experimental data of unimplanted samples will then be presented as α_2 vs. λ. However, since sapphire is a transparent material in the wavelength region of analysis then $\alpha_2(\lambda)$ is close to zero (in fact it has values of the order of 10^{-5} cm^{-1}, as determined in chapter 4), and the spectra is dominated by reflection.

In the case of implanted samples, the model diagrammed in Figure 3.12b will be applied, with further simplifications to account for the limitations inherent to the use of a single technique to obtain the optical characterization of our samples. In this scope, the refractive index of the implanted layer will be considered very similar to that of the unchanged sample (and thus $R_3 = 0$). This assumption is supported by the relatively low amount of the implanted species (in our experiments the maximum concentration is about 25 at. %) typically present in this layer. Even if the presence of the implanted species may raise the value of the refractive index, this increase is minimized by a concomitant drop due to the lower refractive index in the radiation damaged sapphire (n = 1.70 for γ-Al_2O_3). Thus, all changes in the optical spectra due to the implanted species will be reflected in the value of α_3. In these conditions, with only two similar reflections, the intensity of the transmitted light is:

$$I(\lambda) = I_0(1 - R(\lambda))^2 e^{-\alpha_2(\lambda)x_2 - \alpha_3(\lambda)x_3} \quad [3.38]$$

Measuring x_3 from the corresponding RBS-C spectra and using the values obtained for the unimplanted sample, it is finally possible to extract α_3 and represent it vs. λ.

In the absence of scattering:

$$\alpha_{abs} = \frac{4\pi k}{\lambda} \quad [3.39]$$

Equation 3.39 is often used as the definition of absorption coefficient [Per93].

In this work the absorption bands present will be essentially due to the plasmon resonance band in the case of implantations of metal ions and to defect centres originated in sapphire by the ion implantation method.

3.6.2 Plasmon resonance

The research on plasmon resonant in metallic systems (the so-called plasmonic materials) has increased remarkably in the past decade. This revival of interest is caused by the advances and improved expertise in fabrication methods to create metallic structures of well-defined sizes and shapes, and the many possibilities to

use these materials in applications in optoelectronics, sensing, biology and medicine [Dan04, Wil05], as previously mentioned in chapter 2.

In the range of analysis, the dielectric constant $\varepsilon(\omega)$ of metals depends strongly on frequency. Metals tend to be highly absorbing and reflecting at visible and infrared wavelengths. Many metals (like aluminium) can be well described by the simple model developed by Drude [Boh98] which extends the oscillator model of Lorenz by introducing a gas of independent electrons moving "freely" with the "Lorentzian" scattering with phonons, electrons, lattice defects or impurities characterized by a common average relaxation time τ (in the fs regime) giving a damping constant $\gamma_0 = \tau^{-1}$:

$$\varepsilon_D(\omega) = \varepsilon_1(\omega) + i\varepsilon_2(\omega) \qquad [3.40]$$

where:

$$\varepsilon_1(\omega) = 1 - \frac{\omega_p^2}{\omega^2 + {\gamma_0}^2} \qquad [3.41]$$

$$\varepsilon_2(\omega) = \frac{\omega_p^2 \gamma_0}{\omega(\omega^2 + {\gamma_0}^2)} \qquad [3.42]$$

The plasma frequency ω_p is given by:

$$\omega_p^2 = \frac{N_e {e}^2}{m\varepsilon_0} \qquad [3.43]$$

where N_e is the electron density, e and m are the charge and the effective mass of electrons and ε_0 is the permittivity of free space.

The most commonly used data from literature for $\varepsilon(\omega)$ are the (similar) tables from E. Palik compiled in the Handbook of Optical Constants III [Pal98] and by Johnson and Christy [Joh72]. As an example, the real and imaginary parts of the dielectric constants for gold are depicted in Figure 3.13 as a function of photon energy. Fits of the Drude model to the data are shown as well. It is clear that for Au, the Drude model fails to describe absorption at energies below 2.2 eV. At these frequencies, in addition to the free electrons, excitations of electrons from deeper bands into the conduction band (interband transitions) contribute to $\varepsilon(\omega)$ as well. In this case it is necessary to add a contribution of the bound electrons $\varepsilon_b(\omega)$ in the dielectric function of the Drude model:

$$\varepsilon(\omega) = \varepsilon_D(\omega) + \varepsilon_b(\omega) \qquad [3.44]$$

We used the tabulated values determined experimentally where this effect is embedded.

For very small particles, the fields can be considered homogeneous (constant) over the particle, and only the low-order modes contribute to the extinction. Then, the situation can also be considered as a particle placed in a uniform static electric field (quasistatic regime).

For the interaction of light with very small particles embedded in a transparent material, the complex polarizability p of an isotropic sphere with radius a ($a < \lambda$) and complex dielectric constant ε [Hul81, Boh98] is:

$$p = 4\pi a^3 \frac{\varepsilon - \varepsilon_h}{\varepsilon + 2\varepsilon_h} \qquad [3.45]$$

where ε_h is the (real) dielectric constant of the non-absorbing host material.

The relation of the dielectric constants, the Clausius-Mossoti (Lorentz – Lorenz) relation, correlates the optical constants of both media present in the composite system. A resonant enhancement of the polarizability occurs when $\varepsilon_1 = -2\varepsilon_h$, occurring at a frequency denominated the Frölich frequency ω_F (in air $\omega_F = \frac{\omega_p}{\sqrt{3}}$). The dependency of the polarizability of small particles with the dielectric constant of the host medium makes these structures very sensitive to changes in the local environment.

The cross sections of scattering and absorption are:

$$C_{sca} = \frac{8\pi^3}{\lambda^4 3} |p|^2 = \frac{128\pi^5}{3\lambda^4} k^4 a^6 \left| \frac{\varepsilon - \varepsilon_h}{\varepsilon + 2\varepsilon_h} \right|^2 \qquad [3.46]$$

$$C_{abs} = \frac{2\pi}{\lambda} Im[p] = \frac{8\pi^2}{\lambda} a^3 Im\left[\frac{\varepsilon - \varepsilon_h}{\varepsilon + 2\varepsilon_h}\right] \qquad [3.47]$$

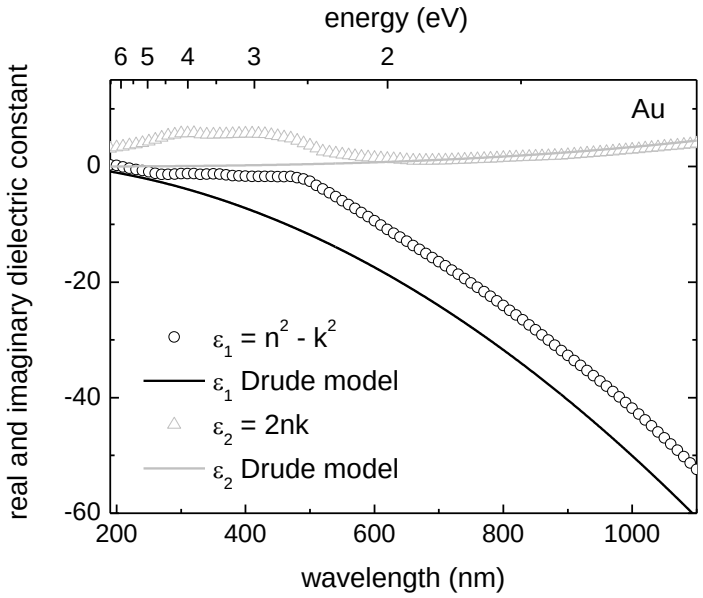

Figure 3.13 – Real and imaginary part of the dielectric constants for bulk Au as tabulated by Johnson and Christy [Joh72]. The solid lines show the Drude model calculated for Au with $\omega_p = 1.35\times10^{16}$ rad s^{-1} and $\gamma = 1.25\times10^{14}$ Hz.

Thus, both scattering and absorption have a resonance at $\varepsilon_1 = -2\varepsilon_h$. In the quasistatic regime a sphere of volume *V* has an extinction cross section given by:

$$C_{ext} = C_{sca} + C_{abs} = \frac{18\pi p \varepsilon_h^{\frac{3}{2}}}{\lambda} \left(\frac{\varepsilon_2}{(\varepsilon_1 + 2\varepsilon_h)^2 + \varepsilon_2^2} \right) \qquad [3.48]$$

where $p = (N/V)\, V_0$ is the metal volume fraction, i.e. the product of the number of nanoparticles per unit volume (N/V) and their average volume V_0. With equation 3.48 for a given wavelength and dielectric constants only the magnitude of the cross section varies with the particle dimension and thus shifts in the resonant frequency are only

achievable by playing with the dielectric constants. However, for particles with dimensions smaller than the mean free path of the conduction electrons (which is ~ 50 nm), the dielectric constants become also size-dependent: $\varepsilon(\omega,R)$. The scattering of the conduction electrons at the surface of the nanoparticle has a strong effect at these scales and that can be taken into account by an additional damping term proportional to the Fermi-velocity v_F divided by an effective length r_{eff} [Kre95]:

$$\gamma = \gamma_0 + \frac{Av_F}{r_{eff}} \qquad [3.49]$$

in which A is a dimensionless parameter that depends on the details of the surface scattering processes (and thus on defects, grain boundaries, chemical interface, etc.) but it is usually set to unity [Kre95]. The additional damping term results in an increase of the imaginary part with respect to the bulk value, the effect being larger at lower photon energies. This results in a broader and a less structured extinction spectrum [Cor03]. The effective length is not uniquely defined, it can be the particle radius or 3/4 of it in the case of a sphere, or even the shell thickness in case of metal shell particles.

The optical properties of metal nanoparticles are thus influenced by particle size. For instance, for metal particles larger than about 30 nm the relative contribution of scattering to extinction (sum of absorption and scattering) increases. Moreover, with increasing particle size the plasmon resonance band of the dipolar mode shifts towards the red, while its bandwidth increases, and higher order plasmon modes may appear in the extinction spectrum and become more dominant. This can be explained by the fact that for larger particles the light cannot polarize the particle homogeneously and retardation effects lead to a gradient of the electromagnetic field that can excite higher order modes. These effects are illustrated in Figure 3.14, representing the calculated extinction spectra for Ag or Au particles in water or sapphire, with a radius from 1 nm to 80 nm. The Ag peak is already red-shifted for the particle with r = 10 nm, compared with the Ag particle having r = 1 nm. For larger particles (r = 80 nm) the red-shift becomes larger and also multipole modes (at higher energies) become visible.

The effect of the optical constants of both the metal and the surrounding medium on the polarizability is illustrated also in Figure 3.14, with the calculated extinction spectrum of spherical Ag particles with diameters of 10 nm in water (n = 1.33) and sapphire (n = 1.76). Changing the embedding medium causes a peak shift for Ag by about 75 nm towards larger wavelengths. Sapphire effectively screens the surface charges resulting in a smaller restoring force and thus a lower resonance frequency.

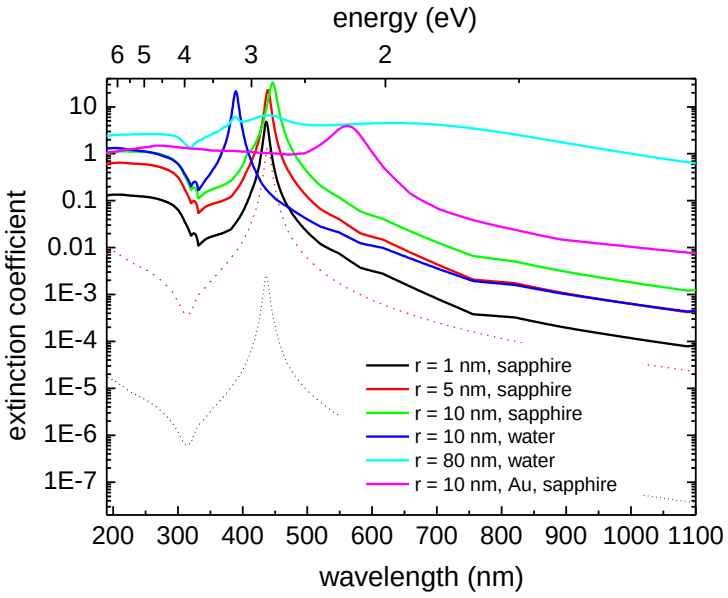

Figure 3.14 – Optical extinction of solid Ag and Au particles in water or sapphire calculated with MiePlot code for several radii [W3].

The spectra of Ag and Au spheres of the same sizes in the same medium are also shown in Figure 3.14. The extinction peak is found at a different wavelength, at 450 nm and 590 nm respectively, a direct consequence of the different dielectric constants for Ag and Au.

The impact of scattering in the extinction coefficient is also shown in Figure 3.14 where the black and red dotted lines represent the scattering from Ag particles with r = 1 nm (scattering is several orders of magnitude lower than extinction) and r = 5 nm (when scattering accounts for 5 % of the extinction), respectively.

The theory by Mie only describes the response of a sphere, but can easily be generalized to ellipsoids in the quasistatic regime. The ease with which the medium is polarized is specified by the polarizability. For an ellipsoidal metal particle, the polarizability p is given by [Boh98]:

$$p = 4\pi\varepsilon_0 V \frac{\varepsilon-\varepsilon_h}{3\varepsilon_h+3L_i(\varepsilon-\varepsilon_h)} \qquad [3.50]$$

with V the volume of the particle and L_i a geometric factor that depends on the ratio of the semi-axes of the particle. The sum of the geometric factors L_i is 1, and for spheres L_i = 1/3. For an anisotropic particle, the geometric factor for light polarized along the long axis of the particle is less than 1/3.

The polarizability is largest when $\varepsilon/\varepsilon_h = (1 - 1/L_i)$, i.e. when the particle becomes excited in resonance. The frequency at which the resonance occurs depends strongly on shape (through L_i), the properties of the metal and of the surrounding medium (through ε and ε_h respectively), as implied in equation 3.50.

Whereas for low metal concentrations the shape of the spectra is determined by the cluster size, at higher concentrations it largely depends on their mutual interaction. This interaction induces a broadening of the resonance in implanted films and, on the contrary, a narrowing in ion beam mixed films.

The Mie theory allows calculating the exact optical response of the system by solving the Maxwell equations in the medium, provided that the clusters are spherical and isolated from each other. But the filling factor of clusters is generally high in ion implanted or ion beam mixed films since it is the purpose of using these techniques. In this case, it is necessary to use an effective medium theory (EMT), not as exact as the Mie theory but permitting to take into account the shape of clusters and their interaction, depending on their spatial arrangement and filling factor.

Some authors, thus, prefer to use EMT, instead of the Clausius-Mossoti relation, where the dielectric function of the composite material reflects the behaviour of a similar homogeneous medium with a dielectric effective function, which is polarised as the composite. By considering a homogeneous medium scattering effects are thus ignored. The choice of EMT is vast with the Maxwell Garnett, Bruggeman or Looyenga theories as top options, depending on the volume fraction of the component present in lower concentration as well as the proximity and interactions of the units of this phase, that is, the degree of connectivity or percolation strength. For example Maxwell Garnett model predicts the absorption peak quite accurately but not the shape of the absorption band, usually underestimating the FWHM. Details of these theories, which follow all from the same integral equation and differ on the approximations made, can be found in [Boh98]. The integral equation is the Bergman theorem, which we will also use:

$$\varepsilon_{eff} = \varepsilon_m(1 - f\int_0^1 \frac{g(j,f)}{b-j}dj) \qquad [3.51]$$

where $b = \varepsilon_m/(\varepsilon_m-\varepsilon)$ and ε_{eff} is the effective dielectric function and ε_m and ε are the dielectric functions of the medium and of the embedded phase, respectively. The function $g(j,f)$ is called the spectral density and holds all the topological details of the microgeometry. It is a real, non-negative function which is normalized in the interval [0,1] for j, and, in case of isotropy, the first moment of the spectral density must satisfy the following condition:

$$\int_0^1 jg(j,f)dj = \frac{1-f}{3} \qquad [3.52]$$

The validity of each group of theories is demonstrated in the example of analysis at the end of this section (Figure 3.15), where the unknown size distribution and morphology of the precipitates, as well as their degree of connectivity and the refractive index of each phase of the composite material leads to two approaches: GMT where assumptions are made regarding size and morphology or EMT where no such assumptions are made and the volume fraction (estimated by RBS) and percolation strength are varied in order to fit the experimental spectrum.

The Mie theory previously presented is embedded in the software codes MiePlot and SCOUT used to simulate the absorption spectra in this work. MiePlot is freeware and runs on Windows XP® and presents a rigorous calculation method of Mie scattering of light (plane waves or Gaussian beams) from a homogeneous sphere, allowing simulations of extinction coefficients or cross sections as a function of wavelength, particle radius, etc.

SCOUT is a commercial software running on Windows XP® for the simulation and analysis of optical spectra like reflectance, transmittance, absorbance, attenuated total reflection (ATR), ellipsometry, photoluminescence and electroluminescence, allowing a variety of inputs (either from its vast database or from user optical constants or optical models) and effective medium approaches. It actually fits the experimental spectra by playing with user defined parameters, e.g. volume fractions, thicknesses, percolation strength, damping constants, etc. The dielectric function of metals may be modelled, allowing varying the free electron plasma frequency and damping, and several oscillators may be input to account for spectral features such as interband transitions. Effective medium theories are only simulated with SCOUT code.

Other simulation codes are available. Nevertheless, MiePlot code for Mie calculations for spheres is easier to use and offers a first order approximation, which, in some cases will be sufficient. Otherwise, SCOUT will be subsequently used.

3.6.3 Optical characterization of defect centres

As discussed in the previous chapter, most optical active defects present in ion implanted sapphire are F-centres, which are oxygen vacancies (F^{2+}) with one electron (F^{+}) or two electrons (F) and aggregations of these (e.g. F_2). The characteristic absorption bands of these structures are situated in the UV region (cf. Table 2.3). These bands can yield the amount N_O (per cm^3) of defects present in the sample by using Smakula formula for Gaussian shaped bands:

$$N_0 = 0.87 \times 10^{17} \frac{n}{(n^2+2)^2} \frac{1}{f} uU \qquad [3.53]$$

where *f* is the oscillator strength of the transition, *n* the (real) refractive index for the wavelength corresponding to the maximum absorption coefficient (*u*, in cm^{-1}) and *U* is the FWHM of the band (in eV) [Dex56]. The values of *f* for F and F^{+} centres are presented in Table 2.3. This formula is better adequate for implanted simples if it reflects the contribution of the implanted (damaged) layer only, $N_{0,imp}$. This is accomplished with:

$$N_{0,imp} = N_0 \frac{t}{x} - N_{0,pris} \frac{(t-x)}{x} \qquad [3.54]$$

where $N_{0,pris}$ is the amount of defects obtained in a pristine sample, *t* and *x* are the thicknesses of the sample and of the implanted layer, respectively. This equation will be used to quantify the amount of defect centres in the implanted region of sapphire, indexed according to Table 2.3.

3.6.4 Band gap measurement

Direct band gap excitation occurs for energies higher than that of band gap energy (E_g). That is, when the joint density of states ($g(\hbar\omega)$) is positive. For $E > E_g$ we have:

$$g(\hbar\omega) = \frac{1}{2\pi^2} \left(\frac{2\mu}{\hbar^2}\right)^{\frac{3}{2}} (\hbar\omega - E_g)^{\frac{1}{2}} \qquad [3.55]$$

where the variables have the usual meaning and μ is the reduced electron-hole mass. Therefore, the joint density of states rises as $(\hbar\omega - E_g)^{\frac{1}{2}}$ for photon energies greater than the band gap. Since the absorption coefficient is proportional to the joint density of states, we expect:

$$\alpha(\hbar\omega) = 0, \ \hbar\omega < E_g \qquad [3.56]$$

$$\alpha(\hbar\omega) \propto (\hbar\omega - E_g)^{\frac{1}{2}}, \quad \hbar\omega > E_g \qquad [3.57]$$

By plotting the square of the absorption coefficient against the photon energy (e.g. a Tauc plot) it is possible to estimate direct E_g. Indirect E_g, phonon assisted and thus exclusive of crystalline materials, is determined by:

$$\alpha(\hbar\omega) \propto (\hbar\omega - E_g)^2 \qquad [3.58]$$

The band gap energy, as other properties, depends on the size (r) of the aggregates of the material, with a blue shift with decreasing size. This dependence is given by:

$$E_g(r) \cong E_g + \frac{\hbar^2\pi^2}{2r^2}\left(\frac{1}{m_e} + \frac{1}{m_h}\right) - \frac{1.8r^2}{4\pi\varepsilon\varepsilon_0 r} \qquad [3.59]$$

3.6.5 Example of analysis

Figure 3.15 shows typical optical absorption spectra of a pristine and a silver implanted sample. The former is well fit using equation 3.29, taking into account the dispersion of the refraction index of sapphire. The minor difference occurs in the UV end of the spectra. Here, absorption and scattering occur due to defect centres, namely F-centres, produced during growth where the inevitable presence of carbon tends to reduce the O content of sapphire. This small absorption maybe fitted by a Gaussian curve with FWHM of 0.2 eV and maximum at 205 nm. Using Smakula formula (equation 3.54) the amount of F-centres is estimated to be around 2.3×10^{15} cm^{-3}, in agreement with the values found in the literature for virgin samples. The implanted sample shows an increase of the UV absorption which is due to the production of more F centres and F^+ centres during irradiation. These are analysed as in the case of the pristine sample with Smakula formula. Another feature of the implanted sample is the strong absorption at 500 nm. This is the SPR band of silver. Most samples will exhibit only these two features: SPR band and F-centres.

The analysis in the UV region is complicated due to the presence of defect related bands with $E > 6$ eV whose tails affect the precise quantification of the wavelength region we can probe with our spectrophotometer. The band-gap absorption of sapphire is expected around 140 nm but lower energy transitions, e.g. Urbach tail, may extend to the region of analysis. Moreover, most of the samples used in this work are one side polished (OSP) and diffuse reflectance and scattering at the unpolished face introduce further complications in the analysis in the UV region since this type of scattering is proportional to the energy of the photon beam. To some extent the damage produced during implantation, which changes the surface roughness, may also produce extra scattering effects. And interband transitions in metals (from *d* to *sp* band in the case of noble metals) tend to occur in the visible up to the UV region, e.g. 1.5 eV for Al, 2.1 eV for Cu, 2.4 eV for Au and 3.9 eV for Ag (cf. Figure 3.14). For these reasons the values obtained for F-type centres in sapphire are estimative and will only be determined for low fluence implantations.

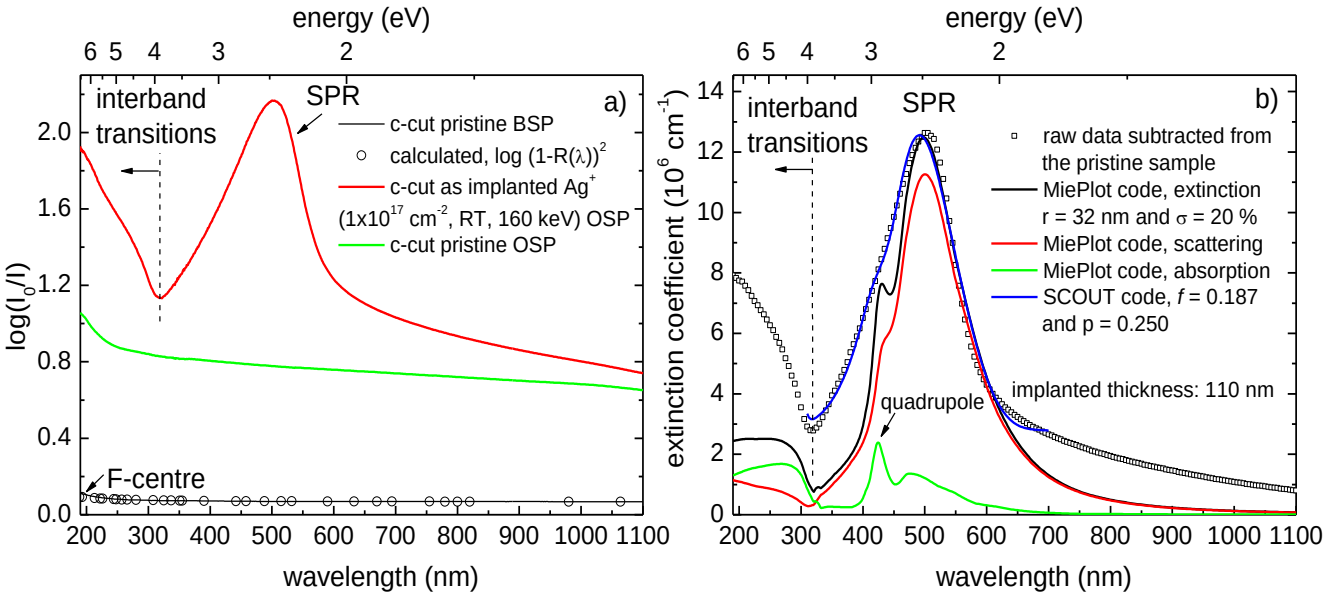

Figure 3.15 – Optical absorption spectra of a) raw data of pristine BSP and OSP and silver implanted samples, with the calculated spectrum of the BSP sample and b) corrected spectrum of the implanted sample with extinction coefficient as ordinate.

The spectrum of the implanted sample is simulated with MiePlot code, using GMT, in Figure 3.15b, with the input of the dielectric constants of silver and sapphire from E. Palik compilation [Pal98], with spherical silver particles, the best fit yielding r = 32 nm (with 20 % standard deviation in a normal distribution of size). The quadrupole resonance is visible, at higher energy, and it is clear that an acceptable fit might only be accomplished by considering a larger size distribution of the nanoparticles. Moreover, the calculated extinction efficiency was multiplied by 0.14 to adjust the magnitude of the simulated spectrum, which yields around 14 % of volume fraction occupied by the particles. It is also possible to observe the large contribution of scattering as compared to absorption, for this size regime.

On the other hand, EMF with Bergman theorem simulation with SCOUT code fits nicely the experimental spectrum, with a volume fraction of about 18.7 %, in agreement with RBS measurements (20 at. %). For the implanted thickness of 110 nm (measured by RBS) this yields average sizes of 63 nm, in excellent agreement with GMT. The percolation strength of 0.25 indicates that the particles have weak interactions. These interactions are also limited by a highly damaged medium preventing phonon coupling.

3.7 Experimental equipment

3.7.1 Ion implanter

The ion implantations were performed in the Unidade de Física e Aceleradores at ITN, with a Danfysik implanter, model 1090, from which a schematic diagram is shown in Figure 3.16. The ion source used in this implanter is a Model 921A High Current Ion Source ("Chordis"), produces stable beam currents of up to 40 mA in the single aperture configuration used for this application. The ion source assembly includes extraction and electron screening electrodes. Ions may be produced from virtually all elements. Target materials may be elemental or compound gases and vapours containing the atomic species to be implanted. A sputtering configuration of the source is used for the production of ions from high melting point materials, such as Ti, Cr, Ta, Mo, and W.

The extracted beam at up to 50 kV is mass analyzed in a double focussing 90° analyzing magnet with mass resolution of $M/\Delta M \approx 150$ to 250. A beam profile monitor and a remotely controlled analyzing slit allow control of the elemental and isotopic purity of the beam. The beam is then post-accelerated up to a maximum voltage of 210 kV. The acceleration tube is specially developed to minimize space charge effects and hence avoid expansion of the beam in an uncontrolled manner. Furthermore, by blocking back-streaming electrons it minimizes X-ray emission from the acceleration section. The beam may be focused by means of a quadrupole triplet magnet to a diameter of 10 mm to 20 mm on target, or it may be defocused to larger dimensions (e.g. 100 mm diameter) in order to minimize instantaneous power load on the sample surface.

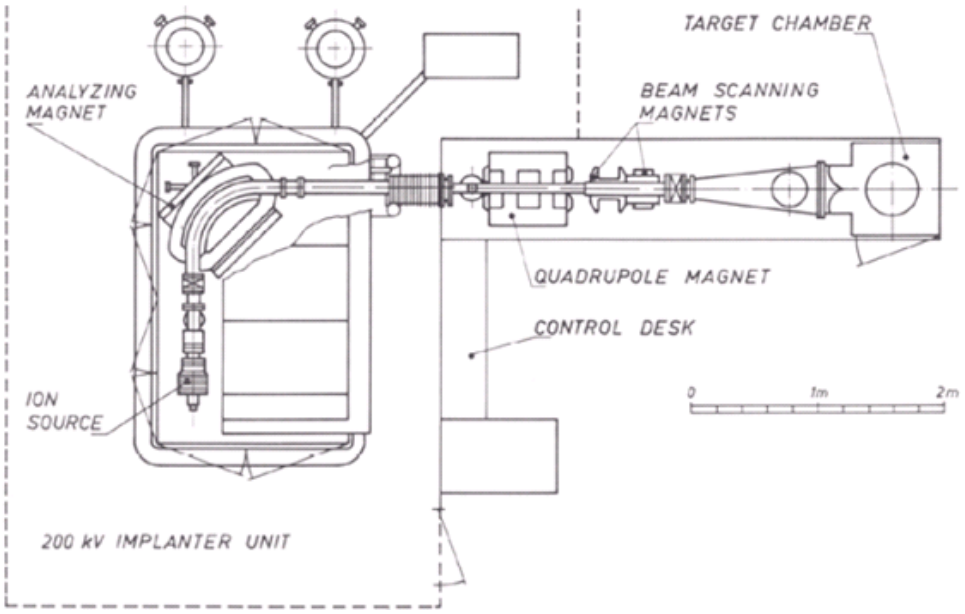

Figure 3.16 – Layout of Series 1090 High Current Implanter in the standard configuration at ITN.

With an electromagnetic two-dimensional beam scanning system the ion beams may be scanned for homogenous exposure over large areas. The maximum beam scanning area depends on the magnetic rigidity of the beam particle. For singly charged ions at 200 keV it is 40×40 cm² for ions up to mass 100 (amu) decreasing to approximately 30×30 cm² for mass 200.

The samples are mounted on a two-axes large metallic target holder (for better heat dissipation) which can be rotated in two perpendicular directions. For (random) implantations, the target holder was tilted about 10º, to minimise channelling. The pressure in the implantation chamber always remained below 10^{-4} Pa during implantation.

3.7.2 Thermal treatments

The implanted samples were annealed in a tubular furnace, shown in Figure 3.17. The annealings were carried up to 1573 K, in vacuum ($p < 10^{-4}$ Pa) or in air at atmospheric pressure, for one hour.

The maximum temperature is about 1573 K in the central region of the tube, with a variation of ± 1 K in a region ± 7 cm from the central point.

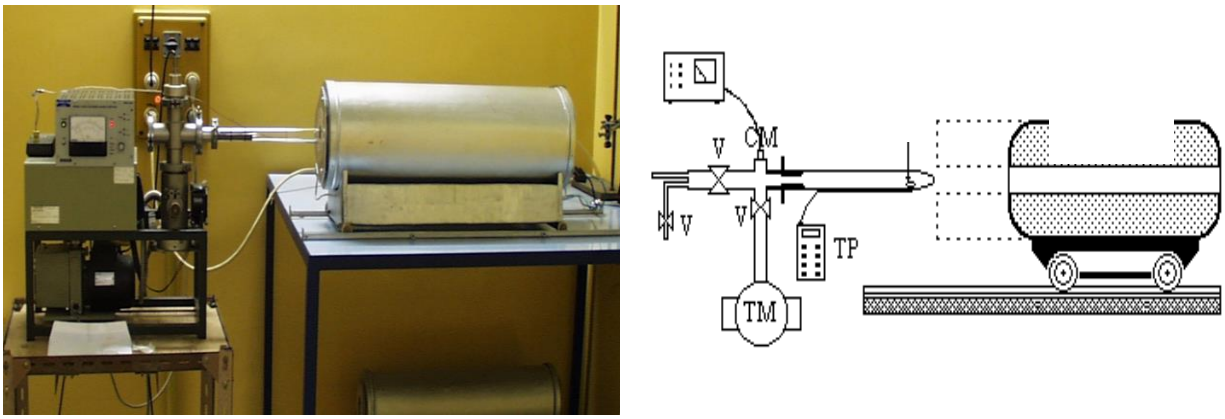

Figure 3.17 – Photograph and schematic representation of the tubular furnace used to anneal the implanted samples [Pru99].

3.7.3 Van de Graaff accelerator and beam line

Figure 3.18 shows a schematic representation of the Van de Graaff accelerator (VGA) installed at ITN, and used in this work to perform RBS, RBS-C and IBIL measurements, with the RBS and microbeam experimental lines. This VGA is a 2.5 MV maximum terminal voltage accelerator that allows obtaining He^+ or H^+ ion beams with energies up to 2.5 MeV. The structure and operation of this equipment is well described in the literature (e.g. [Chu78]). The vacuum system maintains the base pressure better than 10^{-5} Pa in the experimental line.

The beam generated by the accelerator is deflected to the desired drift line and experimental chamber by adjusting the intensity and direction of a magnetic field (2) measured by a NMR probe.

The microbeam line used for IBIL experiments comprises a set of micrometer adjustable object slits with normal apertures varying between 100 μm and 500 μm and a set of collimation slits with normal apertures varying from 0.8 mm and 1.6 mm. The beam is then focused into the sample using a triple set of magnetic quadrupole lens. The demagnification of the object-lens system is approximately 50 in the horizontal plane and 15 in the vertical plane. Specimens in the sample chamber are maintained in a vacuum of 10^{-5} Pa by a diffusion pump vacuum system.

A number of particle and radiation detectors are permanently mounted in the sample chamber. These are one solid state Si detector for charged particle detection, and a Si(Li) detector for X-ray analysis between 1 keV and 25 keV.

The samples to be measured in the RBS chamber are mounted onto a goniometer, as shown in the photography of Figure 3.19. This is a two axes motorized goniometer, allowing 0.04º step rotation in ϕ, the vertical plane containing the sample, and 0.02º step rotation in θ, the horizontal plane. Both motors are computer controlled allowing the automatic performance of angular scans. The conical configuration of the sample holder limits the incidence angle to 58º, e.g. θ has a useful range of ± 58º. The experimental chamber is kept in vacuum ($p < 10^{-4}$ Pa) by a turbo molecular pump backed by a two stage rotary pump.

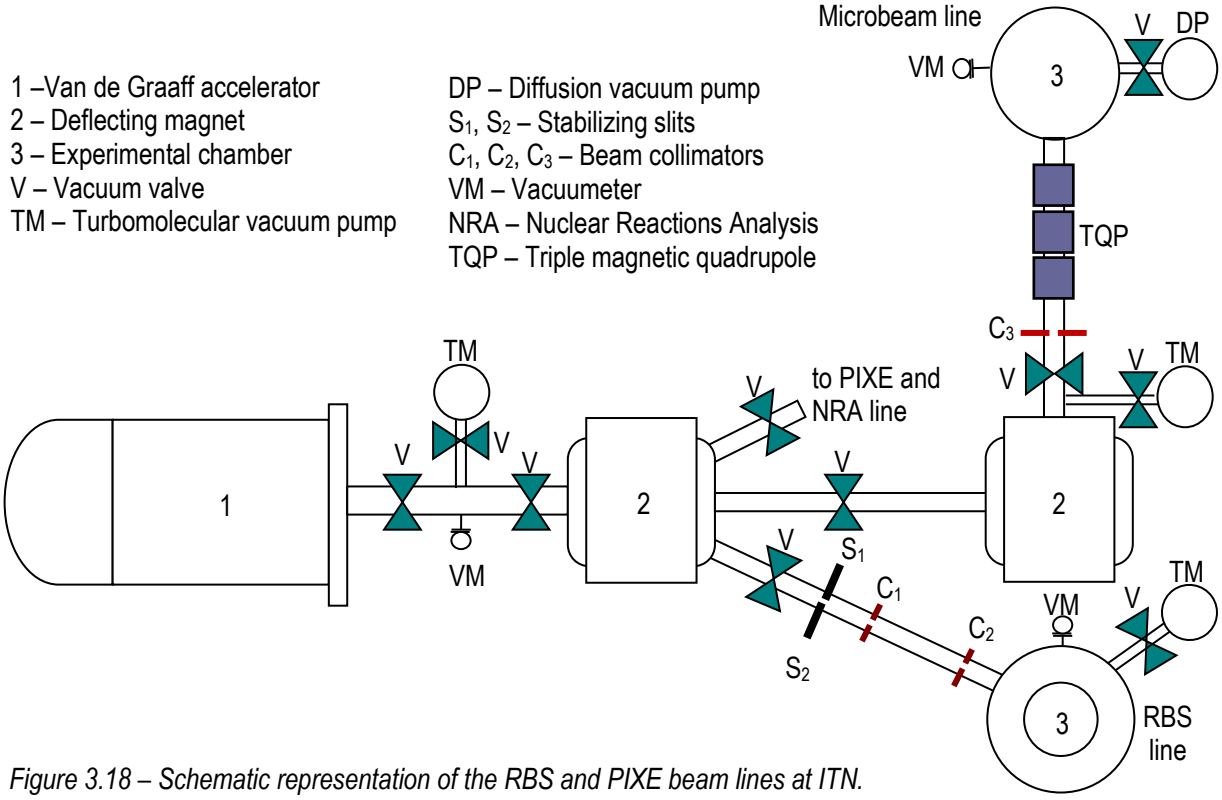

Figure 3.18 – Schematic representation of the RBS and PIXE beam lines at ITN.

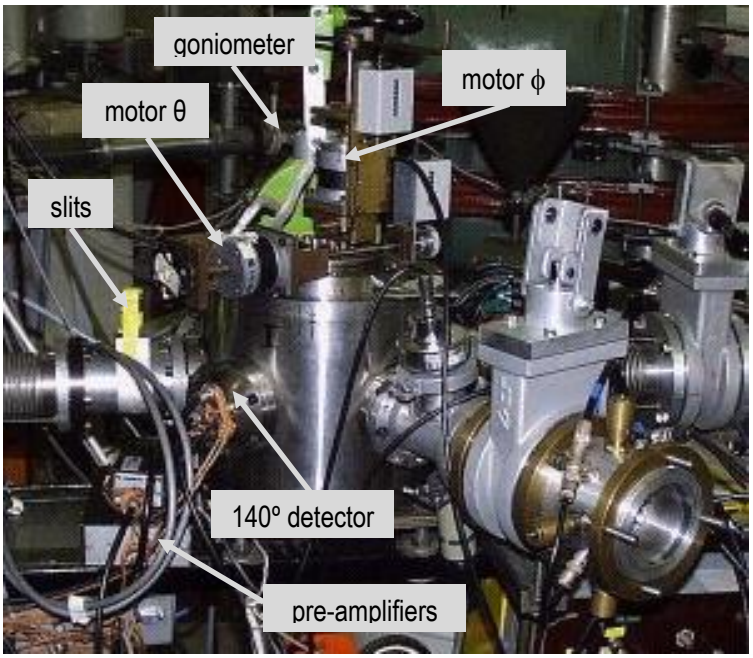

Figure 3.19 – Photography of the goniometer, attached to the vacuum chamber, used in RBS-C experiments.

Each beam line is fitted with a pair of stabilization slits (S_1 and S_2), consisting of two electrically isolated tantalum plates, each one collecting a fraction of the beam current, and feeding it to the input of a differential amplifier whose output signal is fed to the terminal

voltage stabilizer system of the VGA to control the beam energy. The slits' opening is manually adjustable.

Further downstream, before entering the chamber and hitting the sample, the beam is collimated by a pair of collimators (C_1 and C_2), 1 mm^2 in cross-section, placed 1.45 m apart, limiting the angular divergence to close to 2 msr, allowing a beam energy dispersion less than 0.1 %. The backscattered ions are detected at 140º and around 180º to the beam direction by means of two solid state Si detectors subtending solid angles of 3.4 msr and 19 msr and having energy resolutions of 13 keV and 18 keV, respectively, in optimum conditions. Due to its large scattering angle, the detector placed around 180º to the beam direction (annular detector) has a very good mass resolution. However, due to its large solid angle its energy resolution and the depth resolution it provides are poorer than for the standard detector (placed at 140º to the beam direction), degrading somewhat the optimum mass resolution.

The target is positively polarized (V_{pol} ~ 190 V) with a series of batteries in order to minimise secondary electron emission induced by ion beam bombardment, which hinders the correct measurement of the collected beam. The beam current was thus measured in target. In the case of insulating sapphire samples, the beam current was kept below 4 nA in order to minimise charge accumulation effects during analysis.

The signals from the detectors are acquired and processed as shown schematically in Figure 3.20.

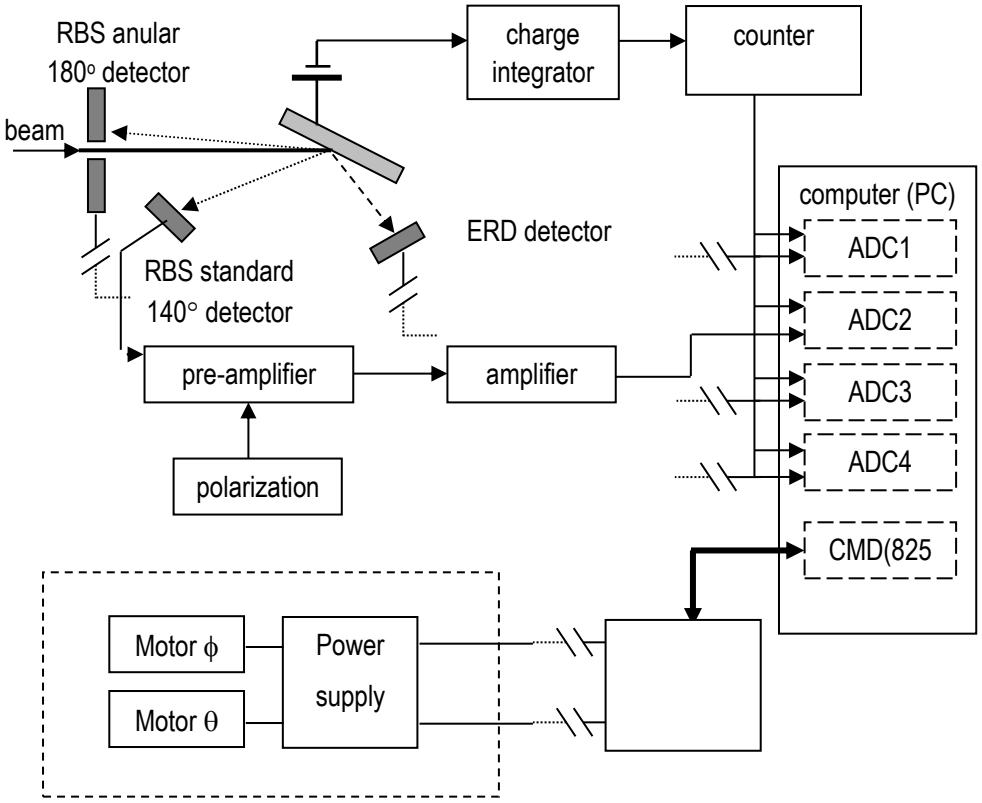

Figure 3.20 – Schematic representation of the electronic chain for signal processing and data acquisition [Vil02].

The backscattered $^4He^+$ ions which collide with the detector generate an electric charge pulse proportional to the energy of the ion. The signal from the detector passes through a charge sensitive pre-amplifier to a linear amplifier, coupled to an analogue to digital converter (ADC) of a multichannel analyser, which divides the selected energy range up into smaller intervals – the channels – each spanning a range of a few keV (typically 1 keV to 3 keV). The number of ions entering the detector in each energy range is summed during the measurement thereby

generating an RBS spectrum which is simply the number of backscattered particles in each energy interval or channel.

3.7.4 IBIL detection System

In this chapter, the components of the ion beam induced luminescence detection system that were developed and adapted to the microprobe end station at UFA – ITN are described. The setup components were chosen to give maximum flexibility for imaging and spectroscopy. Moreover, portable, modular equipment was preferred in view of broader applications by subsequent purchase of visible light source and sample holder (for optical absorption studies), a laser (for photoluminescence measurements) or a solid state detector (extending the analysis to the infra-red range). The imaging capability is not yet available and will not be discussed here. The IBIL signal, ultimately detected by a PMT or a CCD detector, is affected by a number of physical and geometrical parameters. The specific details of our system are presented in the following sections. Nuclear microprobe studies which include the use of IBIL analysis have been reviewed by Ryan [Rya95], Sueno [Sue95], Malmqvist and co-workers [Mal95, Mal96] and Pallon and co-workers [Pal97], etc.

3.7.4.1 Luminescence detection systems

A luminescence spectroscopy system is comprised of three main components: a light collector, a dispersion grating, or equivalent, to separate the different wavelengths, and a device to detect and measure the light intensity at each wavelength. Each component needs to be accurately coupled to the other, minimising stray light and maximising throughput.

The light collector usually includes some form of refractive or reflective optics, the most efficient being a semi-ellipsoidal mirror with a lens and optical fibre light guide, as that of our custom-made system, shown in Figure 3.21. The light collected is coupled through a single core fibre to the spectrometer. A set of filters is located at the entrance of the spectrometer, used to remove high order diffraction lines.

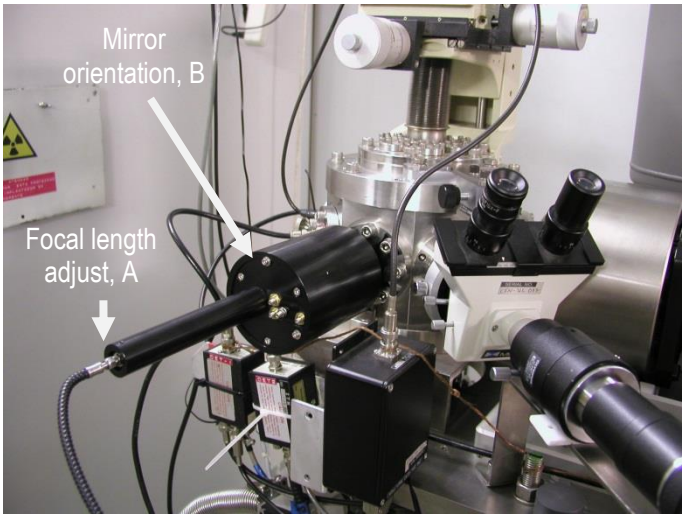

Figure 3.21 – Photography of the light collector device coupled to the experimental chamber and, on the other end, to an optical fibre; on the right side is visible the microscope which allows to view the irradiated spot.

The alignment of the system is performed at the beginning of an experiment with a laser pointer. The fibre is disconnected from the coupling device and laser light is allowed to shine into the chamber. The laser spot on the sample is then viewed through a microscope coupled to the chamber. The focal length of the collimating lens is adjusted by moving

the optical fibre coupling to the light collector and also the coupling of the light collector to the chamber itself (A). The x-y-z position of the sample is varied to choose the spot to be analysed and the mirrors are adjusted (B) until the laser spot coincides with the beam spot. This ensures that the whole optical system is aligned, provided the surface of all samples remains in the plane that contains the rotation axis.

Wavelength dispersion can be achieved with a prism or grating monochromator/spectrometer. Gratings are more efficient than prisms but must be carefully selected to maximise the throughput for the desired wavelength. The maximum throughput of a grating occurs at the blaze wavelength. The wavelength resolution that can be achieved with a spectroscopy system is determined by the dispersion power of its grating, and the width of the entrance slit of its monochromator. For the Jobin Yvon (JY) spectrometer used in this system, the TRIAX 190, the entrance slit width varies from 2 µm to 2 mm. The dispersion power of a grating is given by the spacing of the grating lines or groove density (i.e. the number of lines per mm). When designing a spectroscopy system, a compromise between resolution and band width must be considered. As a consequence a higher resolution system will have a narrower wavelength range. Modern grating spectrometers, as is the case under discussion (Figure 3.22), have a grating turret which allows the user to choose between several gratings, each optimised for particular applications.

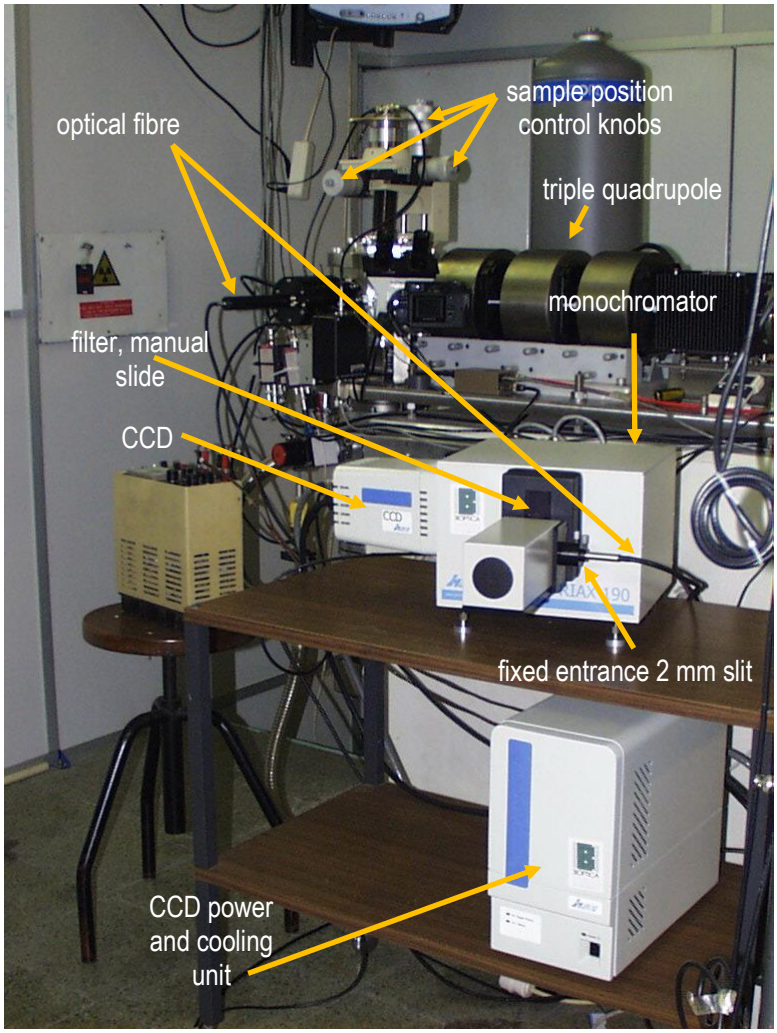

Figure 3.22 – Photography of the assembled system with the Jobin Yvon TRIAX 190 spectrometer and Symphony CCD detection system with Peltier cooling.

The TRIAX 190 is a very compact imaging spectrometer offering both interchangeable triple grating turret and automated dual exit port selection (thus allowing for two detectors). The TRIAX 190 is ideally suited for extended wavelength range applications where multiple detectors are required. In our system the turret takes two gratings for the wavelength range from 200 nm to 1100 nm, since we have only one visible light detector at present. Figure 3.23a shows the theoretical spectral efficiencies for each of these gratings, having 300 lines/mm and 1200 lines/mm respectively. These are in a quasi - Littrow configuration and blazed, by ion-etching, at 1000 nm and 250 nm, respectively. The best resolution attainable in this system is 0.3 nm.

There are two main methods for detecting light. The most sensitive light detector is a PMT. The advantages of using a PMT is high efficiency and speed, which makes it perfect for nuclear microprobe IBIL imaging and luminescence lifetime measurements. Some of the disadvantages include the physical dimensions of the tube, the high voltage bias, high dark counts unless cooled and the low damage threshold if it is exposed to ambient light. Another shortcoming is that a PMT is not practical for spectroscopy since spectra need to be acquired by scanning the monochromator.

A much better method of detecting light for spectroscopy is to use either a CCD or a photodiode array (PDA), which have the advantage of being able to simultaneously collect light over a large range of wavelengths. Furthermore these detectors are more robust when exposed to ambient light. The disadvantages of CCD and PDA detectors are that their sensitivities are not as good as that of a PMT, thus requiring large integration times to acquire good spectra. The sensitivity can be improved by cooling the detectors, but the quantum efficiencies are still not comparable to PMTs. The spectral sensitivity of both PMT and CCD/PDA detectors are limited in the infra-red region of the spectrum. IR detection for CCD/PDA is limited by the band gap of Si, with a cut off at about 1100 nm. The cut-off for a PMT is even shorter; GaAs photocathode materials can extend the efficiency of a PMT to about 960 nm. In the UV part of the spectrum, CCD and PDA usually need to be UV sensitised. This is done by coating the array with a UV fluorescent material which essentially shifts the wavelength of the incident light towards the visible region of the spectrum.

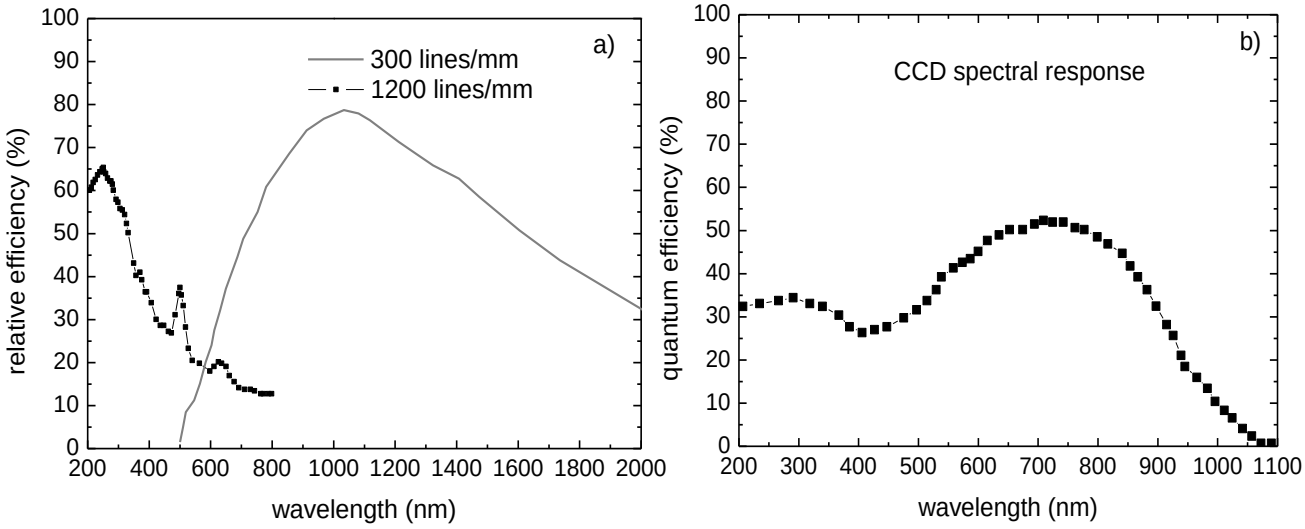

Figure 3.23 – a) theoretical spectral efficiency curves for unpolarized light for the two diffraction gratings (300 grooves/mm and 1200 grooves/mm) used in our system and b) CCD spectral sensitivity at RT.

The detector chosen for the system was a Symphony CCD. Although much more efficient CCD based detectors were available on the market, the JY system provided a good balance between ease of implementation, sensitivity and price. The CCD sensitivity curve is shown in Figure 3.23b. The CCD consists of 1024 × 256 pixels and is Peltier cooled and the recommended working temperature is about 203 K [Symphony Manual].

3.7.4.2 Calibration and responsivity

Spectra obtained with optical detection systems must be corrected for the system response before any analysis is undertaken. The interpretation of spectra from an uncalibrated source will inevitably be misleading and usually results in incorrect assignment of features. If the raw data consists of single or superimposed broad bands, such as those observed in silica or transition metal activated minerals, both the shape and peak positions will be affected by the correction. Less affected are sharp and well isolated peaks such as those produced by rare earth impurities in minerals or diamond ZPL. In this case, the major effect of applying a correction is to change the relative intensity of peaks; the peak position is only slightly altered. The wavelength calibration of an optical system involves acquiring a spectrum of an atomic emission lamp which has a number of well separated and accurately known emission lines. In practice, wavelength calibration is performed by matching the 546 nm mercury line from a fluorescent lamp for both diffraction gratings. Table 3.2 lists the wavelength of the lines used for wavelength calibration and are obtained from the CRC Handbook [Lid02].

Table 3.2 – Most intense emission lines of mercury I, from [Lid02].

Emission lines of Hg^+, present in typical fluorescent lamps

wavelength (nm)	relative intensity	wavelength (nm)	relative intensity
184.95	1000	407.78	150
253.65	15000	433.92	250
265.20	250	434.75	400
265.37	400	435.83	4000
289.36	150	546.07	1100
296.73	1200	567.59	160
302.15	300	576.92	240
312.57	400	578.97	100
313.16	320	579.07	280
313.18	320	580.38	140
365.02	2800	690.75	250
365.48	300	708.19	250
366.33	240	709.19	250
404.66	1800	1013.97	2000

Figure 3.24 shows the spectra of a fluorescent tube around the 546 nm line, in the IBIL data interface. Usually one line (the 546 nm line) is enough to calibrate each diffraction grating (simple translation). However, if necessary, a number of lines covering the entire detection range of the spectrometer are identified and the corresponding pixel numbers are used to fit a polynomial. The polynomial is then used to predict the wavelength of all 1024 channels of the CCD for each of the gratings.

After the spectrometer wavelength calibration is performed, the detection system needs to be corrected for the spectral response of all the optical components. It is too difficult to determine the response of each component individually, so a calibration experiment was devised to determine a single response function for the entire system,

measuring the light emitted by a fluorescent lamp at the same point and angle. A manual of operation of the equipment covering these topics is online at http://www.itn.pt/facilities/lfi/manual_ibil.pdf.

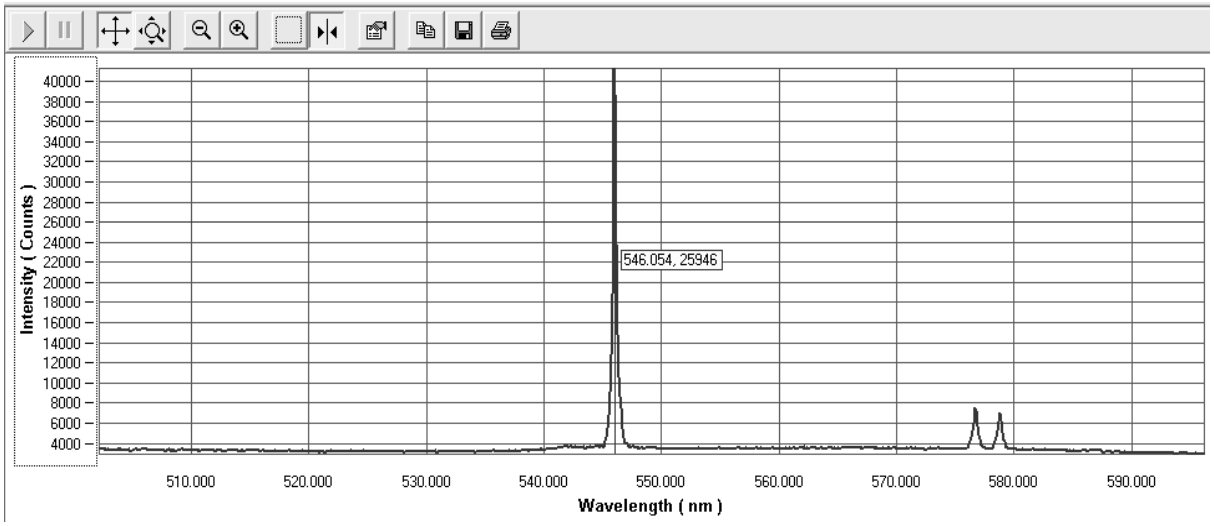

Figure 3.24 – Atomic lines used for spectrometer calibration from a fluorescent tube in the data acquisition interface for IBIL.

3.7.4.3 Spectral analysis

Spectra are acquired with JY proprietary software SynerJY with Microcal ORIGIN© interface running on Windows XP® operating system. The communication with the JY spectrometer is achieved through a RS-232C interface for monochromator positioning control and an Ethernet card for data transfer. A background spectrum can also be stored in a software buffer so that automatic background subtraction may be performed during data acquisition. An image of the graphical user interface of the spectrum acquisition software is shown in *Figure 3.24*.

In summary, the main components which make up the IBIL detection system developed for the UFA – ITN microprobe are:

- JY TRIAX 190 spectrophotometer with a three grating turret, with one light entry and two detector exits. The spectrometer is controlled via RS-232C and Ethernet ports.
- Custom made light collector attached to the experimental chamber;
- An optical fibre terminated with sub miniature version A (SMA) connectors for coupling the light collector to the spectrometer;
- filter slide at the entrance of the monochromator to avoid high order diffractions;
- Symphony Peltier cooled 1024 × 256 CCD array;
- Software SynerJY to control the spectroscopic system for Windows XP® operating system.

Whenever necessary the equipment could also be coupled to the standard RBS-C chamber to allow IBIL measurements under channelling conditions. A coupling flange was made of stainless steel, equipped with and a sapphire window, in order to connect it to the chamber.

3.7.5 Spectrophotometer

Figure 3.25 shows an image and the schematic representation of the light paths in the spectrophotometer used in this work, a Shimadzu 1800 double beam double detector spectrophotometer, which allows measurements from 190 nm to 1100 nm, with 1 nm resolution.

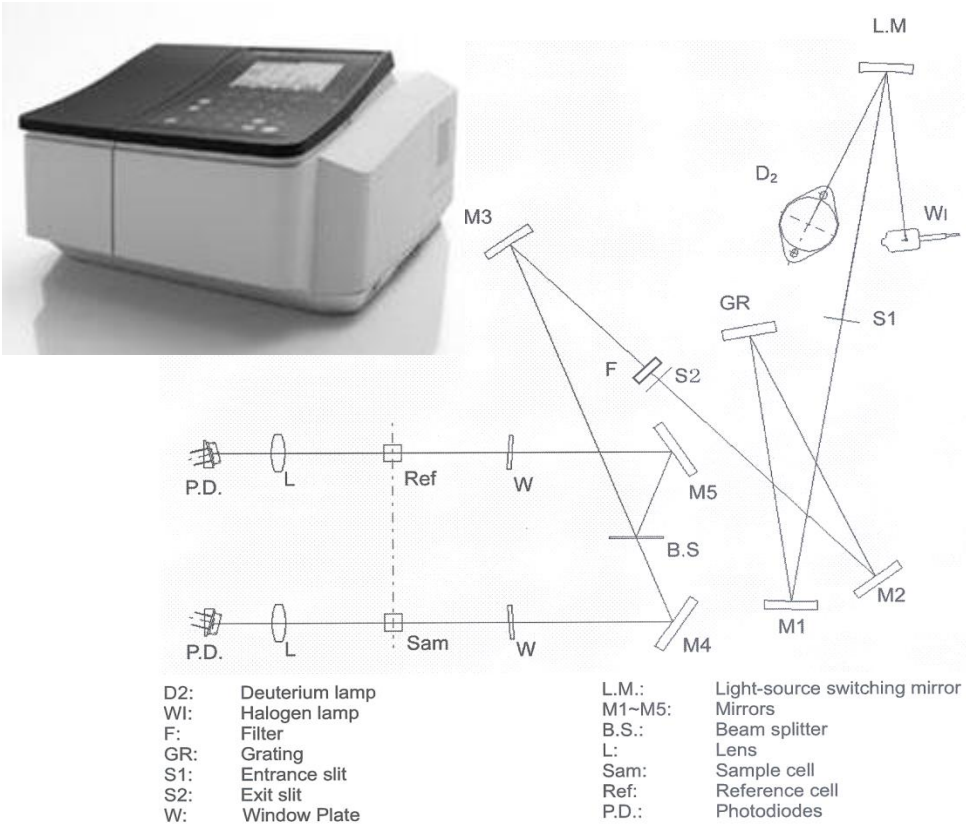

Figure 3.25 – Photography and schematic representation of the Shimadzu 1800 dual beam dual detector spectrophotometer.

The spectrometer is equipped with two continuous light sources *i)* halogen lamp to supply the wavelengths from the near infrared to the near UV range (i.e. from 375 nm to 1100 nm) and *ii)* a deuterium lamp for the measurement in the ultraviolet range (from 190 nm to 375 nm). The light beam is first directed to a blazed, holographic grating with a Czerny-Turner mount and then split in two beams. One beam is incident on the sample and the transmitted light is directed to the detector reaching it with intensity *I*. The other beam goes through a reference sample (usually air), after which it is collected in a similar detector (with intensity I_0). In the scope of this work a sample holder for thin films was separately acquired and three custom made sets of sample holders were manufactured at ITN. The detection system is comprised of two photodiodes and the spectral bandwidth of this equipment is 1 nm. The output is a plot of $log(I_0/I)$ vs. wavelength. Regarding these measurements, it should be noticed that reflection and scattering are not always negligible and their contribution affects the final data.

4 Results

4.1 Introduction

This chapter is dedicated to the presentation and discussion of the experimental results obtained in the course of this work. It begins with the description of the general experimental details and methodology used, after which the experimental results are presented. These are divided into three subgroups: the transition metals Ni, Cu and Zn, the noble metals Ag and Au, and the rare-earths Eu and Yb. Since Cu belongs both to the 4th row transition metals and to the XI group of noble metals it will link the first two subgroups of results. The first set of experimental results (Al_2O_3:Ni system) contains also the characterization of pristine sapphire samples.

The presentation of each individual set of the experimental results is divided in two sections, one for the structural characterization (e.g. with RBS, RBS-C, XRD, complemented, in some cases, with TEM and AFM), the other for the optical description (OA and IBIL measurements), the same division previously followed in chapter 3. The presentation will generally start with the RBS-C analysis of the as implanted state of all samples followed by the characterization, with the other techniques, of the samples implanted with the highest fluence and annealed in air or vacuum (usually for two types of samples, except in the case of RE implantations where only c-cut samples were used). Each subgroup ends with a cumulative discussion of the results presented.

4.2 General experimental details and methodology

High purity colourless transparent, Czochralsky grown, sapphire single crystals, with (0001) (c-cut samples), $(10\bar{1}0)$ (m-cut samples) and $(10\bar{1}2)$ (r-cut samples) surface plane orientations, 0.4 mm thick and optically polished surfaces (one side polished – OSP – except in the case of Zn and Yb implantations in which 0.5 mm thick samples had both sides polished – BSP), purchased from Crystal Systems Inc., were used throughout this work. The different crystallographic surfaces were used to study potential anisotropic effects. The purity of the samples was confirmed by PIXE measurements which only revealed some traces (of the order of 1 μg/g) of sapphire's typical impurities: iron, titanium and chromium.

These samples were implanted at room temperature (RT) in vacuum (10^{-4} Pa) with Ni, Cu, Zn, Ag, Au, Eu and Yb ions, the implantation energies ranging from 100 keV to 300 keV. All samples were previously cleaned in an ultrasonic bath of acetone, a procedure used also prior to each annealing. The effective implantation fluences were in the range of 1.5×10^{15} cm^{-2} to 1.8×10^{17} cm^{-2}, the lower fluences aiming at reducing the radiation damage and performing site location studies while the higher fluences, well above the solubility limits of the implanted species in sapphire, were used to obtain extensive metallic or compound aggregates. Selected samples were analysed in several spots, as well as compared with other materials implanted simultaneously, and the fluences were found homogeneous within 5 %. The beam current density, which has an important impact on the implantation outcome, was kept constant and not larger than about 10 μA cm^{-2} to prevent self annealing effects during implantation. All samples were tilted 8º to avoid channelling during implantation.

The projected range and straggling of the ions were calculated using SRIM simulation code [Zie09]. The SRIM code also predicts the number of vacancies produced per incident ion, considering an isotropic amorphous

material and the displacement energies for oxygen and aluminium as 51 eV and 31 eV, respectively [Cau93]. The sputtering yields are also an output of these simulations.

To recover from the implantation damage isochronal (1 hour) thermal annealings were carried out in a tubular furnace (cf. diagram on Figure 3.17) at temperatures up to 1573 K in ambient atmosphere (air) or in vacuum (2×10^{-4} Pa). The temperature range was chosen as to start probing the system below the γ to α transition of alumina up to full recrystallization. The quartz or alumina tubes holding the samples during the annealings were periodically cleaned with aqua regia, a (1:3) mixture of HNO_3 and HCl, to avoid contaminations.

Rutherford backscattering spectrometry (RBS), RBS under channelling conditions (RBS-C) was performed with a beam of 2.0 MeV He^+ ions after implantation and each of the annealing steps to characterize the structural changes induced by these processes. The backscattered particles were detected at 140º and close to 180º using solid state silicon detectors with optimal resolutions of 13 keV and 18 keV, respectively. The beam has about 1 mm^2 cross sectional area and the beam current was measured on the target and kept below 4 nA in order to minimize the effects of charge accumulation and radiation damage at the surface during analysis. Typical collection times and charge were less than 20 minutes and 2 μC, keeping the He fluence below 10^{16} cm^{-2} (and at about 4 μm depth). Prior to the experiments a calibration sample was used (homogeneous polymer having C, O, Si, Zr and Hf at the surface, cf. Figure 3.6) to establish the energy calibration of the RBS spectra. This method, involving a regression analysis, allows an uncertainty of less than 5 keV (or about 5 nm) when the correlation coefficient is close to unity.

Ion beam induced luminescence (IBIL) was produced at RT at the microbeam line with 1.0 MeV H^+ beam (probing the first 6 μm) and measured in the 200 nm – 1100 nm range with a wavelength resolution of 0.3 nm. The beam used had 0.2×0.2 mm^2 in cross section and the current was kept below 1 nA again to avoid charge accumulation and minimize radiation damage. The sample is tilted at least 45º relative to the incoming beam due to geometry constraints in the experimental chamber.

The optical absorption (OA) measurements were performed in the 190 nm – 1100 nm wavelength range, at RT, with a rectangular beam of 0.8×9.0 mm^2, with 1.0 nm resolution.

The X-ray diffraction (XRD) studies were performed using the Cu $K_{\alpha1}$ line collimated with a Gobël mirror, a 2-bounce Ge (111) monochromator and a divergent slit of 0.1×4.0 mm^2. The data was collected with a MBraun ASA 50M position sensitive detector, acquiring a 2θ range of 7º simultaneously.

Atomic force microscopy (AFM) and magnetic force microscopy (MFM) measurements were done with a Veeco CP II microscope working at RT and atmospheric pressure. For AFM measurements the non contact (tapping) mode was used.

All experimental measurements were performed soon after implantation and each annealing stage to avoid ageing effects at RT and ambient atmosphere, such as diffusion, hydration or oxidation.

Whenever possible, OA and AFM measurements preceded XRD analysis while ion beam techniques (RBS, PIXE and IBIL) were the last to be used (except for the samples to be analysed in TEM). This sequence of measurements prevents the introduction of damage by the analysing beam, which would alter the OA, AFM and XRD results.

4.3 Transition metals implantations (4th period)

Table 4.1 presents the most relevant information regarding the implantation of Ni, Cu and Zn, as well as some bulk properties of these metals, useful for the interpretation of the experimental results.

Table 4.1 – Pertinent parameters associated to each implantation or element and to the analysis of the experimental results [Oma93, Lid02 and W4].

	Ni	Cu	Zn
energy (keV)	150	100	150
current density (μA cm^{-2})	6	8	10
samples	c, r, OSP, 0.4 mm	c, m, OSP, 0.4 mm	c, m, BSP, 0.5 mm
fluence (cm^{-2})	1.6×10^{15} – 1.8×10^{17}	1.4×10^{15} – 1.6×10^{17}	4.0×10^{16} – 1.2×10^{17}
SRIM R_p (nm)	71	47	63
SRIM straggling (nm)	24	16	20
SRIM FWHM (nm)	56	37	47
SRIM vacancies per ion	1260	910	1220
SRIM sputtering yield (at. per ion)	4.9	4.6	5.6
n_{dpa}	5 – 554	4 – 253	134 – 402
electronic and nuclear dE/dx (keV nm^{-1})	0.39 and 1.60	0.23 and 1.86	0.48 and 1.81
Van der Walls and ionic radii (pm)	Ni: 163 Ni^{2+}: 63 – 83 Ni^{3+}: 70 – 74	Cu: 140 Cu^{+}: 74 – 91 Cu^{2+}: 71 – 87	Zn: 139 Zn^{+}: 88 Zn^{2+}: 74 – 104
melting point (K)	1728	1358	693
boiling point (K)	3186	3200	1180
space group, structure and lattice parameters	Fm3m; bcc; 0.35 nm	Fm3m; bcc; 0.36 nm	$P6_3/mmc$; hcp; 0.27 nm; 0.49 nm
atomic density (cm^{-3})	9.13×10^{22}	8.46×10^{22}	6.54×10^{22}
compounds and thermal stability	NiO up to 2233 K Ni_2O_3 up to 873 K $NiAl_2O_4$ up to 2350 K	CuO up to 609 K Cu_2O up to 1503 K $CuAl_2O_4$ up to 1343 K	ZnO up to 2073 K ZnO_2 up to 423 K $ZnAl_2O_4$ up to 2226 K
Fermi velocity (m s^{-1})	2.04×10^{6}	1.57×10^{6}	1.83×10^{6}
Fermi level (eV)	11.7	7.0	9.4
ground state electronic configuration	[Ar].3d^8.4s^2	[Ar].3d^{10}.4s^1	[Ar].3d^{10}.4s^2
Debye temperature (K)	450	343	327
bulk plasma frequency (Hz)	1.13×10^{15}	7.35×10^{15}	3.18×10^{15}
surface plasma frequency (Hz)	7.98×10^{14}	5.20×10^{15}	2.24×10^{15}
free electron density (m^{-3})	18.26×10^{28}	8.45×10^{28}	13.10×10^{28}
electron mean collision time (s)	3.10×10^{-15}	2.72×10^{-14}	4.92×10^{-15}

Bulk properties are simply indicative since nanoparticles will exhibit, as mentioned in the previous chapter, different behaviour. It is worth noting the low melting points of Zn and Cu as well as the similar crystal structure of Ni and Cu. Moreover, Ni and Zn present very stable monoxides, besides the spinel aluminates ($MeAl_2O_4$). Regarding the electronic configuration, both Ni and Zn have even number of valence electrons, Zn also presenting closed sub-shell configuration.

4.3.1 Ni implantation

In this study we focus on the structural and optical behaviour of c- and r-cut sapphire implanted with Ni ions, aiming at the production of embedded Ni compounds (Ni precipitates or mixed oxide phases). The evolution of the radiation damage, resulting from the implantation process, with the annealing parameters (temperature and atmosphere) as well as with the matrix crystalline orientation will be followed, while also analysing the optical and structural properties and thermal stability of the systems created. In the context of this thesis this first set of experimental results also includes a detailed characterization of unimplanted, pristine sapphire samples, as previously mentioned.

As summarized in Table 4.1, sapphire single crystals with (0001) and $(10\bar{1}2)$ orientations were implanted at RT with 150 keV $^{58}Ni^{+}$ ions. Implantation fluences were in the range of 1.6×10^{15} cm^{-2} to 1.8×10^{17} cm^{-2}. After implantation the samples were annealed for one hour up to 1273 K in air or vacuum (2×10^{-4} Pa) and the resulting phases characterized and identified at RT by RBS, RBS-C, XRD, AFM and OA.

4.3.1.1 Results and discussion

4.3.1.1.1 Structural studies

The RBS-C spectra obtained after implantation of the lowest Ni fluence, 1.6×10^{15} cm^{-2}, is shown in Figure 4.1 (the arrows point to the surface position of the elements, as discussed in chapter 3). The aligned spectrum in the Al lattice reveals that the topmost layer (~30 nm) retains good crystalline quality after this implantation (the minimum normalized yield, χ_{min}, is 25 %). This region is followed by a higher dechanneling region, with the χ_{min} in the most damaged region (around 1110 keV, or 75 nm) already reaching 40 % for this low fluence, well above the value obtained for a virgin sample (typically ~2 %, as also shown in Figure 4.1, where the dashed line belongs to the aligned spectra of an unimplanted sample). The damage extends to about 125 nm (this value will be considered the thickness of the implanted layer and input in further analysis, e.g. in optical measurements), yielding a damage energy deposition density (cf. equation 3.6) E_D of 1.9×10^{22} keV cm^{-3}, below the amorphization threshold for sapphire of 3×10^{23} keV cm^{-3} given by Mouritz and co-workers [Mou87].

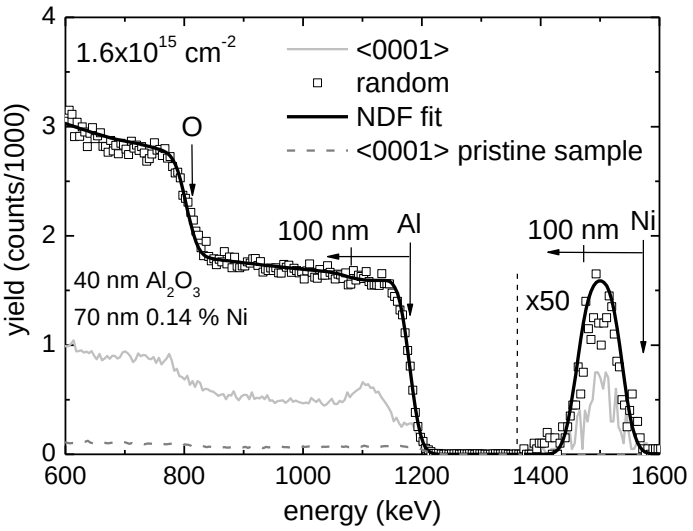

Figure 4.1 – Random (with the corresponding NDF code composition fit) and <0001> – aligned RBS-C spectra of c-cut α-Al_2O_3 implanted at RT with 150 keV 1.6×10^{15} cm^{-2} Ni ions. An aligned spectrum of an unimplanted sample is included for comparison.

Below the damaged (or implanted) region (E < 1050 keV) the χ_{min} is 30 % even if it is unlikely that any damage occurs at such depths in these implantation conditions. The increase in the minimum yield (as compared to that of a pristine sample) beyond the damaged region is due to the fact that the probing ions reaching it have crossed the damaged region where their trajectories are perturbed and are thus more likely to get dechanneled. As the damage builds up (in extension and concentration) in the top layers with increasing irradiation, the dechanneling in deeper regions increases concomitantly. The aligned RBS-C profile in the O sublattice region is similar to that of Al, owing the smaller intensity to its lower scattering cross section.

The Ni profile presents a nearly Gaussian shape, with maximum Ni concentration found at a depth of 75 nm, in good agreement with the theoretical prediction for the projected range (R_p) of SRIM code (71 nm, cf. Table 4.1, see also *Figure 4.2*). This depth coincides with the maximum of Al damage. The χ_{min} in the Ni profile, in the energy interval from 1450 keV to 1550 keV, is about 45 %, an indication of a non-random distribution of this ion in the sapphire structure, typical of low fluence implantation at RT. In fact, the similarity of χ_{min} to that observed on the corresponding region of the Al profile, implies an apparent substitutionality close to 100 %. This suggests that some Ni ions are already found in regular sites along the c-axis of the host matrix, either substituting Al ions, despite the low number of displaced Al atoms per implanted ion (n_{dpa} = *5*, cf. Table 4.1 and equation 3.5) or occupying the structural vacancies. This can result from a self-annealing driven diffusion process during the implantation or, most likely since the implantation current density was kept low, from the high mobility of this small sized ion (about 70 pm for Ni^{3+} vs. 53 pm for Al^{3+}, cf. Table 4.1 and Table 2.2, respectively). This diffusivity may be facilitated in a damage rich region, that is, could be a radiation enhanced diffusion (RED) process. Moreover, the full width at half maximum (FWHM) of the Ni profile is 70 nm, which is about 25 % larger than that predicted by SRIM code, 56 nm (cf. Table 4.1), an extra indication of the mobility of Ni in this system and implantation conditions.

To estimate the composition of the sample the random RBS spectrum is fitted with the NDF code [Bar97], represented by the black line in Figure 4.1, by considering a 40 nm thick pure Al_2O_3 layer at the surface, followed by 70 nm of 0.14 % Ni in sapphire, with a total of 1.5×10^{15} cm^{-2} Ni ions, in excellent agreement with the experimental measurements of fluence and thicknesses. The simulated thicknesses were calculated assuming the atomic density of crystalline sapphire (1.1768×10^{23} at. cm^{-3}, cf. Table 2.1), which is thus found valid for this low damage and impurity concentrations.

Regarding calculations, SRIM code predicts the Al (and O) displacements to have a maximum around 50 nm, before the depth of Ni maximum concentration (R_p = 71 nm), as shown in *Figure 4.2*. This figure shows the calculated Al and O primary recoils distribution, as well as that of Ni, and the aligned spectra in the Al region obtained after implantation of 1.6×10^{15} cm^{-2} and 1.8×10^{17} cm^{-2} Ni ions. However, for the lower fluence the maximum of disorder (i.e. dechanneling maximum) in the Al sublattice, resulting from displacements produced by the Ni ions, occurs at a higher depth, 75 nm, exactly where the maximum of Ni concentration occurs. This difference is more evident for the highest fluence (1.8×10^{17} cm^{-2}) where the Al displacements extend over 200 nm. This is probably due to a limitation of SRIM code, which considers the target as an amorphous isotropic material. In crystals, however, this is not the case and the crystal potential field affects not only the paths of the impinging ions but also the cascades and paths of the displaced ions (more stringent for Al which has lower displacement energy). These displaced ions are susceptible to be guided through the crystal potential field and some will probably prefer

channelled paths, which may increase their range significantly. Moreover, the presence of Ni ions (and aggregates) up to 200 nm (cf. *Figure 4.3*a) must distort the sapphire lattice, exposing Al (and O) ions which would otherwise be "invisible" to the incoming probing beam. This distortion and exposure effect explains also the larger thickness of displaced Al atoms measured by RBS-C (up to 200 nm for the higher fluence vs. 140 nm from SRIM).

Regarding the end of range of Ni ions, it's also worth noting that SRIM does not account for dynamic effects during implantation, such as self annealing or RED, as discussed in chapter 3. The depression around 60 nm in the Al (and O, cf. *Figure 4.3*a) aligned spectrum for the implantation of 1.8×10^{17} cm^{-2} simply reflects the decrease of the relative concentration of this element due to the presence of a large concentration of Ni at the same depth. This feature was used to match the depth scales of the random and aligned spectra (otherwise the latter would have to be corrected by the decrease in the stopping power observed along crystallographic directions).

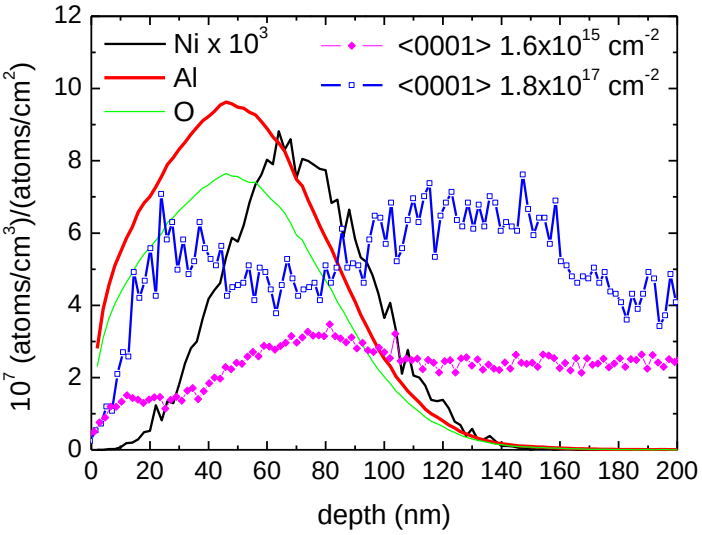

Figure 4.2 – Ni ion and Al and O primary recoils distribution computed by SRIM code, as well as the aligned RBS-C spectra of c-cut samples as implanted with 1.6×10^{15} cm^{-2} and 1.8×10^{17} cm^{-2} Ni ions.

In any case, after implantation the implanted species profile sits entirely in the damaged layer.

After implantation of 1.8×10^{17} cm^{-2} (where n_{dpa} = 554) a 200 nm thick, highly damaged surface layer is produced, as revealed by the corresponding RBS-C spectra of *Figure 4.3*a. In fact this region is defined as amorphized as seen by RBS-C, since the aligned spectrum matches the random one in this region (χ_{min} = 100 %). It's important to notice that this is a very particular definition of amorphization, as mentioned in chapter 3, and simply implies that there are no channelling paths available in that region, a condition which encompasses several cases, e.g. randomly oriented polycrystallites or even the complete absence of crystalline order in the region. This definition differs, for example, from that used in the context of XRD measurements. The value of E_D is now 1.35×10^{24} keV cm^{-3}, well above the amorphization threshold of sapphire. At higher depths (E < 1000 keV) χ_{min} rises to about 50 %, a consequence of the higher disorder on the surface layer. The O sublattice profile is similar to that found in the Al sublattice.

The Ni profile is again nearly Gaussian, with a small tail towards lower energies, and somewhat narrower (65 nm FWHM) and peaking closer to the surface, at 60 nm, in comparison to the low fluence implantation. This latter effect may be related to target densification or sputtering which become significant in high fluence implantations. Naturally it does not display any channelling effect. The fit of the random RBS spectrum with the NDF code [Bar97], yields a 25 nm thick pure Al_2O_3 layer at the surface, followed by 65 nm with 20 % Ni in sapphire

and 35 nm with 6 % Ni, with a total of 1.76×10^{17} cm^{-2} Ni ions, in excellent agreement with the measured fluence. This composition reflects the very low concentration of Ni in the first nanometres of the sample in these implantation conditions (as predicted by SRIM, cf. *Figure 4.2*), a central layer where most Ni sits and a lower Ni concentration layer before the bulk unchanged matrix starts. Again, the simulated thicknesses were calculated assuming the atomic density of crystalline sapphire, despite the possibility of some volume increase related to the destruction of the sapphire lattice.

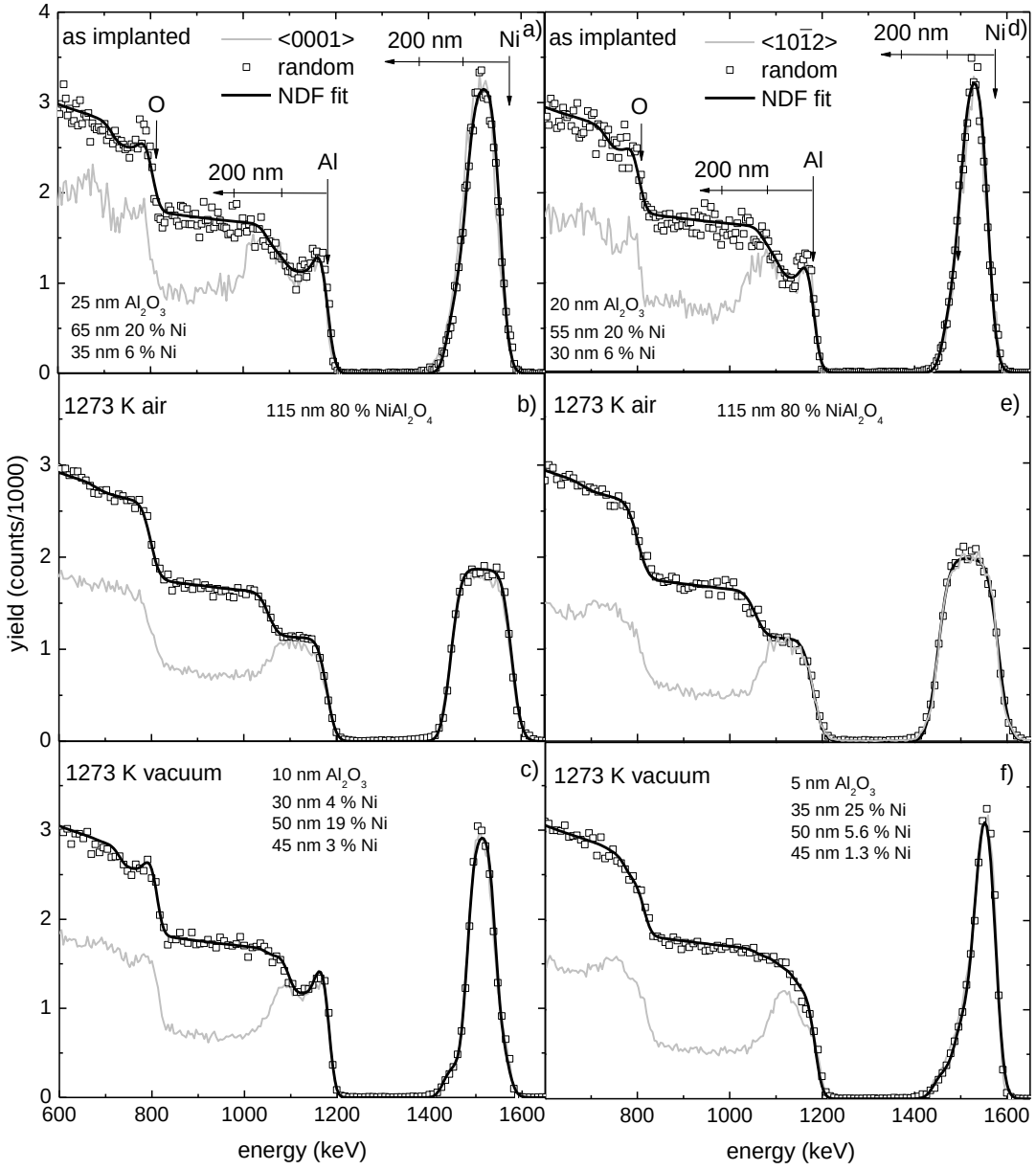

Figure 4.3 – Random and $< 0001 >$ or $< 10\bar{1}2 >$ aligned RBS-C spectra of c-cut sapphire implanted with 1.8×10^{17} cm^{-2} (left-hand side of the figure) and r-cut sapphire implanted with 1.6×10^{17} cm^{-2} (right side): a) and d) as implanted (RT with 150 keV); after annealing for one hour at 1273 K in b) and e) air and c) and f) vacuum. All random spectra were fit with NDF code, with the compositions shown.

To compare the effect of the crystallographic orientation, a similar fluence was implanted on r-cut samples, whose RBS-C spectra are shown in *Figure 4.3*d.

The comparison with *Figure 4.3*a shows identical matrix profiles for c- and r-cut samples, the latter with a somewhat lower damage extension (180 nm), giving E_D of about 1.33×10^{24} keV cm^{-3}. This may explain the lower χ_{min} found in deeper regions (40 %) as compared to that found for c-cut samples (50 %). Moreover, r-cut samples may retain a lower damage concentration (or even different types of defects) in the damaged layer.

The Ni distributions are also similar but in the case of r-cut samples the FWHM decreases to 55 nm while R_p is found closer to the surface, at 50 nm, a consequence of the anisotropic structure of sapphire, where r-plane shows a higher areal density of matrix ions which limits the range of the implanted ions. The simulated composition is analogous to that of c-cut samples, but distributed in a thinner region. Table 4.2 summarizes the RBS-C findings on the as implanted samples.

Table 4.2 – RBS-C values obtained in sapphire c- and r-cut samples as implanted with Ni ions.

sample	c, 1.6×10^{15} cm^{-2}	c, 1.8×10^{17} cm^{-2}	r, 1.6×10^{17} cm^{-2}
host matrix			
max. damage depth (nm)	75	0 – 200	0 – 180
χ_{min} (%)	40	100	100
damage extension (nm)	125	200	180
E_D (10^{22} keV cm^{-3})	1.9	135	133
deep region χ_{min} (%)	30	50	40
implanted profile			
max. conc. depth (nm)	75	60	50
χ_{min} (%)	45	100	100
f_{sub}	100	0	0
FWHM (nm)	70	65	55
max. conc. (at. %)	0.14	20	20

The damage recovery and thermal stability of these systems implanted with the higher fluences was followed performing annealings in air or vacuum up to 1273 K. The relevant results obtained with RBS-C on these samples are summarized in Table 4.3.

After annealing in air at 1273 K the damage extension decreases in both types of samples, as presented in the spectra in *Figure 4.3*b and *Figure 4.3*e for c- and r-cut samples respectively. This is revealed by the thinning of the dechanneling region to approximately 115 nm in both cases. However, the level of damage seen through RBS-C remains close to amorphization in the Al sublattice. The main difference is the dechanneling in deep regions, with r-cut samples recovering to χ_{min} = 30 % while c-cut samples still show χ_{min} = 50 %. The most striking features are the appearance of a rectangular shaped Ni profile extending to the surface, which implies a constant concentration of Ni, and a correspondingly flat plateau on the Al profile having similar thickness, 115 nm. These are indications for the possible formation of a mixed Ni-Al oxide. Simulations of the RBS spectra with the NDF code show average compositions that are consistent with formulas reflecting some Al_2O_3 diluted in the Ni aluminate spinel phase: about $NiAl_2O_4{\cdot}0.27Al_2O_3$ for c-cut samples and $NiAl_2O_4{\cdot}0.23Al_2O_3$ in the case of r-cut samples. These phases are expected to have similar atomic concentration to sapphire since the spinels have about 12.6×10^{22} at. cm^{-3} vs. 11.7×10^{22} at. cm^{-3} for sapphire, which validates the thickness determination using the density of sapphire. After this annealing stage in air a small loss (6 %) of Ni was observed only in c-cut samples. The absence of channelling in the Ni profile after this annealing stage indicates a non alignment of the Ni ions with the

host crystallographic structure along the c-axis direction of sapphire. The impossibility of sensing their location results from the matrix status, possibly devoid of long range crystalline order in the implanted region.

When the annealing is carried out in vacuum at the same temperature a different behaviour is observed. In the case of c-cut samples (*Figure 4.3*c), the damage extension decreases from 210 nm to about 170 nm (still amorphized, but with χ_{min} = 40 % for E < 1000 keV) and there is a small increase of the Al content at the topmost surface layer after this annealing, indicating some stoichiometric recovery of the surface. This leaves the Ni profile sandwiched by a nearly unchanged crystal and polycrystalline alumina surface layer. In fact, the Ni profile remains with an overall nearly Gaussian shape, with a small tail into lower energies, still centred around R_p, where the Ni concentration reaches 19 at. %, but with FHWM of 50 nm (vs. 65 nm after implantation). This thinning may thus be due to combined action of the motion towards the surface of the recrystallization front with the reconstruction of the topmost surface layer. At this stage there is a 26 % loss of Ni, possibly resulting from the dissolution of Ni precipitates which diffuse out through the grain boundaries of the surface layer and eventually evaporate in these annealing conditions. No channelling is measured in the Ni profile while at higher depths χ_{min} = 40 %.

On the other hand, in the case of r-cut samples the damage extension decreases to about 130 nm, where the average χ_{min} drops to 80 %, and showing again a lower damage level (χ_{min} = 30 %) for E < 1000 keV. The higher level of recrystallization observed in the Al sublattice of r-cut samples results from the higher mobility of Al and O ions along the c-plane, which crosses the damaged layer in these samples. Again, the recrystallization front is probably the driving force that causes the Ni profile to clearly shift to the surface (*Figure 4.3*f), peaking at 25 nm, where the Ni concentration reaches 25.0 at. %. The FWHM decreases to 35 nm at this stage and a 14 % loss of Ni is measured. No channelling is observed in the Ni profile. Since the diffusion to the surface is faster in r-cut samples, one would expect a larger evaporation of Ni in this case. However, the crystalline recovery observed in the damaged layer may limit the out diffusion process. As a result of different losses, the retained amounts of Ni are similar for both vacuum annealed samples, about 1.3×10^{17} cm^{-2}.

Table 4.3 – RBS-C results of Ni implanted samples annealed at 1273 K.

sample	c, 1273 K air	r, 1273 K air	c, 1273 K vac.	r, 1273 K vac.
host matrix				
max. damage depth (nm)	0 – 115	0 – 115	0 – 170	0 – 130
χ_{min} (%)	100	100	100	80
damage extension (nm)	115	115	170	130
deep region χ_{min} (%)	50	30	40	30
implanted profile				
max. conc. depth (nm)	0 – 115	0 – 115	60	25
χ_{min} (%)	100	100	100	100
retained fluence (10^{15} cm^{-2})	170	160	133	137
fluence loss (%)	6	0	26	14
FWHM (nm)	115	115	50	35
max. conc. (at. %)	11.3	11.6	19.0	25.0

XRD measurements were carried in these samples, in order to detail the phases present after implantation and those developed after the annealing at 1273 K. The spectra obtained for c- and r-cut samples are shown in Figure 4.4a and Figure 4.4b, respectively.

In the case of c-cut samples, after implantation only a weak and broad reflection identified with (111) plane of metallic Ni (with 0.3527 nm lattice constant) is seen along with the sharp (0006) reflection of sapphire. This implies that the <111> direction of cubic Ni is aligned with <0001> direction of hexagonal sapphire, suggesting solid phase epitaxy reaction, i.e. epitaxial formation and growth of Ni clusters during the implantation process. From the Scherrer formula [Cul72]:

$$D = \frac{0.9\lambda}{B\cos\theta_B} \qquad [4.1]$$

where λ is the X-rays wavelength, B the FWHM of the diffraction peak (in radians) and θ_B is the Bragg diffraction angle, the average size D (if below ~200 nm) of such clusters may be determined. Using this method, the metallic Ni aggregates obtained after implantation are estimated to have an average size of 4 nm. This is similar to the dimensions of 1 nm to 5 nm observed with transmission electron microscopy (TEM) by Xia and co-workers [Xia05] after 64 keV Ni implantation onto sapphire. However, it is worth noting that D is the crystallite size, a measure of the size of a coherently diffracting domain. For polycrystalline aggregates, crystallite size is not generally the same as particle size. In fact, it is expected to be lower, either for multiple crystalline domains or due to highly defective material in the aggregate.

Thus we find that by implantation of high fluences a composite material has been obtained, which in fact is a cermet (ceramic-metallic) layer, embedded in sapphire.

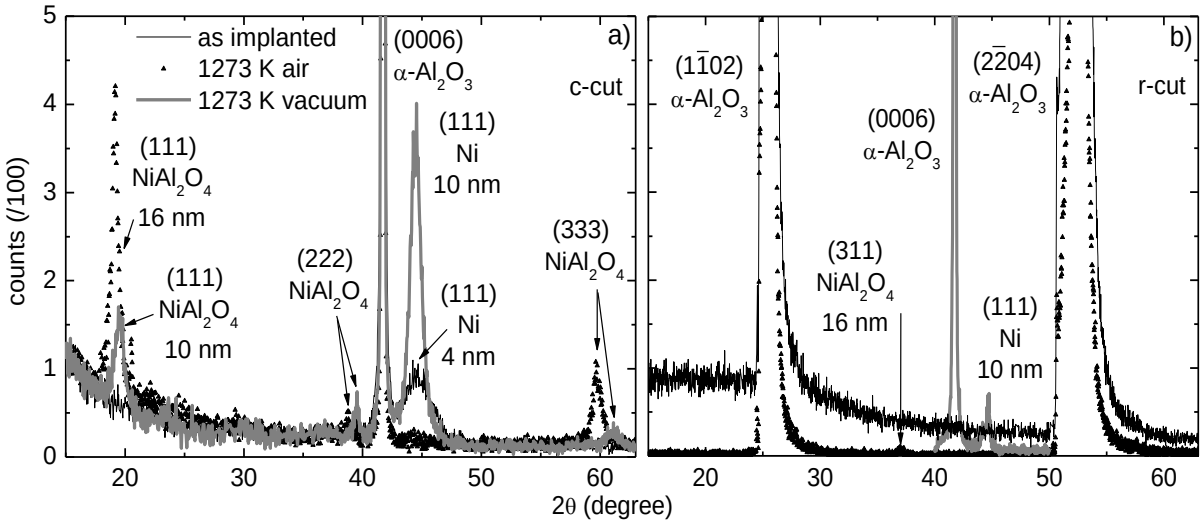

Figure 4.4 – XRD spectra of 150 keV Ni implanted a) c-cut samples (1.8×10^{17} cm^{-2}) and b) r-cut samples (1.6×10^{17} cm^{-2}) after implantation and after annealing at 1273 K in air or vacuum for one hour. The dimensions of the precipitates were estimated using the Scherrer formula.

As seen also in Figure 4.4a, the annealing in air produces exclusively the spinel phase, as seen by the (111), (222) and (333) reflections parallel to the c-plane of sapphire (or $<0001>_{sapp}$ // $<111>_{spi}$) with aggregates of ~16 nm average size, while the metallic Ni is exhausted, in agreement with the RBS-C findings. These results are consistent with those of Fujimura and co-workers [Fuj97] obtained on the high temperature oxidation of a Ni thin film (T > 1468 K) deposited on polycrystalline sapphire which resulted in pure spinel phase. A small and narrow peak at 20.5^{o} was not identifiable.

The annealing in vacuum at 1273 K produces a marked increase of the metallic Ni phase, $<0001>_{sapp}$ // $<111>_{Ni}$, the aggregates having an average size of about 10 nm and lattice constant of 0.352 nm, somewhat smaller than in the as implanted state. It is also observed the development of a small amount of the cubic spinel $NiAl_2O_4$, with about 10 nm and the same family of reflections and epitaxial relations found for the air annealed samples: $<0001>_{sapp}$ // $<111>_{spi}$. This oxide is possibly formed with unbound or non-bridging oxygen atoms freed during the implantation process.

There is a clear shift in the reflections from the {111} family of planes of the spinel phase formed in air or vacuum in c-cut samples, which implies different lattice constants. In fact, the spinel phase formed in vacuum has a smaller lattice constant (0.790 nm) than that formed by annealing in air (0.801 nm). The lattice constants *d* were determined by adjusting the diffraction patterns generated by CaRine Crystallography 3.1 code in order to fit all diffraction maxima of a given phase. This is accomplished using:

$$\Delta(\theta) = -\frac{\Delta(d)}{d\ tan(\theta)} \qquad [4.2]$$

where θ is the reflection angle, $\Delta(\theta)$ the angular difference and Δd the lattice dimension difference [Cul72]. The spinel formed in oxygen deficient environment is probably in a more disordered state and thus more compressed [Hal02], possibly with an higher degree of inversion between cations, e.g. formation of inverted spinel, common in $NiAl_2O_4$ [Ust00], thus explaining the 0.011 nm difference in the lattice constant.

For r-cut samples the XRD measurements of Figure 4.4b show no Ni precipitates after implantation, possibly due to the absence of crystalline phases, their reduced size or misalignment with the matrix.

Annealing in air promotes the formation of the Ni spinel phase with (311) plane parallel to the r-plane, as expected from the epitaxial relation $<0001>_{sapp}$ // $<111>_{spi.}$, with the same precipitate size as observed in c-cut samples but showing a larger cell dimension, 0.806 nm, the closest to the tabulated value of 0.805 nm. We ascribe this to a more ordered spinel phase, resulting from the lower implantation damage in r-cut samples.

Upon annealing in vacuum again no reflections are observed. However, tilting the sample by 58° and finding the c-plane allows to observe the $(111)_{Ni}$ reflection, parallel to c-axis of sapphire, with about 10 nm, as in c-cut samples after similar annealing, but with a slightly smaller lattice constant (0.352 nm vs. 0.353 nm).

The reduced size of these precipitates may also be a key factor (along with the orientation of c-plane) on the remarkable surface diffusion observed in the RBS-C measurements in r-cut samples.

Despite these epitaxial relations between sapphire and the Ni phases no channelling effect was found in the corresponding RBS-C spectra, which may indicate that aligned Ni phases are present in minor concentration or randomly oriented or even stressed due to lattice mismatch. The lattice match between hexagonal and cubic lattices is achieved when, as shown in *Figure 4.5* for the case of $(0001)_{sapp}$ // $(111)_{spi}$, the lattice relation is:

$$n\ a_{hex} \approx \sqrt{2}\ a_{cub} \qquad [4.3]$$

where *n* is the whole number closer to the ratio between the larger and the smaller lattice constant. Given the lattice dimensions of sapphire (*a* = 0.475 nm) and the spinel, *n* = 2 and the calculated mismatches for the spinel phase is about 8 % in any case. This is the maximum mismatch since, for example, a 30° rotation would decrease the interface tension. Regarding the cubic Ni phase (*n* = 1) this mismatch is around 2.4 %. This misfit is small enough to support the occurrence of epitaxy in both phases [Ohk88].

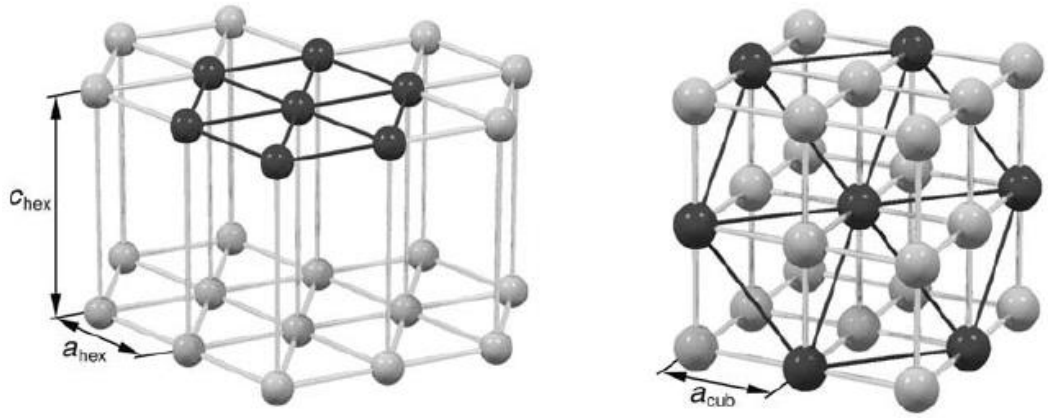

Figure 4.5 – Hexagonal (left-hand side) and cubic structure (right side). Some c-plane atoms of the former and those of (111) plane of the latter are displayed in a darker colour.

No reflections from other nickel compounds or from γ-Al_2O_3 or other transition aluminas were observed at any stage. Table 4.4 summarizes the findings obtained with XRD measurements. The indexation of the diffraction lines was based on the database of the International Centre for Diffraction Data with the Powder Diffraction Files (PDF) cards given.

Table 4.4 – XRD results of Ni implanted sapphire samples.

sample	2θ	phases	size (nm)	calculated and tabulated lattice dimensions (nm)	PDF card
c, 1.8×10^{17} cm^{-2} as imp.	44.45	Ni (111)	4	0.353 / 0.352	00-004-0850
1273 K air	19.18	$NiAl_2O_4$ (111)	16	0.801 / 0.805	00-010-0339
1273 K vacuum	19.45 44.45	$NiAl_2O_4$ (111) Ni (111)	10 10	0.790 / 0.805 0.353 / 0.352	00-010-0339 00-004-0850
r, 1.6×10^{17} cm^{-2} as imp.	-	-	-	-	-
1273 K air	36.94	$NiAl_2O_4$ (311)	16	0.806 / 0.805	00-010-0339
1273 K vacuum	44.60	Ni (111)	10	0.352 / 0.352	00-004-0850

Atomic force microscopy (AFM) measurements (*Figure 4.6*) were performed to detect Ni structures at the surface of the samples, in particular in r-cut samples annealed at 1273 K in vacuum where diffusion to the surface was suggested by the RBS-C spectra (cf. *Figure 4.3*f). Given the magnetic nature of Ni, these measurements were performed in the magnetic force microscopy (MFM) mode, which simultaneously allows measuring the topography, but no magnetic behaviour was detected on the surface structures. After implantation (*Figure 4.6*a) the surface is very similar and smooth in both samples (only c-cut is shown), with a lot of small (~100 nm) structures, the surface presenting *rms* roughness of about 7 nm (pristine samples show subnanometre roughness). After annealing in

vacuum (*Figure 4.6*b), the morphology obtained in c-cut samples changes to larger and irregular structures, with average dimension of 250 nm, the *rms* roughness reaching 10 nm. On the other hand, the r-cut sample subject to the same annealing (Figure 4.6c) shows regular faceted structures with about 300 nm width and 30 nm to 40 nm height, and 15 nm surface *rms* roughness. The formation of larger and ordered precipitates is another indication of a faster diffusion of Ni ions to the surface in the case of r-cut samples, as inferred by RBS. These structures are probably Ni precipitates capped with a very thin oxide surface layer since Ni oxides have low formation enthalpies at RT (-241.3 kJ mol^{-1} and -489.5 kJ mol^{-1} for NiO and Ni_2O_3, respectively), a possibility consistent with the presence of Ni at the surface and absence of its oxides in the correspondent XRD spectrum.

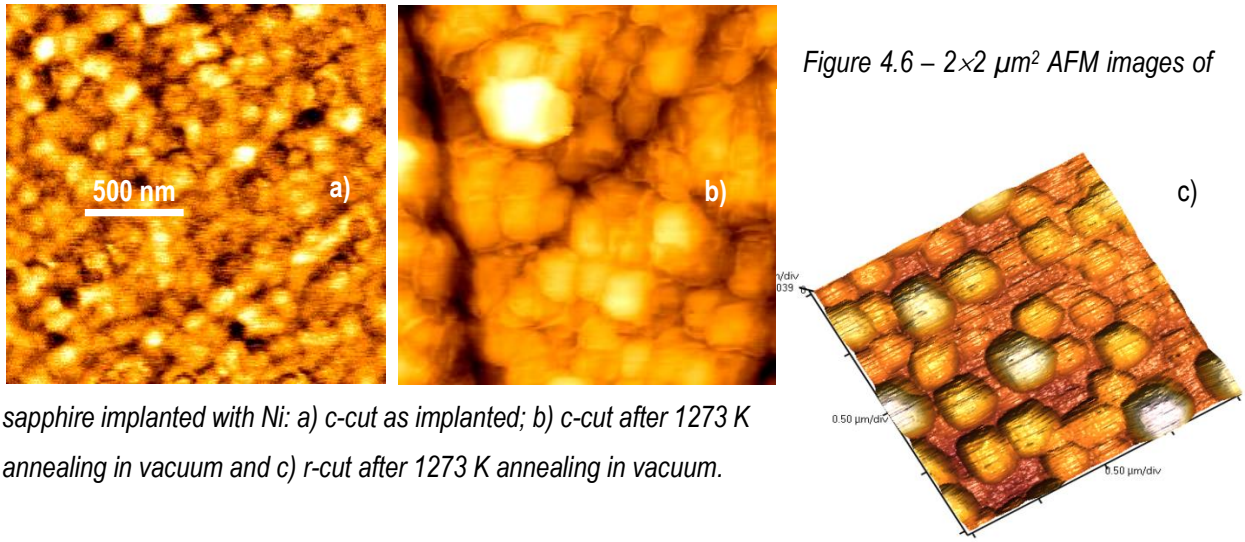

Figure 4.6 – 2×2 µm² AFM images of sapphire implanted with Ni: a) c-cut as implanted; b) c-cut after 1273 K annealing in vacuum and c) r-cut after 1273 K annealing in vacuum.

The phase diagram of the Ni-Al-O system at 1273 K, depicted in *Figure 4.7*, shows that a spinel phase is expected, after annealing in air, for the measured composition of about 11 % of Ni, 29 % of Al and 60 % of O (cf. NDF fits of *Figure 4.3*b and *Figure 4.3*e), as well as the absence of NiO (bunsenite). The system formed in air is thus explainable in terms of thermodynamic equilibrium.

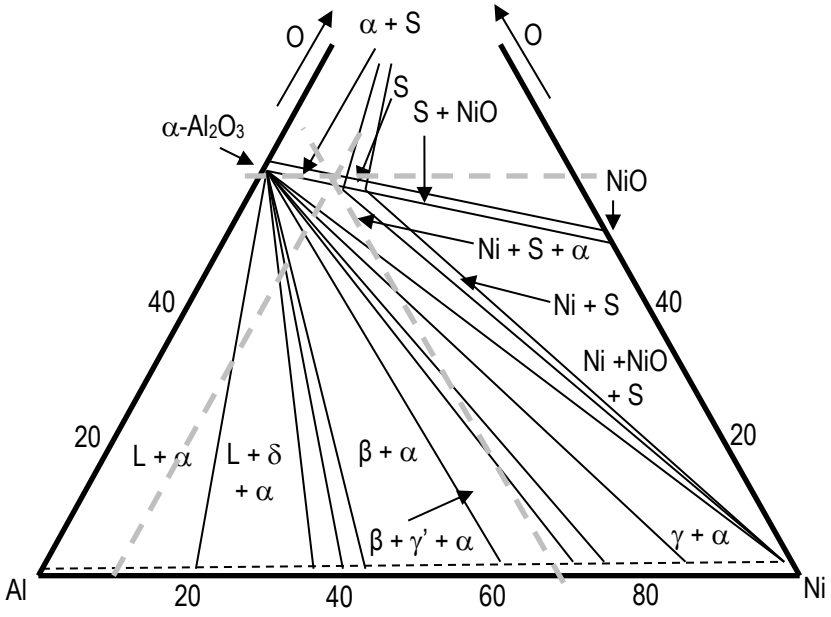

Figure 4.7 – Phase diagram of Ni-Al-O at 1273 K (adapted from [Elr81]), the intersection of the grey dashed lines indicating the composition (at. %) region obtained with RBS for the samples annealed in air at 1273 K.

This does not mean that the spinel formation evolved directly from Ni and Al_2O_3 reaction. In fact, the most probable process, as observed by Fujimura and co-workers [Fuj97] on Ni vacuum deposited in polycrystalline α-Al_2O_3 and annealed in air atmosphere, is the initial oxidation of Ni, forming NiO. This would be the first step for the formation of the spinel, a process governed

by subsequent Al and Ni counter diffusion (Wagner mechanism) in NiO and Al_2O_3 [Bol95]. The NiO phase was completely exhausted after one hour annealing in air at temperature as low as 1468 K. In fact, Fujimura and co-workers found that similar annealing but in N_2 atmosphere produced no oxide or spinel, which supported the assumption of this mechanism. Assuming a similar mechanism in our samples, for the same annealing period we observed a total exhaustion of NiO at lower temperature, 1273 K, which is related to the lower quantity of Ni present in our system and to the higher scattering of reacting elements (Ni and Al) in these ion implantation conditions, where all elements are mixed together and no clear interface exists as in the work above mentioned.

Figure 4.8 presents the phase diagram of Ni-Al-O also at 1273 K but in low oxygen pressure conditions [Elr81]. Under the vacuum (2×10^{-4} Pa) annealing conditions used in this work the partial pressure of oxygen is about 4×10^{-5} Pa.

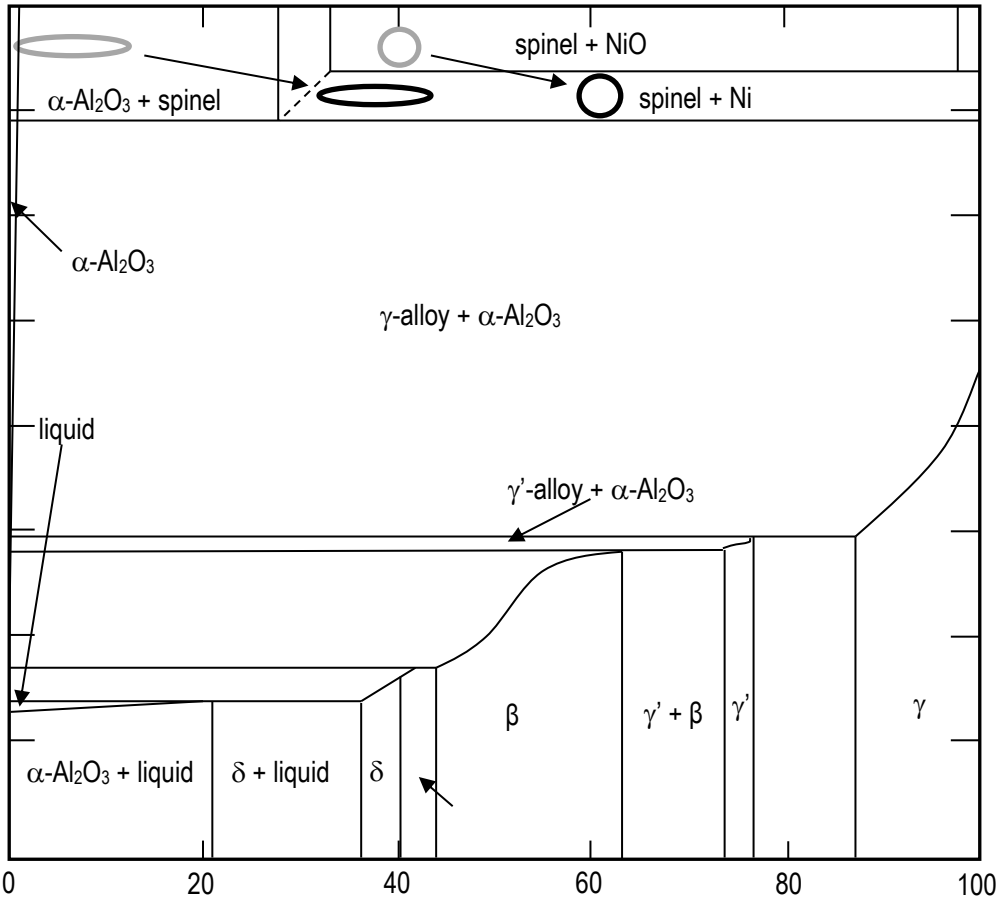

Figure 4.8 – Phase diagram of the Ni-Al-O at 1273 K, relative Ni % vs. oxygen pressure [Elr81], the black and gray circle and ellipse indicating the composition obtained with RBS after annealing in vacuum at 1273 K.

According to this phase diagram, in the layers with lower Ni relative concentration, below 13 % (cf. fit in Figure 4.3c and *Figure 4.3*e), the composition region represented by the gray ellipse, under thermodynamic equilibrium both spinel and α-Al_2O_3 would be present. If the spinel phase is in fact present (in c-cut samples), as well as sapphire (cf. Figure 4.4, although the observed reflections of α-Al_2O_3 contain essentially signal from the bulk matrix), the presence of Ni is not expected.

Another discrepancy occurs for the higher Ni relative concentrations layers (37 % and 45 % for c- and r-cut samples respectively), region represented with the grey circle, where only spinel and NiO are expected. Again, spinel is observed (in c-cut samples) but not NiO. Moreover, sapphire is also observed, but for the reasons mentioned above.

The absence of Ni in the phase diagram in the case of the low concentration layers is explained by the presence, in the mixed Al and Ni layer, of sapphire crystallites which accelerate the formation of large sapphire grains (these have random orientations and thus the RBS-C spectra of *Figure 4.3*c and *Figure 4.3*e show χ_{min} of about 100 %), consuming both Al and O. Ni is thus left with less Al and O and probably this moves these layers to another compositional regime in the phase diagram, represented with the black ellipse, with higher Ni relative concentration and lower oxygen pressure (below 3.8×10^{-6} Pa). The same argument applies for the layers with higher Ni content and justifies the absence of NiO and the presence of Ni (black circle). NiO may again have been exhausted as a first step for the production of the spinel phase.

This is consistent with the work of Trumble and co-workers [Tru90], who observed that the spinel phase is expected to be reduced to Ni and Al_2O_3 when there is less than 0.006 at. % of available O. In our case, the rapid formation, at the beginning of this annealing, of NiO is followed by $NiAl_2O_4$ via Wagner mechanism and, in an increasing reducing environment, as Al competes for the existing oxygen, Ni is eventually obtained. And, in this assumption, the process was not complete in c-cut samples at 1273 K, possibly due to the lower mobility of the ions across the damaged region.

4.3.1.1.2 Optical studies

Optical extinction measurements were performed to further characterize the samples. This technique allows inspecting both the O lattice defects (F-type centres, cf. Table 2.3) and the characteristic features of phases involving the implanted material and its reactions with the surrounding media (matrix and atmosphere), namely metallic Ni aggregates, through the surface plasmon resonance (SPR) absorption band or interband (IB) transitions, or bands related to the oxidation state of Ni. We'll start with the characterization of pristine samples.

4.3.1.1.2.1 Pristine samples

Undoped sapphire single crystals are colourless and transparent in the visible region. Indeed, the optical extinction spectrum of unimplanted samples, presented in Figure 4.9a (raw data: $log(I_0/I)$ vs. wavelength), shows nearly no extinction, in particular in both sides polished (BSP) samples where the measured extinction is actually due to reflection losses at the air-sapphire interfaces. Samples with one side polished (OSP) show higher optical extinction due to scattering at the unpolished surface, proportional to λ^{-4}, explaining the increase of extinction with photon energy.

For BSP samples, in order to calculate the extinction coefficient of pristine sapphire it is necessary to subtract the contribution from reflection $R(\lambda)$ at the air-sapphire interfaces. To use equation 3.36 we must first determine the relation dispersion of sapphire's refractive index. That may be accomplished with a Cauchy or

Sellmeier-type dispersion formula, valid in the 200 nm to 5500 nm wavelength range (a normal dispersion zone, where *n* slowly increases as the wavelength decreases towards a resonance, in this case in the deep UV region):

$$n^2 - 1 = \sum_j \frac{A_j \lambda^2}{(\lambda^2 - \lambda_j^2)} \qquad [4.4]$$

with the empirical factors A_1 = 1.4313493, A_2 = 0.65054713 and A_3 = 5.3414021 and $\lambda_1 = 0.0726631\ \mu m$, $\lambda_2 = 0.1193242\ \mu m$ and $\lambda_3 = 18.028251\ \mu m$ [Tro98]. The calculated spectrum, considering only two reflections, is displayed in Figure 4.9a and fits nicely the experimental data from the BSP sample. The dispersion formula is thus validated to be used as input for the remaining calculations and also for the simulations, e.g. for SCOUT or MiePlot codes. The computed spectrum differs somewhat from the experimental one in the UV region, where the previously mentioned F-type centres determine the absorption and whose concentration varies slightly with the origin and supplier of the material [Yal99]. These oxygen vacancies are usually related to oxygen loss via unwanted reactions during growth, namely with carbon present in the reactor components [Lee78].

We may now assume that the difference Δ between the calculated (considering two reflections only) and experimental spectrum of the sample with BSP is thus uniquely due to extinction phenomena (absorption and scattering). Following the method presented in chapter 3 (equation 3.43) it is possible to extract, from the BSP spectrum, the extinction coefficient of virgin sapphire which, neglecting scattering phenomena, equals the absorption coefficient and is represented in Figure 4.9b. In this case, $k = 10^{-5}$ cm^{-1}, in agreement with the literature [Zho06].

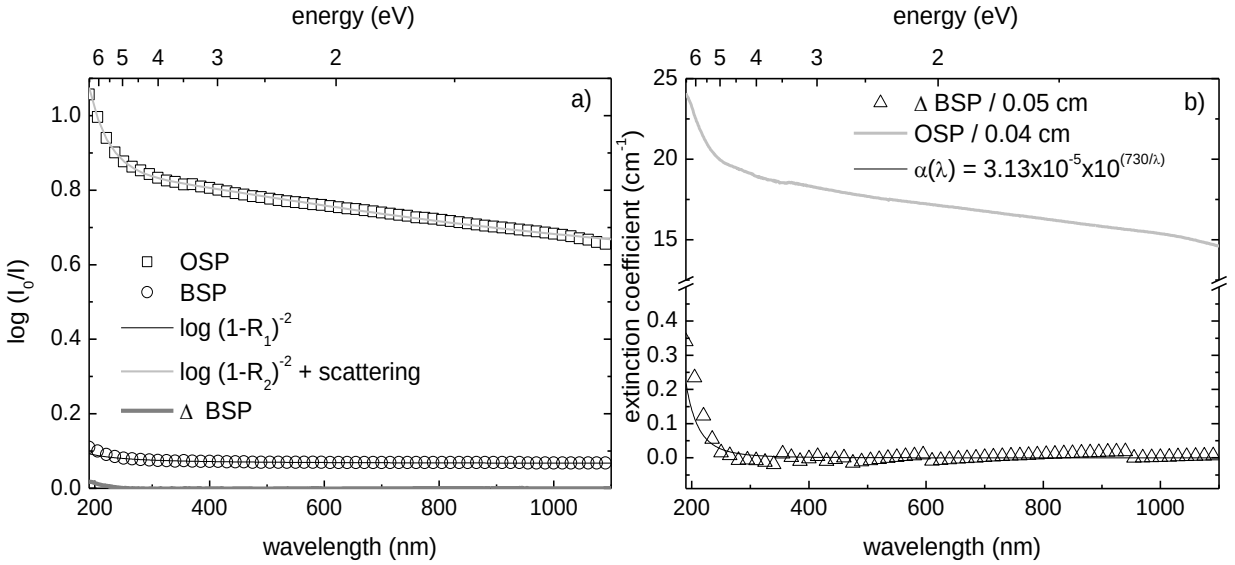

Figure 4.9 – Spectra of one side polished (OSP) and both sides polished (BSP) pristine sapphire samples: a) raw data, along with calculated spectra for BSP and OSP samples and b) data in operational parameter extinction coefficient units (cm^{-1}).

Regarding the concentration of defect centres, Smakula's equation [Dex56], equation 3.54, applied to this band yields about 2.3×10^{15} cm^{-3} and 3.2×10^{15} cm^{-3} F- and F$^+$-centre concentration, respectively, for these unimplanted samples (cf. *Table 4.5*). This is in poor agreement with the literature for as-grown samples where

higher values (10^{17} cm^{-3}) are reported [Sur01, Zho06]. This is due to the subtraction method used in this work. That is, since the data used for the determination of the refractive index of sapphire used as input in our calculations (Sellmeier formula) must have been obtained in real samples, e.g. via ellipsometric measurements, that inevitably have intrinsic defects which are thus embedded in the reference values of refractive index. Hence, the value we found is just the extra defect concentration above that of the (purest) samples used to obtain the tabulated values of optical constants of sapphire.

The spectrum of the OSP sample was also fit with a Sellmeier type formula, the parameters of which are input in the forthcoming optical simulations. Furthermore, one may also calculate the dispersion of the absorption coefficient of the BSP sample (Figure 4.9b) using an empirical equation for the absorption coefficient of sapphire [Tro98] valid between 8.5 eV and 0.9 eV:

$$\alpha(\lambda) = \alpha(\lambda_0)10^{\frac{\lambda_0}{\lambda}} \qquad [4.5]$$

where $\lambda_0 = 730$ nm and $\alpha(\lambda_0) = 3.13 \times 10^{-5}$ cm^{-1}. Again, this fits very well the experimental spectrum but underestimating the UV absorption due to the aforementioned defect centres.

4.3.1.1.2.2 As implanted

These experimental pristine spectra (OSP and BSP) are subtracted from the corresponding as implanted samples in order to remove the intrinsic characteristics and thus yield only the features related to the implantation. This is the case of the spectra presented in *Figure 4.10*a, where the original experimental spectra of as implanted samples is subtracted by the OSP spectra and also slightly shifted vertically and made to coincide, in this case, at 700 nm (no significant features appear in the 700 nm to 1100 nm wavelength range) to minimize reflection and scattering differences. This does not alter the determination of the operational parameters, namely the area of the bands or the peak position. The samples implanted with the lowest fluence remained colourless and transparent while the samples implanted with the highest fluence acquired a dark brown colouration, due to both the implanted species and radiation damage introduced during implantation. In fact, after these implantations the UV and blue region of the spectra show an increase of absorption, which comprises not only sapphire's F centres at 205 nm and F^+ centres, with triplet absorption at 203 nm, 225 nm and 258 nm (cf. Table 2.3), but also interband (IB) transitions of Ni which in fact overshadow the defect signatures at high fluences. For this reason the amount of F-type centres was determined only for the lowest implantation fluence. Using Smakula formula, equation 3.54, with n = 1.834 and x = 125 nm, yields 8.4×10^{19} cm^{-3} and 3.9×10^{19} cm^{-3} for F- and F^+-centres, at 205 nm and 225 nm, respectively, in the implanted layer. These values, resumed in *Table 4.5* (where the defect concentration of pristine samples is also presented), add to about 0.2 % of the total oxygen concentration (~7×10^{22} cm^{-3}), and imply a similar fraction of surviving defects after implantation.

In the case of c-cut samples implanted with 1.8×10^{17} cm^{-2} a wide absorption band centred on 351 nm with FWHM of 208 nm is also observed. This absorption is related to the presence of Ni aggregates which (dipolar) SPR band is expected around 375 nm to 400 nm with about 2.2 eV [Ame05, Xia04a, Xia05]. In the case of copper, the appearance of the SPR band reveals the presence of metallic aggregates larger than ~0.7 nm, the threshold size

for significant SPR absorption to develop [Che90]. In fact Xiang and co-workers ascribed a large and weak absorption band centred around 400 nm to SPR band from 1 nm to 5 nm Ni particles resulting from 1×10^{17} cm^{-2} 64 keV implantation at RT in sapphire. In our case, having larger average sized precipitates, the band is stronger. In the case of r-cut samples, implanted with a lower fluence (1.6×10^{17} cm^{-2}), this band is less intense and blue-shifted, centred around 337 nm, with FWHM of 208 nm. The blue shift and the larger energy FWHM indicate a size reduction of the precipitates, as discussed in chapter 3.

The simulation with MiePlot code (input with the optical constants of Ni and Al_2O_3 from Palik's compilation [Pal98]) of the optical extinction of several Ni spheres (radii from 1 nm up to 21 nm), is shown in *Figure 4.10*b. From these, the as implanted spectrum is better fitted with the simulations of spheres with 2.5 nm and 1.0 nm radius for c- and r-cut samples, respectively. The contribution of scattering for the larger sphere is also shown in *Figure 4.10*a, validating the assumption of the absence of scattering effects in these conditions. The difference to the experimental results in the blue and UV regions is due to the presence of F-centres and scattering. In fact, the swelling in the implanted region that develops as the sapphire lattice is destroyed may contribute to a large scattering observed in the as implanted state. Moreover, from the simulations it is clear that UV absorption (< 308 nm) also arises from IB transitions in Ni, in agreement with the work of Isobe and co-workers who observed a similar absorption band centred around 230 nm [Iso95].

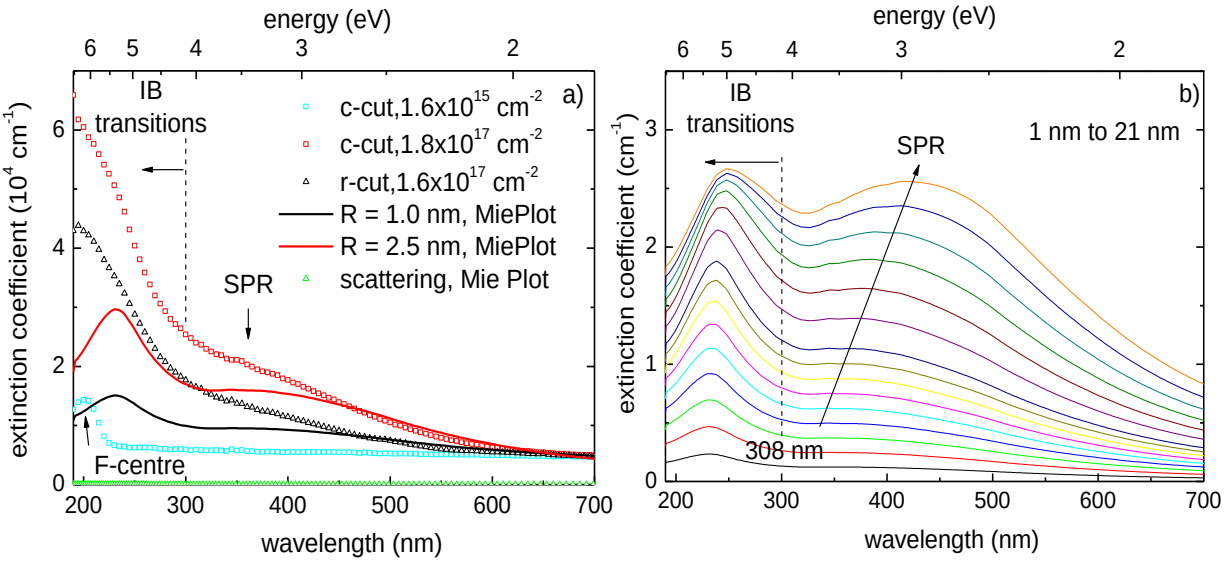

Figure 4.10 – a) optical absorption spectra recorded at RT of c- and r-cut α-Al_2O_3 as implanted with Ni for all fluences, shifted to overlap at 700 nm, with MiePlot simulations; b) MiePlot simulations for the optical extinction of Ni particles with radii from 1 nm to 21 nm.

In the case of c-cut samples these dimensions are similar to those inferred by XRD (4 nm). The minor differences, as previously stated, may be due to the fact that XRD measurements yield the average dimensions of crystalline domains, which may not be the case of the entire nanoparticle. Optical measurements, on the other hand, probe the particle as a whole. For r-cut samples, the small size found by OA may justify the absence of Ni phases in the corresponding XRD spectrum.

Table 4.5 – F-type centre concentration on pristine and nickel implanted sapphire samples.

sample	experimental data				F-type centre concentration	
	λ (nm)	FWHM (nm)	U (eV)	u (cm^{-1})	N_0 ($\times 10^{16}$ cm^{-3})	$N_{0,imp}$ ($\times 10^{19}$ cm^{-3})
pristine	200.33	27.02	0.84	0.64	0.23	0.00023
	224.72	37.52	0.93	0.41	0.32	0.00032
	258.07	40.52	0.76	0.22	0.14	0.00014
1.6×10^{15} cm^{-2}	201.56	26.37	0.81	6.06	2.09	8.37
	224.01	33.70	0.84	1.38	0.97	3.90
	258.07	49.22	0.92	0.82	0.63	2.54

4.3.1.1.2.3 After annealing

When applying subtraction procedure to OSP annealed samples we noticed a strong and physically unexplainable decrease in the absorption coefficient in the UV region, an indication that the pristine OSP sample spectra overestimate the absorption in this region. We consider this effect to be related with the reduction of the surface roughness, both on the unpolished and implanted surfaces, due to the annealing, which decreases the scattering contribution. For this reason, the spectra of the annealed samples are only corrected by the reflections. This method is not entirely correct, in particular in the UV region, but does not strongly affect the inherent limited understanding of the optical phenomena in this region, as explained in chapter 3. The spectra obtained after annealing the samples implanted with higher fluences at 1273 K in air show a general decrease of the absorption intensity (red curves in Figure 4.11a and Figure 4.11b for c- and r-cut samples, respectively).

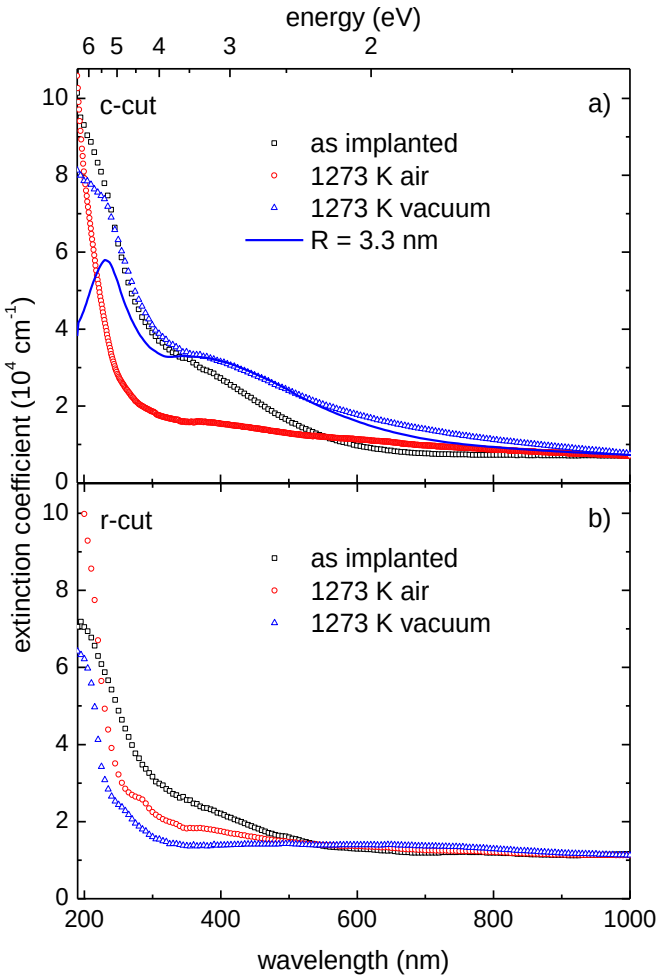

Figure 4.11 – Optical absorption spectra recorded at RT of α-Al_2O_3 implanted with Ni, as implanted and after one hour annealing at 1273 K in air or vacuum: a) c-cut and b) r-cut samples. All spectra were shifted to overlap around 1000 nm.

At this stage these samples become transparent, in consistency with the RBS-C and XRD measurements of crystalline recovery and formation of the transparent colourless spinel phase. The main feature of the samples annealed in air is the presence of a weak band starting around 350 nm.

This spinel has a characteristic absorption triplet at 455 nm, 526 nm and 667 nm due to the presence of the optically active Ni^{2+} in tetrahedral positions [Pok94, Ull03] which we could not detect possibly due to the low concentration of this phase in our system. The disappearance of the absorption band from 250 nm – 500 nm and the simultaneous loss of metallic Ni seen by XRD in these samples validate the assignment of this band to Ni^0.

The shoulder at 287 nm (more visible in r-cut samples) may be ascribed to band-gap transitions in some residual NiO [Xia05] or even Ni^{3+} [Pok94, Bal97]. Nevertheless, this is also near the region where Al clusters would have a SPR band, predicted by Gossick and co-workers to occur in the 220 nm to 270 nm wavelengths [Gos60]. These Al precipitates were reported after implantation of yttrium into sapphire and explained due to the enthalpy of formation of yttria, thermodynamically more favoured than alumina [Mor97]. However, the latter is quite unlikely in this particular system given the enthalpy of formation of Al_2O_3 from metallic Al, the lowest in this system, of about -1676 kJ mol^{-1}.

For the samples annealed in vacuum we found a distinct behaviour, suggested also by the fact that all samples remain with the dark brown colouration of the as implanted state.

In the case of c-cut samples the SPR band develops, probably due to the increase of the average size of the nanoparticles, estimated, with MiePlot code, to have grown to 3.5 nm radius, agreeing with the increase in size estimated by XRD (from 4 nm to 10 nm). The difference may be due to a broad size distribution where only the largest particles tend to acquire better crystalline ordering.

On the other hand, a large decrease of intensity in the blue region is observed for the r-cut sample, while developing a large absorption band centred at 535 nm (Figure 4.11b). According to MiePlot calculations, this is the maximum absorption of Ni spheres with about 35 nm radius. These results are presented in Table 4.6, along with the values obtained from the fits to the spectra.

This large size yields some consistency with AFM results, where the large precipitates observed at the surface may be preceded by smaller ones, still embedded in sapphire. However, this is in clear disagreement with XRD measurements that estimated 10 nm for the average size of the precipitates at this stage.

Table 4.6 – Optical features observed at each experimental stage on Ni implanted samples.

sample		SPR			MiePlot
		peak (nm)	FWHM (eV)	area	radius (nm)
c-cut	1.8×10^{17} cm^{-2}	351	2.29	51.5	2.5
	1273 K air	-	-		-
	1273 K vacuum	371	2.69	40.4	3.5
r-cut	1.6×10^{17} cm^{-2}	337	2.52	31.4	1
	1273 K air	-	-		-
	1273 K vacuum	536	2.77	16.4	< 0.7

Considering the RBS and XRD results, which confirm the presence of $NiAl_2O_4$, it is possible to estimate the direct band gap energy (E_g) of the nickel spinel from the extinction spectra of the samples annealed in air at 1273 K, as presented in chapter 3. *Figure 4.12* shows the Tauc plot (i.e. α^2 vs. E) of the samples annealed in air where the band gap of the spinel phase may be estimated to be 3.51 eV, assuming that this spinel phase is related to the absorption band starting at 350 nm, while F-centres and IB transition in Ni may be responsible for the 5.90 eV and

5.21 eV gaps, respectively [Iso95]. The lower intensity extrapolations (*Figure 4.12*b) may give the energy levels associated to defects (F^+ at 4.85 eV, the triplet transition less affected by the energy transitions of spinel and IB gaps) while the lowest energy may reflect only the scattering effect from the unpolished surface. It was not possible to find in the literature another value for the band gap of this spinel. It is much lower than that of $MgAl_2O_4$ (7.8 eV) and similar to the value observed in $ZnAl_2O_4$ (3.8 eV).

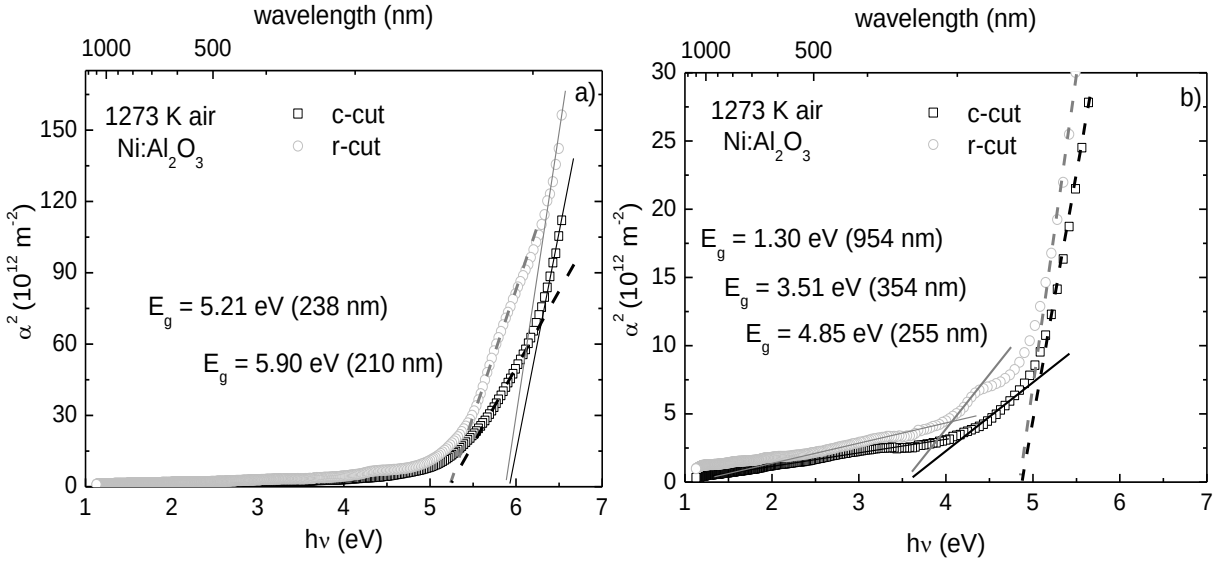

Figure 4.12 – Tauc plot for the determination of the band gap of $NiAl_2O_4$: a) high and b) low extinction coefficient regimes.

4.3.2 Cu implantation

In this work we study the effect of Cu implantation in c- and m-cut α-Al_2O_3 single crystals, and follow the changes on the structural and optical properties resulting from subsequent one hour furnace annealings in air or vacuum up to 1273 K. As previously with Ni implanted sapphire, we aim at producing new surface structures, therefore changing, in a controllable way, the properties of the resulting systems.

The implantations were carried out with 100 keV $^{63}Cu^+$ ions at RT with fluences ranging from 1.4×10^{15} cm^{-2} to 1.6×10^{17} cm^{-2}. The energy of implantation was chosen so as to match the R_p of the other NM studied in this work (Ag and Au). The resulting structural changes were studied using RBS, RBS-C and XRD, and the optical properties were measured through OA, all at RT.

4.3.2.1 Results and discussion

4.3.2.1.1 Structural studies

The RBS-C measurements performed after implantation of the lower fluences (1.4×10^{15} cm^{-2} to 8.6×10^{16} cm^{-2}) in m-cut samples (and c-cut for the 8.6×10^{16} cm^{-2} implantation) are shown in *Figure 4.13*. These reveal that the damage evolution in the Al sublattice (the damage profiles are identical for both oxygen and aluminium sublattices) follows the same trend observed in our previous studies. In fact, the m-cut samples

implanted with the lowest fluence show the same damage degree observed in c-cut samples implanted with similar Ni fluence. At this fluence implantation (Figure 4.13a) the topmost layer (~25 nm) retains good crystalline quality (χ_{min} = 20 %) after which significant radiation damage is observed, peaking around 60 nm or 1130 keV, where χ_{min} = 45 %. The damaged region extends to 80 nm and $E_D = 1.8\times10^{22}$ keV cm^{-3}. Below this implanted region the χ_{min} decreases to 30 %.

The measured Cu distribution profile is nearly Gaussian and peaks around 50 nm, being well fit by 0.2 at. % Cu layer with FWHM of 55 nm (on top of 25 nm of Al_2O_3). If R_p is in excellent agreement with SRIM prediction (47 nm), the FWHM is 50 % larger than SRIM prediction, 37 nm, a difference that doubles that observed in Ni implantation. Since E_D is similar in both cases (1.8×10^{22} keV cm^{-3} vs. 1.9×10^{22} keV cm^{-3} for Cu and Ni, respectively), RED processes are expected to be comparable and so this is probably related to chemically driven diffusion or to thermal effects during implantation. In fact, the current density used for Cu implantation was about 33 % higher than in the case of Ni (cf. Table 4.1). Stepanov and co-workers have measured larger and deeper implantation profiles than those predicted by SRIM code with increasing implantation current density [Ste05]. Moreover, a small channelling effect is found on the Cu profile, with χ_{min} of 65 %, which is higher than that observed in the case of Ni implantation with similar fluence. This may result from the higher atomic concentration present in this case (0.20 at. %). The apparent substitutional fraction is about 65 %.

For the 1.4×10^{16} cm^{-2} fluence (Figure 4.13b) the topmost layer (~25 nm) still retains good crystalline quality, with χ_{min} = 50 %, followed by a highly damaged region around 60 nm with χ_{min} = 85 %. The damaged layer has 100 nm in this case, corresponding to $E_D = 1.4\times10^{23}$ keV cm^{-3}, and the deep χ_{min} rises to about 50 %. The Cu distribution profile remains nearly Gaussian and peaks around 50 nm, being well fit by 1.9 at. % Cu layer with FWHM of 50 nm. Minor channelling (χ_{min} = 90 %) is observed in the Cu profile, the apparent substitutional fraction decreasing to about 20 %.

Amorphization is reached for fluences of 8.6×10^{16} cm^{-2} for both c- and m-cut samples (the random spectrum of c-cut sample is similar to that of m-cut sample and only the latter is shown in Figure 4.13c, for clarity). In these conditions, the disordered layer extends up to 120 nm (E_D = 7.2×10^{23} keV cm^{-3}) in both cases. However, the χ_{min} found in deep regions is higher for the m-cut sample (~55 %) than in c-cut samples (~45 %). Since the thickness of the damaged layer is similar, this is an indication of a higher defect concentration in m-cut samples. This may be due to the fact that m-cut samples are easier to damage than c-cut samples [Nar83]. Moreover, c-channel is larger than m-channel which, for these aligned spectra, means that m-cut samples are more sensitive than c-cut samples to damage and strain induced by the presence of the implanted ion.

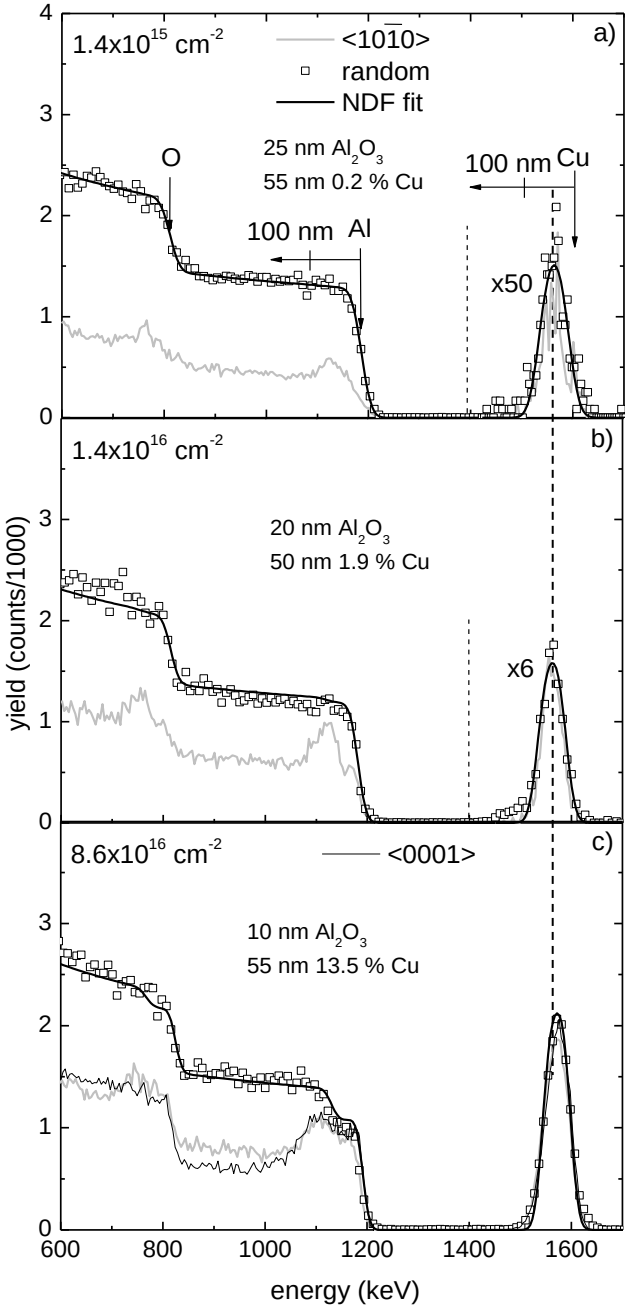

The maximum damage in the Al lattice is found behind the maximum concentration of Cu ions, as opposed to SRIM prediction, which is explained as for the Ni implantation. The step in the Al profile of simply reflects the presence of a large concentration of Cu in the topmost layers. No channelling is observed in the (Gaussian shaped) Cu profile in the normal direction (c- or m-axis), an indication of the degree of damage introduced, preventing access to the site location of the implanted ions.

Figure 4.13 – RBS-C spectra of m-cut sapphire after implantation at RT with 1.4×10^{15} cm^{-2} to 8.6×10^{16} cm^{-2} Cu$^+$ ions of 100 keV energy, with NDF code simulated composition.

The maximum Cu concentration (13.5 at. % in both cases) occurs closer to the surface, around 40 nm (see *Figure 4.13* where the vertical line crosses the maximum of the RBS Cu profile of the lowest fluence), still in agreement with SRIM prediction of 47 nm (cf. Table 4.1). This may again be due to target densification or to sputtering effects, which become significant in high fluence implantations. At this stage the FWHM of the Cu profile reaches 55 nm. Table 4.7 summarizes the RBS-C findings on these m-cut as implanted samples (up to 8.6×10^{16} cm^{-2}).

The implantation of 8.6×10^{16} cm^{-2} in c-cut samples results in a the lower χ_{min} in deep regions (up to 800 keV) which is, surprisingly, compensated by a deeper and constant disorder in the O sublattice that brings the χ_{min} to about 60 % at 600 keV, where it matches that of m-cut samples. This indicates that the extension of the damage in the O lattice is larger in c-cut samples than in m-cut samples, even if the concentration of defects is higher on the latter.

Table 4.7 – RBS-C results obtained on m-cut samples as implanted with up to 8.6×10^{16} cm^{-2} Cu ions.

sample	1.4×10^{15} cm^{-2}	1.4×10^{16} cm^{-2}	8.6×10^{16} cm^{-2}
host matrix			
max. damage depth (nm)	60	60	0 – 120
χ_{min} (%)	45	85	100
damage extension (nm)	80	100	120
E_D (10^{22} keV cm^{-3})	1.8	14	72
deep region χ_{min} (%)	30	50	55
implanted profile			
max. conc. depth (nm)	50	50	40
χ_{min} (%)	65	90	100
f_{sub}	65	20	0
FWHM (nm)	55	50	55
max. conc. (at. %)	0.20	1.9	13.5

Higher fluences were also implanted in c- and m-cut samples. *Figure 4.14*a and *Figure 4.14*d show the corresponding RBS-C measurements, after implantation of 1.6×10^{17} cm^{-2} and 1.1×10^{17} cm^{-2}, respectively. These as implanted spectra are again similar, the surface layer is fully amorphized, the damage extending to 120 nm in both cases. This, along with the implantation fluence, leads to E_D of 13.3×10^{23} keV cm^{-3} and 9.2×10^{23} keV cm^{-3}. However, m-cut samples still retain more damage (even if similar to that measured in the 8.6×10^{16} cm^{-2} implantation) than c-cut samples despite the lower implanted fluence, as measured by the higher dechanneling present in the samples for E < 1050 keV. Again, it is also worth noting the higher damage in the O lattice in the case of m-cut samples. Despite these differences, at 600 keV we found χ_{min} = 60 % in both cases. The most striking difference occurs in c-cut samples, with the significant decrease in the χ_{min} measured in deep regions from the 1.6×10^{17} cm^{-2} implantation (30 %) to the 8.6×10^{16} cm^{-2} implantation (45 %). The lower dechanneling effect in the Cu richer layer may result from the formation of more crystalline implanted material or to thermal effects that increase the overall crystalline quality of the surface layer or change the nature of the defects present. The decrease in the FWHM of the Cu profile from 55 nm to 50 nm may have contributed as well.

For these higher fluences the Cu concentration is distributed in a nearly Gaussian shaped profile, 50 nm wide and peaking closer to the surface, at 30 nm, a trend also observed in the case of Ni implantation, possibly due to target densification with increasing Cu concentration or sputtering effects. The average concentration, as simulated by NDF code, reaches 28.1 at. % and 20.0 at. % for c- and m-cut samples, respectively.

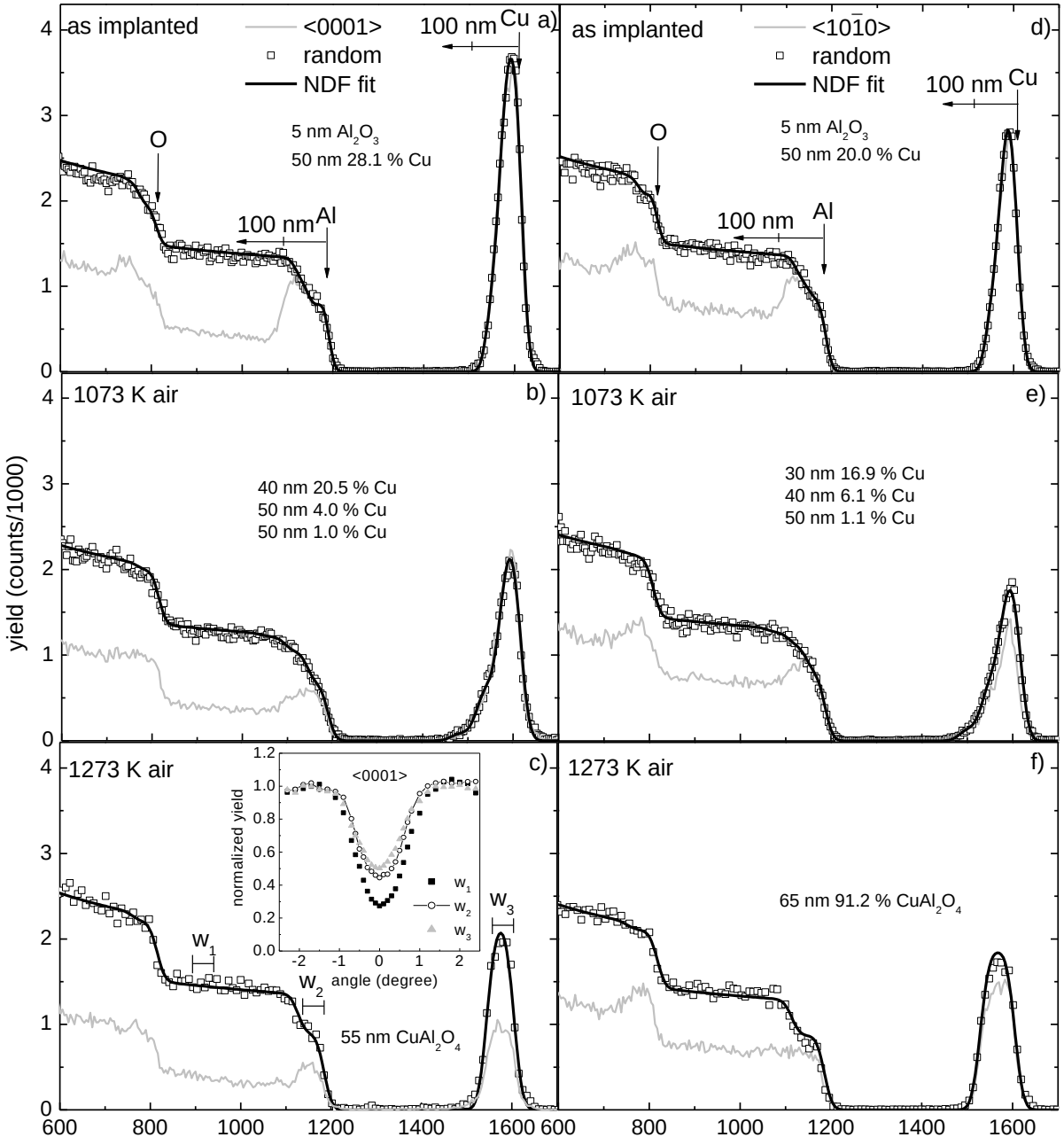

Figure 4.14 – RBS-C spectra of α-Al_2O_3 c-cut implanted with 1.6×10^{17} cm^{-2} (left side of the figure) and m-cut implanted with 1.1×10^{17} cm^{-2} (right side) taken after implantation (a, d) and after annealing for one hour at 1073 K (b, e) and 1273 K (c, f) in air, with NDF code composition fit. The inset in c) is the corresponding detailed angular scan.

The samples implanted with these higher fluences were heat treated in air or vacuum atmospheres for one hour at 1073 K and 1273 K. The RBS-C spectra obtained after the 1073 K annealing in air (*Figure 4.14*b and *Figure 4.14*e, for c- and m-cut samples, respectively) reveal some surface matrix recrystallization, which is more evident for c-cut samples (even if implanted with a higher fluence, 1.6×10^{17} cm^{-2}). In fact, the χ_{min} on the surface region (from 1050 keV to 1200 keV) decreased to 60 % and to 70 % on c- and m-cut samples, respectively. The damage extension reduces to about 100 nm in both cases. As a result the χ_{min} in deep regions improves to 25 % for c-cut samples,

remaining at 50 % for m-cut samples. Despite the better crystalline quality found on c-cut samples, the corresponding Cu profile shows no channelling while m-cut samples present χ_{min} = 80 %. This suggests that some crystalline phase or solid solution is already formed.

The Cu profile appears closer to the surface, particularly on m-cut samples (peaking at ~20 nm and ~15 nm for c- and m-cut samples, respectively), and broadens, showing a FWHM of 70 nm while developing a pronounced tail towards the lower energies in both cases, indicating in diffusion, due to the enhanced mobility of Cu ions at 1073 K. There is also out diffusion with a loss of the implanted Cu in both samples: 28 % and 18 % for c- and m-cut samples, respectively, the difference probably related with the amount of Cu initially available and pinned to unannealed defects (in higher concentration in m-cut samples). These losses may be related to the formation and partial sublimation of CuO at the surface (which boils at 609 K).

When the as implanted samples are placed directly at 1273 K (*Figure 4.14*c and *Figure 4.14*f), the Cu profiles become almost flat topped with χ_{min} = 50 % for c-cut samples and χ_{min} = 80 % for m-cut samples, while the Al profile in the corresponding surface region develops a plateau, with similar channelling. This was also observed in the case of the 8.6×10^{16} cm^{-2} implantations, after 1273 K annealing in air (not shown). These plateaus suggest, as in the case of Ni:Al_2O_3 system, the formation of a new crystalline phase. For c-cut samples the random spectrum of the topmost 55 nm can be simulated with NDF code by an average composition of $CuAl_2O_4$ while for m-cut samples the best fit yields 65 nm of $CuAl_2O_4 \cdot 0.08Al_2O_3$, i.e. about 8 % of aluminium oxide diluted in the spinel phase. The thicker layer on m-cut samples results from the larger diffusion that occurs along the c-plane, which crosses the damaged layer in this type of samples. The presence of diluted alumina may retard the full spinel crystallization and hence these samples exhibit higher dechanneling in the Cu region than c-cut samples. Since significant channelling is visible in the Cu profile, reaching 50 %, in the case of c-cut samples, detailed angular scans were performed through the c-axis. These show the alignment between the proposed oxide phase and the substrate along this direction (inset in *Figure 4.14*c).

In the case of c-cut samples, a 42 % loss of Cu is observed after the annealing at 1273 K, which is larger than the loss measured at 1073 K. On the other hand, m-cut samples loose a similar amount of copper (14 %) at this higher temperature. Therefore, despite having been implanted with different fluences, there is nearly the same amount copper in c- and m-cut samples at this stage. This hints at a solubility limit if, as in the case of other similar systems, the spinel is formed as a result of the diffusion of the metal (Al into CuO and, to some extent, Cu into Al_2O_3) through the oxide phases. The stoichiometric limit is related to the available (displaced) Al content which once exhausted leaves Cu in volatile phases. As the spinel phase is formed the copper loss stops.

On the other hand, in a similar way to the Ni system, the initial step may have been the formation and partial sublimation of CuO. As the Al diffusion into this oxide develops, the formation of the more stable spinel phase is achieved and thus the Cu loss is limited. Since the fast diffusion c-plane crosses the damaged layer in the case of m-cut samples, the formation of the spinel phase is more extensive and faster (possibly already at 1073 K, where channelling is observed in the Cu profile) in these samples which concomitantly show smaller copper losses. In both annealings it is also evident that the amount of O defects is always larger in m-cut samples.

Annealing in vacuum results in a clearly different behaviour, as revealed by the RBS-C spectra shown in *Figure 4.15*.

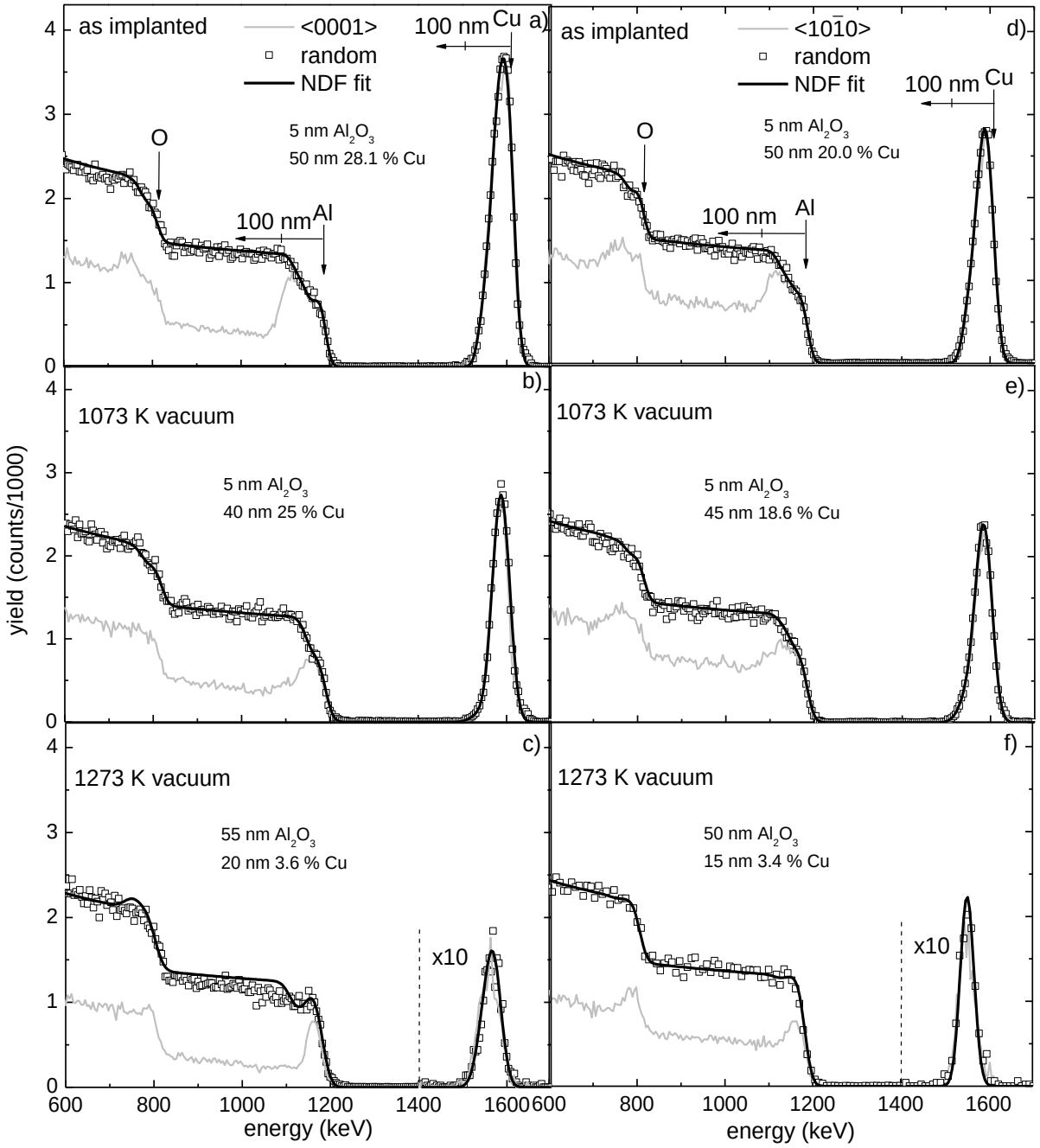

Figure 4.15 – RBS-C spectra α-Al_2O_3 c-cut implanted with 1.6×10^{17} cm^{-2} (left side of the figure) and m-cut implanted with 1.1×10^{17} cm^{-2} (right side) after implantation (a, d) and after annealing for one hour at 1073 K (b, e) and 1273 K (c, f) in vacuum, with NDF code composition fit.

At 1073 K the Cu profile remains Gaussian shaped still centred around 30 nm but narrows to 40 nm and 45 nm, for c- and m-cut samples, respectively (*Figure 4.15*b and *Figure 4.15*e). A fluence loss amounting to 36 % and 16 % is observed on c- and m-cut samples, respectively. Concomitantly, there is a significant crystalline recovery on c-cut samples, both in extension and defect concentration, while m-cut samples show little recovery. This hint at the possibility of in-plane reorganization upon annealing, that is, the high mobility along c-plane allows a faster

recrystallization plane by plane which also drives the implanted ions to the surface, which thus results in better ion channelling along the c-axis. In any case this crystalline recovery is smaller than that observed after similar annealing in air.

At 1273 K the crystalline recovery is more evident (but still somewhat below that observed in the annealing in air) and there is almost a total loss of Cu, the retained fluence dropping by more than 90 % in both cases. This can be attributed to the recovery of the host matrix impelling Cu to the surface. Here, at this temperature and under 10^{-4} Pa the metallic aggregates, or even a thin film of Cu or copper oxide, sublimates. In fact, the vapour pressure of copper at 1273 K is about 10^{-2} Pa.

The small fraction of copper present in the samples is the amount located in the lower energy side of the as implanted profile, distributed in a still Gaussian shape with maxima of about 3.5 at. % at 65 nm and 60 nm for c- and m-cut samples, respectively, showing no significant channelling in any case. The remaining copper is either attached to unannealed defects or in oxide phases. Again, m-cut samples retain a higher concentration of defects, as measured by the χ_{min} in deep regions in the Al sublattice, possibly also related to m-plane presenting thinner channels than c-plane. Moreover, as after the annealing in air, the disorder in the O lattice remains very high.

The major loss of Cu after the 1273 K annealing in vacuum suggested a new annealing step at lower temperature to determine the maximum thermal stability of the system. This was carried at 1173 K and in both cases the RBS-C spectra (not shown) reveal a minor crystalline recovery in comparison to the 1073 K annealing. Moreover, for c-cut samples the amount of Cu lost is the same as that observed in the 1073 K, with m-cut samples showing a somewhat larger loss (25 % vs. 16 % at 1073 K). In these conditions, therefore, most Cu is retained up to 1173 K and almost totally lost between 1173 K and 1273 K.

Table 4.8 and *Table 4.9* resume the RBS-C findings on c- and m-cut samples, respectively.

Table 4.8 – RBS-C findings on c-cut samples as implanted with 1.6×10^{17} cm^{-2} and annealed up to 1273 K.

sample	1.6×10^{17} cm^{-2}	1073 K air	1273 K air	1073 K vac.	1273 K vac.
host matrix					
max. damage depth (nm)	0 – 120	0 – 80	40	0 – 50	0 – 20
χ_{min} (%)	100	60	40	85	70
damage extension (nm)	120	100	80	100	70
E_D (10^{22} keV cm^{-3})	133	-	-	-	-
deep region χ_{min} (%)	30	25	25	30	20
implanted profile					
max. conc. depth (nm)	30	20	0 – 55	30	65
χ_{min} (%)	100	100	50	100	100
retained fluence (10^{15} cm^{-2})	160	115	92	103	7.6
fluence loss (%)	-	28	42	36	95
FWHM (nm)	50	70	55	40	20
max. conc. (at. %)	28.1	20.5	14.3	25.0	3.6

Table 4.9 – RBS-C findings on m-cut samples as implanted with 1.1×10^{17} cm^{-2} and annealed up to 1273 K.

sample	1.1×10^{17} cm^{-2}	1073 K air	1273 K air	1073 K vac.	1273 K vac.
host matrix					
max. damage depth (nm)	0 – 120	0 – 60	-	0 – 110	20
χ_{min} (%)	100	70	70	80	50
damage extension (nm)	120	120	-	110	80
E_D (10^{22} keV cm^{-3})	92	-	-	-	-
deep region χ_{min} (%)	50	50	50	50	40
implanted profile					
max. conc. depth (nm)	30	15	0 – 65	30	60
χ_{min} (%)	100	80	80	100	100
retained fluence (10^{15} cm^{-2})	110	90	95	92	6.5
fluence loss (%)	-	18	14	16	94
FWHM (nm)	50	70	65	45	15
max. conc. (at. %)	20.0	16.9	13.2	18.6	3.4

XRD measurements were performed on the samples implanted with the higher fluences. The XRD patterns obtained after the annealing in air at 1273 K for these fluences are shown in *Figure 4.16*a and *Figure 4.16*b for c- and m-cut samples, respectively. The XRD spectrum obtained after implantation clearly shows a broad band centred at the position of the copper (111) reflection parallel to c-plane of sapphire, with a lattice constant (0.363 nm) close to the tabulated value (0.362 nm). XPS measurements by Futagami and co-workers also found that in Cu implanted c-cut sapphire the charge state after implantation is Cu^0 [Fut94]. From the FWHM of this band, using the Scherrer formula we obtain an average dimension for the Cu aggregates of 9 nm.

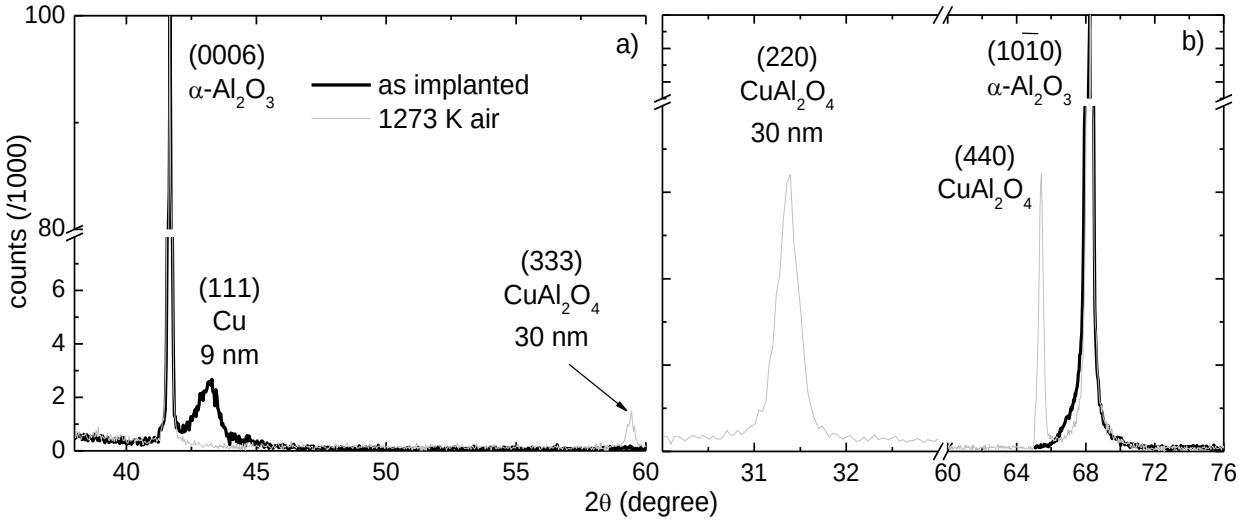

Figure 4.16 – XRD spectra of α-Al_2O_3 a) c-cut implanted with 1.6×10^{17} cm^{-2} and b) m-cut implanted with 1.1×10^{17} cm^{-2} after implantation at RT and after annealing at 1273 K for one hour in air. The dimensions of the precipitates were estimated with the Scherrer formula.

On the other hand, no reflections are observed in the corresponding spectrum of m-cut samples (*Figure 4.16*b). This is similar to the case of Ni: c-cut samples show metallic precipitates while r-cut samples don't. That is, c-cut samples seem to favour the epitaxial growth of the precipitates. However, the lattice is heavily damaged after implantation which should limit the epitaxial correlations. Thus, the most likely explanation involves the damage

degree observed by RBS-C in m-cut samples, much higher than that observed in c-cut samples, as revealed by the deep dechanneling for E < 1000 keV, resulting from stronger deviation of the incoming particles in the more damaged layer. A highly damaged region may limit the extension of the precipitates obtained after implantation.

The metallic Cu reflections are no longer detected after the annealing in air at 1273 K. In fact, in the XRD spectra of both c- and m-cut samples only a new diffraction line appears and was identified as belonging to the $CuAl_2O_4$ spinel phase, consistently with the corresponding RBS spectra and NDF simulation (*Figure 4.14*c and *Figure 4.14*f). For c-cut samples this spinel phase is present in crystalline form epitaxially aligned with the substrate: $<0001>_{sapp}$ // $<111>_{spi.}$ while for m-cut samples the relation is $<10\bar{1}0>_{sapp}$ // $<220>_{spi.}$. The $CuAl_2O_4$ phase has the tabulated lattice parameter of a = 0.8075 nm in the case of c-cut samples while in m-cut samples the spinel formed has a lower value a = 0.806 nm, indicating, as in the case of Ni, that the spinel formed in the less damaged sample is less disordered. The average crystallite size is 30 nm in both cases. These features were not observed at 1073 K (not shown). The calculated lattice mismatch is about 8 %, as in the case of Ni spinels.

When the annealing is performed in vacuum the metallic Cu crystalline phase is preserved (as well as its epitaxial relation with the substrate) in c-cut samples and its fraction increases up to 1173 K, as seen in the XRD diffraction pattern of *Figure 4.17*a. In fact the FWHM of the Cu reflections remains constant, an indication of constant average dimensions of the precipitates. However, a small shift occurs from in the peak position after annealing at 1173 K, giving a lattice constant of 0.3612 nm, closer to the tabulated value.

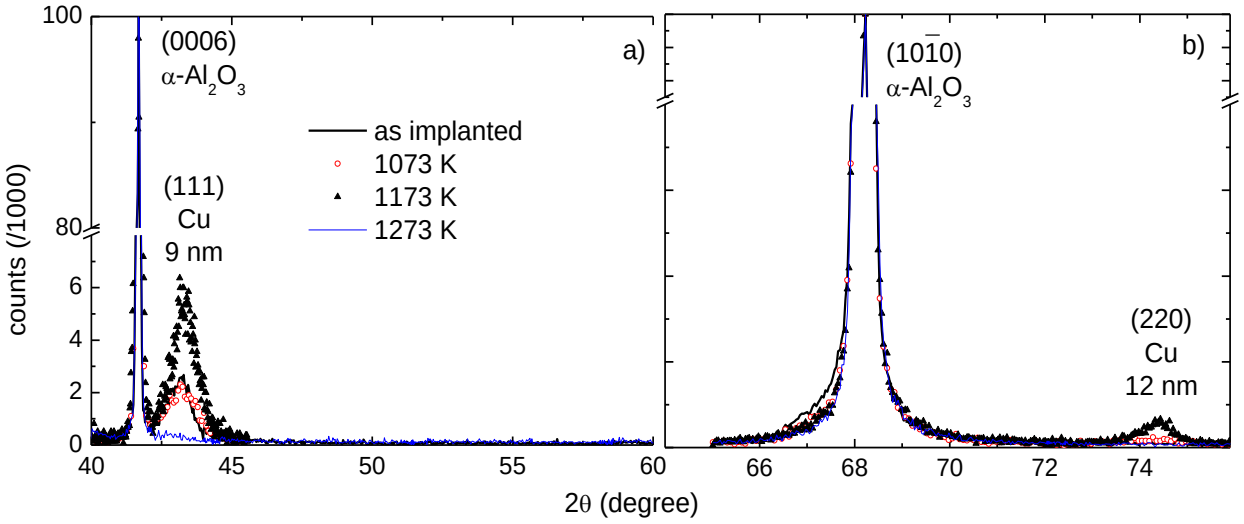

Figure 4.17 – XRD spectra of a) c- and b) m-cut α-Al_2O_3 implanted at RT with 1.6 $\times 10^{17}$ cm^{-2} and 1.1$\times 10^{17}$ cm^{-2}, respectively, and after annealing up to 1273 K for one hour in vacuum. The dimensions of the precipitates were estimated with the Scherrer formula.

On the other hand, in m-cut samples 12 nm precipitates develop during annealing at 1173 K, with epitaxial relation: $<10\bar{1}0>_{sapp}$ // $<220>_{Cu}$. The lattice constant is estimated to be somewhat smaller in this case: 0.360 nm. In both cases this reflection vanishes at 1273 K. This is again due to the loss of Cu, previously detected by RBS-C (cf. *Figure 4.14*c and *Figure 4.14*f). No spinel phase was observed using this annealing procedure.

In the case of c-cut samples the crystal plane relationship between the copper containing phases and the host matrix follows that observed for Ni, shown in Figure 4.4, which has identical space group and similar cell dimensions. No other reflections were observed in any case, either from metastable phases of aluminium oxide or copper compounds, such as $CuAlO_2$ observed by Fujimura and co-workers [Fuj98] after oxidation at high temperature (T > 1411 K) of a copper film deposited on sapphire. In fact, $CuAlO_2$ is the product of decomposition of $CuAl_2O_4$ at high temperatures.

Table 4.10 summarizes the results obtained from the XRD measurements on Cu implanted samples.

Table 4.10 – XRD results of Cu implanted sapphire.

sample	2θ	phases	size (nm)	calculated and tabulated lattice dimensions (nm)	PDF card
c, 1.6×10^{17} cm^{-2} as imp.	43.18	Cu (111)	9	0.363 / 0.362	00-004-0836
1273 K air	59.42	$CuAl_2O_4$ (333)	30	0.808 / 0.808	00-033-0448
1073 K vacuum	43.18	Cu (111)	9	0.363 / 0.362	00-004-0836
1173 K vacuum	43.36	Cu (111)	9	0.3612 / 0.362	00-004-0836
1273 K vacuum	-	-	-	-	-
m, 1.1×10^{17} cm^{-2} as imp.	-	-	-	-	-
1273 K air	31.36	$CuAl_2O_4$ (220)	30	0.806 / 0.808	00-033-0448
	65.42	$CuAl_2O_4$ (440)	30	0.806 / 0.808	00-033-0448
1073 K vacuum	-	-	-	-	-
1173 K vacuum	74.41	Cu (220)	12	0.360 / 0.362	00-004-0836
1273 K vacuum	-	-	-	-	-

The spinel obtained upon annealing in air is coherent with the phase diagram of the system CuO-Al_2O_3, shown in *Figure 4.18* where the experimental composition region measured with RBS is represented with a grey ellipse (50 % to 54 % of Al_2O_3). However CuO is also expected in this composition regime but not observed through XRD. If, in fact, CuO is not present (although the absence of XRD reflections results either from the absence of the phase or its random dispersion in subnanometre sizes), this, as in the case of Ni implantation, may result from the lower availability of Al and O, consumed for the reconstruction of sapphire, decreasing the relative amount of Al_2O_3 and moving the composition region to that represented by the black ellipse. It was not possible to find in the literature a phase diagram for vacuum reactions.

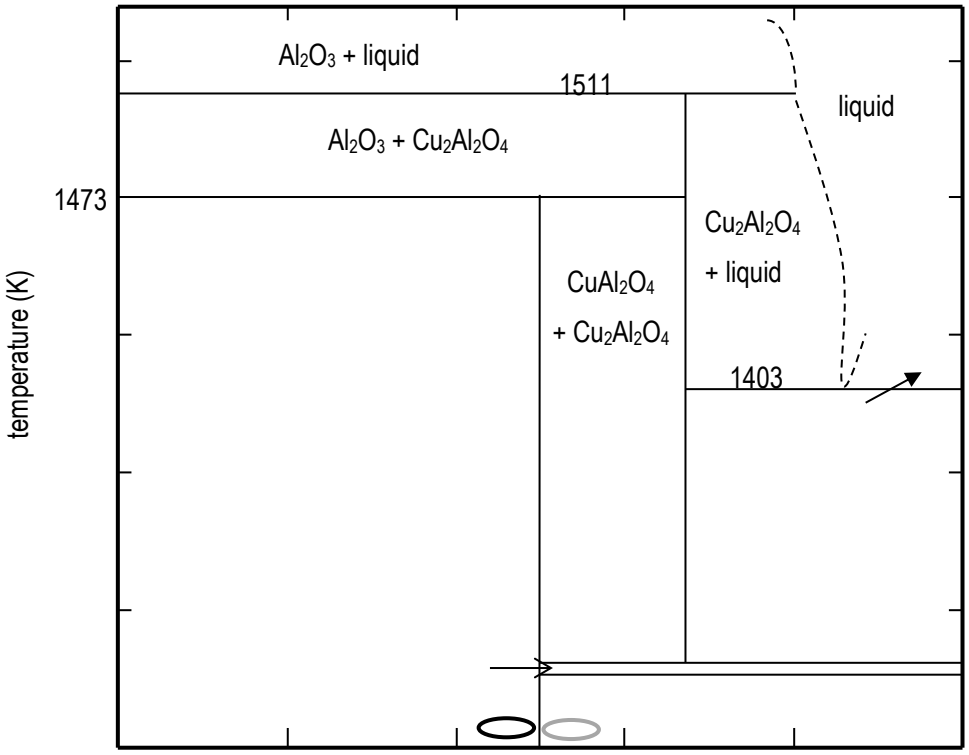

Figure 4.18 – Phase diagram of the Cu-Al-O system at $P(O_2) = 0.2\times10^5$ Pa [Gad64].

4.3.2.1.2 Optical studies

4.3.2.1.2.1 As implanted

The changes of the optical characteristics of sapphire after Cu implantation and after annealing were followed by optical extinction measurements. The optical extinction spectra taken after implantation of m-cut samples are depicted in

Figure *4.19*a.

The absorption bands related to matrix defects are clearly resolved only for the lowest fluence implantations, as was the case of Ni system. Using Smakula formula, the F-centre concentration is about 10.5×10^{19} cm^{-3} and 11.2×10^{19} cm^{-3} for the 1.4×10^{15} cm^{-3} and 1.4×10^{16} cm^{-3} implantation, respectively (cf. *Table 4.11*). The SPR band is not present for the implanted fluences below 8.6×10^{16} cm^{-2} in either type of sample. Furthermore, after implantation with 1.4×10^{16} cm^{-2} sapphire remains nearly transparent while the implantations with 8.6×10^{16} cm^{-2} and above yield a goldish yellow colouration, which is characteristic of a defect and implanted species rich state (F-centres and IB transitions).

The appearance of the SPR band centred around 600 nm after implantation of fluences of 8.6×10^{16} cm^{-2} and above reveals the presence of copper aggregates larger than ~0.7 nm, the threshold size for significant SPR absorption to develop [Che90]. The area of this band increases with the size of the precipitates (according to MiePlot prediction, cf.

*Figure 4.21*b), as well as with its quantity and it is thus expected to be proportional to the implanted fluence. From Figure *4.19*b, where the area of the SPR band is plotted against the implanted fluence, it is found that for the same fluence the SPR band is stronger for m-cut samples than for c-cut samples, which thus hints to the presence of more or larger precipitates (but not crystalline, according to XRD results) in the former. As the band at 600 nm is a signature for the presence of copper aggregates, it shows that the threshold for colloid formation must lie in the range 1.4×10^{16} cm^{-2} to 8.6×10^{16} cm^{-2} in these experimental conditions.

Table 4.11 – F-type centres concentration of as implanted sapphire with Cu ions.

sample	experimental data				F-centre concentration	
	λ (nm)	FWHM (nm)	U (eV)	u (cm^{-1})	N_0 ($\times10^{16}$ cm^{-3})	$N_{0,imp}$ ($\times10^{19}$ cm^{-3})
1.4×10^{15} cm^{-2}	203.87	21.29	0.64	6.16	1.68	10.5
	225.81	33.07	0.81	1.74	1.18	7.4
	258.07	59.52	1.12	0.64	0.60	3.8
1.4×10^{16} cm^{-2}	204.22	21.82	0.65	8.08	2.24	11.2
	224.02	29.20	0.72	2.80	1.69	8.4
	256.66	33.31	0.63	1.86	0.98	4.9

It's worth noting that in the case of Cu, the IB transitions start to occur at 2.2 eV or 560 nm, close to the SPR band which further difficult its analysis. Nevertheless, it should be possible, and desirable, to measure the implanted fluence (F) by measuring the SPR band area (*A*, adimensional product of extinction coefficient and wavelength). In fact, assuming that there is a threshold fluence (F_t) for the SPR band appearance, a simple (linear) model would relate these quantities as follows:

$$F = s \times A + F_t \qquad [4.6]$$

where *s* is a factor that contains information on the nature of the implanted material (e.g. oscillator strength, etc.) and host matrix. F_t may be taken from the linear regression of a SPR absorption area vs. fluence relation (
Figure *4.19*b) and then substituted in equation 4.6. The value of *s* may then be determined for one of the known implantation fluences. Using this procedure, with the data from
Figure *4.19* we found, $F_t = 6.3\times10^{16}$ cm^{-2} and $F_t = 5.6\times10^{16}$ cm^{-2}, *s* being 5×10^{15} cm^{-2} and 4×10^{16} cm^{-2}, for c- and m-cut samples respectively.

The SPR band is best fitted with two Gaussian curves in any case (correlation coefficient close to unity). The peak difference between these curves is about 40 nm in every sample. For the same fluence the SPR band of c-cut is blue-shifted in comparison to m-cut samples. We attribute this to larger precipitates in these latter samples, as already suggested by the comparison of the SPR area of c- and m-cut samples (

Figure *4.19*b). However, a small contribution (up to 3 nm) to the different peak positions between c- and m-cut samples is due to the birefringence characteristic of sapphire, presenting an index of refraction of about 1.768 parallel to the c axis and 1.760 in the perpendicular direction. As the fluence increases there is a red-shift in both cases: 3 nm for m-cut samples and about 12 nm for c-cut samples, while the FWHM is kept in both cases. The

shifts are thus proportional to the implanted fluences. However, the major change with the implantation fluence is the area of the SPR band (cf. Figure 4.19b).

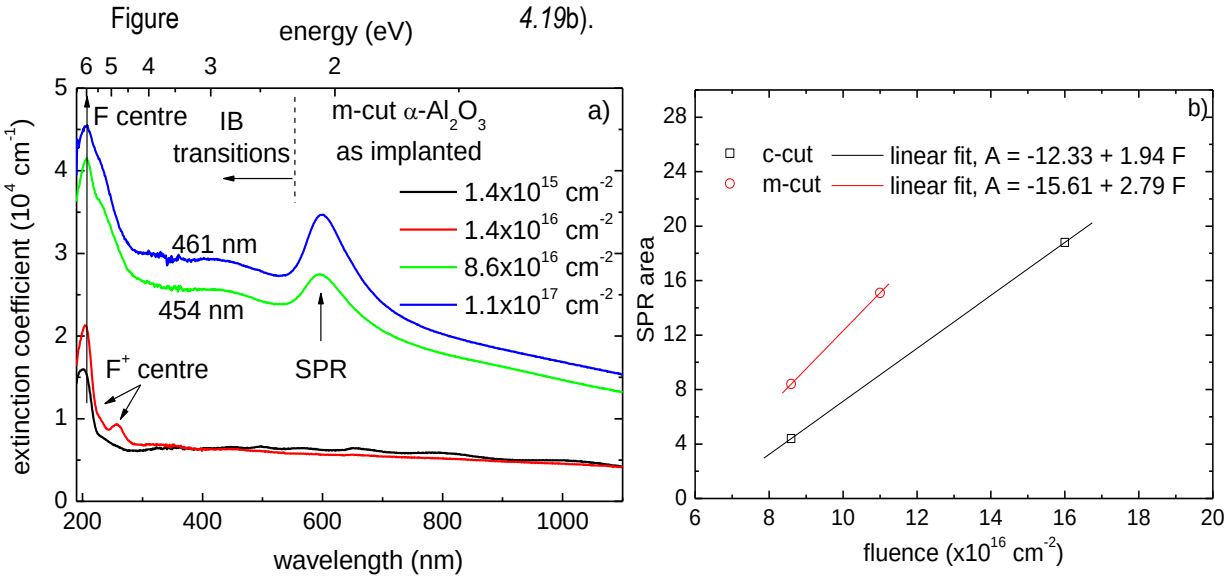

Figure 4.19 – a) Optical absorption spectra of m-sapphire after implantation at with 100 keV Cu^+ at RT; b) SPR band's area after implantation vs. fluence for the as implanted states.

Table 4.12 summarizes the optical absorption results of the as implanted samples. Sizes are estimated with MiePlot code, which simulations are depicted in *Figure 4.21*b using the optical constants from Palik's compilation for Cu and Al_2O_3 [Pal98] and no size distribution, considering only the position of the peak absorption. From these simulations, the dipole SPR band peaks at 587 nm for r = 1 nm and has its maximum intensity at 618 nm, for r = 35 nm, red-shifting in a non-linear trend with increasing size. For larger particles there is a decrease in the SPR intensity, this band continuing red shifting and broadening while some quadrupole contribution develops around 570 nm. A slowly increasing band centred at 440 nm is also observed, possibly related to deep IB transitions. The threshold for IB transitions is found around 564 nm (2.2 eV), as previously mentioned. In fact, this threshold nearly coincides with the high energy Gaussian component of the SPR band. This means that maybe only the larger sizes presented in *Table 4.12* truly reflect the dimensions of the particles.

Table 4.12 – Optical features of the samples as implanted with Cu ions.

sample	SPR			MiePlot
	peak (nm)	FWHM (nm)	area	radius (nm)
m, 8.6×10^{16} cm^{-2}	594 634	54 86	8.4	18 41
m, 1.1×10^{17} cm^{-2}	597 636	53 86	15	20 41
c, 8.6×10^{16} cm^{-2}	589 627	52 80	4.4	11 38
c, 1.6×10^{17} cm^{-2}	600 641	54 86	19	22 43

4.3.2.1.2.2 After annealing

The evolution of the optical absorption of the samples implanted with the highest fluences upon annealing in air is shown in *Figure 4.20*.

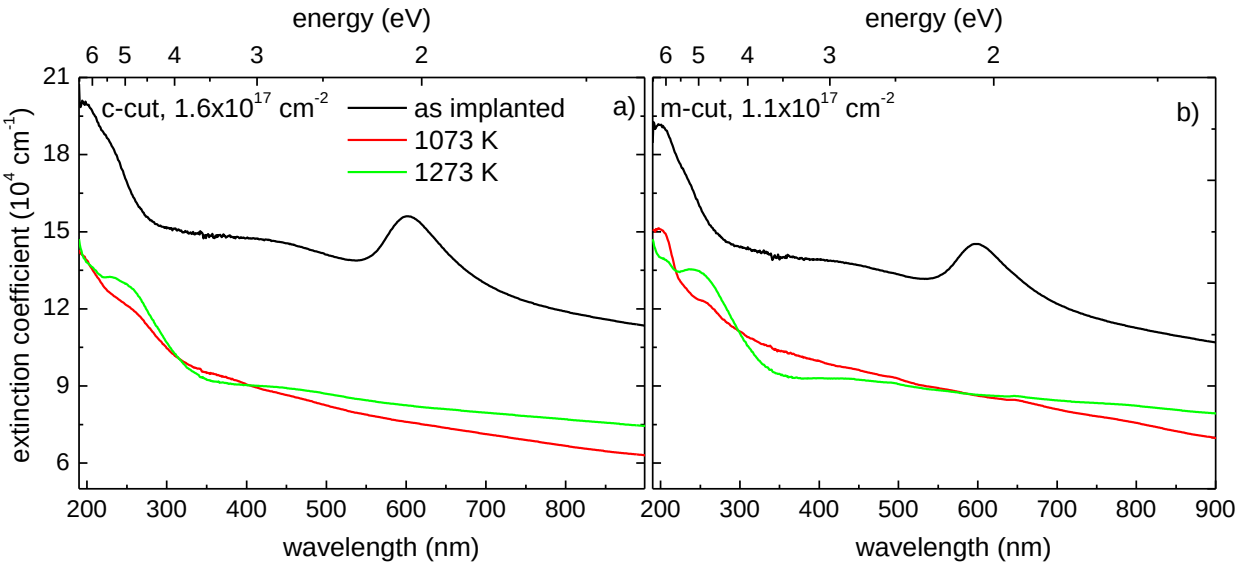

Figure 4.20 – Optical absorption spectra of α-Al_2O_3 (a) c-cut implanted with 1.6×10^{17} cm^{-2} and (b) m-cut implanted with 1.1×10^{17} cm^{-2} after implantation at RT and after annealing up to 1273 K for one hour in air.

The SPR band disappears after annealing at 1073 K in both samples, an indication of the dissolution of the aggregates (without SPR absorption for $r < 0.35$ nm [Che90]), most copper now possibly combined in mixed oxides with the matrix elements. This is consistent with the assumption of the chemically driven in diffusion suggested earlier to explain the corresponding RBS-C spectra in *Figure 4.14*b and *Figure 4.14*e upon annealing. Moreover, it highlights the role of the diffusion of atmospheric oxygen into the amorphized layer since for higher energy implantations ($E > 380$ keV) the SPR band of Cu is kept or even enhanced after similar annealing [Kur00].

The presence of the colourless spinel phase at 1273 K is possibly responsible for the absorption band at 275 nm detected after this annealing stage. According to RBS and XRD measurements, the spinel phase is present and extends to 55 nm and 65 nm in c- and m-cut samples, respectively. Using this information it is possible to estimate the band-gap of this phase using equation 3.58, as in the case of Ni:Al_2O_3 system, assuming that it is responsible for the absorption band that arises at 275 nm. The Tauc plot presented in *Figure 4.21*a shows that the band gap of $CuAl_2O_4$ is about 4.74 eV. Leu and co-workers found $E_g = 4$ eV, with the same type of analysis, in thin films (~400 nm thick) of $CuAl_2O_4$ synthesized by solid phase epitaxy [Leu07]. This difference may arise from a size effect, that is, in our case we have precipitates of $CuAl_2O_4$ instead of a continuous film, which affects the band gap energy. In fact, there is a known blue-shift of the band-gap with decreasing size in

these circumstances. The other values obtained may be related to deep IB transitions in Cu (2.58 eV) while the lower value may correspond to scattering from the unpolished surface.

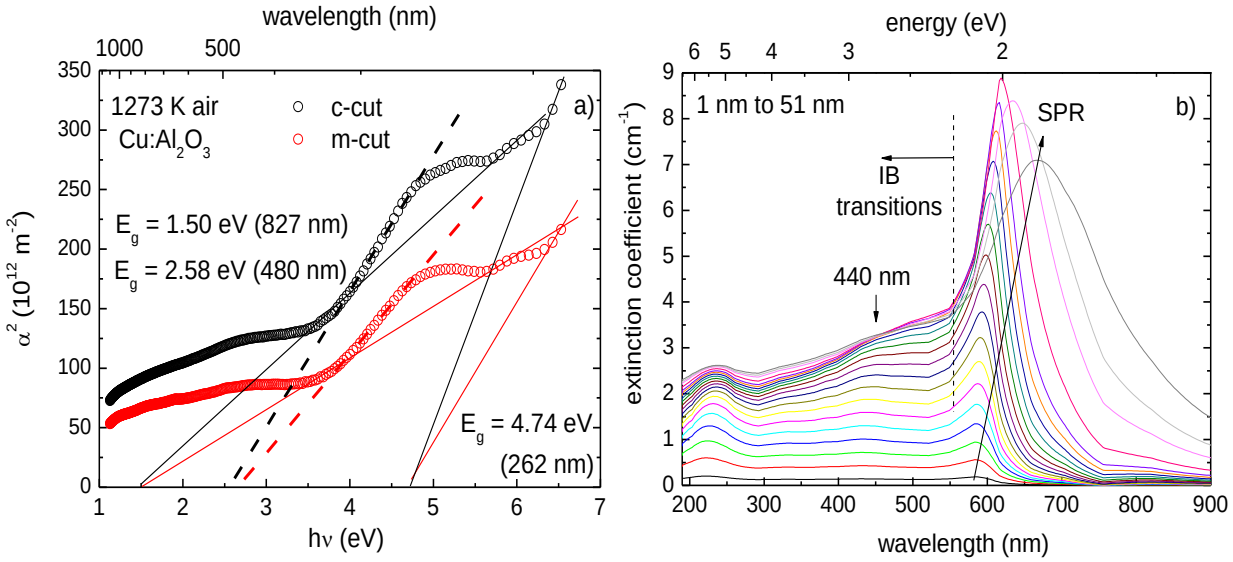

Figure 4.21 – a) Tauc plot for the determination of the band gap of $CuAl_2O_4$ and b) MiePlot simulations of Cu particles with radius from 1 nm to 51 nm.

Similar measurements were performed after annealing in vacuum and are shown in Figure 4.22. In the case of c-cut samples, the SPR bands position red shifts 14 nm and 24 nm upon annealing at 1073 K, indicating the growth and changing morphology of the precipitates. This is in disagreement with the XRD data of *Figure 4.16* and *Figure 4.17*, where essentially constant sized precipitates are observed and it is explained by the growth of highly defective precipitates or with an oxide external thin shell, which eventually suffer dissolution and evaporation while the more stable crystalline material remains embedded in sapphire. From 1073 K to 1173 K there is a blue-shift in both Gaussian components of each SPR band as the size of the precipitates decreases. At 1273 K the SPR band nearly vanishes, a consequence of the 90 % loss of Cu observed by RBS.

For m-cut samples a small red shift (2 nm and 3 nm) is also observed at 1073 K for both components of the SPR band. However, as the temperature increases to 1173 K there is a blue-shift on the high energy band while the red-shift continues to develop on the lower energy band, an indication of a morphology change, the increasing separation of the two modes possibly indicating the presence of ellipsoid-shaped precipitates, with longitudinal and transverse resonances. At 1273 K the behaviour is similar to what is observed in c-cut samples. The defect related bands also decrease with the annealing temperature as a result of the recrystallization of sapphire. Table 4.13 and *Table 4.14* resume the optical absorption features observed on c- and m-cut samples, respectively, as implanted and annealed in vacuum up to 1173 K, as well as the best radius estimated with MiePlot code, considering two modes of oscillation, either from a size distribution of spheres or due to ellipsoidal particles. It is possible that the higher energy mode is due to IB transitions.

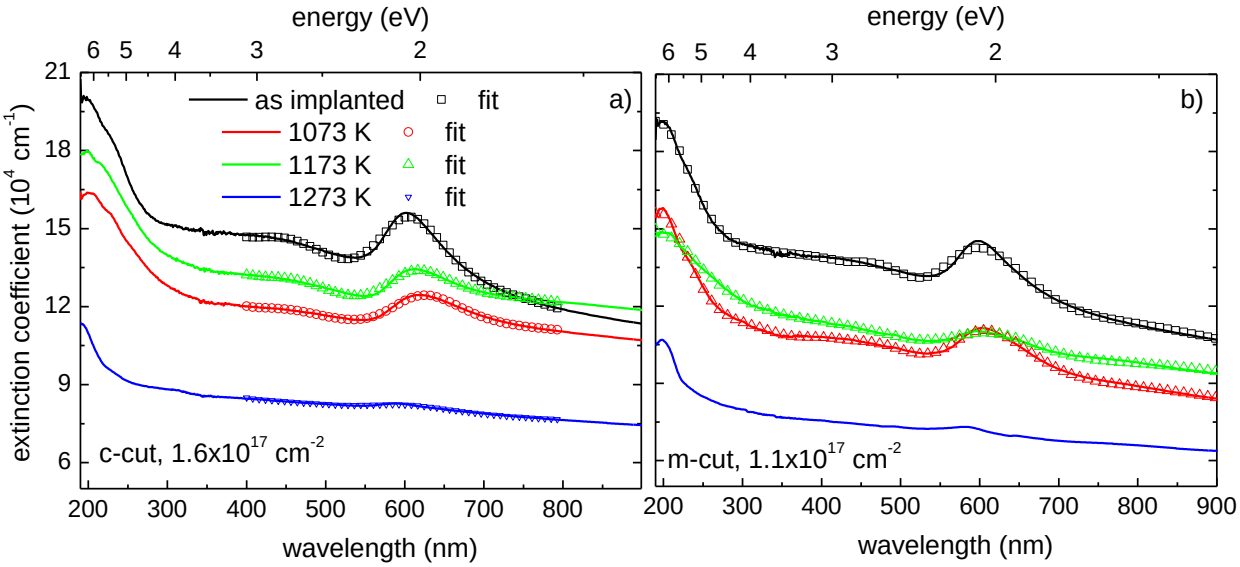

Figure 4.22 – Optical absorption spectra of α-Al_2O_3 (a) c-cut implanted with 1.6×10^{17} cm^{-2} Cu^+ and (b) m-cut implanted with 1.1×10^{17} cm^{-2} Cu^+ after implantation at RT and after annealing up to 1273 K for one hour in vacuum. SCOUT code fits of the SPR band are included.

Table 4.13 – Optical features and MiePlot code radius estimative of c-cut samples implanted with 1.6×10^{17} cm^{-2} Cu ions, as implanted and annealed in vacuum.

sample	experimental data			MiePlot
	peak (nm)	FWHM (nm)	area	radius (nm)
as implanted	601 642	57 91	10 10	22 44
1073 K	615 666	65 109	5.5 6.8	31 51
1173 K	610 656	55 96	4.9 5.3	27 47

Table 4.14 – Optical features and MiePlot code radius estimative of m-cut samples implanted with 1.1×10^{17} cm^{-2} Cu ions, as implanted and annealed in vacuum.

sample	experimental data			MiePlot
	peak (nm)	FWHM (nm)	area	radius (nm)
as implanted	596 634	55 91	7.5 8.7	20 41
1073 K	598 637	54 86	4.8 7.4	21 42
1173 K	594 640	53 68	2.6 2.7	18 43

The spectra obtained after implantation and after annealing in vacuum up to 1173 K (all containing a significant amount of copper) were simulated using the SCOUT code, presented in chapter 3. In this case, the Bergman representation of the composite medium was used, with copper, tentatively represented by different empirical optical constants, embedded in sapphire. The use of the standard bulk Cu constants from Palik [Pal98] or Johnson and Christy [Joh72] revealed a major misfit, as did a third optical set of constants built in the code. The option was then to use a model of the copper optical characteristics which allowed playing with most of the optical parameters, e.g. resonance frequency, damping constant or oscillators' features. The fits presented used the smallest set of possible variables. The thickness of the implanted profile and the volume fraction extracted from RBS measurements were used as initial input for each spectrum. The model parameters used are resumed in Table 4.15 and Table 4.16 for c- and m-cut samples, respectively.

The fits for the as implanted samples yield very similar parameters, as expected. From the damping constant it is possible to determine the size of the precipitates, using equation 3.49 and the values from Table 4.1. The results obtained are also presented in Table 4.15 and Table 4.16 for c- and m-cut samples (size 1 column), respectively. There are some differences of the size of the precipitates, which may arise from the presence of an IB band so close to the SPR band. That is, the oscillator used to model this feature may impact on the characteristics of the SPR band.

Table 4.15 – SCOUT fit parameters of c-cut samples implanted with 1.6×10^{17} cm^{-2} Cu ions, as implanted and annealed in vacuum.

sample	volume fraction (%)	percolation	thickness (nm)	damping constant (cm^{-1} / Hz)	size 1 (nm)	size 2 (nm)
as implanted	0.35	0.20	55	4069 1.22×10^{14}	13	24
1073 K	0.32	0.22	39	3298 9.89×10^{13}	25	17
1173 K	0.35	0.31	36	3383 1.01×10^{14}	24	16

Table 4.16 – SCOUT fit parameters of m-cut samples implanted with 1.1×10^{17} cm^{-2} Cu ions, as implanted and annealed in vacuum.

sample	volume fraction (%)	percolation	thickness (nm)	damping constant (cm^{-1} / Hz)	size 1 (nm)	size 2 (nm)
as implanted	0.25	0.32	51	5294 1.58×10^{14}	13	20
1073 K	0.24	0.21	45	5804 1.74×10^{14}	11	17
1173 K	0.30	0.57	23	5713 1.71×10^{14}	12	10

Another possibility for size determination is from the volume fraction and thickness of the layer containing the implanted species, considering an equal volume sphere (size 2 column). For the c-cut as implanted sample,

the copper volume would consist of spheres with radius of 24 nm, within the bounds of MiePlot code prediction. This could, in fact, be extracted directly from the RBS spectra, providing a first estimate of the size of the precipitates.

For c-cut samples the annealing temperature increases the percolation strength, which implies that the interaction between particles increases. This is consistent with the growth of the precipitates, moreover confined in a narrower region, and better crystalline quality of the matrix. The evolution of the precipitates is coherent with that observed with MiePlot simulations.

In the case of m-cut samples, the volume fractions are lower, since the implanted fluence was also lower. The estimated size of the precipitates obtained after implantation is 13 nm, like for c-cut samples, slightly decreasing after either annealing.

However, annealing at 1073 K results in a decrease of the percolation strength. This reflects a lower degree of connectivity between precipitates and may be explained by the shape of the precipitates which are expected to grow perpendicular to the surface in the case of m-cut samples.

In any case, however, the threshold limit for significant interactions between particles (e. g. considerable percolation) to occur is for volume fractions higher than 33 % [Pic08].

MiePlot estimate is higher than SCOUT predictions, the result of percolation considerations and, most of all, of an effective medium calculation in the latter code. Moreover, the fits performed with SCOUT implied a modification of the optical constants of copper, as presented in Figure 4.23a, most notably in ε_2, which is natural since it is related to *k*, which increases at the plasmon resonance. The composite material (Figure 4.23b), with Bergman representation, presents small variation in both constants. As the volume fraction increases larger variations are observed. Serna and co-workers studied with ellipsometry the linear optical constants (*n* and *k*) of nanocomposite films of $Cu:Al_2O_3$ constructed by PLD [Ser01] in the wavelength region of 300 nm to 750 nm. These are shown in *Figure 4.24*. It was also noted an increase in both indexes with increasing volume fraction of copper, up to 12 at. %. A comparison between our results and those from Serna and co-workers is displayed in *Figure 4.24*.

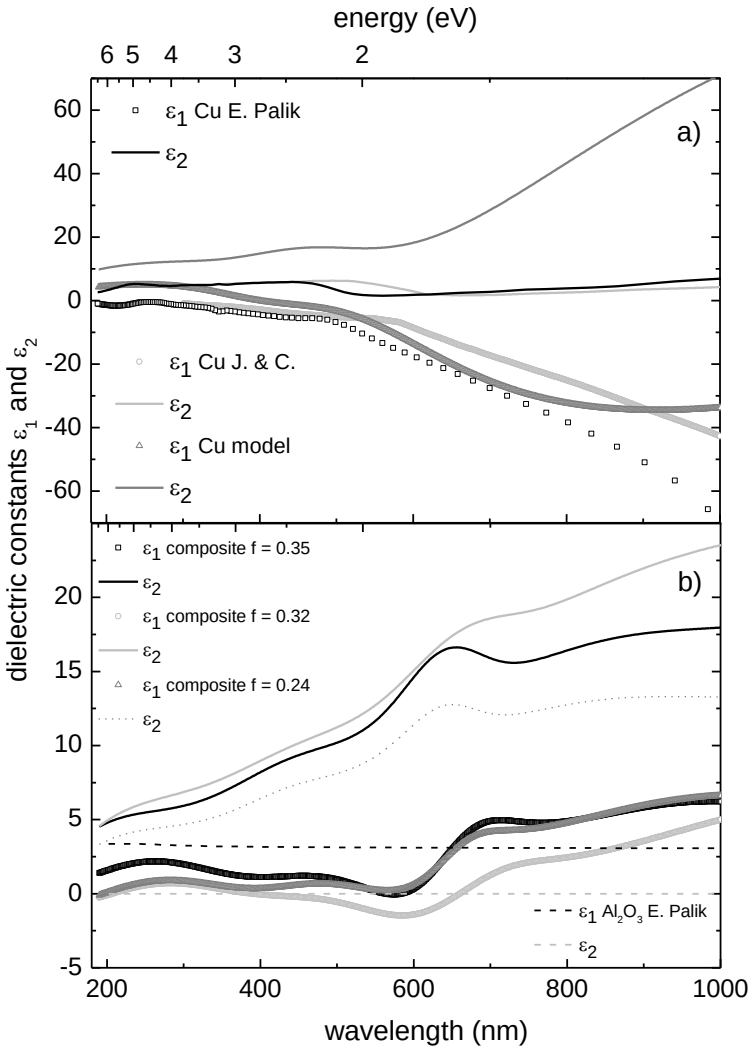

Figure 4.23 – Optical constants of a) bulk copper and b) sapphire and the effective composite medium.

The amount of copper used in our work, about 28 at. % in the as implanted case, justifies the significant increase observed in *n* and *k*, mainly for $E < 2$ eV, where IB transitions appear and are stronger in our system. Nevertheless, Serna and co-workers attribute the 460 nm maximum of *k* to morphology or coalescence effects. Moreover, we assumed a crystalline medium, which slightly red shifts our measurements, and modified the bulk constants of Cu. This latter procedure is found, for example, in the work of Isobe and co-workers on Ni implanted silica [Iso95], where the real part of the dielectric constant of Ni is measured to be lower than that of the bulk value. By considering an effective medium described by Bruggeman theory, the inverse problem (finding the metal content and film thickness from ellipsometric data, assuming the optical constants from bulk materials) was qualitatively solved for the low copper content films only (up to 2 at. %). The solution of the inverse problem for higher volume fractions is quite complex and it is still an open issue (see, for example, in [Zha09]).

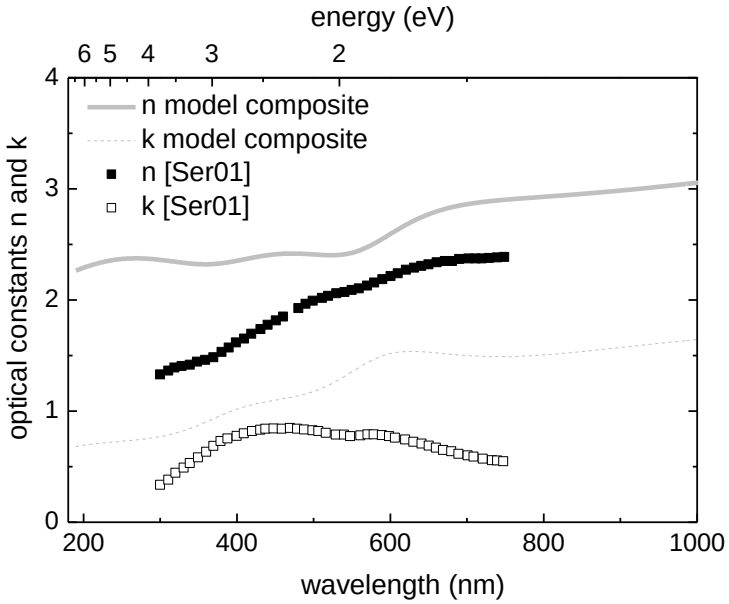

Figure 4.24 – Optical constants obtained in this work and in [Ser01] for a Cu:Al_2O_3 composite material.

4.3.3 Zn implantation

In this work we study the effect of Zn implantation into single crystalline c- and m-cut α-Al_2O_3. After implantation subsequent one hour furnace annealings are carried either in air or in vacuum (10^{-4} Pa) atmosphere, up to 1573 K, aiming at the production of metallic Zn particles and Zn compounds, namely ZnO, whilst fully recovering the ion implantation induced defects. The implantation was performed at RT with 150 keV $^{64}Zn^{+}$ ions to fluences from 4.0×10^{16} cm^{-2} to 1.2×10^{17} cm^{-2}. The resulting structural changes were studied using RBS, RBS-C, TEM (with EELS) and XRD. The optical characterization was performed at RT with OA in the 190 nm – 1100 nm range, which comprises the zinc SPR band and F-centres of sapphire. IBIL was followed in the same spectral region. In this case the presentation of the whole set of RBS-C results from c-cut samples precedes that of m-cut samples.

4.3.3.1 Results and discussion

4.3.3.1.1 Structural studies

The RBS-C measurements performed on c-cut samples after implantation of the lower fluences are presented in Figure 4.25. These spectra reveal that all samples show significant radiation damage around 1100 keV and a less damaged surface layer. As the fluence increases the damage level in this surface region rises slightly, as observed in the previous studies on Ni and Cu systems. In fact, after implantation of the lowest fluence (4×10^{16} cm^{-2}) the top most 35 nm retain good crystalline quality (χ_{min} = 60 %), as observed in low fluence implantation of Ni. This region is followed by a heavily damaged layer, between 1050 keV and 1150 keV, where χ_{min} = 80 %. This region, where most of the displaced matrix ions end up during implantation, is approximately 70 nm wide, at depths from 40 nm to 110 nm.

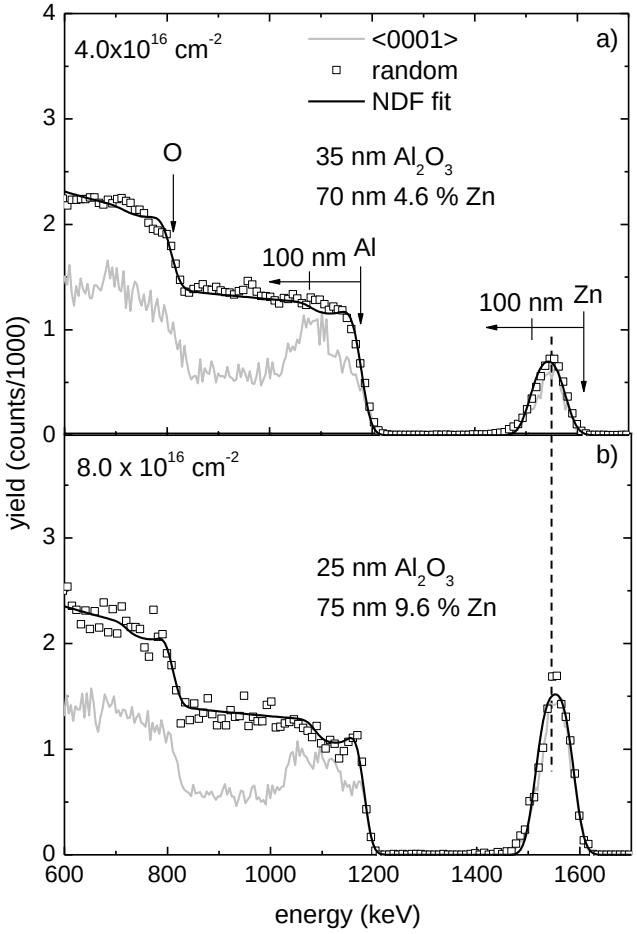

Figure 4.25 – RBS-C spectra of c-cut α-Al_2O_3 after implantation of 150 keV Zn^+ at RT of: a) 4×10^{16} cm^{-2} and b) 8×10^{16} cm^{-2} with NDF code composition fit.

The total damage extends to 150 nm, around the end of range of Zn ions, and E_D reaches 4.0×10^{23} keV cm^{-3}. In deep regions, around 950 keV, χ_{min} = 40 %. The highly damaged region contains the Zn profile, a Gaussian shape with FWHM of 70 nm and peaking at 70 nm, in close agreement with SRIM prediction of R_p = 63 nm (see Table 4.1). However, the FWHM is almost 60 % larger than SRIM prediction, 47 nm, possibly due to RED effect, as in the cases of Ni and Cu. Some dechanneling is measured in the Zn profile at this stage, χ_{min} = 80 %. This profile is well fit by NDF code with a 70 nm layer with 4.6 at. % Zn, topped with a sapphire layer with 35 nm.

As the fluence increases to 8×10^{16} cm^{-2} the damage extends to about 200 nm but the damage level remains essentially the same (Figure 4.25b), with a thinner (20 nm) surface layer showing χ_{min} = 65 %. At higher depths the χ_{min} is again 40 %. The composition simulation by NDF yields a 20 nm layer of sapphire followed by a 75 nm layer with 9.6 at. % of Zn.

The surface region becomes essentially amorphous for fluences of the order of 1.2×10^{17} cm^{-2} (Figure 4.26a), the damage extending again to 200 nm, where E_D reaches 9.0×10^{23} keV cm^{-3}. However, the region (~20 nm) immediately beneath the surface retains some crystallinity (χ_{min} = 85 %). The FWHM of the Zn profile is about 75 nm. The maximum concentration is found closer to the surface as the fluence increases, reaching to 14.5 at. % at 60 nm. No channelling is observed in the Zn profile: the site location of the zinc atoms is no longer detectable through RBS-C. The deep χ_{min} slightly increases to 45 %. *Table 4.17* summarizes the RBS-C results obtained for c-cut sapphire samples as implanted with Zn.

Table 4.17 – RBS-C results of c-cut sapphire samples as implanted with 150 keV Zn ions.

sample	c, 4.0×10^{16} cm^{-2}	c, 8.0×10^{16} cm^{-2}	c, 1.2×10^{17} cm^{-2}
host matrix			
max. damage depth (nm)	40 – 110	40 – 200	0 – 200
χ_{min} (%)	80	90	100
damage extension (nm)	150	200	200
E_D (10^{22} keV cm^{-3})	40	60	90
deep region χ_{min} (%)	40	40	45
implanted profile			
max. conc. depth (nm)	70	65	60
χ_{min} (%)	80	95	100
FWHM (nm)	70	75	75
max. conc. (at. %)	4.6	9.6	14.5

The c-cut samples implanted with the highest fluence were annealed up to 1273 K in air or vacuum for one hour. The annealing step at 1073 K (not shown) produced little changes, only minor crystalline recovery under vacuum annealing. After annealing in air at 1273 K (Figure 4.26b) the RBS-C spectra show some damage recovery, namely in the extension of the damaged layer, that decreases from 200 nm to about 120 nm, with a near amorphization damage concentration (χ_{min} = 90 %). At higher depths, E < 1000 keV, χ_{min} = 40 %. The Zn profile changes to an almost rectangular distribution, characteristic of a constant composition, with a width of about 85 nm. This is a good indication for the presence of a Zn compound, an observation similar to what was previously found for Ni and Cu implantations after the same annealing procedure. In fact, simulations with NDF code of the corresponding RBS spectrum show that an average composition of $ZnAl_2O_4{\cdot}0.27Al_2O_3$, i.e. semiconductor zinc spinel (gahnite) $ZnAl_2O_4$ with some diluted alumina, gives a good description of the experimental RBS results. Moreover, it exhibits channelling with χ_{min} = 60 %, suggesting a crystalline phase having some type of orientation relationship with the substrate matrix. The χ_{min} in the Zn profile decreases from the interface with bulk sapphire to the surface. Lattice mismatch and, possibly, a lower pre-existing damage concentration at the surface account for this effect. Detailed angular scans performed through the c-axis confirm that the crystalline structure of this surface region is strongly correlated with that of the matrix (cf. inset of Figure 4.26b), having at least one common crystallographic direction. No loss of zinc is detected even though this metal boils at 1180 K, giving an extra indication of the formation of more stable compounds.

On the other hand, thermal treatments at 1273 K in vacuum, Figure 4.26c, lead to a significant damage recovery, with the first 80 nm showing χ_{min} = 55 %. Concomitantly, the damage at higher depths decreases to χ_{min} = 30 %. Regarding the Zn profile, it narrows, from 75 nm to 55 nm, and peaks closer to the surface, at 50 nm, where the concentration of Zn reaches 15.2 at. %. Moreover, a 27 % loss of Zn is observed, as was the case for Ni implantations after the same annealing treatment. The low loss of Zn even at this temperature (about 100 K above its boiling temperature) may be related to an encapsulating effect, where a relatively stoichiometric alumina surface layer hinders out diffusion. Some channelling develops, expressed in a χ_{min} value in the Zn profile of 80 %. The corresponding angular scan (inset of Figure 4.26c) confirms the alignment between Zn and the host matrix.

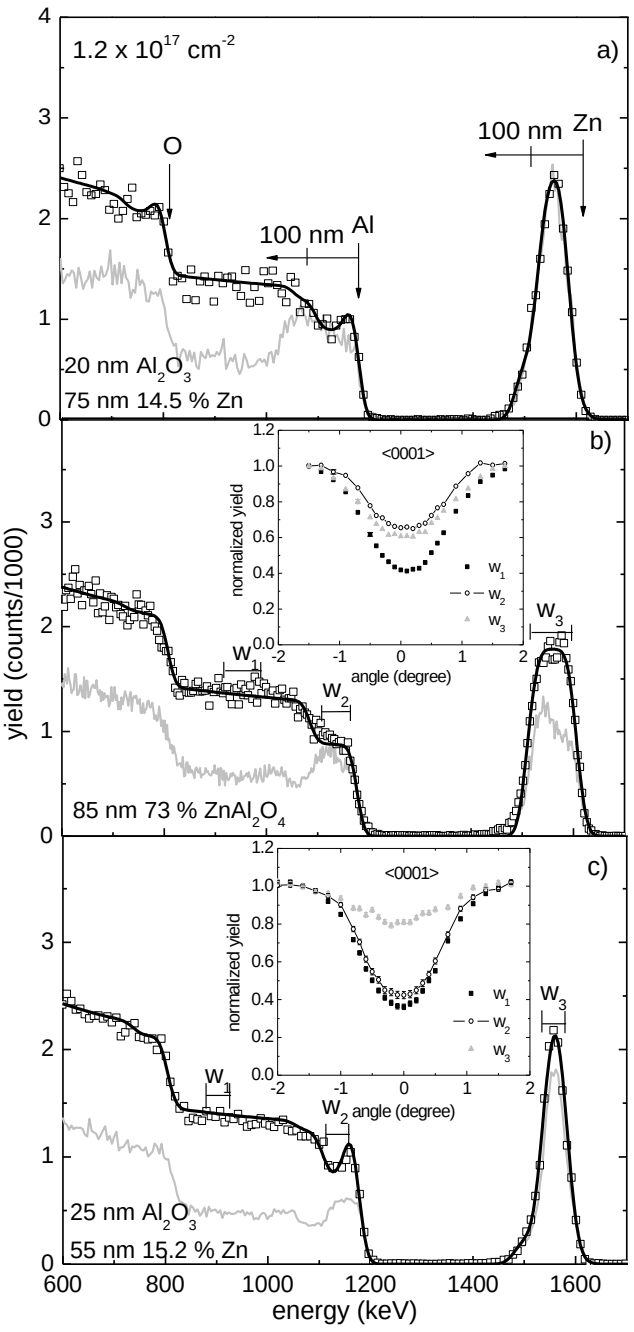

In any case, even after the 1273 K annealing, the dechanneling yield at the surface remains high, either due to the presence of radiation damage or to a systematic misfit of the structures present.

Figure 4.26 – RBS-C spectra of c-cut α-Al_2O_3 implanted with 1.2×10^{17} cm^{-2} 150 keV Zn^+ at RT: a) after implantation and after annealing for one hour at 1273 K in b) air and c) vacuum, with NDF composition fit. Inset are the corresponding angular scans.

Table 4.18 presents the RBS-C results obtained on Zn implanted c-cut samples after annealing at 1273 K.

Table 4.18 – RBS-C results of the Zn implanted c-cut samples as implanted and after annealing at 1273 K.

sample	1.2×10^{17} cm^{-2}	1273 K air	1273 K vac.
host matrix			
max. damage depth (nm)	0 – 200	40 – 120	0 – 80
χ_{min} (%)	100	90	55
damage extension (nm)	200	120	80
E_D (10^{22} keV cm^{-3})	90	-	-
deep region χ_{min} (%)	45	40	30
implanted profile			
max. conc. depth (nm)	60	0 – 85	50
χ_{min} (%)	100	60	80
retained fluence (10^{15} cm^{-2})	120	121	88
fluence loss (%)	-	0	27
FWHM (nm)	75	85	55
max. conc. (at. %)	14.5	11.3	15.2

Regarding m-cut samples, the as implanted behaviour after implantation of with 0.9×10^{17} cm^{-2} is similar to that observed in c-cut samples, as shown in the RBS-C spectra of *Figure 4.27*a. In fact, the highly damaged (amorphized) layer extends to about 200 nm, with the Gaussian Zn distribution profile peaking at 60 nm, where it reaches 13 at. %, with FWHM of 65 nm. No channelling effect is observed at this stage. However, the χ_{min} in deep regions rises to 60 %, as was the case of m-cut samples implanted with Cu. E_D is 6.8×10^{23} keV cm^{-3}.

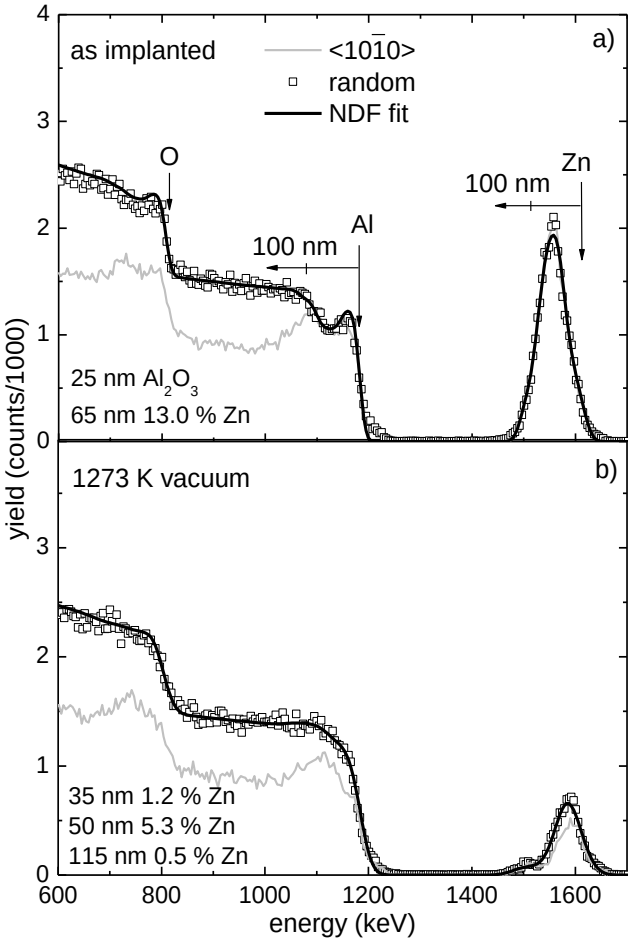

Annealing in air was not attempted on m-cut samples since it would only promote the formation of spinel phase and not ZnO, which was the major interest of our study. After annealing at 1273 K in vacuum (*Figure 4.27*b) the damage level decreases only slightly (χ_{min} = 80 %), much less than the recrystallization observed for c-cut samples (χ_{min} = 55 %, cf. Figure 4.26c). The damaged layer is now 130 nm thick.

Figure 4.27 – RBS-C spectra of m-cut α-Al_2O_3 implanted with 150 keV Zn^+: a) after implantation at RT of 0.9×10^{17} cm^{-2}; b) after annealing for one hour in vacuum at 1273 K.

Despite this crystalline recovery, the minimum yield is the same (60 %) at E < 1000 keV. The Zn profile shifts towards the surface, peaking at 35 nm (where the concentration of Zn is 5.3 at. %). This large Zn out diffusion

contributes to the 67 % loss measured at this stage. This is due to the higher mobility of Zn ions along the c-plane, which is normal to the sample surface in m-cut samples. This loss of Zn is similar to that observed by Mouritz and co-workers (69 % to 81 %) in m-cut sapphire implanted with 3×10^{16} cm^{-2} 100 keV Zn at RT and annealed in air at 1473 K for one hour [Mou87]. Another difference to c-cut samples in the much higher disorder retained in the Al sublattice, as it was the case of Cu implantation.

Annealing at 1573 K promoted the near complete loss of Zn (not shown), irrespective of the annealing atmosphere and sample orientation, as well as major crystalline recovery of sapphire. In the case of the annealing in vacuum this may indicate the initial fast formation of Zn spinel, followed by its reduction to sapphire and metallic Zn, the latter eventually evaporating, a process known to occur in $NiAl_2O_4$.

Table 4.19 presents the RBS-C results obtained on Zn implanted samples after annealing at 1273 K.

Table 4.19 – RBS-C results of the Zn implanted m-cut samples as implanted and after annealing at 1273 K.

sample	9.0×10^{16} cm^{-2}	1273 K vac.
host matrix		
max. damage depth (nm)	0 – 120	50 – 120
χ_{min} (%)	100	80
damage extension (nm)	200	130
E_D (10^{22} keV cm^{-3})	68	-
deep region χ_{min} (%)	60	60
implanted profile		
max. conc. depth (nm)	60	35
χ_{min} (%)	100	80
retained fluence (10^{15} cm^{-2})	90	30
fluence loss (%)	-	67
FWHM (nm)	65	50
max. conc. (at. %)	13.0	5.3

In this system it was possible to perform TEM analysis to observe the morphology of the precipitates as well as their composition and crystallinity. The limited availability of this type of measurements in sapphire is due to the extreme hardness of this material making it difficult the preparation of samples for TEM.

*Figure 4.28*a and *Figure 4.28*b show the cross sectional TEM image and the EELS elemental Zn map of a c-cut sample implanted with 1.2×10^{17} cm^{-2}, which RBS-C spectra are shown in *Figure 4.26*a. It is clearly seen that the implanted Zn is arranged in irregular amorphous stripes, with precipitates sized in the range of 5 nm to 15 nm, centred at about 70 nm depth. The selected area electron diffraction (SAD) patterns (cf. inset in *Figure 4.28*a) show that some (hexagonal) Zn is aligned with its c-axis parallel to that of sapphire.

*Figure 4.28*c and *Figure 4.28*d represent the sample after annealing at 1273 K in vacuum for 1 hour. Both TEM image (c) and the Zn map (d) show nanoparticles with a large size distribution with average dimensions about 20 nm that are centred around 60 nm, the depth of maximum concentration of zinc after implantation. In addition, the presence of Kirkendall voids (K voids) in the implanted region [Smi47] was proved by TEM as indicated in (c). The formation of the K voids found in these samples is due to a remarkable diffusion of the mobile components during heat treatment in a crystallized environment. This is consistent with a loss of Zn in the thermally recrystallized substrate (cf. RBS-C spectra of *Figure 4.26*c). Moreover, the particles grew longer parallel to the c-plane, which is

certainly a consequence of the higher ion mobility along this plane [Mar02]. The SAD pattern shows that metallic Zn coexist along with some $ZnAl_2O_4$ phase, the latter having its <111> axis parallel to the c-axis of sapphire. It is probably this spinel phase that prevents further losses of Zn under these annealing conditions.

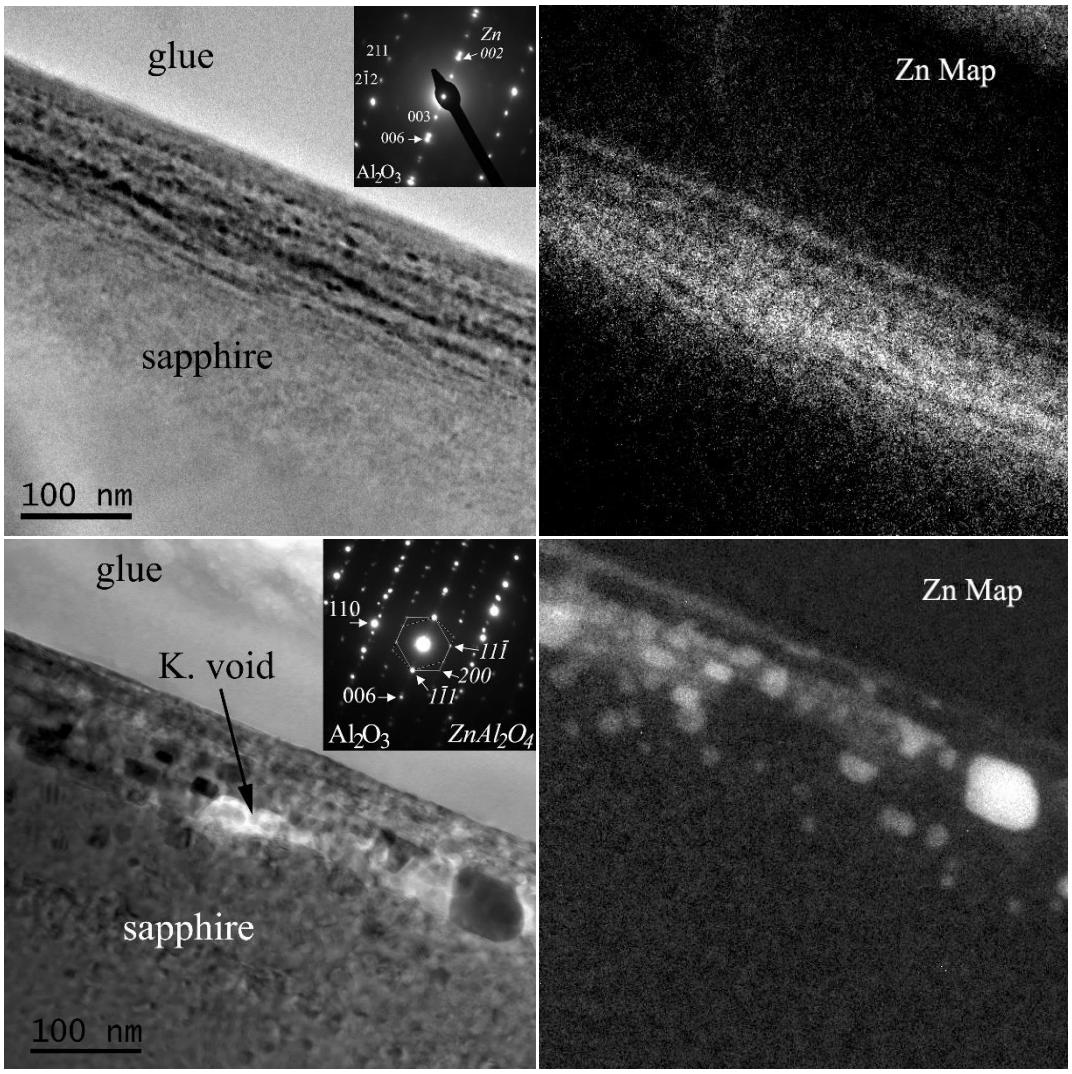

Figure 4.28 – a) and c) TEM cross-section of c-Al_2O_3 as implanted with 1.2×10^{17} cm^{-2} of Zn and after annealing at 1273 K in vacuum for 1 hour, respectively; b) and d) EELS Zn maps ditto. Insets in a) and c) are the corresponding SAD patterns.

XRD studies were performed on the samples implanted with the highest fluences, after implantation and after the annealings at 1273 K. The results are shown in *Figure 4.29*. After implantation a fraction of Zn particles are found essentially aligned with its <0001> direction parallel to the <0001> direction of c-cut sapphire, with lattice constant *c* = 0.494 nm. Using the Scherrer's formula, the large FWHM of this reflection indicates the presence of 6 nm average sized particles, in agreement with TEM measurements. As also seen in *Figure 4.29*a, when annealed in air the Zn particles disappear and apparently give place to a $ZnAl_2O_4$ cubic phase, in accordance with the RBS results, as 22 nm precipitates having their <111> directions parallel to the c-axis of sapphire. The lattice constant

of this phase is 0.806 nm (similar to the tabulated value), and thus producing a lattice mismatch of about 8 %, as in the other spinels of Ni and Cu.

When annealed in vacuum at 1273 K the Zn nanoparticles grow to 12 nm, in spite of the 27 % Zn loss found by RBS. This growth of the Zn particles may be achieved through coalescence or Ostwald ripening and the value of 12 nm obtained by XRD is consistent with the dimensional range found from cross sectional TEM and EELS (cf. *Figure 4.28*c and *Figure 4.28*d). Some (222) spinel reflections are observed, in agreement with the SAD pattern of *Figure 4.28*c.

On the other hand, the XRD spectrum of *Figure 4.29*b shows no Zn related reflections at the as implanted state of m-cut samples. This, as in the case of Cu implantation, is related to the high defect concentration retained by m-cut samples. After annealing at 1273 K in vacuum for one hour two reflections ascribed to the presence of (hexagonal) ZnO nanoparticles appear, with lattice constants *a* = 0.326 nm. These particles are estimated to have about 7 nm and are aligned with its a-axis parallel to a-axis of sapphire.

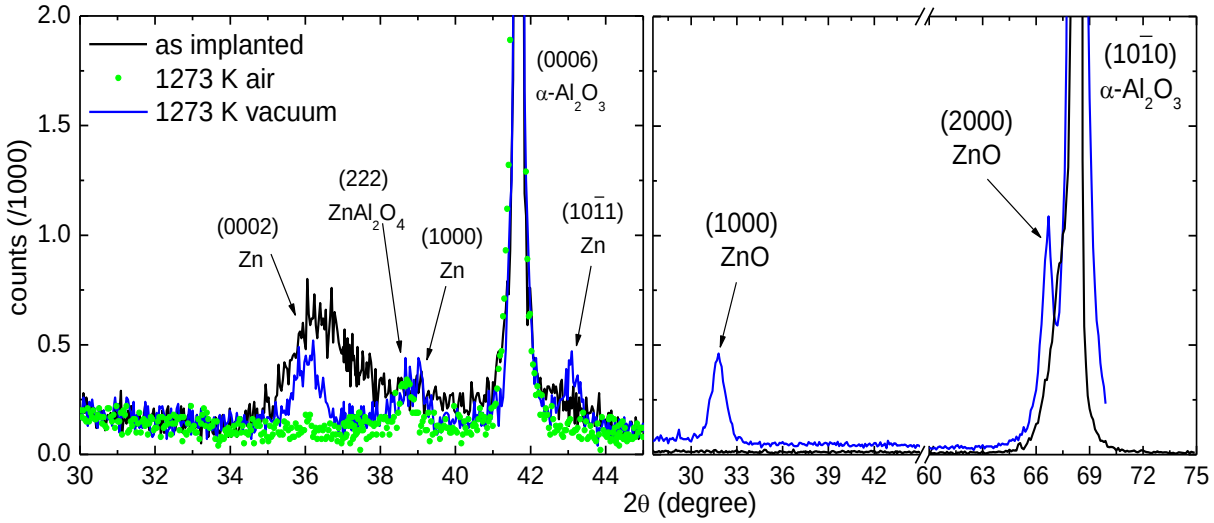

Figure 4.29 – XRD spectra of c- (left hand side) and m-cut (right) α-Al_2O_3 implanted at RT with 1.2×10^{17} cm^{-2} and 0.9×10^{17} cm^{-2} 150 keV Zn^+ and after annealing at 1273 K for one hour in air or vacuum.

No other reflections were observed, namely from metastable phases of aluminium oxide, zinc peroxide or Zn/Al alloys. The production of ZnO in sapphire proves to be difficult, and one reason could be the high solubility of Al in ZnO, this system evolving to $ZnAl_2O_4$ for concentrations as low as 3 mol. % of Al [Yoo02].

Table 4.20 summarizes the XRD measurements.

Table 4.20 – XRD results obtained on Zn implanted samples.

sample	2θ	phases	size (nm)	calculated and tabulated lattice dimensions (nm)	PDF card
c, 1.2×10^{17} cm^{-2} as imp.	36.35	Zn (0002)	6	0.494 / 0.495 (c)	00-004-0831
1273 K air	38.65	$ZnAl_2O_4$ (222)	22	0.806 / 0.809	01-070-8181
1273 K vacuum	36.06	Zn (0002)	12	0.498 / 0.495 (c)	00-004-0831
m, 1.1×10^{17} cm^{-2} as imp.	-	-	-	-	-
1273 K vacuum	31.72	ZnO (1000)	7	0.323 / 0.325 (a)	01-070-8070

4.3.3.1.2 Optical studies

4.3.3.1.2.1 As implanted

The optical absorption spectra taken after implantation are depicted in Figure *4.30*a. Again, the absorption band at 205 nm – 250 nm range indicates the presence of F and F^+ centres. Since no low fluences were used in this work, a spectrum of c-cut samples implanted with 1.0×10^{16} cm^{-2} 48 keV Zn ions taken from [Xia06a] is included as the F-centre concentration is still possible to calculate (8.07×10^{19} cm^{-3}) after this implantation and also because it offers an indication of a threshold for SPR formation.

As the fluence increases the defect-related bands are overshadowed by lower energy bands. In fact, the main feature of the spectra is the appearance of an absorbance band in the 275 nm region which increases with the implantation fluence. This is probably related to the SPR band of zinc, an indication that Zn is present in the metallic state, as also seen by Xia and co-workers in a similar system [Xia06a], Huis and co-workers in MgO [Hui04], and Lee and co-workers in silica [Lee05]. Furthermore, a linear red shift (from 260 nm to 290 nm, represented by the dot arrow across the extreme absorption maxima) is also observed for this band as the fluence increases, an indication of the growth of the Zn nanoparticles with fluence. As for the shape and FWHM of SPR absorption band, Zn nanoparticles are like noble metals, e.g. Au, Ag, Cu (cf. Figure *4.19* for Cu), rather than other transition metals, such as Fe, Co, Ni (cf. *Figure 4.10* for Ni). The SPR bands are broader and weaker for the latter than for the former. This is because of the similar electron configuration between metal Zn and Au, Ag, Cu with closed *d* bands. The difference of SPR absorption between metal nanoparticles with closed *d*-bands and partially filled *d*-bands has been discussed by Amekura and co-workers [Ame04].

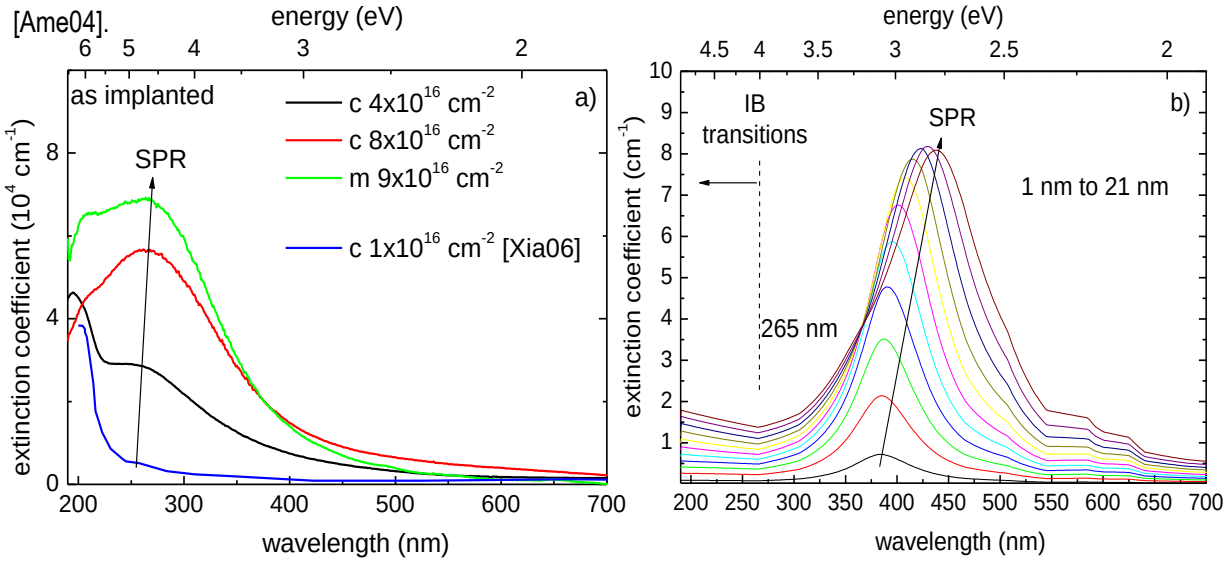

Figure 4.30 – a) optical absorption spectra of c- and m-cut α-Al_2O_3 as implanted with 150 keV Zn^+ at RT with fluences up to 9×10^{16} cm^{-2} (included is a spectrum from [Xia06] of 48 keV Zn RT implantation in sapphire) and b) MiePlot simulations of Zn particles with radius between 1 nm and 21 nm.

Regarding simulations, MiePlot code prediction for a zinc sphere with 1 nm radius embedded in sapphire matrix reveal that the SPR band should be centred at 370 nm, using the optical constants from Palik's compilation [Pal98], as shown in
Figure *4.30*b. The shift of more than 100 nm between MiePlot estimative and the experimental spectra indicates that the optical constants of Zn must be significantly modified to account for size effects. It's worth noting that Zn is a semimetal, its conduction electrons cannot be considered as free electrons, and hence the use of metal models in this case may be somewhat inadequate.

4.3.3.1.2.2 After annealing

Figure 4.31 shows the thermal evolution of the optical spectra. The simulations obtained with SCOUT code are also presented for all samples. By annealing c-cut samples (*Figure 4.31*a) in air there is a decrease of the intensity of the SPR band at 1073 K, which eventually disappears completely at 1273 K, leaving only a low concentration of radiation induced defects as indicated by the transparency across the entire spectrum from visible to UV. In fact, the absorption starts around 300 nm, possibly related to the presence of Zn spinel, whose band gap is located in this region. On the contrary, by annealing these samples in vacuum, the 290 nm SPR band is enhanced and red-shifts at 1073 K. Further annealing at 1273 K lead to a decrease in the intensity of this band, while keeping its peak position. This is fully consistent with the RBS results, where some Zn loss is observed after this annealing procedure.

The OA results obtained for m-cut samples are shown in *Figure 4.31*b. Upon annealing at 1073 K a minor decrease in the intensity of the SPR band is observed. At 1273 K this tendency continues. At 1323 K a major decrease on the SPR band is observed and at 1573 K this band completely vanishes. These high temperature annealings were performed in order to further develop the ZnO phase and to promote an extensive recrystallization of the sapphire matrix. However, the optical absorption studies did not reveal the typical band-gap absorption band of ZnO around 430 nm [Ame05] at any stage, probably due to the low quantity of particles formed.

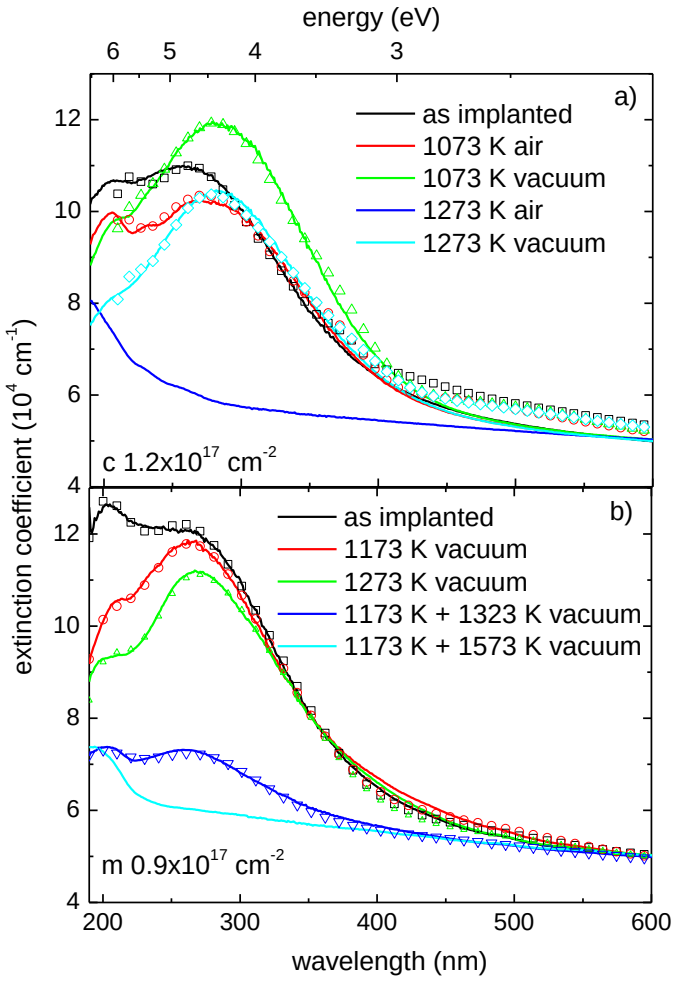

Figure 4.31 – Optical absorption spectra of α-Al_2O_3 as implanted with 150 keV Zn^+ and after annealing up to 1273 K for one hour in air or vacuum: a) c-cut 0.8×10^{17} cm^{-2} and b) m-cut 0.9×10^{17} cm^{-2}, with the corresponding SCOUT code simulations.

These optical absorption results for c- and m-cut samples are summarized in Table 4.21 and Table 4.22, respectively. The SPR band was adjusted with a Gaussian curve and simulated with SCOUT code. These simulations were performed considering a free electron metal model since using Palik's compilation data of the optical constants of Zn it was not possible even to match the peak position of the SPR band, as shown with the MiePlot calculations depicted in Figure *4.30*b. The estimate for the size of the precipitates obtained after implantation taken from the damping constant is about 5 nm while volume fraction and thickness yield 32 nm, the former within the size distribution observed in TEM pictures of similar samples (cf. *Figure 4.28*). After the annealing in air at 1073 K the precipitates reach 16 nm. Similar annealing in vacuum yields 14 nm sized particles. Further annealing at 1273 K in this atmosphere leads to a decrease to 10 nm.

The volume fraction is constant in all cases, as percolation strength, both assuming low values, an indication of the low degree of connectivity between the precipitates.

The behaviour of m-cut samples after implantation is similar. SCOUT code estimate give average sizes of 4 nm (from the damping constant) and 29 nm (from the volume fraction and thickness). Considering the former, the average size of the precipitates increases to 7 nm by annealing at 1073 K in vacuum, with further increase to 8 nm after annealing at 1273 K. At 1323 K the average size drops to 5 nm.

Table 4.21 – Optical features of Zn implanted c-cut samples.

sample	experimental data			SCOUT code simulation					
	peak (nm)	FWHM (nm)	area	volume fraction (%)	percolation	thickness (nm)	damping constant (cm^{-1}/ Hz)	size 1 (nm)	size 2 (nm)
as implanted	282	190	177	0.25	0.19	81	17963 5.39×10^{14}	5	32
1073 K air	274	163	139	0.24	0.19	77	10634 3.19×10^{14}	16	30
1073 K vacuum	280	160	175	0.24	0.18	82	11021 3.31×10^{14}	14	32
1273 K vacuum	283	150	133	0.25	0.19	65	13191 3.96×10^{14}	10	25

Table 4.22 – Optical features of Zn implanted m-cut samples.

sample	experimental data			SCOUT code simulation					
	peak (nm)	FWHM (nm)	area	volume fraction (%)	percolation	thickness (nm)	damping constant (cm^{-1}/ Hz)	size 1 (nm)	size 2 (nm)
as implanted	237	212	305	0.21	0.15	79	14263 4.28×10^{14}	4	29
1173 K vacuum	261	164	187	0.23	0.18	74	15006 4.50×10^{14}	7	28
1273 K vacuum	270	144	149	0.19	0.15	69	13955 4.19×10^{14}	8	24
1323 K vacuum	255	162	64	0.13	0.25	86	17965 5.39×10^{14}	5	27

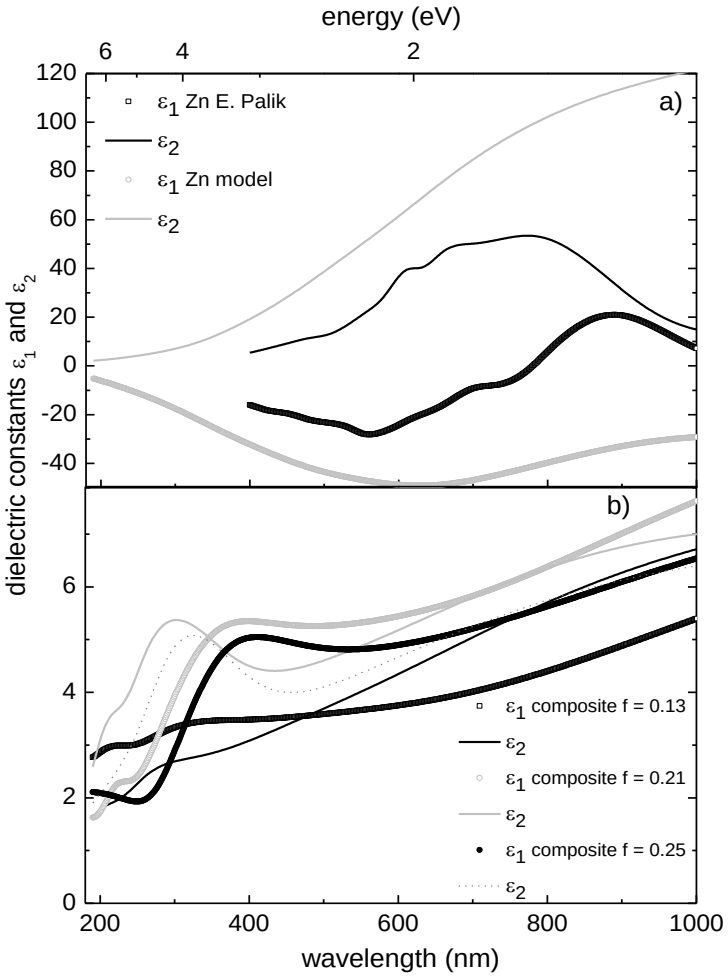

As was the case of copper, these fits implied a substantial modification of the optical constants of zinc, as presented in *Figure 4.32*a. Again, the major change is in ε_2 of the Zn model. Regarding the composite, *Figure 4.32*b, as the Zn fraction increases the UV behaviour changes, ε_2 reaching the first maximum around the SPR band while ε_1 has that maximum around 400 nm. Both constants show a red shift with increasing volume fraction.

Figure 4.32 – Dielectric constants of a) zinc and b) those from the effective medium model used.

According to RBS and XRD measurements, the spinel phase is present and extends to 85 nm in c-cut samples. Using this information it is possible to estimate the band-gap of this phase using equation 3.58, as in the previous systems with Ni and Cu, assuming that it is responsible for the absorption band that arises at 300 nm. The Tauc plot of Figure 4.33 shows that the band gap of $ZnAl_2O_4$ is about 3.75 eV, in excellent agreement with the bulk values found in the literature, e.g. 3.8 eV [Sam98]. The minor difference is ascribed to size effects, e.g. the increase of band gap energy with decreasing size of the aggregate. The lower energy gaps may be related to impurity levels or IB transitions. It's worth noting the lowest energy gap may also be related to the roughness of the implanted surface, since these are BSP samples, and its value is lower than that observed on OSP surfaces, which is about 1.4 eV.

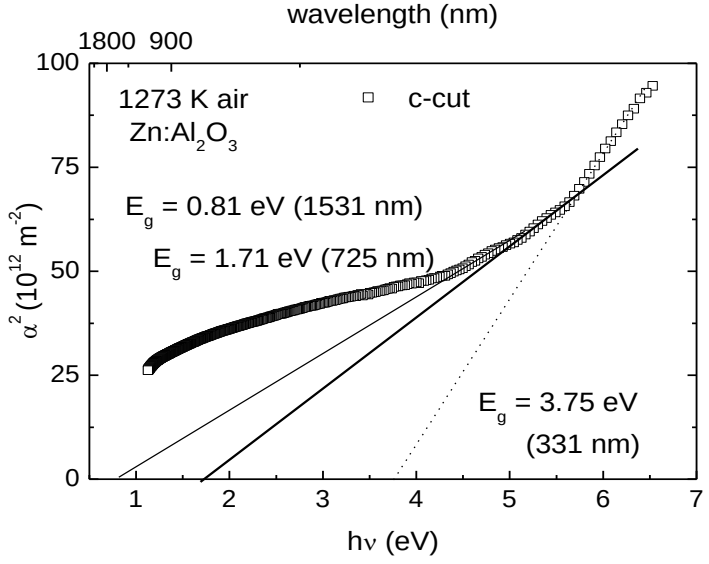

Figure 4.33 – Tauc plot for the determination of the band gap of $ZnAl_2O_4$.

IBIL measurements were carried to assess the presence of ZnO. The IBIL spectra of the m-cut samples are shown in Figure 4.34. The characteristic emission of F^+ centres of sapphire is visible at 330 nm while the band around 440 nm is usually ascribed to F centres [Tow94], as described in Table 2.3. The emission of direct band-gap transition in ZnO is expected around 375 nm [Ame05] and is thus shadowed by that of defect structures of sapphire. However, a broad band develops at 520 nm in m-cut samples annealed in vacuum. This band has been attributed to deep states in ZnO nanoparticles [Ame05], and agrees well with the XRD results of *Figure 4.29*. The IBIL spectra were taken in grazing incidence to minimize the signal originating in the unimplanted layers. A detailed description of the defect centres features present in the IBIL spectra of sapphire based systems is presented in the last section of this chapter, where IBIL technique was extensively used in the study of RE doped sapphire.

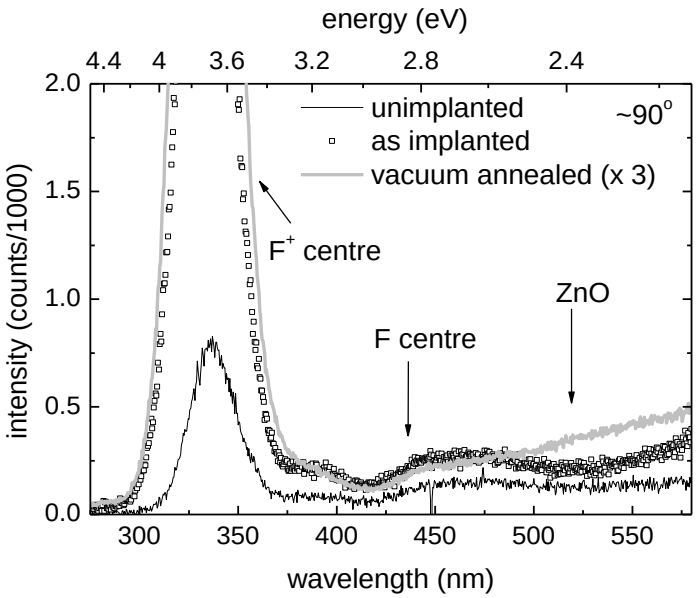

Figure 4.34 – IBIL spectra of m-cut α-Al_2O_3 as implanted with 0.9×10^{17} cm^{-2} Zn and after annealing at 1273 K in vacuum for one hour. The spectrum of an unimplanted sample is included for comparison.

4.3.4 Discussion

After implantation at RT of low fluences (about 10^{15} cm^{-2}) of Ni and Cu, a fraction of the implanted ions is found in regular lattice sites, probably substituting displaced Al ions during implantation or sitting in vacant octahedral sites along the c-axis of sapphire. Zn was not implanted in the low fluence regime.

The threshold for total dechanneling for TM implanted in sapphire at RT with E < 200 keV is between 0.20 at. % and 0.75 at. %.

Only for the lower fluences it was possible to estimate the defects in the O sublattice by measuring the F-type centre concentration through Smakula formula, since features related to the implanted species (IB transitions or SPR band) are negligible. The results are presented in *Figure 4.35* and compared with another measure of the lattice damage, the χ_{min} in the Al sublattice. In this figure the Zn results (48 keV, 1×10^{16} cm^{-2}) are taken from [Xia06] and our results from Mn implantation are included [Mar06]. It's noteworthy the higher F-centre concentration produced by Cu ions as compared to Ni, following the same trend revealed by the minimum yield. This is related to the nuclear stopping power, which is higher in the case of copper.

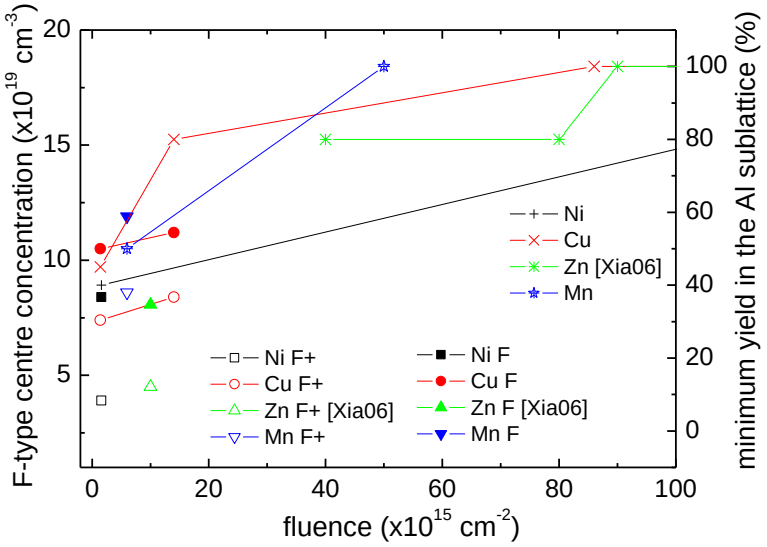

Figure 4.35 – F-type centre concentration and minimum yield vs. implantation fluence of TM.

Regarding the damage concentration in the O sublattice, the use of the Smakula formula may yield an excessive amount of defects, since one may expect the formation of aluminium precipitates during implantation. In fact, MiePlot simulations of the optical extinction of nanosized aluminium spheres, shown in

*Figure 4.36*a, demonstrate that these are potential candidates for extra absorption.

Moreover, there is a systematic increase in the slope of the absorption spectra towards lower wavelengths with increasing fluence, which may be related to both surface scattering effects but also to the formation of voids during implantation, related with the destruction of the lattice and vacancies accumulation. These voids tend to show absorption proportional to their size and to the photon energy, as shown in MiePlot simulation in

*Figure 4.36*b for voids with 1 nm, 5 nm and 10 nm radii. These effects further complicate the analysis in the F-centre absorption region and must be taken into account if a complete description of the OA behaviour in the UV region is to be given.

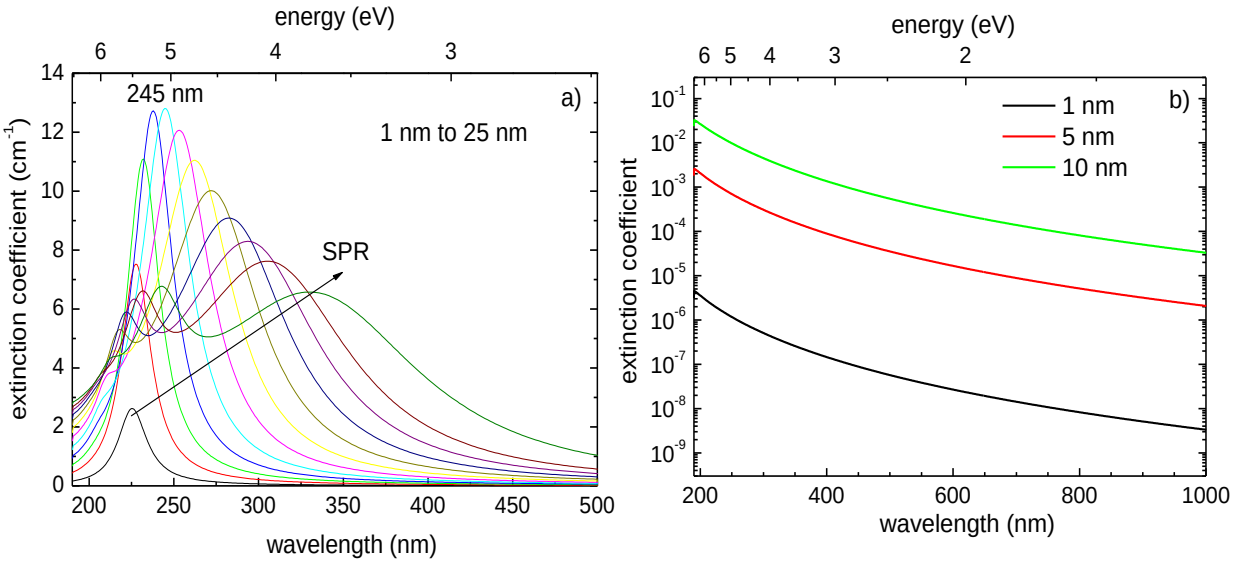

Figure 4.36 – MiePlot simulations of the optical extinction of: a) Al spheres with radius from 1 nm to 25 nm and b) voids with 1 nm, 5 nm and 10 nm radii.

The amorphous phase, as seen by RBS-C in the Al sublattice, occurs for fluences below 8.6×10^{16} cm^{-2} in the case of Cu (also shown in *Figure 4.35*) and 1.2×10^{17} cm^{-2} for Zn, while for Ni it happens below 1.8×10^{17} cm^{-2}. At the maxima implantation fluences the amorphized region extends to about 200 nm for Ni and Zn and 120 nm for Cu (implanted at lower energy). This is shown in *Figure 4.37*, where the RBS-C spectrum of the as implanted state in each case is presented, along with the evolution upon annealing at 1273 K, as measured in the matrix. The grey spectra are the as implanted ones and amorphization is clearly reached in any case. This figure will be later referred to when analysing the annealing behaviour of the matrix. The high concentration of the implanted species produces a marked dip in the Al profile in the case of Ni and Zn, while for Cu, implanted with lower energy, a step in the Al barrier is observed. That is, in the case of Ni and Zn the implanted species is encapsulated, in an amorphous region with about 120 nm sandwiched by the crystalline material and a top layer of near amorphous or polycrystalline alumina. In fact, the topmost layer was the last to be amorphized as the fluence increased. Copper, on the other hand, is distributed closer to the surface and thus more exposed to external atmosphere.

The anisotropy of sapphire becomes evident and of relevance in the radiation damage behaviour, as measured by the χ_{min} around 250 nm, with m-cut samples retaining more damage than c-cut samples in the case of Cu and Zn implantation and r-cut samples being less damaged than c-cut samples in the case of Ni implantation. In any case, the damage profiles are similar in the O and Al sublattices.

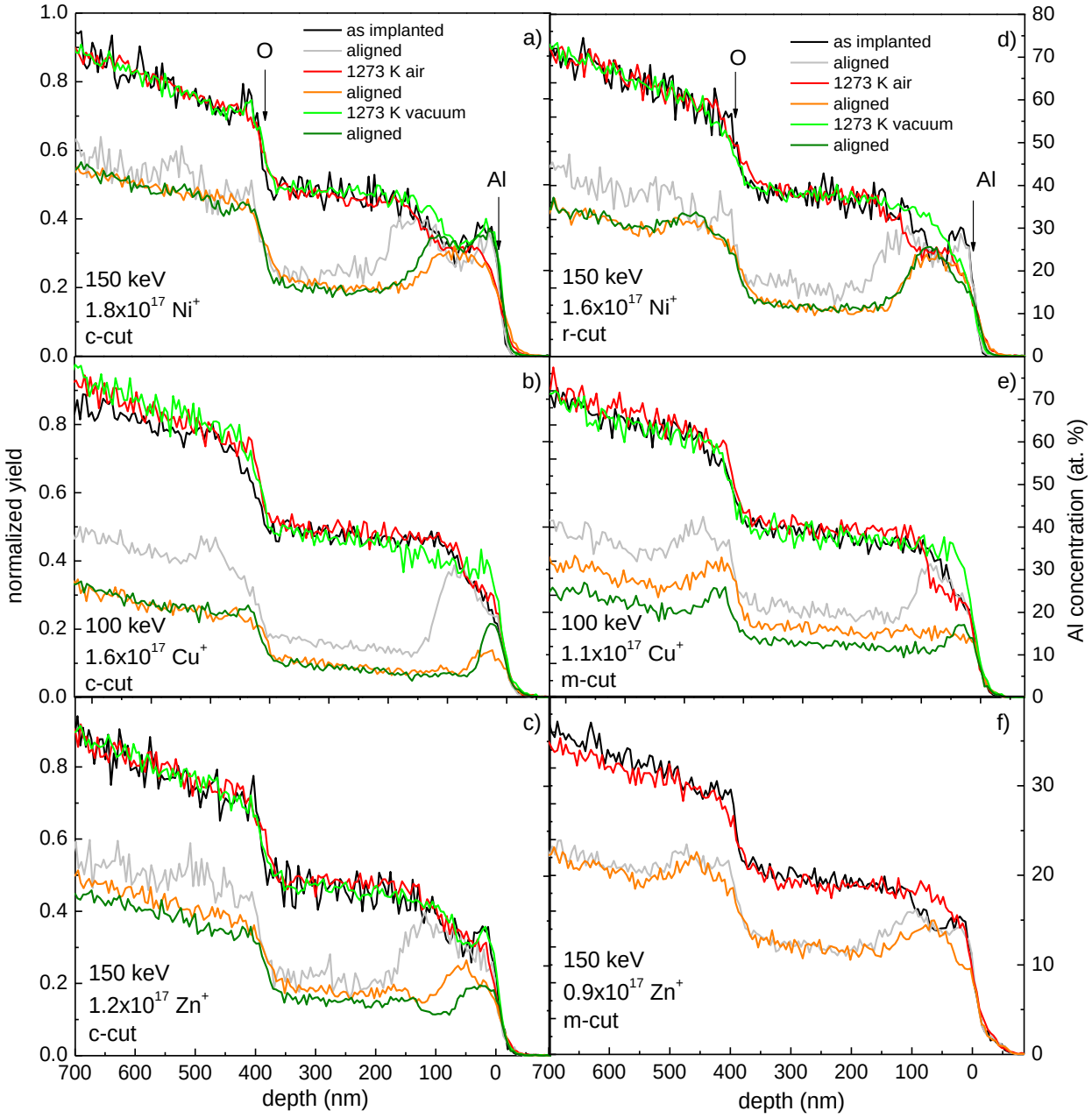

Figure 4.37 – RBS-C spectra recorded in the matrix after implantation and after annealing at 1273 K for the systems studied (the depth scale is only valid for the Al sublattice).

Figure 4.38 shows the surface plane presented to the impinging ions for c-, m- and r-cut samples. There are clear differences between these crystallographic planes. Even tilting the samples by around 8º during implantation does not change this asymmetry, the higher amount of Al exposed in m-cut samples as compared to c-cut and this may explain the higher damage observed. Moreover m-axis is less symmetrical and thinner than c-axis and thus easier to obtain dechanneling effect. For Ni implantation, r-cut samples are less damaged than c-cut but were also implanted with a lower fluence.

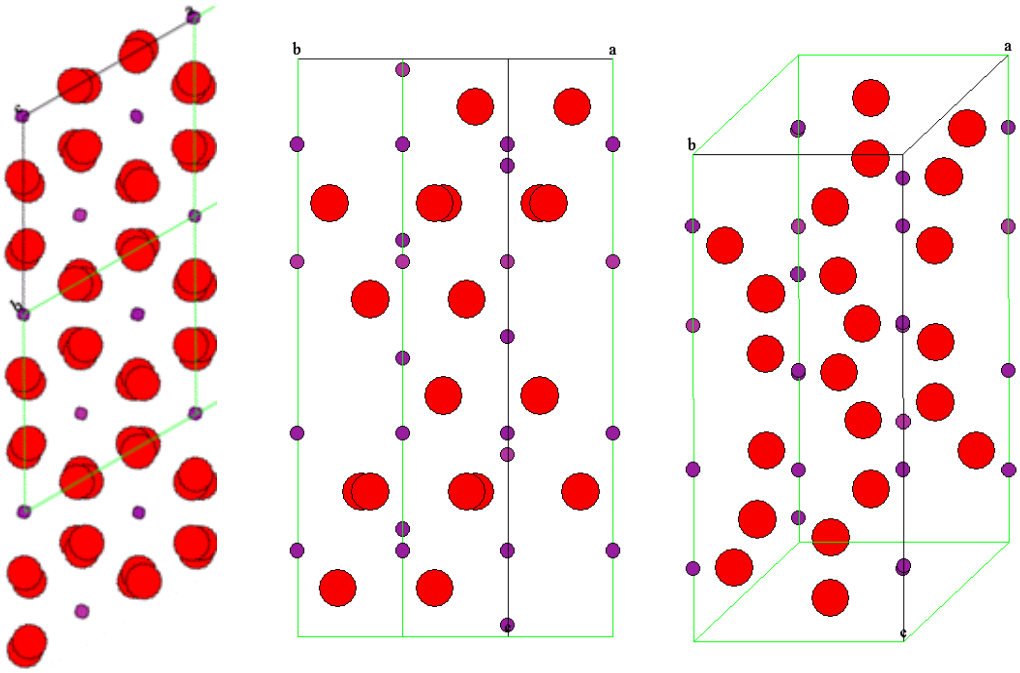

Figure 4.38 – Surface plane of sapphire for (from left to right) c-, m- and r-cut samples.

Continuing the as implanted analysis, *Figure 4.39* shows the effect of the damage energy deposition on the surface crystallinity, measured as the χ_{min} in the Al lattice (full marks) and in the implanted profile (open marks), for the implantation of TM in sapphire (again including Mn implantation [Mar06]). A significant amount of damage is already visible for the lowest fluences, increasing almost linearly with the implantation fluence, as complex defects such as dislocation loops and point defect clusters build-up. For $E_D > 7\times10^{23}$ keV cm^{-3} the overall χ_{min} reaches values close to 100% in the Al lattice, meaning that at depths around R_p (~1100 keV) full amorphization is observed, possibly irrespective of the implanted ions (the data lacks some points for Ni implantation), thus excluding chemical effects. The implantation profile shows systematically a higher dechanneling, as expected for a phase constructed by an ion implantation process.

The discrepancy of this threshold value with literature values, 3×10^{23} keV cm^{-3} [Mou87], arises from the implantation conditions here used (higher current density and energy) but, mainly, on the selected signature of amorphization. Mouritz and co-workers based their analysis on the FWHM of absorption bands of F-centres. As shown in our work, in this region of the spectra it is possible to find IB transitions and SPR bands, as well as absorption tails from defects of sapphire absorbing in the deep UV region. It is also where scattering related extinction is stronger. Taking the observed absorption bands as uniquely related to F-centres would then lead to an underestimation of this threshold of amorphization.

The as-implanted profiles show a nearly Gaussian shape, as predicted by SRIM, but with FWHM and R_p that differ from the theoretical simulation, in particular for high fluences. It is clear that the calculated R_p values are usually overestimated for high fluences, a result of the increasing density of defects and of the implanted species with implantation fluence. On the other hand, the experimental FWHM values systematically exceed the predictions, in particular for Cu and Zn, with a slight decrease of this difference with the implantation fluence. This is essentially the result of the mobility of the implanted ion in a RED process. However, the current density varied amongst

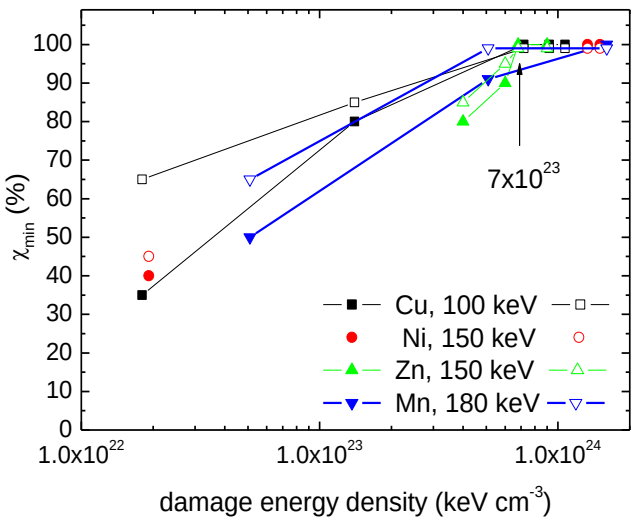

implantations and may influence the distribution of the implanted species. In fact, Stepanov and co-workers have measured larger and deeper implantation profiles than those predicted by SRIM code with increasing implantation current density [Ste05]. For higher fluences the RED process may also be limited by the presence of the implanted species and at this stage the experimental FWHM converges to SRIM prediction.

Figure 4.39 – Dependence of the χ_{min} in the Al lattice and in the implanted profile with the damage energy deposition at RT observed in TM implantation in sapphire.

Metallic nanoparticles were produced through implantation of high fluences. The first signature of these precipitates obtained after implantation is observed in the optical absorption spectra, where large bands develop with increasing fluence (the presence of Ni is shown by a band peaking in the 360 nm region, Cu at 600 nm and Zn at 300 nm). These are SPR bands related to the presence of metallic particles. In the case of Zn the location of the SPR band absorption is blue-shifted by about 100 nm relative to the expected position as calculated with MiePlot input with Zn bulk optical constants. Zn is a semimetal and the use of Mie Theory may thus be inadequate.

The SPR signature shows that the threshold for the formation of precipitates lies in the range of 1×10^{16} cm^{-2} to 6×10^{16} cm^{-2} for these ions. Finding the threshold fluence may allow estimating the implanted fluence directly from optical absorption measurements.

The precipitates obtained after implantation have dimensions of a few nanometres and the samples develop a dark brown colouration as a result of their presence (SPR and IB transitions) and of the build-up of radiation damage defects. Rough estimates based on optical absorption measurements give ~ 20 nm for Cu, 32 nm for the average dimension of the Zn particles, and ~5 nm in the case of Ni clusters.

The dimensions of these precipitates were also determined by XRD measurements in the samples implanted with the highest fluences. After implantation of c-cut samples the Cu aggregates are estimated to have ~ 9 nm, 4 nm for Ni while in the case of Zn are estimated to have average dimensions of 6 nm. These particles are shown to be aligned along the c-axis of sapphire. However, in m-cut samples (Cu and Zn) or in r-samples (Ni) no metallic XRD reflections were found, an indication of the randomness of the distribution of the aggregates or its minute size (below 2 nm) in these types of samples. In fact, c-cut samples seem to promote a faster solid state epitaxial reaction.

The difference between the values derived from these two techniques is related to the fact that XRD gives the size of crystallites, while optical analysis probes all particles and as a whole, crystalline and non-crystalline region. We thus conclude that most of the metallic particles are highly defective (justifying also the lack of channelling effects in the corresponding RBS-C spectra) or that each particle consists of a small crystalline region surrounded by highly defective material. *Figure 4.40* shows the relation between the estimated sizes of the precipitates via these two techniques vs. the implantation fluence. The optical estimate is systematically larger than that obtained by XRD.

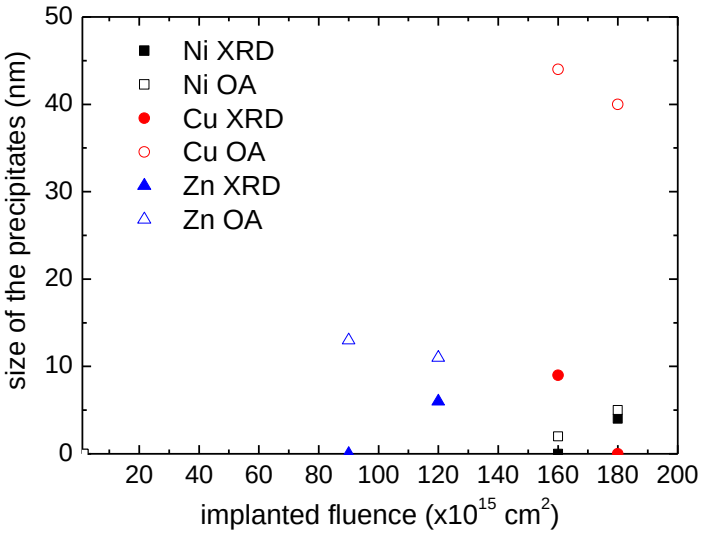

Figure 4.40 – Size of the precipitates formed after implantation vs. implantation fluence.

It is possible that a better correspondence is obtained by comparing the maximum concentration instead of the implanted fluence. *Figure 4.41* shows this comparison. The optical signature seems to start below 12 at. %. This is consistent with the threshold fluence for SPR band absorption found for Cu (~6×10^{16} cm^{-2}) which, for a FWHM of ~50 nm implies about 10 at. % in sapphire. On the other hand, XRD reflections only occur at about 14 at. %.

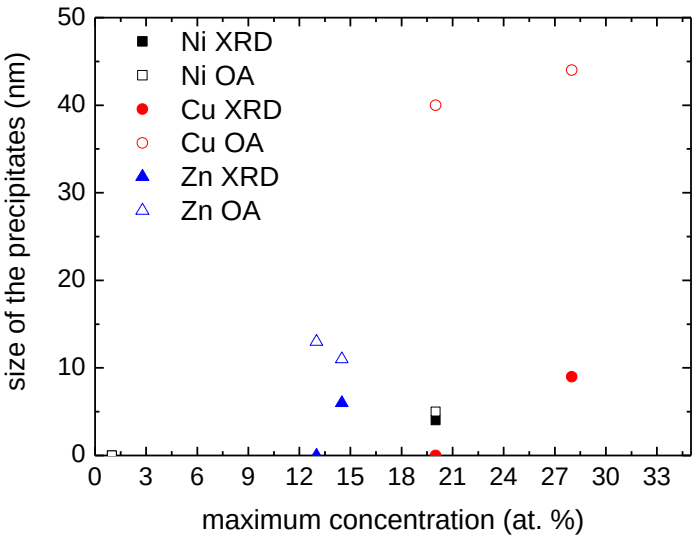

Figure 4.41 - Size of the precipitates formed after implantation vs. maximum atomic concentration of the implanted species.

In every case these precipitates concentrate at about R_p and are thus inside the radiation damaged layer.

In summary, after implantation of low fluences (below 5×10^{15} cm^{-2}) some of the implanted ions take definite positions on the matrix lattice, possibly substituting displaced Al ions during implantation. As the fluence increases (up to 5×10^{16} cm^{-2}) the radiation damage increases and optically active metallic nanoprecipitates develop. Fluences of 1×10^{17} cm^{-2} turn the surface region amorphous and crystalline metallic precipitates grow, with epitaxial preferential crystalline orientation in c-cut samples only.

The proposed evolution of the as implanted TM systems as measured with the experimental techniques with increasing atomic concentration of the implanted species is summarized in *Table 4.23*. The appearance of the first XRD reflections seems to be related to the amount of damage in the matrix.

Table 4.23 – Evolution of the as implanted TM systems with the atomic concentration of the implanted species.

RBS-C implanted profile	channeling	total dechanneling		
RBS-C matrix	channelling			total dechanneling
XRD	no reflections			nanometre precipitates
OA	no SPR		SPR	
concentration of the implanted species (at. %)	0.75	10	14	30

The annealing behaviour of the samples implanted with the highest fluences was studied by performing furnace annealings in air or vacuum up to 1573 K. The dynamics of the systems formed depends on the initial conditions of the matrix and implanted species. The behaviour of the matrix is shown in *Figure 4.37* for the 1273 K annealing.

In any case there is crystalline recovery, the extension and defect concentration of the damaged region decreases. The exception are m-cut samples implanted with Zn where little changes are observed.

Two striking differences occur between c- and m-cut samples upon any annealing: the disorder in the O sublattice and in deep regions in the Al sublattice is always higher in m-cut samples.

On the other hand, c-cut samples seem to retain more damage in the Al sublattice than in the O sublattice after annealing. This may mean that during the implantation of c-cut samples the Al sublattice is more damaged in comparison to O sublattice, more resilient.

The behaviour of the implanted profile upon annealing is shown in *Figure 4.42*. It is clear the formation of the spinel phase in any case after annealing in air at 1273 K, where a rectangular profile extending to the surface develops, with minor loss of the implanted species. The spinel phase is in fact the only reflection obtained in the XRD spectra after annealing in air.

This annealing promotes the formation of a Ni spinel, $NiAl_2O_4$, in nanosized crystallites of about 16 nm average dimension, in the near surface region of sapphire (115 nm). This cubic compound has its <111> axis aligned with the c-axis of hexagonal α-Al_2O_3. In the case of r-cut samples the alignment is $(311)_{spi.}$ // $(10\bar{1}2)_{sapp}$.

In the case of copper, $CuAl_2O_4$ is created, with large precipitates (~30 nm) which are epitaxially aligned with the substrate (<111> // <0001> or <110> // $<10\bar{1}0>$ for c- and m-cut samples, respectively).

In the case of zinc, annealing at 1273 K in air also produces a spinel phase, $ZnAl_2O_4$, in the form of 22 nm sized precipitates, having <111> // <0001>.

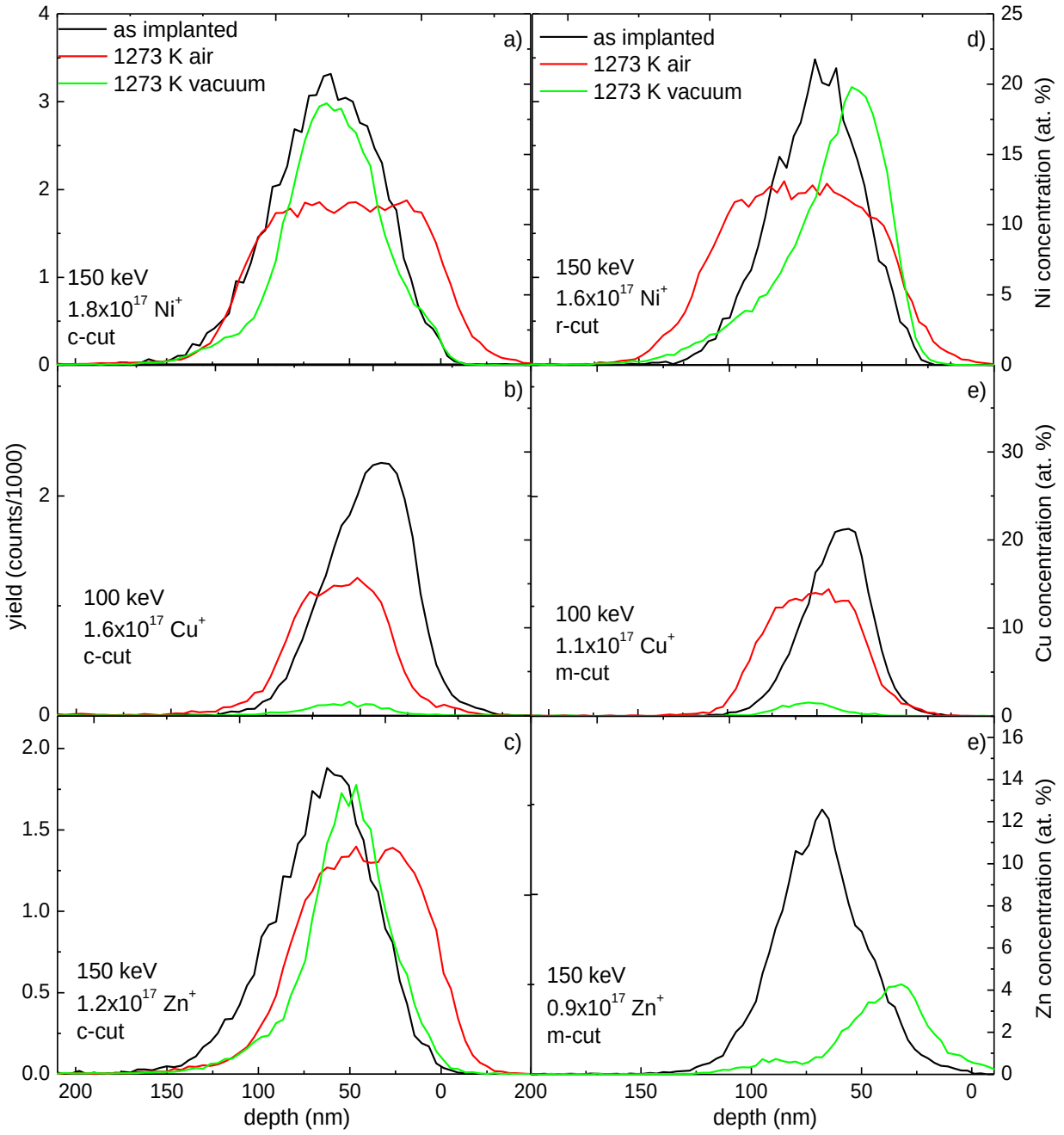

Figure 4.42 – RBS-C spectra in the implanted species region, obtained after implantation and after annealing at 1273 K in air or vacuum for c-cut (left side) and r- or m-cut samples (right side): a) and d) Ni:Al_2O_3, b) and e) Cu:Al_2O_3 and c) and f) Zn:Al_2O_3.

In general, annealing in air promotes the formation of the spinel phase of these elements, aligned with the substrate axis. The crystalline quality, as seen by RBS-C from the χ_{min} or from the size of the precipitates inferred by XRD measurements, of this phase increases from Ni to Zn to Cu. This is consistent with several studies measuring the thermodynamics of spinel formation [Bol98] and, given their ion size similarity (same strain effects), it is related with the site preference of each of these ions which affects their voidal diffusion in the sapphire lattice, a process which forces continuous and alternated tetrahedral to octahedral empty site migration. Copper has no significant preference and thus shows high mobility while Ni has a strong octahedral preference (50 kJ mol^{-1}) and

Zn shows tetrahedral preference (35 kJ mol^{-1}) [Col94, Bol98]. The low melting point of Zn may allow for the Hedvall effect in the temperature range studied and further enhance the spinel formation. This effect can also occur in all three cases due to phase transitions of the Al_2O_3 phases since the recrystallization process from the amorphous or polycrystalline state after implantation encompasses *γ* to *θ* (even if this phase is suppressed by the presence of the implanted specie, as found in case of Co implantation) to α transitions in the temperature range of 1073 K to 1273 K.

The possible paths for the formation of the spinels phase are:

$$2Me + O_2 + 2Al_2O_3 \rightarrow 2MeAl_2O_4 \quad [4.7]$$

but also:

$$Me + ½\ O_2 + \gamma\text{-}Al_2O_3 \rightarrow MeO + \gamma,\alpha\text{-}Al_2O_3 \rightarrow MeAl_2O_4 \qquad [4.8]$$

The latter equation is governed by the counter diffusion of cations, Al in the monoxide phase, Me in alumina, in a Wagner mechanism. Moreover, the as implanted amorphization and the proximity to the surface may also facilitate the oxygen diffusion.

In any case the samples become transparent, none of the characteristic absorption of the spinels was observed in the optical spectra due to the small concentrations present.

From Tauc plots it was possible to estimate the band gap of the spinels phases formed to be: 3.51 eV for $NiAl_2O_4$, 4.74 eV for $CuAl_2O_4$ and 3.75 eV for $ZnAl_2O_4$.

The epitaxial relation between c-cut sapphire and a cubic lattice, in this case either the spinel phases or the metallic Ni or Cu, detected through XRD measurements, is sketched in *Figure 4.43*a, for a general $MeAl_2O_4$ spinel, along with the two most likely configurations possible: superposition of hexagons (Figure 4.43b) or 30º tilt between hexagons (Figure 4.43c).

The presence of the (311) reflection parallel to the r-plane indicates that the configuration is that of *Figure 4.43*c for $NiAl_2O_4$. Previous work by Mouritz and co-workers suggested configuration of *Figure 4.43*b [Mou88]. In the case of Zn, its metallic form as well as that of its oxide, ZnO, correspond to hexagonal structures and thus tend to grow parallel to sapphire's identical directions.

Given the lattice dimensions of sapphire and the spinels the maximum calculated mismatches for the spinel phases are about 8 % in all cases. This contributes to the high RBS dechanneling in every case but does not prevent epitaxy reactions. Regarding the cubic Ni and Cu metallic phases (n = 1) this mismatch is 2.5 % and 4 %, respectively.

Annealing in vacuum at 1273 K promotes the growth of the metallic Ni aggregates (~10 nm) embedded around the R_p. The cubic Ni phase is also aligned with the host lattice, its <111> axis being parallel to the c axis of sapphire. A small amount of spinel phase is present after this annealing, possibly due to the internal reaction of Ni with unbound or non-bridging oxygen that has been freed in the damage region during the implantation process. The spinel phase formed in vacuum has a smaller lattice constant than that formed by annealing in air, as can be seen by the shifts in the reflections from the <111> family. This shift reflects a 0.017 nm difference in the lattice constant. The spinel formed in oxygen deficient environment is more compressed and thus in a more disordered

state [Hal02]. On the other hand, r-cut samples show Ni diffusion to the surface and AFM measurements show large precipitates at the surface. This faster diffusion is related to the orientation of the fast diffusion plane but may also be due to poor encapsulation. That is, in the case of r-cut samples the Ni profile is found closer to the surface after implantation.

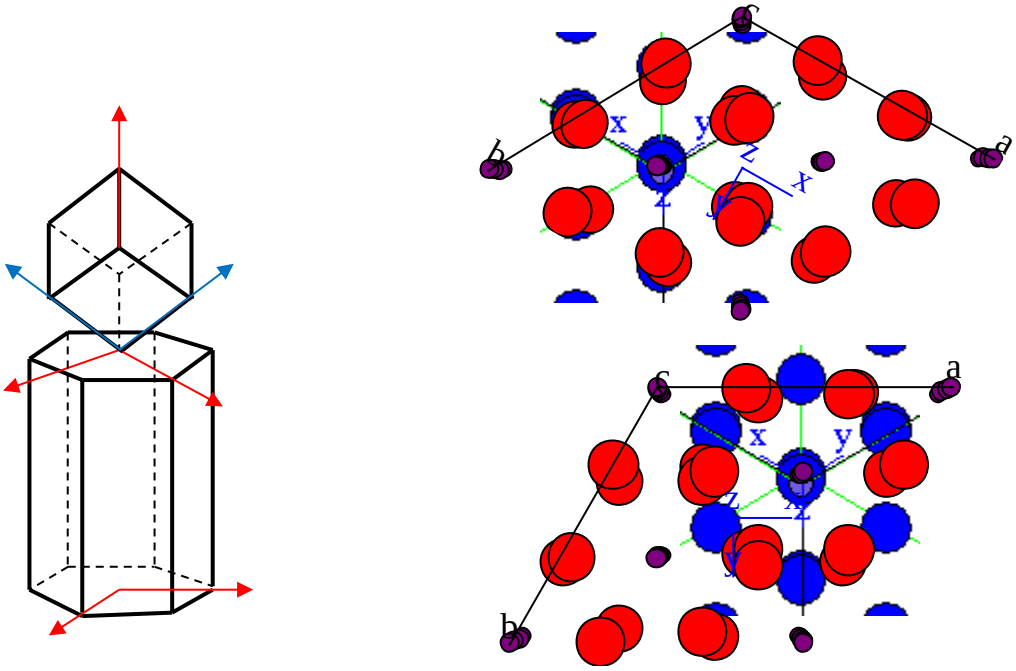

Figure 4.43 – a) Typical epitaxial relation between a cubic phase (for example a generic $MeAl_2O_4$ spinel, blue atoms) and c-cut sapphire (red atoms); b) superposition of hexagons on the c-plane of sapphire; c) 30º tilt of hexagons in the c-plane of sapphire.

For copper, annealing in vacuum promotes the thinning of the Cu profile and its migration to the surface. Metallic Cu aggregates are observed with increasing alignment $<111>_{Cu}$ // $<0001>_{sapp}$ up to 1173 K, being somewhat larger (12 nm) for m-cut samples than for c-cut samples (9 nm constant size). At 1273 K a major loss of Cu is observed in both types of samples (the total Cu content drops by 90%, while the matrix remains with a thin highly damaged surface layer which probably pins the remaining copper).

In the case of zinc implantation, annealing in vacuum of c-cut samples promotes the coalescence of the as implanted precipitates (by Ostwald ripening), the precipitates reaching average dimensions of 12 nm in this stage, with significant size dispersion, according to TEM measurements. The evolution of the precipitates with temperature is limited by out diffusion, impelled by the recrystallization front of sapphire, and evaporation, with major losses of the implanted ions at 1273 K. The remaining ions are pinned to unannealed defect or in stable phases. In fact, some spinel phase is observed at this stage but the formation of alloys or other oxides is also possible. In the case of m-cut samples, ZnO particles form during similar annealing in vacuum, the difference is attributed to both the higher level of radiation damage in the Al sublattice of c-cut samples (implanted with higher fluence), and to the higher mobility of Zn ions along the c-plane, normal to the surface of m-cut samples. The combination of high mobility and amount of Al defects allows the pinning of Zn in available Al sites and the formation

of ZnO precipitates. The Al content is critical since the compound formation is a counter diffusion process of Al^{3+} and Zn^{2+} through a nearly immobile anion lattice and a high Al content (> 3 mol. %) in ZnO leads to the formation of the spinel phase.

The presence of Ni and Zn spinels upon annealing in vacuum corroborate the assumption of equation 4.8 even in vacuum, but only in the initial stages. As the annealing proceeds the reduction of spinel occurs, incompletely in these two cases.

The thermal stability, as measured by the absence of significant losses of the implanted species, of the systems formed in air is at least 1273 K in all cases, since stable spinel forms. On the other hand, samples annealed in vacuum are stable up to 1273 K in the case of Ni implantation and c-cut samples implanted with Zn. In the case of Cu and m-cut samples implanted with Zn, the limit temperature is around 1173 K.

These limits depend on the implantation energy since higher implantation energies promote the encapsulation of the implanted material which limits segregation and evaporation, as may have happened in the case of Ni. Moreover, it depends on the crystalline orientation of the substrate, namely on the orientation of the fast diffusion c-plane of sapphire. In m- and r-cut samples this plane crosses the damage layer and allows for easier diffusion to the surface. Moreover, the precipitates tend to grow parallel to the c-plane, acquiring oblong features. At the surface, depending on the atmosphere, unstable oxides may form which sublimation may promote the loss of the implanted material. That was the case of copper. Ni and Zn have more stable oxides. Table 4.24 shows the enthalpy of formation of Al, Ni, Cu and Zn oxides. It is thus expected that the aluminium oxide formation prevails when these elements are in an environment with a low content of oxygen.

Table 4.24 – Formation enthalpy of oxides $(-\Delta H^0_{298})$ / kJ mol^{-1}.

Al_2O_3	NiO	Ni_2O_3	CuO	Cu_2O	ZnO	ZnO_2
1676	241.3	489.5	162.0	173.1	354.5	347.0

Regarding the fluence loss with annealing temperature and atmosphere, Cu was the most volatile ion in any case, as observed in *Figure 4.44*, where fluence losses are plotted vs. annealing temperatures and atmospheres. Considering only the melting and boiling points of these metals, Zn would be expected to evaporate at a higher rate than Cu while Ni is expected to be stable at the annealing conditions used. If in fact Ni presents the lowest losses, the behaviour of copper must be related either to chemical effects, that is compound formation and sublimation, or result from the local structure embedding these ions. That is, during copper implantation the damage level is higher and in a shallow surface layer, as compared to Zn implantation, which remains encapsulated upon annealing. Copper is thus closer to the surface and in a radiation damage rich environment that facilitates its out diffusion. As expected, annealing in vacuum produced larger losses, while m-cut samples are clearly favourable to out diffusion in the case of Zn and Cu systems.

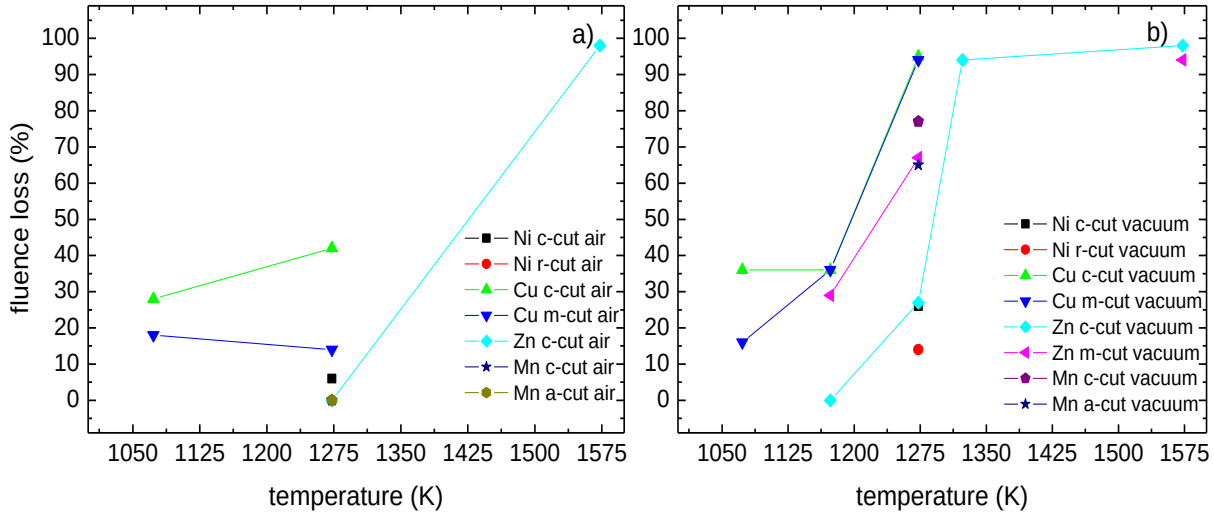

Figure 4.44 – Fluence loss vs. annealing temperature for TM systems for: a) air and b) vacuum atmospheres.

The process of formation of embedded precipitates via ion implantation followed by annealing is schematically summarized in *Figure 4.45*. For low fluences the implanted species is highly diluted essentially in atomic form and, in the case of sapphire, occupying lattice sites of the matrix. As the fluence increases a saturation limit is achieved and the implanted species start to aggregate. The SPR band develops at this stage. In this process the host matrix becomes increasingly damaged and amorphization is reached, easing the formation of large precipitates. These precipitates now have a large size distribution and even in anisotropic materials as sapphire are expected to grow in spheroidal shapes. The formation of a continuous film may be reached by further implantation or by annealing in specific atmospheres. The latter produces recrystallization on the host matrix, which occurs around 1100 K for sapphire, segregating non-soluble species to the surface or to the highly damaged inner layer that thins by compression, if a sufficiently large and crystalline surface layer is present.

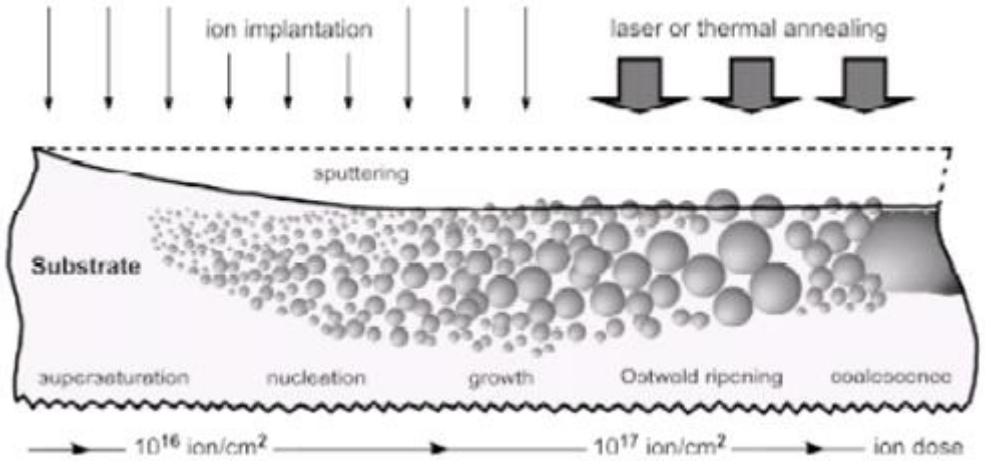

Figure 4.45 – Basic physical process involved in the formation of nanoparticles by ion implantation as a function of the implanted fluence (adapted from [Leu07]).

This method of producing layers with high concentrations of metallic precipitates embedded in sapphire may be preferable for applications targeting encapsulated structures since the alternative of high fluence implantation not

only will amorphize the surface layer but is accompanied by a high sputtering yield that will eventually expose the implanted layer. The growth of the precipitates may eventually promote the proximity between individual clusters and the optical analysis based on isolated and non-interacting precipitates (e.g. Mie theory) is no longer valid. Instead, percolation must be considered in order to account for interactions between them.

The fit of the complete optical spectra (190 nm to 1100 nm) with SCOUT code allowed determining the dielectric constants of the composite medium and of the implanted species. These are shown in *Figure 4.46*. The dielectric constants of the composite material steeply increase near the SPR band.

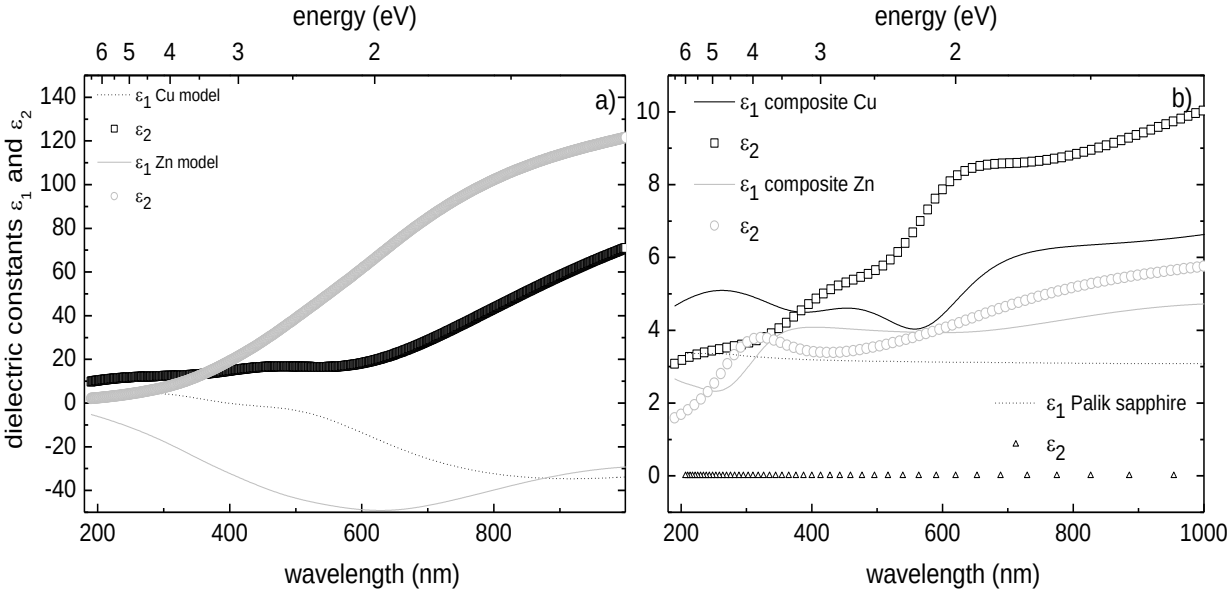

Figure 4.46 – Dielectric constants obtained with SCOUT code for: a) the implanted species and b) the composite material.

It's worth noticing that the characteristics of the metal include features input to fit the spectra, such has an oscillator in the UV region to account for F-centres.

The general evolution upon annealing up to 1273 K of the samples implanted with the highest fluences of TM ions is presented in *Table 4.25*.

Table 4.25 – Evolution of the TM systems implanted with the highest fluences upon annealing in air or vacuum.

as implanted (~RT)	γ-Al_2O_3, Me^0, O_2, possibly some amorphous Me_xO_y	
temperature	annealing in air	annealing in vacuum
1073 K	O_2, γ-Al_2O_3, Me_xO_y Unstable oxides (CuO) decompose with some loss of the implanted species	γ-Al_2O_3, Me^0 Unstable oxides (CuO) decompose with loss of the implanted species
1273 K	O_2, cation counter diffusion and formation of $MeAl_2O_4$, γ to α-Al_2O_3 transition complete	Partial γ to α-Al_2O_3, Me^0 low melting point elements near the surface evaporate (Zn)

4.4 Noble metals implantations

4.4.1 Introduction

Silver and gold ions, which along with copper make the noble metal group in the periodic table of the elements, were implanted at RT with 160 keV in sapphire. Table 4.26 summarizes the most important quantities associated with the implantations of Ag and Au and some of their relevant bulk properties. It is worth noting the low thermal stability of oxide phases of these elements as well as their similar electronic properties and crystalline cells. Moreover, the melting point of both elements is close to the maximum temperature used (1573 K).

Table 4.26 – Parameters pertaining the implantations and species implanted discussed in this chapter [Oma93, Lid02 and W4].

	Ag	Au
energy (keV)	160	160
current density (μA cm^{-2})	<5	<5
samples	c, m, OSP, 0.4 mm	c, m, OSP, 0.4 mm
fluence (cm^{-2})	1×10^{15} – 1×10^{17}	1×10^{16} – 7×10^{16}
SRIM R_p (nm)	47	37
SRIM straggling (nm)	12	7
SRIM FWHM (nm)	28	16
SRIM vacancies per ion	1350	1410
SRIM sputtering yield (at. per ion)	4.6	7.2
n_{dpa}	5 – 520	78 – 468
electronic and nuclear dE/dx (keV nm^{-1})	0.63 and 3.30	0.96 and 5.32
Van der Walls and atomic radius (nm)	0.166; 0.135	0.172; 0.160
melting point (K)	1235	1337
boiling point (K)	2435	3129
space group, structure and lattice parameters	Fm-3m; bcc; 0.41 nm	Fm-3m; bcc; 0.41 nm
atomic density (m^{-3})	5.86×10^{28}	5.90×10^{28}
compounds and thermal stability	Ag_2O stable up to 733 K	Au_2O_3 stable up to 423 K
Fermi velocity (ms^{-1})	1.40×10^{6}	1.39×10^{6}
Fermi level (eV)	5.5	5.5
ground state electronic configuration	[Xe].4d^{10}.5s^{1}	[Xe].4f^{14}.5d^{10}.6s^{1}
Debye temperature (K)	215	170
bulk plasma frequency (Hz)	8.59×10^{16}	1.36×10^{16}
surface plasma frequency (Hz)	6.07×10^{16}	9.61×10^{15}
free electron density (m^{-3})	5.85×10^{28}	5.90×10^{28}
electron mean collision time (s)	4.1×10^{-14}	2.9×10^{-14}

4.4.2 Ag implantation

Sapphire single crystals were implanted with silver ions aiming at the production of metallic nanoprecipitates embedded in the sapphire lattice. These aggregates display SPR absorption in the visible range, which features depend on several factors, namely the precipitate size and shape. By controlling these factors it is possible to tune the SPR band.

The optical and structural properties of c- and m-cut single crystalline α-Al_2O_3 were changed by RT implantation of 160 keV $^{107}Ag^+$ ions with fluences from 1×10^{15} cm^{-2} to 1×10^{17} cm^{-2}. Subsequent thermal annealings, up to 1273 K, either in air or vacuum (2×10^{-4} Pa), were carried to recover from the radiation damage introduced during the implantation process and evaluate the thermal stability of the structures formed.

The effects of the implantation fluence and substrate crystalline orientation and of the annealing parameters were studied and correlated with the optical behaviour of the samples in order to produce controllable shifts of the position and intensity of the SPR absorption band, thus allowing tailoring of the optical properties of the system. RBS, RBS-C, XRD and OA measurements were used to characterize the systems formed.

4.4.2.1 Results and discussion

4.4.2.1.1 Structural studies

The RBS-C spectra obtained after implantation of all but the highest fluence are shown in Figure 4.47. The implantation of 1×10^{15} cm^{-2} in m-cut samples (Figure 4.47a) produces a damage layer of about 70 nm ($E_D = 2.3\times10^{22}$ keV cm^{-3}), with the maximum disorder at 65 nm, where χ_{min} = 30 %. The χ_{min} in deeper regions is about 25 %.

The distribution of silver is nearly Gaussian with FWHM of 40 nm and the maximum concentration found at 50 nm depth. While the measured R_p is in accordance with SRIM code prediction of 47 nm, the FWHM is larger (28 nm, cf. Table 4.26), possibly due to thermal diffusion during implantation. Some channelling was observed on the silver profile with χ_{min} = 70 %. The spectrum is well fitted by NDF code considering a 30 nm sapphire surface layer, followed by a 40 nm thick layer with 0.18 at. % of Ag.

At 1×10^{16} cm^{-2} (Figure 4.47b) the maximum dechanneling in the Al sublattice reaches 70 %, at 60 nm, within a damaged region which extends again to 100 nm ($E_D = 1.6\times10^{23}$ keV cm^{-3}). Below this region the χ_{min} rises to 50 %.

The distribution of silver is again nearly Gaussian with the maximum concentration at 50 nm but with FWHM of 50 nm. The increase in the FWHM hints again at the possibility of thermal diffusion during implantation. No channelling is observed in the Ag profile. The NDF simulation yields a 25 nm thick surface layer of sapphire, followed by a 50 nm layer with 1.37 at. % of Ag.

The implantation damage naturally increases with the fluence and complete dechanneling is observed at the surface for a fluence of 6×10^{16} cm^{-2} for c- and m-cut samples (the random spectrum of c-cut sample is similar to that of m-cut sample and only the latter is shown in Figure 4.47c, for clarity). This reveals the complete surface

amorphization, as seen by RBS-C, in agreement with previous studies with other ions [Far90]. The damage layer extends up to 130 nm in both cases and E_D amounts to 7.4×10^{23} keV cm^{-3}. However, c-cut samples show χ_{min} = 90 % before bulk material starts and the damage at E < 1000 keV is also lower in c-cut samples (χ_{min} = 30 %) than in m-cut samples (χ_{min} = 65 %). This is the result of the anisotropy of sapphire, whose lattice present an m-plane which has a higher areal atomic density than c-plane and thus more susceptible to damage and blocking, as observed in the case of Cu and Zn implantation.

At this fluence the maximum concentration of Ag in the implanted layer is 9.7 at. % for c-cut samples and 8.5 at. % for m-cut samples, respectively, reached at 45 nm depth, thus slightly approaching the surface as the fluence increases. The implanted profile, nearly Gaussian, with a FWHM of 55 nm for c-cut samples and 60 nm for m-cut samples, is thus entirely placed inside the disordered surface layer. At this stage, both RED and thermal processes may contribute the enlargement of the profile. No significant channelling was observed on the silver profile. The difference in the FWHM between c- and m-cut samples is related to the faster diffusion along c-plane, perpendicular to the surface in the case of m-cut samples.

The presence of silver changes the local stoichiometry and the subsequent decrease of RBS yield in the corresponding Al part of the spectra (E = 1050 keV) is visible. Table 4.27 summarizes the RBS-C results obtained on these as implanted samples.

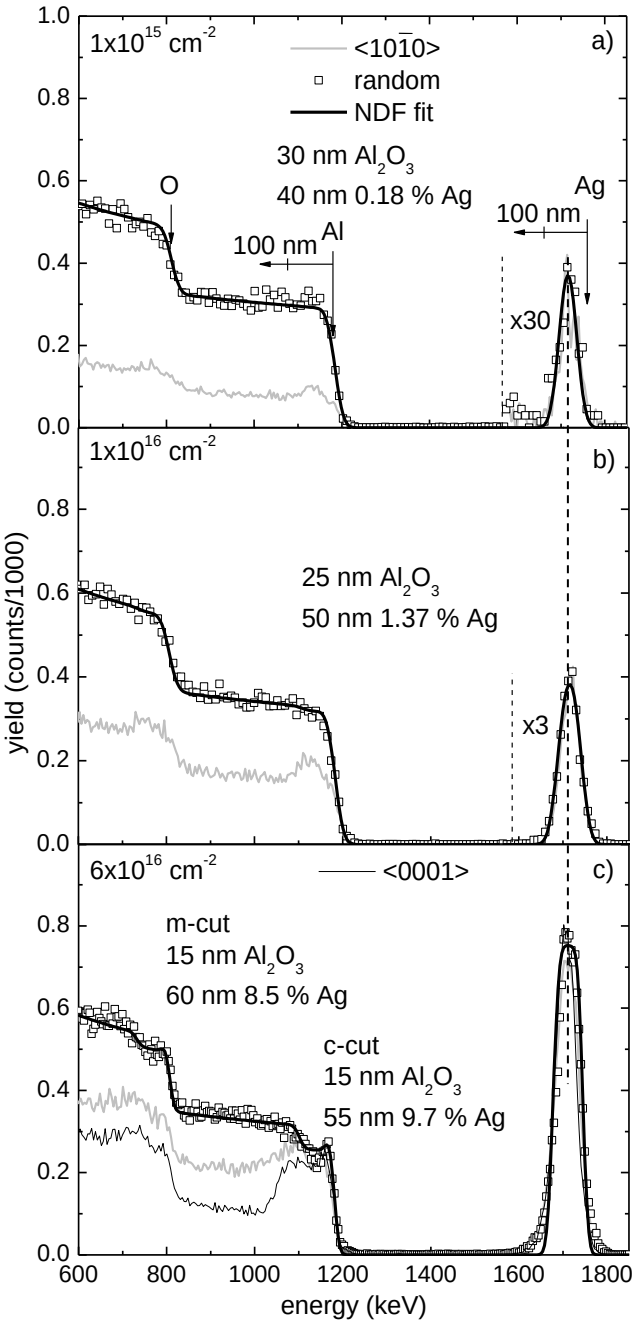

Figure 4.47 – RBS-C spectra of m-cut samples as implanted with 160 keV Ag⁺ ions with fluencies up to 6×10^{16} cm^{-2} (for this fluence a c-cut sample aligned spectrum is also shown), with NDF code composition fit.

Table 4.27 – RBS-C results of the as implanted samples with Ag ions up to 6×10^{16} cm^{-2}.

sample	m, 1×10^{15} cm^{-2}	m, 1×10^{16} cm^{-2}	m, 6×10^{16} cm^{-2}	c, 6×10^{16} cm^{-2}
host matrix				
max. damage depth (nm)	65	60	0 – 130	0 – 130
χ_{min} (%)	30	70	100	90
damage extension (nm)	70	100	130	130
E_D (10^{22} keV cm^{-3})	2.3	16	74	74
deep region χ_{min} (%)	25	50	65	30
implanted profile				
max. conc. depth (nm)	50	50	45	45
χ_{min} (%)	70	100	100	100
FWHM (nm)	40	50	60	55
max. conc. (at. %)	0.18	1.37	8.5	9.7

The RBS-C results obtained after implantation of 1×10^{17} cm^{-2} in c- and m-cut sample are presented in Figure 4.48a and Figure 4.48d, respectively. For c-cut samples, these show the usual Gaussian type implantation profile (peaking around 40 nm with FWHM of 45 nm) while a double peaked profile appears after implantation in m-cut samples, peaking at 60 nm and closer to the surface, at 15 nm, with FWHM of 15 nm and 25 nm, respectively. Similar behaviour was also reported in single crystal SiO_2 by Liu and co-workers [Liu98] and suggests fast mobility of Ag in samples particularly rich in radiation defects. Assuming that the lattice is destroyed by the implantation damage and thus crystalline anisotropy is absent, another possibility could be the higher atomic density on m-plane which would interact more effectively with the Ag ions which may then accumulate closer to the surface. A major fluctuation on the current density during implantation may also account for this feature. The damage profile is very similar to that observed for the 6×10^{16} cm^{-2} implantations, but with amorphization now observed in the entire damaged layer in c-cut samples.

To recover from the implantation damage and stabilize the implanted system, thermal annealings were performed. Since for higher concentrations it is more likely that the implanted ions precipitate in small clusters [Far90], the annealings were performed only for the highest implanted fluence (1×10^{17} cm^{-2}). Figure 4.48 shows the RBS-C spectra obtained after annealing in air at 1073 K and 1273 K for one hour of c- and m-cut samples implanted with 1×10^{17} cm^{-2} Ag ions.

In the case of c-cut sapphire, the 1073 K annealing produces a narrowing of the Ag profile (Figure 4.48b), from 45 nm to 35 nm, the silver concentration rising to about 30 %, accompanied with some in diffusion, revealed by the development of a small tail into lower energies, and out diffusion since the maximum concentration is found somewhat closer to the surface than R_p. Significant damage recovery occurs, the amorphized layer thinning to 100 nm. This hints at the coalescence of the silver precipitates driven by the matrix recovery. No loss of Ag was measured at this stage.

This annealing has a different impact in m-cut samples where a 78 % loss of the implanted silver is observed, distributed in a nearly rectangular profile, with 100 nm and about 1.9 at. % of silver. No significant damage recovery occurs on the host matrix (Figure 4.48e). The absence of response of sapphire means that the energy supplied was essentially used in the silver diffusion and evaporation processes. Oxide formation and decomposition may also occur since silver oxides can form during this annealing in air. These are known to be unstable at T > 733 K, and, should they form at the surface, providing another means for loss of silver (cf. Table 4.26).

At 1273 K an almost complete crystalline recovery of the host matrix is produced in c-cut samples (χ_{min} = 5 % at the surface, χ_{min} = 15 % in deep regions), accompanied by the loss of 91 % of the implanted Ag, with no significant channelling effect in the silver profile, still Gaussian (FWHM of 60 nm) but peaking around 75 nm, with 1.7 at. % (Figure 4.48c). The loss of Ag may again be due to direct evaporation and/or oxide formation followed by evaporation, the remaining (in deeper regions) silver pinned to unannealed defects.

Similar loss (90 %) is also observed for m-cut samples (Figure 4.48f), with no channelling effect in the Ag profile, which is nearly rectangular, with about 100 nm and average 0.8 at. % of silver. In this case, the crystalline recovery is much slower, the damage decreasing slightly to 100 nm with only χ_{min} = 60 % channelling in the bulk beyond the damage region. This highly disordered state may be the result of fast evaporation of Ag oxides.

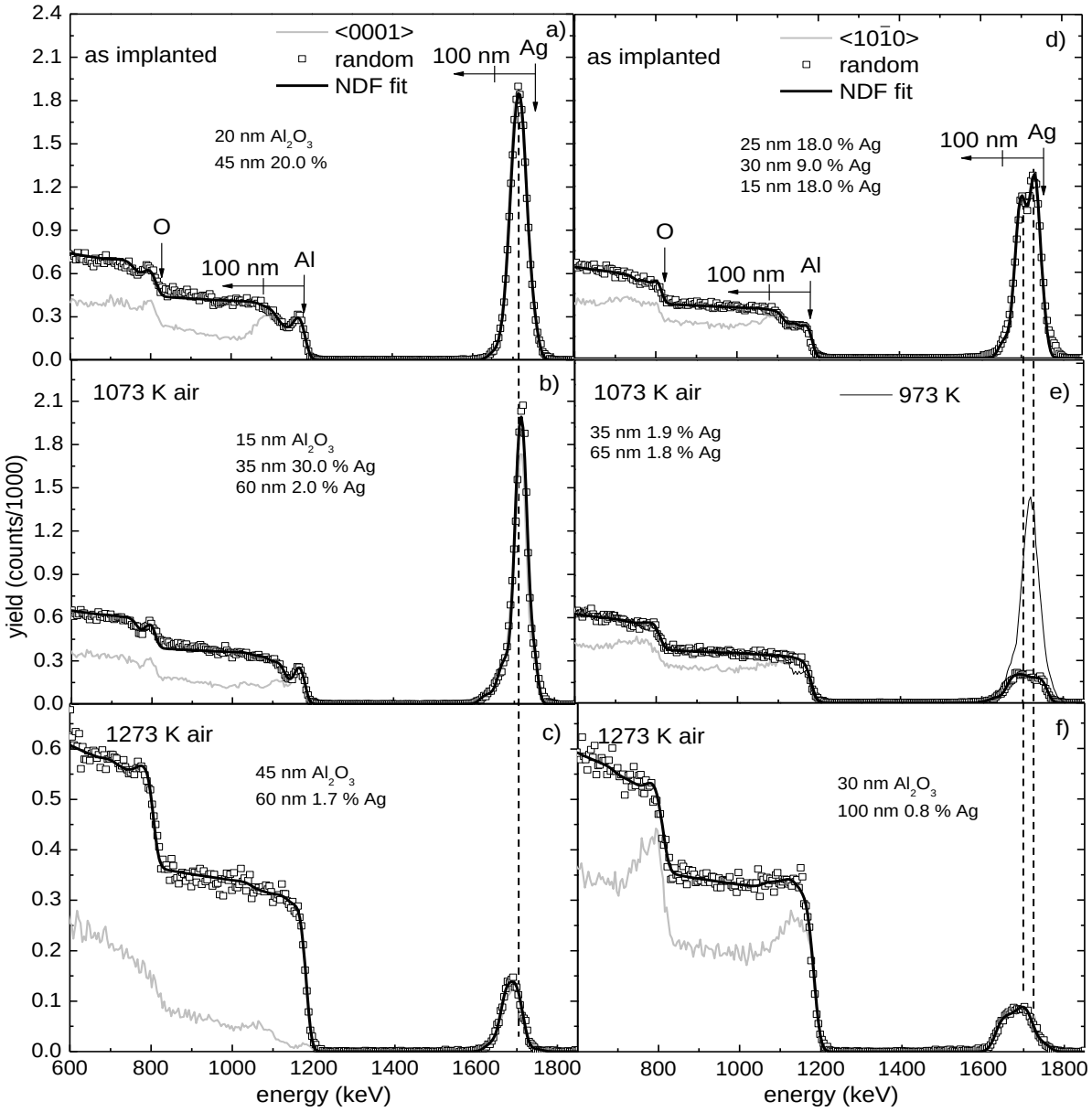

Figure 4.48 – RBS-C spectra of c-cut (left-hand side) and m-cut (right side) sapphire implanted with 1×10^{17} cm^{-2} 160 keV Ag^{+}: a) and d) as implanted; b) and e) after annealing in air at 1073 K; c) and f) after annealing in air at 1273 K. All random spectra are fitted with NDF code.

Given the strong loss of Ag observed at 1073 K in m-cut samples, an annealing step was performed at 973 K, and included in *Figure 4.48*e. At this stage the Ag redistribution occurs, the Ag profile changes from bimodal

to near Gaussian shaped, and a 10 % loss of Ag is observed. This profile peaks in the same region of the topmost peak of the as implanted sample, which implies out diffusion. This redistribution occurs impelled by the crystalline recovery of the matrix, as revealed by the step in the Al profile which is found closer to the surface. The stability of these systems is thus below 1273 K for c-cut samples and 1073 K for m-cut samples.

Similar annealings were performed in vacuum conditions. Figure 4.49 shows the RBS-C spectra obtained at 1073 K and 1273 K for c- and m-cut samples.

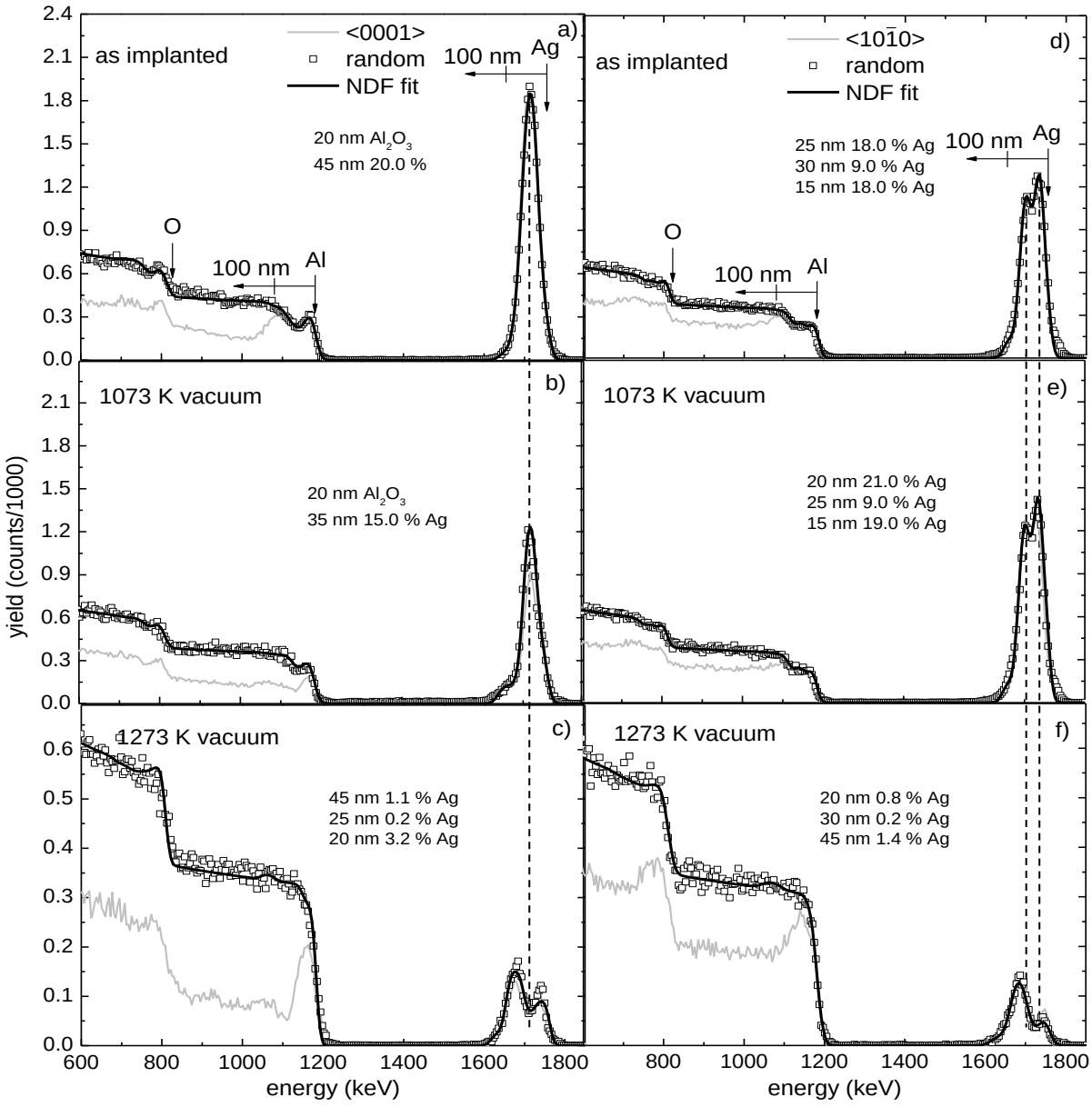

Figure 4.49 – RBS-C spectra of c-cut (left-hand side) and m-cut (right side) sapphire implanted with 1×10^{17} cm^{-2} 160 keV Ag^{+}: a) and d) as implanted; and after annealing in vacuum at: b) and e) 1073 K; c) and f) 1273 K (note the scale difference). All random spectra are fitted with NDF code.

After annealing at 1073 K significant damage recovery occurs for c-cut samples (Figure 4.49b). This effect in the host matrix is more intense than that observed in the 1073 K annealing in air, namely in the topmost layer. Moreover, in this case there is a loss of silver, around 41 %. This is due to easier silver evaporation in this low pressure atmosphere. No loss of silver is observed for m-cut samples (Figure 4.49e), to which this annealing temperature

and atmosphere seem to produce little effect: the RBS-C spectra are similar to those obtained after implantation, with some thinning of the profile and increase in Ag maximum concentration, as concluded from theoretical RBS spectra for a simulated composition, obtained with NDF code. This supports some stabilizing thermal effect during implantation, used to explain the double peak feature obtained after implantation and the need of oxide formation for significant loss of Ag.

After annealing at 1273 K a double peaked structure is observed in the Ag profile for both c- and m-cut samples (Figure 4.49c and Figure 4.49f, respectively), with maxima found at 20 nm and 80 nm and at 10 nm and 75 nm, respectively. The retained fluence drops by 87 % for c-cut samples and 90 % for m-cut sapphire, as in the case of the annealing in air. The crystalline recovery is again more evident for c-cut samples, even if a large damage concentration (dechanneling ratio over 60 %) is still present in the topmost 50 nm.

These results suggest that at 1073 K the presence of oxygen could help both the recrystallization of the matrix (which may then contribute to drive the non soluble silver ion to the surface) and favour the loss of silver through oxide formation and decomposition since oxides of this element are known to be unstable above 733 K.

Since major silver loss occurs at 1273 K in similar way irrespective of the atmosphere, it indicates that if there is any oxide formation the surface out diffusion and evaporation is also as effective as oxide formation and sublimation to account for the losses of Ag. Diffusion processes into the matrix are ruled out both by PIXE measurements and also by the absence of an Ag peak tail to lower energies, i.e. to larger depths. Table 4.28 and *Table 4.29* summarize the RBS-C results for annealed c- and m-cut samples, respectively.

Table 4.28 – RBS-C results of c-cut samples implanted with 1×10^{17} cm^{-2} Ag ions

sample	as imp.	1073 K air	1273 K air	1073 K vac.	1273 K vac.
host matrix					
max. damage depth (nm)	0 – 130	0 – 100	-	0 – 50	0 – 50
χ_{min} (%)	100	90	5	65	60
damage extension (nm)	130	100	-	50	50
E_D (10^{22} keV cm^{-3})	123	-	-	-	-
deep region χ_{min}	33	30	15	30	25
implanted profile					
max. conc. depth (nm)	40	35	75	40	20/60
χ_{min} (%)	100		100	100	100
retained fluence (10^{15} cm^{-2})	-	100	10	65	14
fluence loss (%)	-	0	91	41	87
FWHM (nm)	45	35	60	35	45/20
max. conc. (at. %)	20.0	30.0	1.7	15.0	1.1/3.2

Table 4.29 – RBS-C results of m-cut samples implanted with 1×10^{17} cm^{-2} Ag ions.

sample	as imp.	1073 K air	1273 K air	1073 K vac.	1273 K vac.
host matrix					
max. damage depth (nm)	0 – 130	0 – 100	50	0 – 100	0 – 100
χ_{min} (%)	100	100	75	100	80
damage extension (nm)	130	100	100	110	80
E_D (10^{22} keV cm^{-3})	123	-	-	-	-
deep region χ_{min}	65	65	60	65	60
implanted profile					
max. conc. depth (nm)	15/60	10 – 90	40 – 120	10/55	10/75
χ_{min} (%)	100	100	100	100	100
retained fluence (10^{15} cm^{-2})	-	22	10	100	10
fluence loss (%)	-	78	90	0	90
FWHM (nm)	25/15	100	100	20/15	20/45
max. conc. (at. %)	18.0/18.0	1.9	0.8	21.0/19.0	0.8/1.4

The samples implanted with the highest fluences were further analysed with XRD. *Figure 4.50*a shows the XRD spectra of the c-cut samples implanted with the highest fluence, after implantation and after annealing at 1273 K for one hour in air or vacuum.

After implantation there are no reflections related to the presence of metallic Ag precipitates, indicating either that these precipitates do not exist or are present in small sizes or in an highly defective phase.

After annealing in air only a small peak around 39.4º appears, possibly related to the presence of a small amount of a silver oxide, represented with black dots (tetragonal $<004>_{AgO}$ // $<0001>_{sapp}$ or monoclinic Ag_2O_2 or AgO with $<\bar{2}02>$ // $<0001>_{sapp}$).

After annealing in vacuum, on the other hand, the presence of metallic Ag is evident, in well defined, sharp, diffraction peaks at 38.45º, 44.67º, 64.56º and 82.39º, consistent with Ag^0 with 0.405 nm lattice constant, in large precipitates (50 nm to 55 nm, compatible with the measured thickness with RBS) mainly with $<111>_{Ag}$ // $<0001>_{sapp}$ but also with <200> or <220> // $<0001>_{sapp}$ epitaxial relations. This latter texture may prevent the observation of relevant channelling effects with RBS-C.

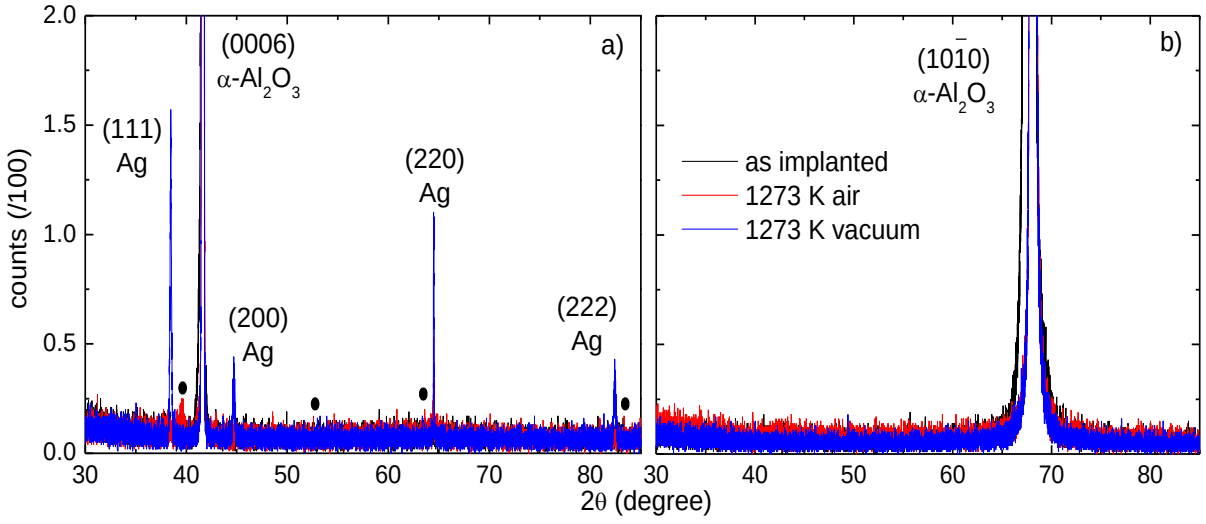

Figure 4.50 – XRD spectra of sapphire samples implanted with 1×10^{17} cm^{-2} as implanted and after annealing at 1273 K in air or vacuum: a) c-cut and b) m-cut samples.

The oxides of silver are highly unstable. Table 4.30 displays the enthalpy of formation of Al and Ag oxides. From these values Ag_2O is expected to prevail as compared to AgO. Moreover, as oxygen is consumed in the more favourable process of alumina formation, low content oxides are easier to form.

Table 4.30 – Formation enthalpy of Al and Ag oxides ($-\Delta H^0_{298}$), kJ mol^{-1}.

Al_2O_3	AgO	Ag_2O
1676	11.4	31.0

The XRD spectra of m-cut samples in similar conditions shows only sapphire reflections in any case (*Figure 4.50*b). Since at this annealing stage these samples retain a similar amount of silver as compared to c-cut samples, the absence of silver related reflections reveal the random orientation of subnanometre precipitates. This is consistent with the disorder observed in the surface region of these samples in the corresponding RBS-C spectra, higher in concentration and extension than that observed in c-cut samples. The width of reflections of sapphire decreases after annealing as a result of the recrystallization process observed by RBS-C. Table 4.31 summarizes the results obtained with XRD on Ag implanted samples.

Table 4.31 – XRD results of sapphire c- and m-cut samples implanted with 1×10^{17} cm^{-2} Ag ions.

sample	2θ	phases	size (nm)	calculated and tabulated lattice dimensions (nm)	PDF card
c, 1.0×10^{17} cm^{-2} as imp.	-	-	-	-	-
1273 K air	39.53	AgO (004)	-	-	01-084-1108
1273 K vacuum	38.49 44.69 64.50	Ag (111) Ag (200) Ag (220)	50 50 55	0.405 / 0.408 0.405 / 0.408 0.408 / 0.408	01-089-3722
m, 1.0×10^{17} cm^{-2} as imp.	-	-	-	-	-
1273 K air	-	-	-	-	-
1273 K vacuum	-	-	-	-	-

4.4.2.1.2 Optical studies

4.4.2.1.2.1 As implanted

The samples implanted up to 1×10^{16} cm^{-2} remain nearly transparent, which translates by the absence of optical absorption in the visible region of the spectrum, cf. *Figure 4.51*. Regarding radiation defects, the characteristic absorption around 200 nm to 250 nm is visible only for the lower fluences, being very similar for 1×10^{15} cm^{-2} and 1×10^{16} cm^{-2} implantations. *Table 4.32* shows the F-type centre concentration after implantation of the lower fluences. As the fluence increases not only the SPR band develops but also interband transitions appear which in the case of silver occur at $E > 3.9$ eV thus overshadowing the defect related bands.

The SPR band is a known mark of the presence of silver aggregates and shows that the threshold for colloid formation is in the range of 1×10^{16} cm^{-2} to 6×10^{16} cm^{-2} under these experimental conditions. By applying the same (linear) method presented for copper implantation, the threshold fluence (F_t) for precipitate formation is

estimated to be very similar for both types of samples: 1.9×10^{16} cm^{-2} and 2.3×10^{16} cm^{-2} for c- and m-cut samples, respectively. This threshold is lower than that observed for copper implantations (~6×10^{16} cm^{-2}). This is probably related to the rate of formation of optically active precipitates, which is faster in the case of silver, as compared to copper. The larger and electron richer silver ions will probably exhibit plasmon resonance with a lower number of ions even in a similar sized aggregate.

Table 4.32 – F-type centre concentration of sapphire implanted with silver.

sample	experimental data				F-centre concentration	
	λ (nm)	FWHM (nm)	U (eV)	u (cm^{-1})	N_0 ($\times10^{16}$ cm^{-3})	$N_{0;imp}$ ($\times10^{19}$ cm^{-3})
1×10^{15} cm^{-2}	204.22	22.30	0.66	5.36	1.51	7.55
	224.65	34.19	0.84	1.54	1.09	5.45
	258.07	47.87	0.90	0.78	0.59	2.95
1×10^{16} cm^{-2}	204.22	21.37	0.64	4.46	1.22	6.10
	224.02	35.84	0.89	1.82	1.36	6.80
	258.07	39.18	0.73	0.52	0.32	1.63

As the fluence increases the SPR band at 460 nm becomes stronger and shifts towards longer wavelengths, probably due to the increase of the number and average size of the precipitates (up to *r* = 9 nm, cf. Figure 4.51b).

There is a clear difference between c-cut samples and m-cut samples. The former show a larger red-shift, up to 40 nm, as the fluence increases from 6×10^{16} cm^{-2} to 1×10^{17} cm^{-2}, while m-cut samples shift by only about 10 nm in similar conditions. For these shifts there is only a minor contribution – of about 3 nm – from the birefringence of sapphire.

MiePlot code estimate for the SPR band extinction of silver spheres with (monodispersed) radius from 1 nm to 29 nm is shown in *Figure 4.51*b. From these simulations we observe the formation of (dipolar) SPR band peaking at 436 nm for *r* = 1 nm and a red shift of this band to 508 nm when *r* = 29 nm. Moreover, when *r* = 9 nm the SPR intensity reaches its maximum (around 444 nm). At this stage the dipole SPR band starts to decrease in intensity and broadening, while quadrupole absorption at 410 nm starts to develop, also red shifting to 424 nm for *r* = 29 nm. The position of the absorption maxima was used to estimate the size of the precipitates, as previously with copper and nickel.

It is worth noting that the feature assigned to the SPR band may also be, to some extent, due to F_2^{2+}, absorbing at 443 nm, as observed by Mohanty and co-workers [Moh03]. However, our work with gold or copper implanted sapphire does not show evidence for such centre and only the SPR band is visible. The larger absorption band presented by the m-cut sample implanted with 1×10^{17} cm^{-2} may be due to the bimodal concentration distribution of Ag observed in Figure 4.49d: the presence of two different size distributions results in two overlapping absorption bands. Another possibility for a double peaked SPR is the presence of non-spherical precipitates with multiple dipole resonances or even quadrupole resonances [Boh98], which are expected to appear when *r* > 9 nm (cf. *Figure 4.51*b). The red shift with increasing fluence can also be understood if one considers a possible refraction index gradient after implantation (either from the damage in the substrate or due to the presence of Ag ions that can lower the refractive index).Table 4.33 summarizes the optical features of the as implanted samples.

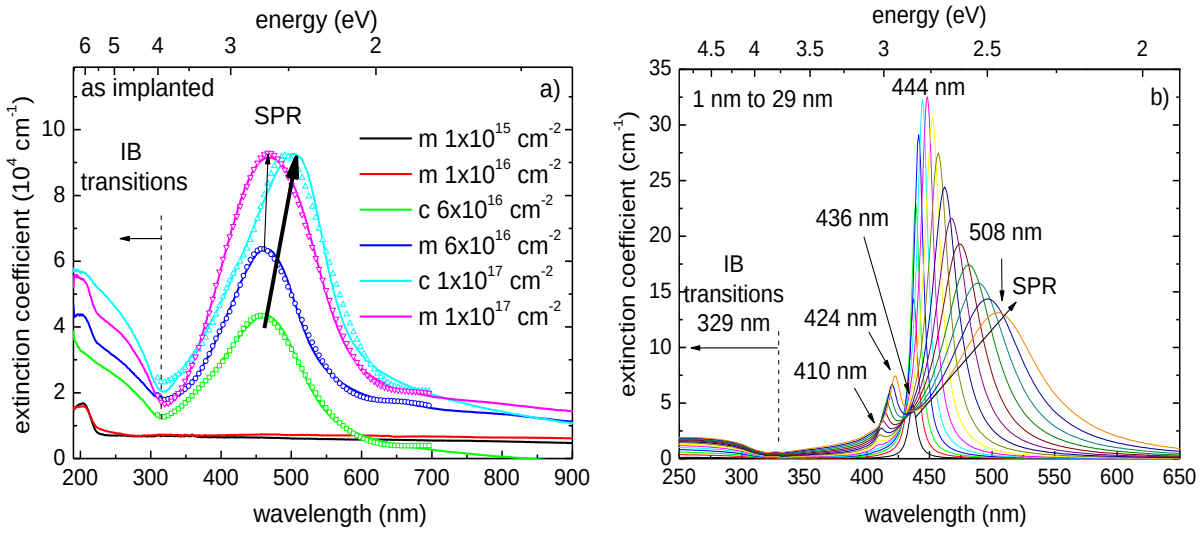

Figure 4.51 – a) optical absorption spectra of c- and m-cut sapphire after implantation of silver up to 1×10^{17} cm^{-2}, with SCOUT code fit of the SPR band; b) MiePlot simulations of Ag spherical particles with 1 nm to 29 nm radius.

Table 4.33 – Optical features of Ag as implanted samples, with MiePlot code size estimate.

sample	SPR			MiePlot
	peak (nm)	FWHM (nm)	area	radius(nm)
m, 6.0×10^{16} cm^{-2}	462	114	82	17
m, 1.0×10^{17} cm^{-2}	471	142	171	20
c, 6.0×10^{16} cm^{-2}	458	127	69	15
c, 1.0×10^{17} cm^{-2}	402 498	74 120	17 136	27

4.4.2.1.2.2 After annealing

The annealing in air causes the SPR band to vanish in all samples implanted with 1×10^{17} cm^{-2} as shown in Figure 4.52, probably due dissolution of clusters or formation of mixed silver oxides in the cubic γ-Al_2O_3 phase present at this temperature range (1073 K to 1273 K) [Far90] and the samples become greyish transparent.

The standard silver oxides AgO or Ag_2O are not stable above 733 K, as previously mentioned, but may form during cooling down of the samples. However, other compounds or non-stoichiometric oxides may be present. In fact, Menning and co-workers [Men97] observed through HRTEM the presence of polycrystalline Ag_xO_y nanoparticles that discoloured their samples. Oxide formation decreases SPR.

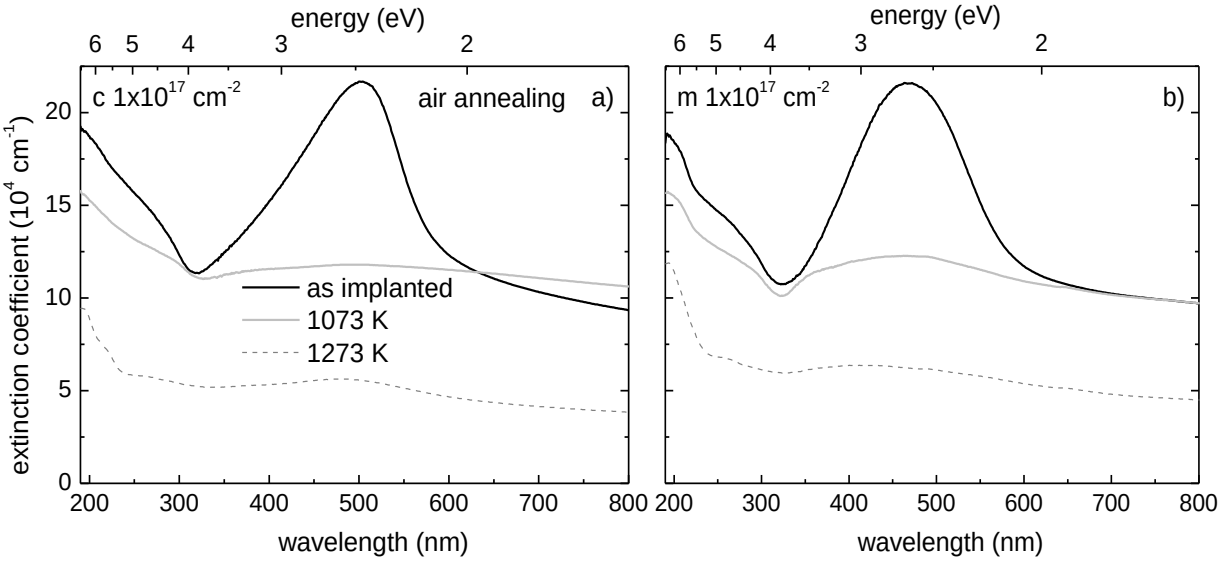

Figure 4.52 – Optical absorption spectra of sapphire implanted with 1×10^{17} cm^{-2} Ag$^+$ ions, as implanted and after annealing at 1073 K and 1273 K for one hour in air: a) c-cut samples and b) m-cut samples.

On the other hand, the samples annealed at 1073 K in vacuum present a strong absorption, in particular the one implanted with the highest fluence, *Figure 4.53*. Further annealing promoted the loss of silver (shown in the RBS spectra, Figure 4.48) which explains the strong decrease of the optical absorption at 1273 K. Most likely the small quantity of silver now present is highly dispersed in sub-nanometre sized particles. The F centres signal also decreases. The SPR red-shift is observed up to 1073 K and the samples acquire greenish reflections. The FWHM slightly increases also. This may indicate the growth of the precipitates at this stage. Table 4.34 and Table 4.35 summarize the OA results on the annealed c- and m-cut samples, respectively.

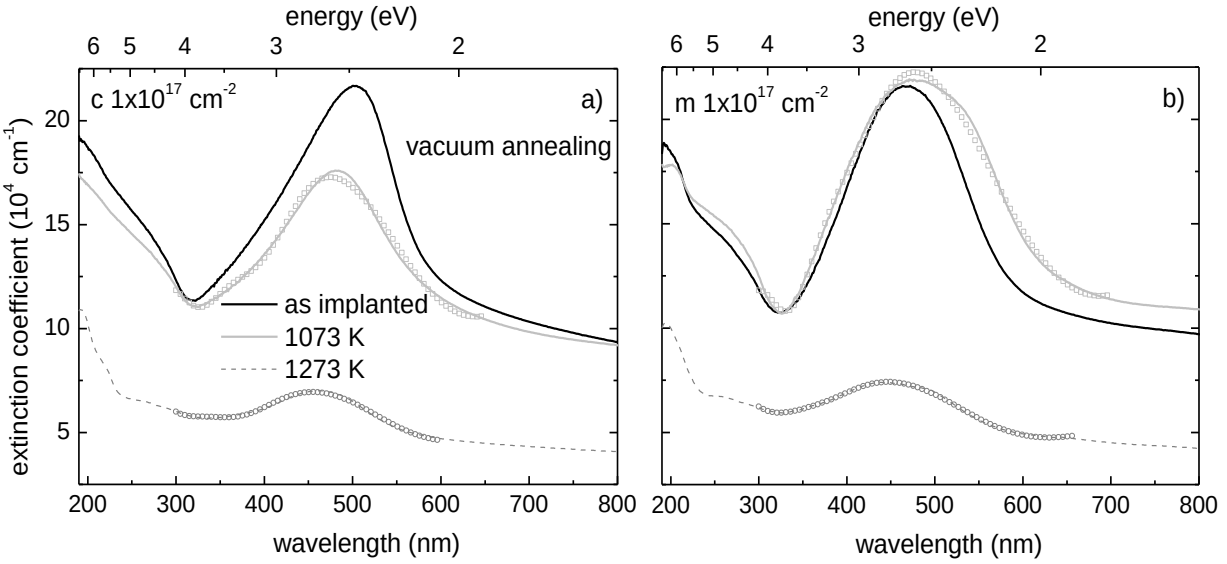

Figure 4.53 – Optical absorption spectra of sapphire implanted with 1×10^{17} cm^{-2} Ag$^+$ ions, as implanted and after annealing at 1073 K and 1273 K for one hour in vacuum: a) c-cut samples and b) m-cut samples, with SCOUT code fit of the SPR band.

Table 4.34 – Optical features of c-cut samples implanted with 1×10^{17} cm^{-2} Ag ions, as implanted and annealed in vacuum up to 1273 K, with MiePlot size estimate.

sample	SPR			MiePlot
	peak (nm)	FWHM (nm)	area	radius (nm)
as implanted	402 498	74 120	17 36	27
1073 K vacuum	477 500	119 205	63 44	22 27
1273 K vacuum	466	114	22	18

Table 4.35 – Optical features of m-cut samples implanted with 1×10^{17} cm^{-2} Ag ions, as implanted and annealed in vacuum up to 1273 K, with MiePlot size estimate.

sample	SPR			MiePlot
	peak (nm)	FWHM (nm)	area	radius (nm)
as implanted	471	142	171	20
1073 K vacuum	419 504	92 153	42 167	29
1273 K vacuum	411 479	80 112	7 21	22

Regarding SCOUT code simulations and fits of the experimental data, the percolation strength increases from the as implanted stage to the first annealing step at 1073 K in vacuum, as resumed in *Table 4.36* and *Table 4.37*, for c- and m-cut samples, respectively. These simulations followed the same method presented for copper and zinc systems. This strengthening of percolation with the implantation fluence is the result of the increase of the average size of the precipitates which are brought closer and interact. The percolation strength then decreases after annealing up to 1273 K as a result of the loss of silver which decrease the average dimensions of the precipitates and therefore its interactions, possibly in an inverse Ostwald ripening process where the outer atoms of a large precipitate are expelled and form smaller precipitates that diffuse out and eventually evaporate. M-cut samples show similar behaviour.

Table 4.36 – SCOUT fit parameters of c-cut samples implanted with Ag ions, as implanted for the higher fluences and after annealing up to 1273 K in vacuum of the highest fluence.

sample	volume fraction (%)	percolation	thickness (nm)	damping constant (cm^{-1} / Hz)	size 1 (nm)	size 2 (nm)
6×10^{16} cm^{-2}	0.16	0.35	58	2321 6.96×10^{13}	31	19
1×10^{17} cm^{-2}	0.30	0.38	73	2435 7.30×10^{13}	29	30
1073 K vacuum	0.32	0.20	82	2243 6.73×10^{13}	33	35
1273 K vacuum	0.10	0.14	49	3857 1.16×10^{14}	15	14

Table 4.37 – SCOUT fit parameters of m-cut samples implanted with Ag ions, as implanted for the higher fluences and after annealing up to 1273 K in vacuum of the highest fluence.

sample	volume fraction (%)	percolation	thickness (nm)	damping constant (cm^{-1} / Hz)	size 1 (nm)	size 2 (nm)
6×10^{16} cm^{-2}	0.11	0.18	74	2025 3.64×10^{13}	38	22
1×10^{17} cm^{-2}	0.22	0.29	51	2612 7.84×10^{13}	26	19
1073 K vacuum	0.20	0.25	55	1722 5.17×10^{13}	51	20
1273 K vacuum	0.08	0.14	66	3986 1.20×10^{14}	15	18

These fits imply the modification of the optical constants of silver, as presented in Figure 4.54a. The dielectric constants of the Ag model needed to fit the full spectrum are qualitatively similar to those from bulk material. However, ε_1 is larger except at the cross over at 300 nm while ε_2 is comparable to the bulk data except in the UV region, where it assumes lower values. Regarding the matrix, *Figure 4.54*b, there are obvious differences, due to the inclusion of a fraction of silver. As the volume fraction *f* of the implanted material increases the maxima of the dielectric constants red shifts.

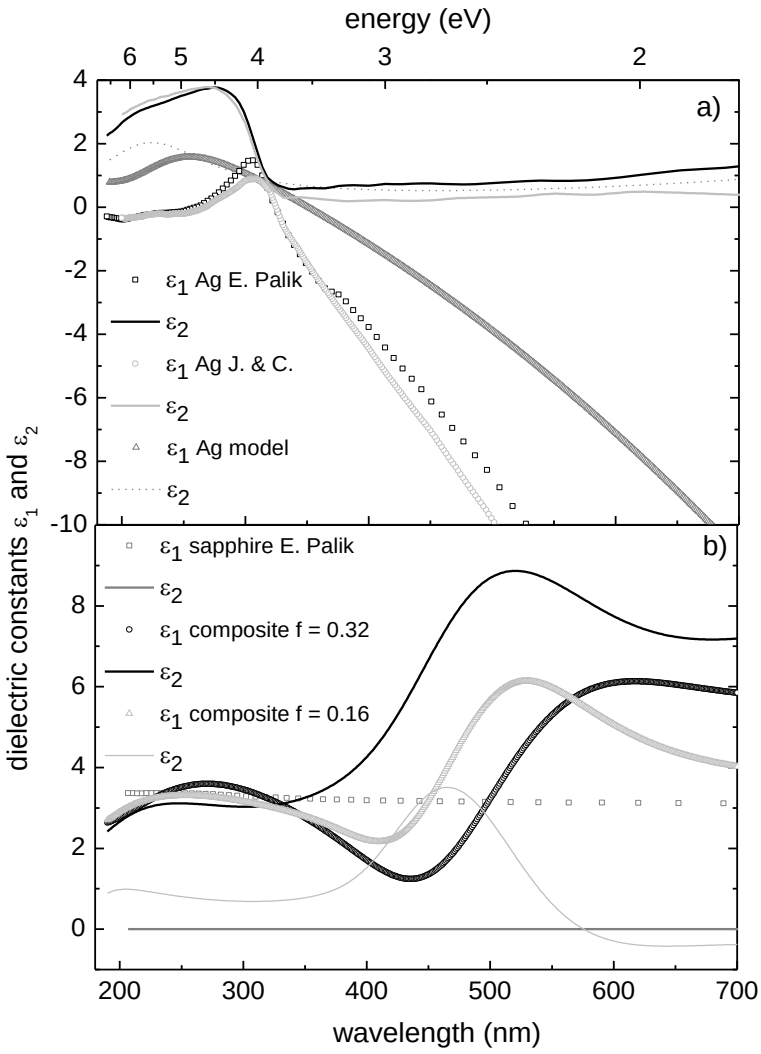

Figure 4.54 – Dielectric constants of a) silver and of b) sapphire and those from the effective medium model used.

4.4.3 Au implantation

In this section we discuss the optical and structural properties of single crystalline α-Al_2O_3 implanted with high fluences of Au ions, aiming at producing structures with SPR absorption.

Colourless transparent c- and m-cut sapphire samples were implanted at RT with 160 keV $^{197}Au^+$ ions with fluences up to 7×10^{16} cm^{-2}. To recover from the implantation damage thermal annealings were carried out at 1073 K and 1273 K for 1 hour in air and in vacuum. RBS, RBS-C, XRD, AFM and OA were used to characterize the systems formed.

The effects of the implantation fluence, crystalline orientation of the samples and annealing parameters in the formation of the new compounds were studied and correlated with the optical behaviour of the samples.

4.4.3.1 Results and discussion

4.4.3.1.1 Structural studies

The RBS-C spectra of Figure 4.55a (c-cut sample) and Figure 4.55b (c- and m-cut samples) were recorded after implantation of 1×10^{16} cm^{-2} and 5×10^{16} cm^{-2}, respectively. Already at the lowest fluence implantation the RBS-C spectrum in the region of the Al sublattice reveals an amorphous implanted surface layer, to depths extending to 80 nm. E_D is now 2.0×10^{23} keV cm^{-3}. At higher depths the χ_{min} is about 15 %, this low value resulting from the thin damaged layer. Regarding the implanted species, the spectra reveal a Gaussian shaped Au profile (where no channelling is observed) centred at 25 nm (where the Au concentration is 3.3 at. %) and with FWHM of 30 nm. The R_p is in poor agreement with SRIM prediction of 37 nm while the FWHM is almost twice the expected value (17 nm).

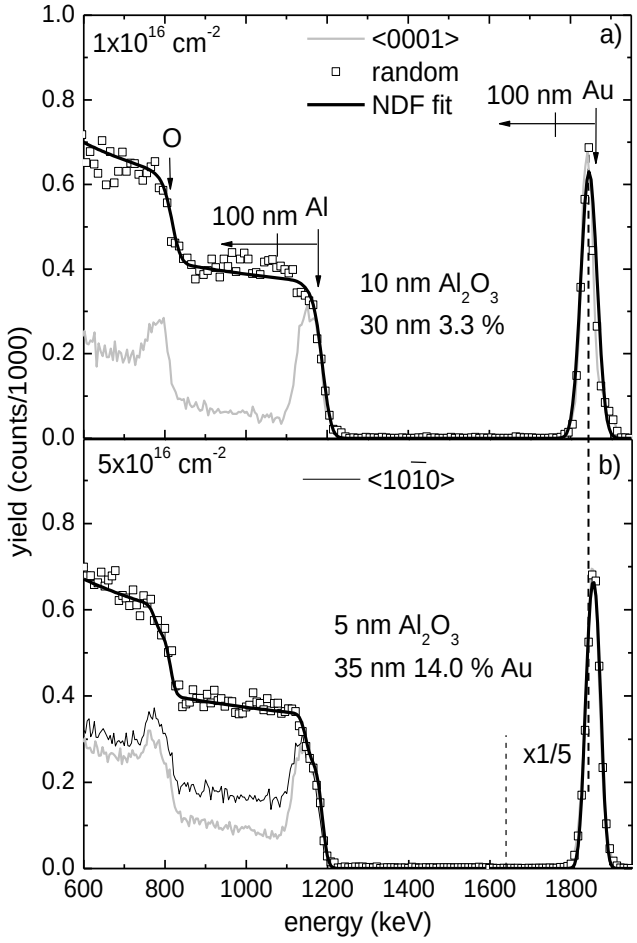

Figure 4.55 – RBS-C spectra of c-cut sapphire as implanted with Au ions: a) 1×10^{16} cm^{-2} and b) 5×10^{16} cm^{-2} (for c- and m-cut samples), with NDF code composition fit.

The target densification may explain the lower R_p while RED, since the Au ions are placed in an amorphized layer, or even self-annealing during implantation, may justify the larger FWHM, as was the case of silver.

For the 5×10^{16} cm^{-2} implantation, in the case of c-cut samples the damage region extends to 100 nm, being somewhat larger for m-cut samples (~110 nm), as shown in Figure 4.55b. The dechanneling yield for E < 1100 keV is also higher for the latter (χ_{min} = 45 % vs. χ_{min} = 25 % for c-cut samples), m-cut samples retaining more damage as previously seen in other systems.

The Gaussian shaped Au profile now peaks at 20 nm but with 35 nm of FWHM. The step in the edges of the Al surface barrier in the RBS-C spectra is due to the presence of the implanted Au (14.0 at. % for c- and m-cut samples). The damage energy density is 8.0×10^{23} keV cm^{-3} and 7.3×10^{23} keV cm^{-3} for c- and m-cut samples, respectively.

A higher fluence was implanted on c-cut samples, 7×10^{16} cm^{-2}. The corresponding RBS-C spectra is shown in *Figure 4.56*a. The damage extension increases to 110 nm at this stage, where $E_D = 1.0\times10^{24}$ keV cm^{-3}, and the dechanneling for E < 1000 keV rises to about 50 %. The Au profile remains nearly Gaussian, with FWHM of 35 nm, and peaks again at 30 nm depth, where the Au concentration reaches 25 at. %.

Table 4.38 resumes the results obtained with RBS-C on the as implanted samples.

Table 4.38 – RBS-C results of sapphire samples as implanted with 160 keV Au ions.

sample	c, 1×10^{16} cm^{-2}	c, 5×10^{16} cm^{-2}	m, 5×10^{16} cm^{-2}	c, 7×10^{16} cm^{-2}
host matrix				
max. damage depth (nm)	0 – 80	0 – 100	0 – 110	0 – 110
χ_{min} (%)	100	100	100	100
damage extension (nm)	80	100	110	110
E_D (10^{22} keV cm^{-3})	20	80	73	102
deep region χ_{min} (%)	15	25	45	50
implanted profile				
max. conc. depth (nm)	25	20	20	30
χ_{min} (%)	100	100	100	100
FWHM (nm)	30	35	35	35
max. conc. (at. %)	3.3	14.0	14.0	25

The samples implanted with higher fluences (7×10^{16} cm^{-2} and 5×10^{16} cm^{-2} for c- and m-cut samples, respectively) were annealed at 1073 K and 1273 K for one hour to study the evolution and stability of the Au:Al_2O_3 system. The RBS-C spectra of the samples annealed in air are shown in *Figure 4.56*.

In the case of c-cut samples, after 1073 K annealing in air the Au profile narrows slightly (from 35 nm to 30 nm), while moving to the surface, R_p = 25 nm, with similar concentration of the as implanted state (*Figure 4.56*b). There is a small crystalline recovery, the amorphized region extending now to 100 nm.

Further annealing at 1273 K results in substantial crystalline recovery of the matrix (the damage extension decreases to 60 nm) and some channelling (10 %) develops on the Au profile, which has FWHM of 30 nm and peaks at the surface region, as shown in *Figure 4.56*c. Detailed angular scans reveal some alignment of the Au phase with the host matrix (inset in *Figure 4.56*c).

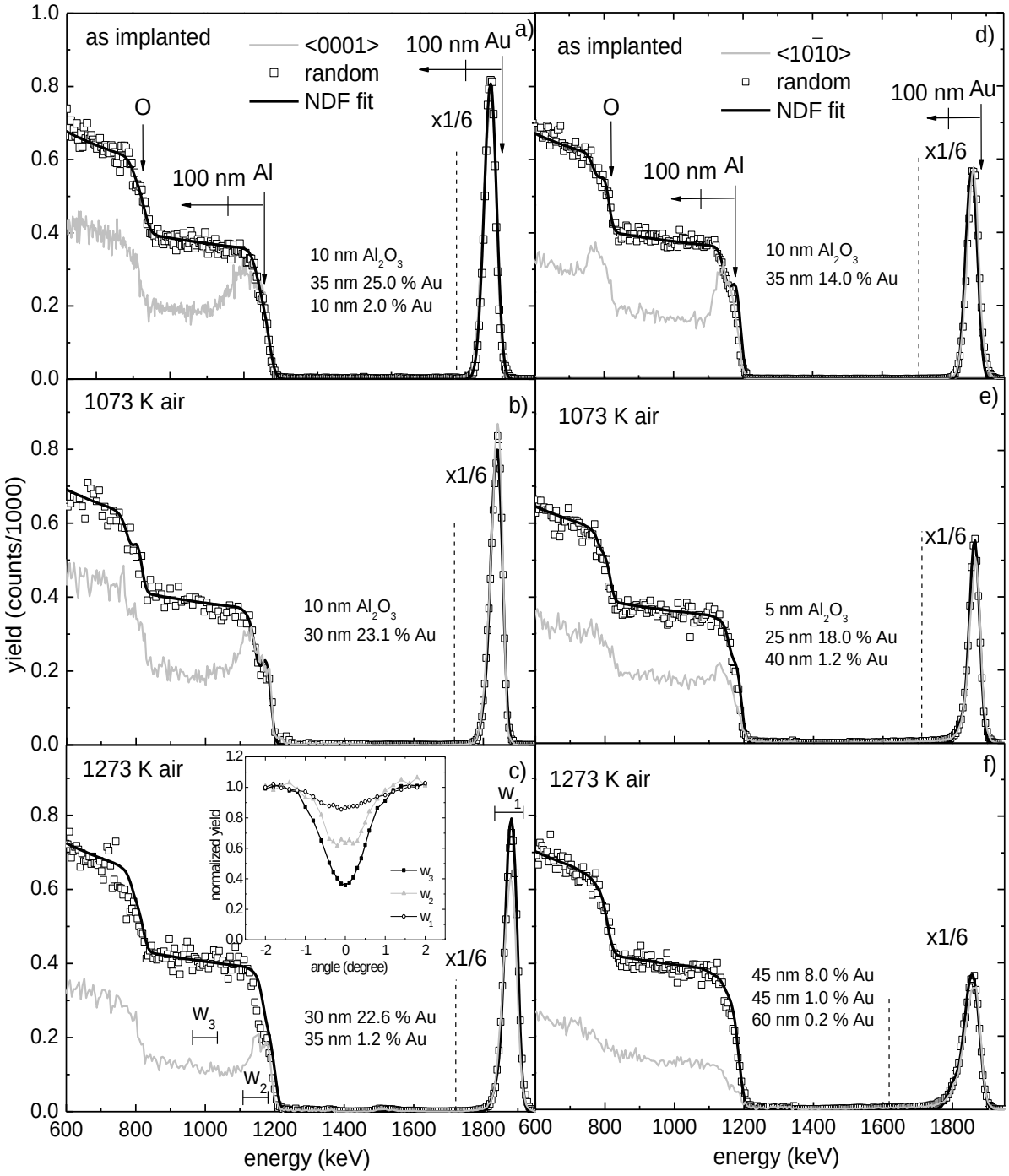

Figure 4.56 – RBS-C spectra of c- and m-cut α-Al_2O_3 samples implanted with 7×10^{16} cm^{-2} and 5×10^{16} cm^{-2}, respectively: a) and d) as implanted; b) and e) after annealing in air at 1073 K and c) and f) ditto at 1273 K, with NDF code fit compositions.

On the other hand, m-cut samples show already crystalline recovery at 1073 K (*Figure 4.56*e). The maximum damage is found at 40 nm, where χ_{min} drops to 60 %. The damage extension also decreases to about 60 nm. The Au profile remains Gaussian shaped but with 25 nm of FWHM, peaking somewhat closer to the surface (~20 nm). Since no loss of Au is observed after this annealing, the maximum Au concentration rises to 18.0 at. %.

At 1273 K the crystalline recovery increases and the Au profile enlarges, showing FWHM of 45 nm near the surface, as a result of in and out diffusion (*Figure 4.56*f). At this stage there is a minor loss of Au (ca. 6 %) and

the maximum Au concentration drops to 8.0 at. %. This behaviour, e.g. higher damage recovery and higher mobility on m-cut samples, is again explained by the strong diffusion that occurs along the c-plane which, in these samples, is perpendicular to the surface and hence facilitates the diffusion of matrix elements, promoting the crystalline recovery, and of the implanted species, particularly non-reactive ones, allowing for diffusion processes.

Table 4.39 summarizes the RBS-C findings on the samples annealed in air up to 1273K for one hour.

Table 4.39 – RBS-C results of the samples implanted with Au and annealed in air.

sample	c, 1073 K	c, 1273 K	m, 1073 K	m, 1273 K
host matrix				
max. damage depth (nm)	0 – 80	0 – 30	40	-
χ_{min} (%)	100	100	60	20
damage extension (nm)	100	60	60	-
deep region χ_{min} (%)	50	30	45	35
implanted profile				
max. conc. depth (nm)	25	15	20	20
χ_{min} (%)	100	60	100	100
retained fluence (10^{15} cm^{-2})	70	70	50	47
fluence loss (%)	0	0	0	6
FWHM (nm)	30	30	25	45
max. conc. (at. %)	23.1	22.6	18.0	8.0

The RBS-C spectra obtained after annealing in vacuum conditions are shown in Figure 4.57. Regarding c-cut samples, the annealing at 1073 K (Figure 4.57b) produced significant crystalline recovery, the damaged extension decreasing to about 60 nm. The Au profile still has FWHM of 35 nm but is found closer to the surface. A minor loss of Au (about 7 %) is also detected.

At 1273 K, Figure 4.57c, significant loss (43 %) and in-diffusion of Au is detected, its profile being now 120 nm in FWHM, with about 20 % channelling. In fact, the detailed angular scan, inset of Figure 4.57c, performed along the c-axis reveals the partial alignment of the Au with sapphire. The crystalline recovery is almost complete, with χ_{min} decreasing to about 10 %. Major loss is only achieved after 1573 K in vacuum (not shown).

In contrast, for the m-cut samples, at 1073 K significant damage recovery is observed and some channelling (20 %) already develops on the Au profile, which enlarges slightly and moves towards the surface, as shown in Figure 4.57e. The corresponding angular scan also reveals some alignment of Au with the sapphire matrix (inset of Figure 4.57e).

At 1273 K the crystalline recovery continues (χ_{min} = 25 %) and a major loss (about 86 %) of gold is observed (Figure 4.57f). The remaining Au is distributed in a Gaussian shaped profile, with maximum concentration of 1.9 at. % around R_p.

Table 4.40 summarizes the results obtained with RBS-C in Au implanted c- and m-cut samples annealed in vacuum up to 1273 K for one hour.

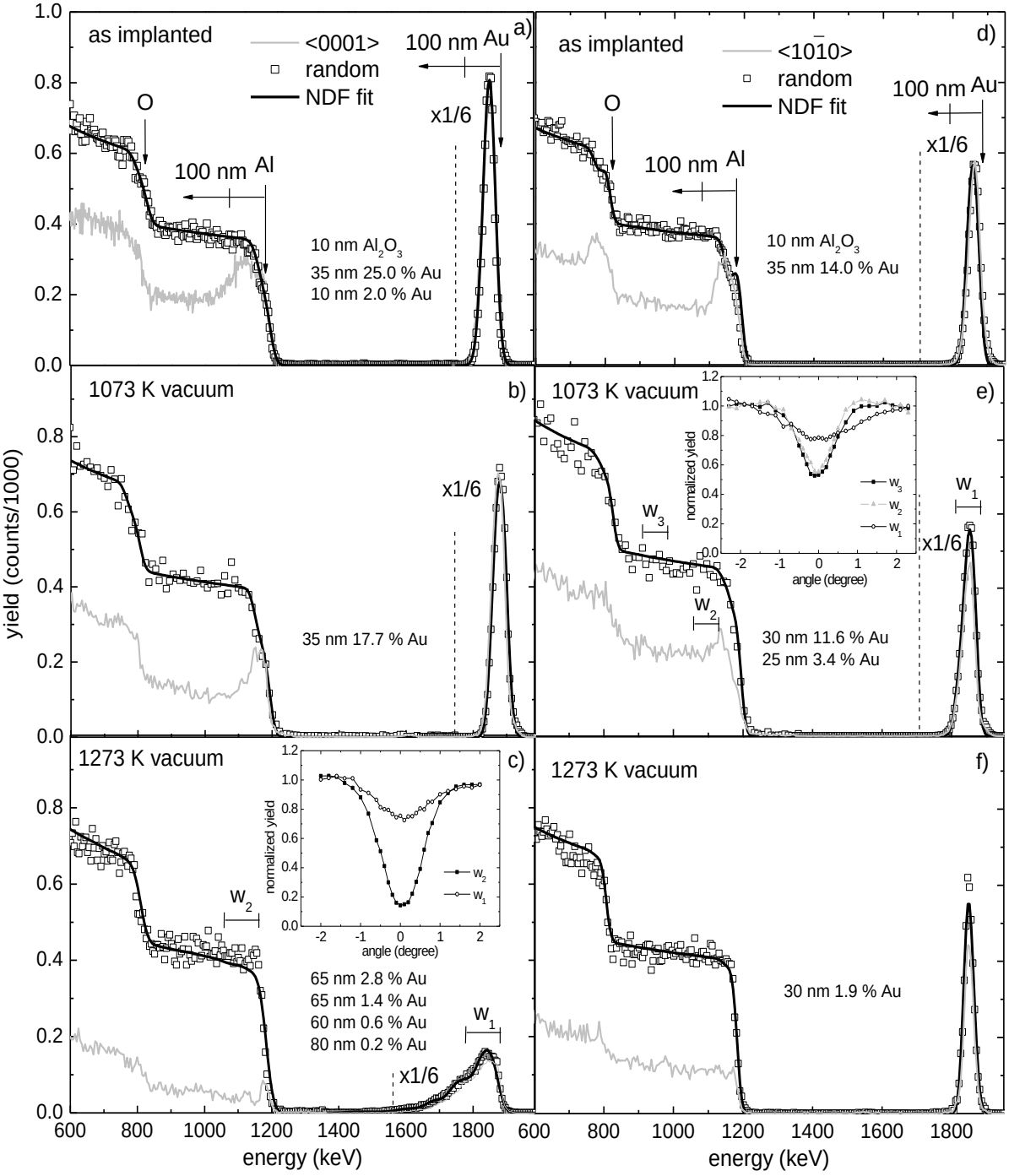

Figure 4.57 – RBS-C spectra of c- and m-cut α-Al_2O_3 samples implanted with 7×10^{16} cm^{-2} and 5×10^{16} cm^{-2}, respectively: a) and d) as implanted; b) and e) after annealing in vacuum at 1073 K and c) and f) ditto at 1273 K, with NDF code fit compositions.

Table 4.40 – RBS-C results of the samples implanted with Au and annealed in vacuum.

sample	c, 1073 K	c, 1273 K	m, 1073 K	m, 1273 K
host matrix				
max. damage depth (nm)	0 – 40	0 – 20	30	-
χ_{min} (%)	100	10	50	30
damage extension (nm)	60	20	80	-
deep region χ_{min} (%)	30	10	50	25
implanted profile				
max. conc. depth (nm)	15	25	15	15
χ_{min} (%)	100	80	80	80
retained fluence (10^{15} cm^{-2})	65	40	48	7
fluence loss (%)	7	43	4	86
FWHM (nm)	35	120	30	30
max. conc. (at. %)	17.7	2.8	11.6	1.9

The samples implanted with the higher fluences and annealed at the highest temperature were subjected to XRD measurements. The XRD spectra on c-cut samples of the as implanted state is shown in Figure 4.58a and reveals the absence of any gold peaks which we take as an indication of the reduced dimensions of the structures formed at this stage, as was the case of silver implantation. After the annealing at 1273 K in air the XRD pattern reveals gold reflections. Furthermore, the spectra indicate that the gold precipitates are mainly aligned with the (111) close packed planes parallel to the matrix c-planes. The size of the precipitates is estimated to be about 35 nm and lattice constant *a* varying between 0.407 nm and 0.408 nm. This is also in accordance with the work of Ohkubo and co-workers [Ohk88], confirming that the shape of nanocrystals is dictated by crystal habits created in the host material during implantation and assisted by a RED process. Similar findings were recorded in Pt implanted sapphire [Alv99]. Moreover, some reflections, marked in the spectra with a black dot, appear and that may be ascribed to transition aluminas, e.g. {111} family from γ-Al_2O_3 (PDF card 00-010-0425). Given the positive enthalpy of formation of Au_2O_3 (+190 kJ mol^{-1} at RT) this phase is not expected to form.

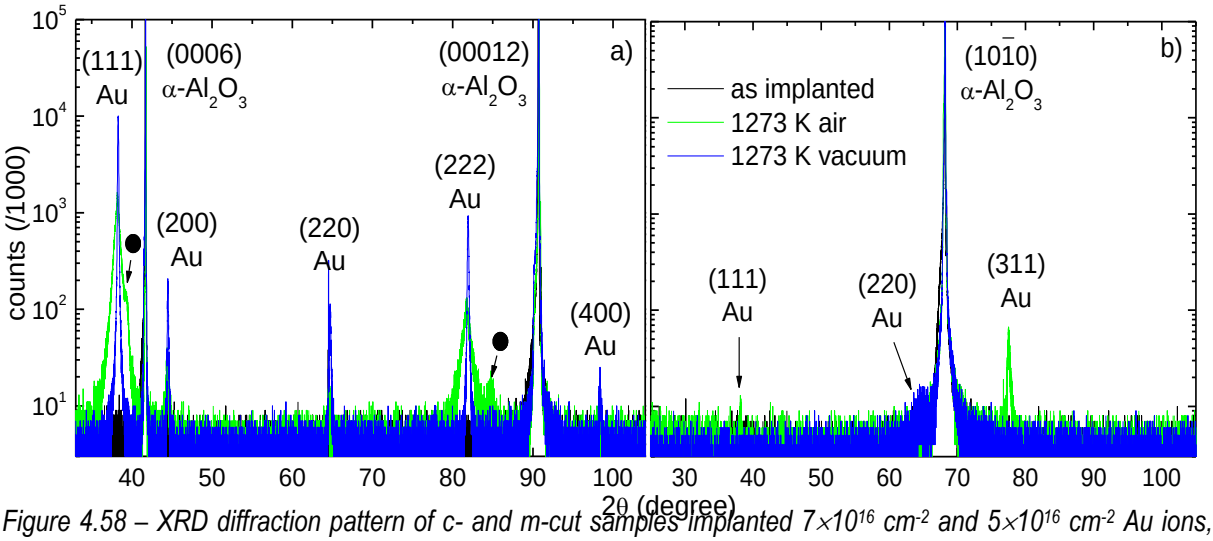

Figure 4.58 – XRD diffraction pattern of c- and m-cut samples implanted 7×10^{16} cm^{-2} and 5×10^{16} cm^{-2} Au ions, respectively, as implanted and annealed at 1273 K for one hour in vacuum or in air.

The annealing performed in vacuum produces narrower reflections and also from several different planes, the precipitates being thus larger, reaching 60 nm, and with the same diversity of orientations than after annealing in air. The lattice constant is somewhat smaller, *a* = 0.407 nm.

Regarding m-cut samples (*Figure 4.58*b), after implantation there are only reflections from sapphire, as was the case of previous studies in this type of samples. Annealing in air promotes the formation of Au precipitates (with about 25 nm and lattice constant *a* = 0.408 nm), mainly with the epitaxial relation <311>$_{Au}$ // $< 10\bar{1}0 >_{sapp}$ with a small reflection possibly from <111>$_{Au}$ // $< 10\bar{1}0 >_{sapp}$.

On the other hand, similar heat treatment but in vacuum produces smaller precipitates (about 5 nm) with the epitaxial relation <220>$_{Au}$ // $< 10\bar{1}0 >_{sapp}$. The calculated lattice constant is again smaller, *a* = 0.4068 nm.

The larger precipitates found in c-cut samples may be due to the higher implanted fluence. These sizes agree very well with the measured thicknesses with RBS, except in the case of m-cut sample annealed in vacuum, where a thickness of 30 nm measured by RBS contains precipitates with 50 nm. This is related to the shape of the precipitates, which are likely to be ellipsoidal and located at the surface. Table 4.41 resumes the findings with XRD measurements.

Table 4.41 – XRD results of Au implanted sapphire.

sample	2θ	phases	size (nm)	calculated and tabulated lattice dimensions (nm)	PDF card
c, 7×10^{16} cm^{-2} as imp.	-	-	-	-	-
1273 K air	38.25 64.63 44.50	Au(111) Au(220) Au(200)	10 35 30	0.407 / 0.408 0.408 / 0.408 0.407 / 0.408	00-004-0784
1273 K vacuum	38.25 64.63 44.50	Au(111) Au(220) Au(200)	60 50 60	0.407 / 0.408 0.408 / 0.408 0.407 / 0.408	00-004-0784
m, 5×10^{16} cm^{-2} as imp.	-	-	-	-	-
1273 K air	77.47	Au(311)	25	0.408 / 0.408	00-004-0784
1273 K vacuum	64.76	Au(220)	5	0.407 / 0.408	00-004-0784

AFM measurements were performed on these c-cut samples implanted with the highest fluence. The images obtained are presented in Figure 4.59.

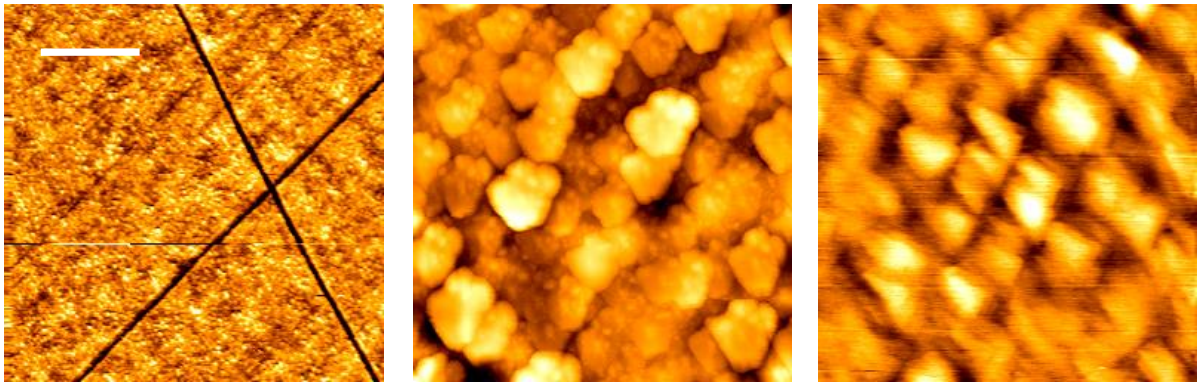

Figure 4.59 – 2×2 μm² AFM images of Au implanted sapphire: a) as implanted and after annealing at 1273 K for one hour in b) air and c) vacuum.

From these images it is possible to observe the growth of surface precipitates upon annealing, these reaching average dimensions of 200 nm. The presence of gold at the surface after the 1273 K annealing was already suggested by the corresponding RBS spectra, where significant losses were observed. In fact, in some samples it was possible to manually remove the gold layer formed at the surface.

4.4.3.1.2 Optical studies

4.4.3.1.2.1 As implanted

After implantation, the sample implanted with 1×10^{16} cm^{-2} remained transparent while the samples implanted with higher fluences acquired a dark brown coloration. Figure 4.60a shows the optical absorption spectra taken from the as implanted state of c- and m-cut samples. Only for the lower fluence it is possible to estimate the concentration of F-centres, which yields 1.5×10^{20} cm^{-3} and 2.4×10^{20} cm^{-3} for F and F^{+} centres, respectively, since interband 5d ⟶ 6sp transitions in the gold clusters develop in the same blue and UV region [Boh98]. The F-type centre concentration calculated with Smakula formula are presented in *Table 4.42*.

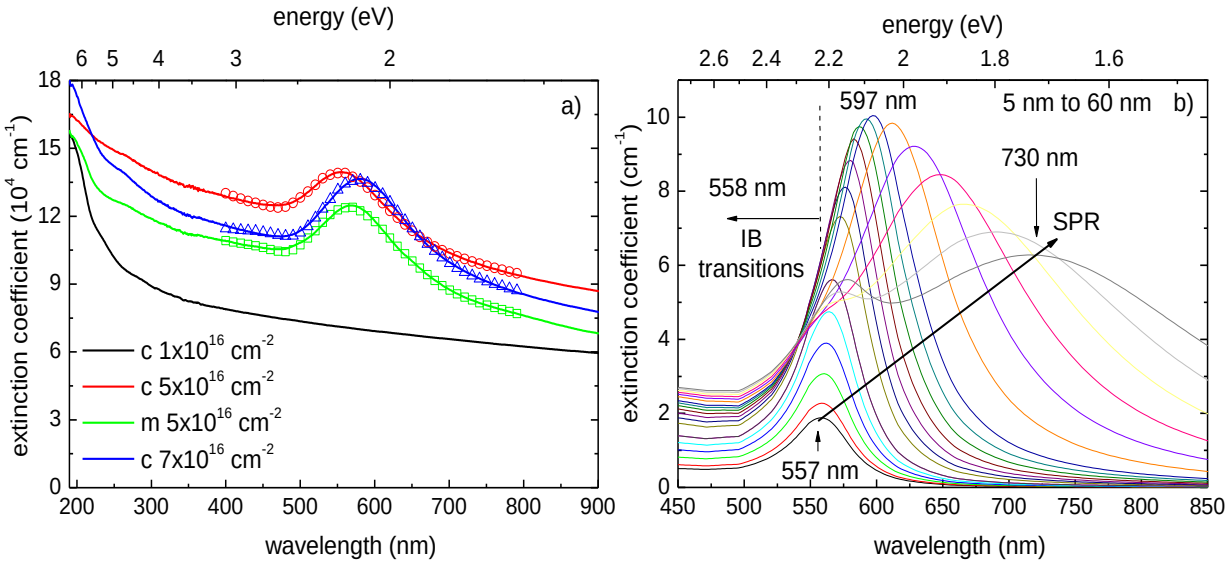

Figure 4.60 – a) optical absorption spectra of c- and m-cut sapphire as implanted with gold, with SCOUT code fit of the SPR band; b) MiePlot simulations of Au spherical particles with up to 60 nm radius.

Table 4.42 – F-type centre concentration on sapphire implanted with 1×10^{16} cm^{-2} Au ions.

sample	experimental data				F-centre concentration	
	λ (nm)	FWHM (nm)	U (eV)	u (cm^{-1})	N_0 ($\times10^{16}$ cm^{-3})	$N_{0,imp}$ ($\times10^{19}$ cm^{-3})
1×10^{16} cm^{-2}	203.77	21.99	0.66	8.52	2.38	14.9
	224.65	38.97	0.96	4.74	3.79	23.7
	258.07	57.83	1.09	2.58	2.34	14.6

The main feature of these spectra is the broad absorption bands centred around 550 nm – 580 nm. As the fluence increases, the absorption band becomes stronger and shifts towards longer wavelengths. This behaviour, the development of a broad absorption band that shifts as a function of fluence has been attributed to the presence and growth of gold aggregates [Boh98].

The absence of any significant absorption for the lowest fluence indicates that the threshold fluence for spontaneous cluster formation at 160 keV is between 1×10^{16} cm^{-2} and 5×10^{16} cm^{-2}, as was the case of silver. Again, from the area of the SPR band the threshold fluence for SPR absorption is calculated to be around 1.9×10^{16} cm^{-2} for c-cut samples (there is only one fluence for m-cut samples), the same value obtained for silver. Therefore, the rate of formation of optically active precipitates should also follow a similar evolution in this case, for the same reasons presented previously in the case of silver implantation.

The best fit of each SPR absorption band is obtained with one Gaussian curve, with the parameters presented in Table 4.43. The position of the peak of this band is different in c- and m-cut samples implanted with similar fluences, peaking at 568 nm and 580 nm, respectively. This 12 nm difference may result from different precipitate geometry that forms in c- and m-cut samples as has been observed for iron [Alv00]. On the other hand, as in previous studies, a small contribution (up to 3 nm) to this effect may be due to the characteristic birefringence of sapphire.

For c-cut samples, as the fluence increases the SPR peak shifts 23 nm, from 568 nm for the 5×10^{16} cm^{-2} implantation to 591 nm for the 7×10^{16} cm^{-2} implantation. The red shift with increasing fluence is due to the growth of the precipitates but can also be understood if one considers a possible refraction index gradient after implantation (either from the amorphization of the substrate or due to the presence of Au ions).

Table 4.43 – Optical features of Au as implanted samples.

sample	SPR			MiePlot
	peak (nm)	FWHM (nm)	area	radius (nm)
m, 5×10^{16} cm^{-2}	580	117	35	22
c, 5×10^{16} cm^{-2}	568	112	29	17
c, 7×10^{16} cm^{-2}	591	122	43	28

Mie scattering simulations of the optical response of Au spheres with (monodispersed) radius of 5 nm to 60 nm embedded in sapphire are shown in Figure 4.60b. The position of the dipolar SPR absorption maxima shifts from 560 nm for particles with r = 5 nm to 730 nm in the case of larger particles with r = 60 nm. The most intense SPR band occurs for r = 30 nm, peaking at 597 nm. As the size of the particles further increases the SPR band red shifts, becomes less intense but broader, as was the case for silver precipitates. Moreover, a quadrupole SPR band starts to develop in this size regime, near the position of the dipolar SPR absorption for small particles (around 550 nm). These maxima were used to estimate the size of the precipitates and are listed in Table 4.43. The difference between the shape of MiePlot simulated spectra and the experimental ones may be due to a larger size distribution, precipitates with non-spherical shapes or close enough to invalidate the non-interaction principle of Mie theory. Despite the large sizes inferred from optical measurements, XRD measurements did not show the corresponding reflections.

4.4.3.1.2.2 After annealing

The optical absorption spectra of c- and m-cut samples annealed up to 1273 K either in vacuum or air atmosphere is shown in Figure 4.61a and Figure 4.61b, respectively. Regarding air annealed samples, the general

behaviour is similar on the two sets: a blue shift after annealing at 1073 K followed by a red shift (compared to the as implanted spectrum) at 1273 K, the SPR band being very intense at this stage. The blue shift in this case may be due to a decrease in the size of the precipitates as the amorphized matrix grows into gamma alumina, possibly segregating gold to the grain boundaries, where it coalesces in small precipitates. In fact at 1073 K only a small crystalline recovery is observed through RBS-C, more evident on m-cut samples. At this stage metastable oxide compounds may form and thus also reduce the size of metallic precipitates. Further annealing at 1273 K recovers the alpha phase and gold accumulates as large precipitates (r = 37 nm), possibly retained in lattice voids, as those observed by TEM in the case of Zn implantation.

On the other hand, the optical absorption spectra of the c-cut samples after annealing in vacuum at 1073 K reveal a broadening of the colloid related band and a red shift after annealing, as shown in Figure 4.61a. Moreover, the SPR band is stronger.

This implies an increase of the dimension of the precipitates that may result from coalescence, possibly also in different shapes, in accordance to the narrowing observed by RBS in the Au profile. In fact the observed anisotropic diffusion would lead to non-spherical clusters with more than one characteristic absorption mode. This effect could be responsible for the absorptions centred at 591 nm and 664 nm and would account also for the decrease in the maximum of the absorption band and its broadening after this annealing at 1073 K provided some size distribution exists. The annealing at 1273 K extinguished the SPR band, leaving a weak band centred about 640 nm, either by the formation of a continuous gold film, the presence of few but large precipitates or by the decrease of the average dimensions and quantity of precipitates. The latter possibilities are consistent with the loss and in diffusion of Au measured with RBS.

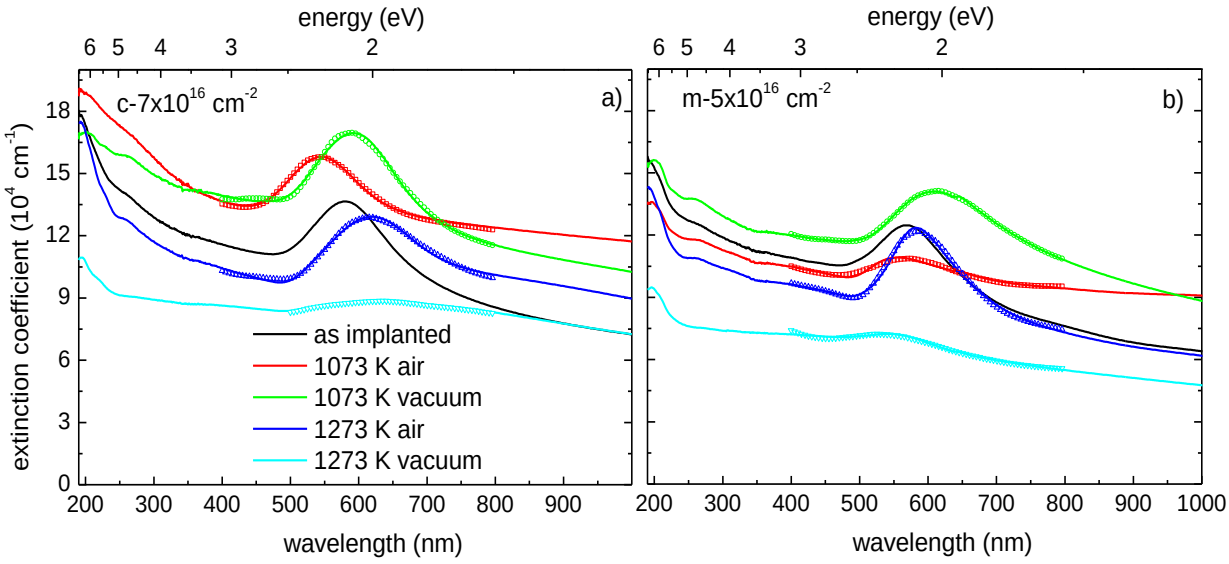

Figure 4.61 – Optical absorption spectra of α-Al_2O_3 samples implanted with gold and annealed up to 1273 K in air or vacuum: a) c-cut and b) m-cut samples.

The m-cut samples show similar behaviour upon annealing in vacuum at 1073 K except for the FWHM of the SPR band, which is much larger. The shape of this band may indicate the presence of a continuous distribution of non-spherical clusters [Boh98] or of larger and interacting precipitates. At 1273 K the SPR also vanishes but the remaining weak band peaks around 560 nm. The 86 % loss of Au measured by RBS-C in this sample allows

concluding that the remaining Au on the sample must be dispersed in few and small precipitates, suggesting an inverse Ostwald ripening process followed by evaporation.

Table 4.44 and Table 4.45 summarize the optical features of c- and m-cut samples, respectively, after implantation and after each annealing stage, along with the size estimative from MiePlot code. It's worth noting that the absence of SPR band results from the disappearance of precipitates due either to its evaporation or dissolution in subnanometre clusters or to the formation of a continuous film.

Table 4.44 – Optical features of c-cut samples implanted with 7×10^{16} cm^{-2} Au ions, with MiePlot size estimative.

sample	SPR			MiePlot
	peak (nm)	FWHM (nm)	area	radius (nm)
as implanted	568	112	29	17
1073 K air	552	109	30	5
1073 K vacuum	599	130	57	30
1273 K air	622	140	45	37
1273 K vacuum	647	130	10	45

Table 4.45 – Optical features of m-cut samples implanted with 5×10^{16} cm^{-2} Au ions, with MiePlot size estimative.

sample	SPR			MiePlot
	peak (nm)	FWHM (nm)	area	radius (nm)
as implanted	580	117	35	22
1073 K air	553 620	69 134	6 9	37
1073 K vacuum	591 662	101 147	18 30	47
1273 K air	579 631	79 130	23 24	40
1273 K vacuum	560	116	7	-

The simulation of the SPR band, presented in Figure 4.60a and Figure 4.61, was performed considering the Bergman representation for the effective medium determination, the calculations performed with SCOUT code, as in the previous studies. The fitting parameters are listed in Table 4.46 and Table 4.47 for c- and m-cut samples, respectively. From these we observe a natural increase on the percolation strength with the implanted fluence and annealing temperature, as was the case of the Cu, Zn and Ag systems.

The size estimation with SCOUT code broadly agrees with MiePlot simulations, with the larger precipitates obtained after implantation. The volume fraction is nearly constants except where major loss of Au was observed.

Table 4.46 – SCOUT fit parameters of c-cut samples implanted Au ions, as implanted for the higher fluences and after annealing up to 1273 K in vacuum of the 5×10^{16} cm^{-2} implantation.

sample	volume fraction (%)	percolation	thickness (nm)	damping constant (cm^{-1} / Hz)	size 1 (nm)	size 2 (nm)
5×10^{16} cm^{-2}	0.20	0.39	36	2594 7.78×10^{13}	32	13
7×10^{16} cm^{-2}	0.16	0.34	40	2541 7.62×10^{13}	33	14
1073 K air	0.21	0.31	39	2744 8.23×10^{13}	29	14
1073 K vacuum	0.20	0.29	39	2719 8.16×10^{13}	29	14
1273 K air	0.19	0.36	39	3262 9.79×10^{13}	22	14
1273 K vacuum	0.03	0.31	114	3624 1.09×10^{14}	19	22

Table 4.47 – SCOUT fit parameters of m-cut samples implanted with 5×10^{16} cm^{-2} Au ions, as implanted and after annealing up to 1273 K in vacuum.

sample	volume fraction (%)	percolation	thickness (nm)	damping constant (cm^{-1} / Hz)	size 1 (nm)	size 2 (nm)
5×10^{16} cm^{-2}	0.15	0.49	34	2508 7.52×10^{13}	34	11
1073 K air	0.20	0.37	32	3756 1.13×10^{14}	18	12
1073 K vacuum	0.18	0.39	39	3197 9.59×10^{13}	23	14
1273 K air	0.08	0.39	38	3243 9.73×10^{13}	22	10
1273 K vacuum	0.03	0.33	28	3645 1.09×10^{14}	19	5

The optical constants of gold have to be changed to get the best fits. The dielectric constants of the model used for gold are presented in *Figure 4.62*a. The main difference occurs in ε_2, which is always positive. Regarding the composite material (*Figure 4.62*b), the dielectric constants show large variations from those of sapphire, showing resonant behaviour as the volume fraction of gold increases.

It was possible to investigate the non-linear properties of these samples with the reflection Z-scan technique. The Z-scan measurement technique is often used for measuring the strength of the Kerr nonlinearity (i.e. the magnitude of the nonlinear index n_2, since it depends on the intensity of light) of an optical material. Essentially, a sample of the material under investigation is moved through the focus of a laser beam, and the beam radius (or the on-axis intensity) is measured at some point behind the focus as a function of the sample position. These quantities are affected by the self-focusing effect. If the nonlinear index is positive, and the sample is placed behind the focus self-focusing reduces the beam divergence and thus increases the detector signal. If the sample is moved to the left-hand side of the focus, the focus is moved to the left, and the stronger divergence after the focus decreases the detector signal.

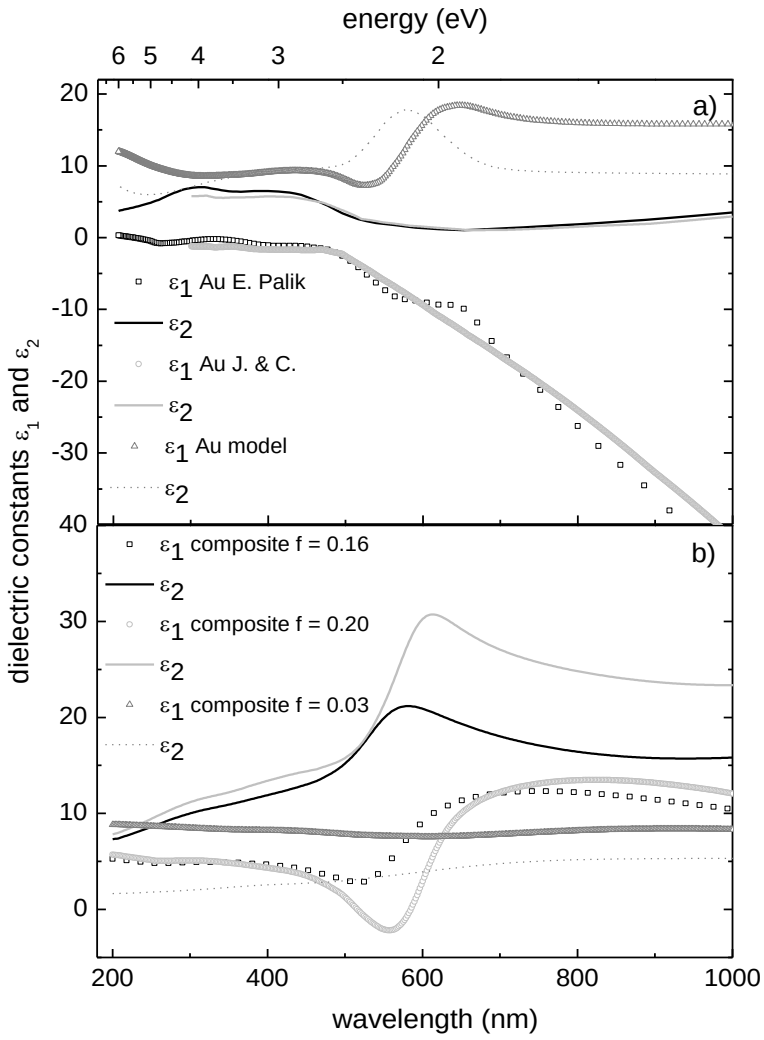

Figure 4.62 – Dielectric constants of a) gold and b) sapphire and the effective medium model used.

From the measured dependence of the detector signal on the sample position, it is possible to calculate the magnitude of the nonlinear index. That is, the Z-scan technique allows determining simultaneously the value (and sign) of nonlinear optical parameters such as the nonlinear refractive index n_2, the nonlinear absorption coefficient β, and the real and imaginary parts of $\chi^{(3)}$. The reflection Z (RZ) scan has an advantage with comparing to the others (e.g. transmission Z scan) that allows investigating the optical nonlinearities of samples with limited transparency. The application of RZ-scan is presented in [Mar00], our results in [Gan06]. Figure 4.63 shows the RZ-scan of c-cut samples implanted with the highest fluence. This scan demonstrates the nonlinearity of the optical behaviour of Au implanted samples. In fact the $R(z)$ dependences have a bell like shape symmetrical with respect to the point $z = 0$, with the top directed downward, and these samples are thus characterized by self-defocusing, which corresponds to a negative n_2 and Re ($\chi^{(3)}$). The values obtained are: $n_2 = -32.68\times10^{11}$ cm^2 W^{-1} and Re ($\chi^{(3)}$) = -3.3×10^{-10} C.

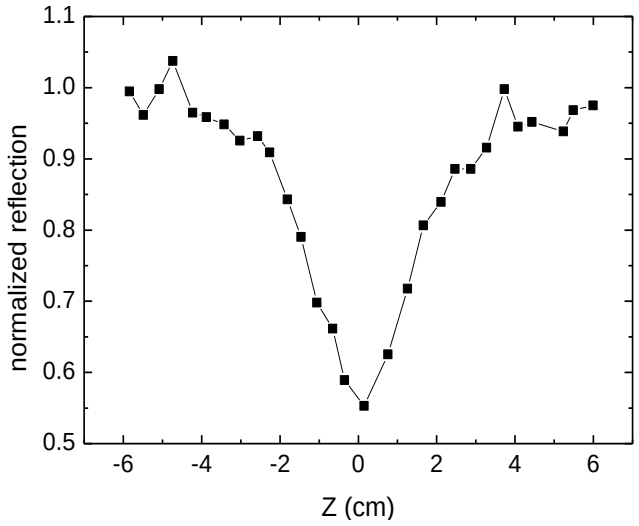

Figure 4.63 – Normalized reflection as a function of the position of Au:Al_2O_3 samples along the z-axis.

4.4.4 Discussion

At this stage it is possible to compare the behaviour of TM and NM implantations in sapphire, with Cu belonging to both groups. Figure 4.64 shows the evolution of the minimum yield of the samples as implanted with TM and NM ions. The minimum yield is measured in the Al sublattice (full marks) as well as in the implanted profile (open marks).

When compared to TM ions, amorphization occurs for lower energy deposition values in the case of the large NM (Ag and Au), a consequence of the large size of these ions, producing more damage as well as more tensions in the host lattice and exposing Al ions. The energy deposition threshold for amorphization of the host lattice is 2.0×10^{23} keV cm^{-3} in the case of Au ions. Silver has an intermediate behaviour, reaching amorphization as a TM ion at $E_D = 7.0\times10^{23}$ keV cm^{-3}.

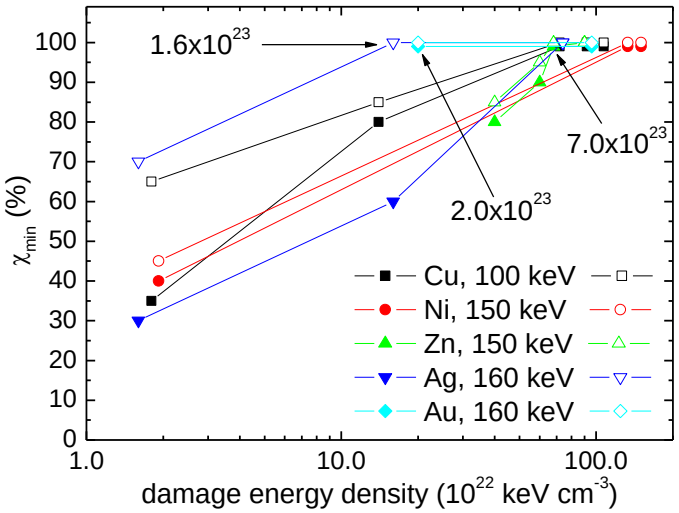

Figure 4.64 – Dechanneling ratio as a function of energy deposition for TM and NM ion implantation.

In the case of Au this is a lower threshold for amorphization than that obtained by Mouritz and co-workers [Mou87]. Since chemical effects may be excluded in the case of noble metal implantation, it must be the result of the large size of Au ions which, in the ballistic implantation process, produce a higher degree of damage. However, the Ag implantation presents the lowest amount of damage, an indication of the mobility of this ion. Moreover, for Ag and Au the implanted profile shows no channelling effects already at 1.6×10^{23} keV cm^{-3}.

For the lower fluences ($F < 2\times10^{16}$ cm^{-2}) it was possible to measure the F-type centre concentration via OA measurements. *Figure 4.65* shows the results obtained for TM and NM ions and compares with the measured minimum yield in the Al sublattice (full marks). It is clear that the higher F-type centre concentration is reached in the samples implanted with Au, which is due to the larger nuclear stopping power (53.2 keV nm^{-1}). Moreover, for silver and gold the F^+-centre concentration exceeds that of F-centres, a consequence of a larger cascade effect in these cases. This was not observed on TM ions implantations.

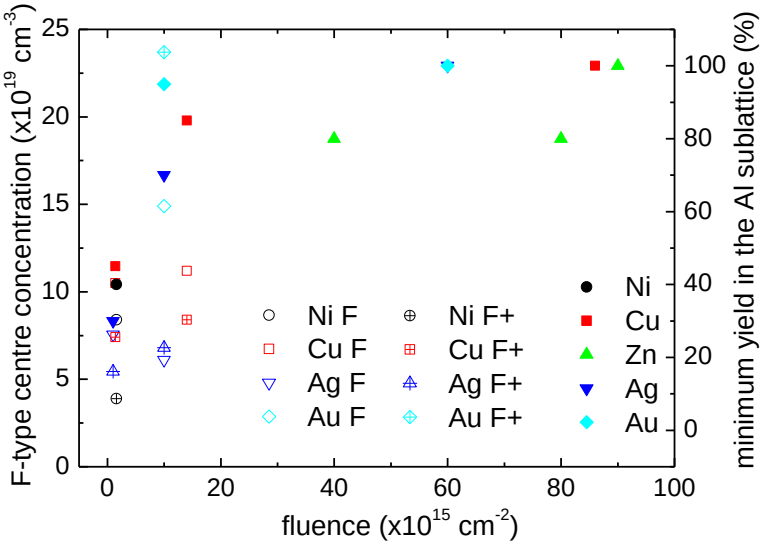

Figure 4.65 – Defect concentration vs. implanted fluence for TM and NM ions.

The predictions of SRIM regarding FWHM and R_p of the implanted profiles were systematically different from the experimental measurements, namely for the higher fluences. As was the case with TM, the code overestimated R_p since it does not account for the densification and composition changes as fluence increases. Regarding the FWHM, in the case of Au this value is always 19 nm higher than the prediction, the result of an amorphized matrix in every case, which thus presents similar RED effects. Silver, on the other hand, implanted with the same energy, show a larger and variable difference, possibly due to its higher mobility.

Bimodal concentration distributions of the Ag ions were observed after implantation of high fluences in m-cut samples, possibly leading to broader distribution of colloid sizes. This distribution is also responsible for the large SPR band. This is explained as the result of fast diffusion, a RED process during implantation. On the other hand, c-cut samples show the typical Gaussian as implanted profile, as was the case for all gold implantations.

NM implanted samples show a strong surface plasmon resonance (SPR) band. In the case of silver, this band develops between 460 nm and 500 nm after implantation while in the case of gold this band appears between 570 nm and 590 nm. Cu, as shown in the TM section, displays SPR absorption at 600 nm.

In both cases this optical signature of metallic precipitates occurs for fluences between 1×10^{16} cm^{-2} and 6×10^{16} cm^{-2}. As in the case of copper implantation, a linear model was applied to estimate the threshold fluence for SPR, yielding similar values for silver and gold (1.9×10^{16} cm^{-2}), one third of the value found for copper. From optical extinction measurements the size of the precipitates is estimated to be between 20 nm and 27 nm after implantation of the highest fluences. However, XRD measurements did not reveal any metallic reflections at this stage, an indication of the absence of significant crystalline domains or its minute size, random orientation and dispersion. *Figure 4.66* shows the size of the precipitates determined by XRD and OA for TM and NM ions.

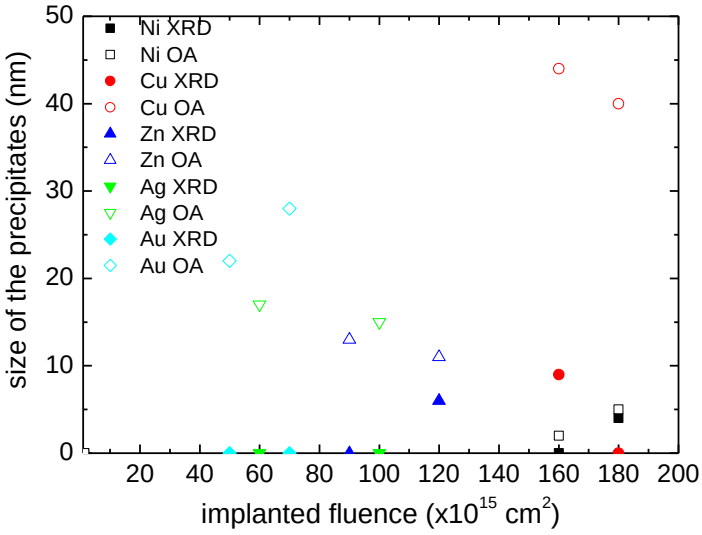

Figure 4.66 – Size of the precipitates estimated by XRD and OA vs. implanted fluence for TM and NM ions.

The size dependence with the atomic concentration is shown in *Figure 4.67*. Optically active precipitates start to form around 9 at. %, in the case of silver, a lower value than that observed in TM.

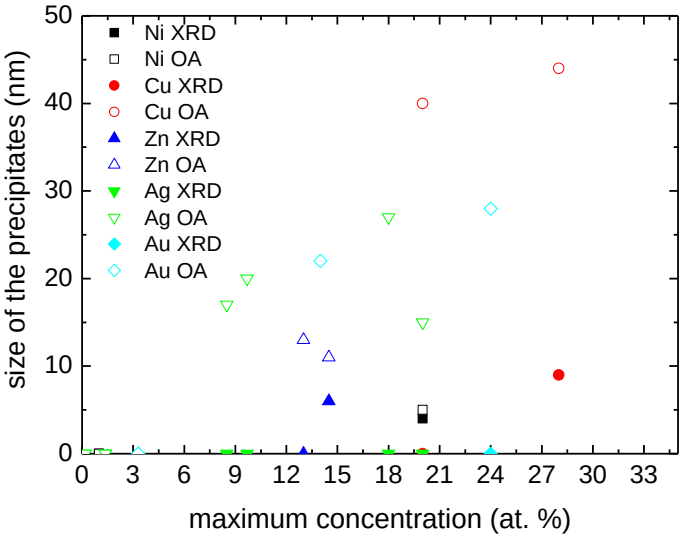

Figure 4.67 - Size of the precipitates estimated by XRD and OA vs. maximum concentration for TM and NM ions.

Regarding the manipulation of the features of the SPR band, in the case of silver the peak position was successfully varied +40 nm or +9 nm with implantation fluence, in the case of c- and m-cut, respectively.

Gold, on the other hand, implanted with lower fluences, shows smaller variations after implantation: +12 nm with sample orientation (from c- to m-cut samples) and +23 nm with increasing fluence (c-cut samples only).

It is obvious that there is a relation between the degree of damage of the matrix and the presence of optically active precipitates. The growth of the precipitates succeed a radiation rich phase that presents both the high mobility environment for the implanted species as well as the absence of structural boundaries for the development of the precipitates. The proposed evolution of the as implanted TM and NM systems as measured with the experimental techniques with increasing atomic concentration of the implanted species is summarized in *Table 4.48*.

Table 4.48 – Evolution of the as implanted TM and NM systems with the atomic concentration of the implanted species.

RBS-C implanted profile	channeling	total dechanneling		
RBS-C matrix	channelling		total dechanneling	
XRD	no reflections		nanometre precipitates	
OA	no SPR		SPR	
concentration of the implanted species (at. %)	0.75	9.0	12	30

Upon annealing in air at 1273 K, silver almost disappears (85 % loss) on both c- and m-cut samples. The annealing in air promotes the damage recovery of the sapphire lattice (close to full recrystallization in the case of c-cut samples) which impels the Ag ions to the surface. These may coalesce into large precipitates or form oxide phases, both of which evaporate at 1273 K.

In the case of gold this annealing promotes also major recrystallization of the matrix, driving the Au to the surface where it forms an easily removable layer, for c- and m-cut samples. This layer remains in the sample since the boiling point of Au is higher than that of silver.

The loss of silver is thus explained by the formation and sublimation of unstable oxides, as was the case of copper. Regarding the thermal evolution of $Ag:Al_2O_3$ the process in air may be modelled as follows:

$$20\ Al + 30\ O + 10\ Ag + n\ O_2 \rightarrow 10\ \gamma\text{-}Al_2O_3 + 1\ Ag + 3\ AgO + 7\ AgO_2 \rightarrow 10\ \alpha\text{-}Al_2O_3 + 1\ Ag + 9\ Ag_{(g)} \quad [4.9]$$

The stoichiometry coefficients simply reflect the estimated atomic percentage of each element, as simulated by NDF.

Significant loss of silver is also observed upon 1273 K annealing in vacuum, as was observed after similar annealing in air atmosphere, for both orientations. However, large precipitates (ca. 50 nm) are only found in c-cut samples, aligned with the sapphire matrix, mainly with $<111>_{Ag}$ // $<0001>_{sapp}$. The annealing in vacuum should essentially skip the formation of silver oxides in equation 4.9.

On the other hand, annealing in vacuum the samples implanted with Au promotes the redistribution with out-diffusion (with 43 % loss) and in-diffusion processes, while m-cut samples show a remarkable out diffusion only, with about 86 % loss of Au. The gold precipitates formed were found to be aligned with the matrix with the (111) planes aligned with the c-planes of the sapphire substrate.

Figure 4.68 shows the evolution of the implanted species profile for the NM ions after annealing at 1273 K. It is clear that 1273 K annealing in vacuum produces major evaporation of any of the NM, limiting its range of operation, namely with high power lasers. The annealing in air may limit the loss of the implanted species, possibly by the formation of stable compounds (the spinel phase in the case of copper) or the recrystallization of the surface layer.

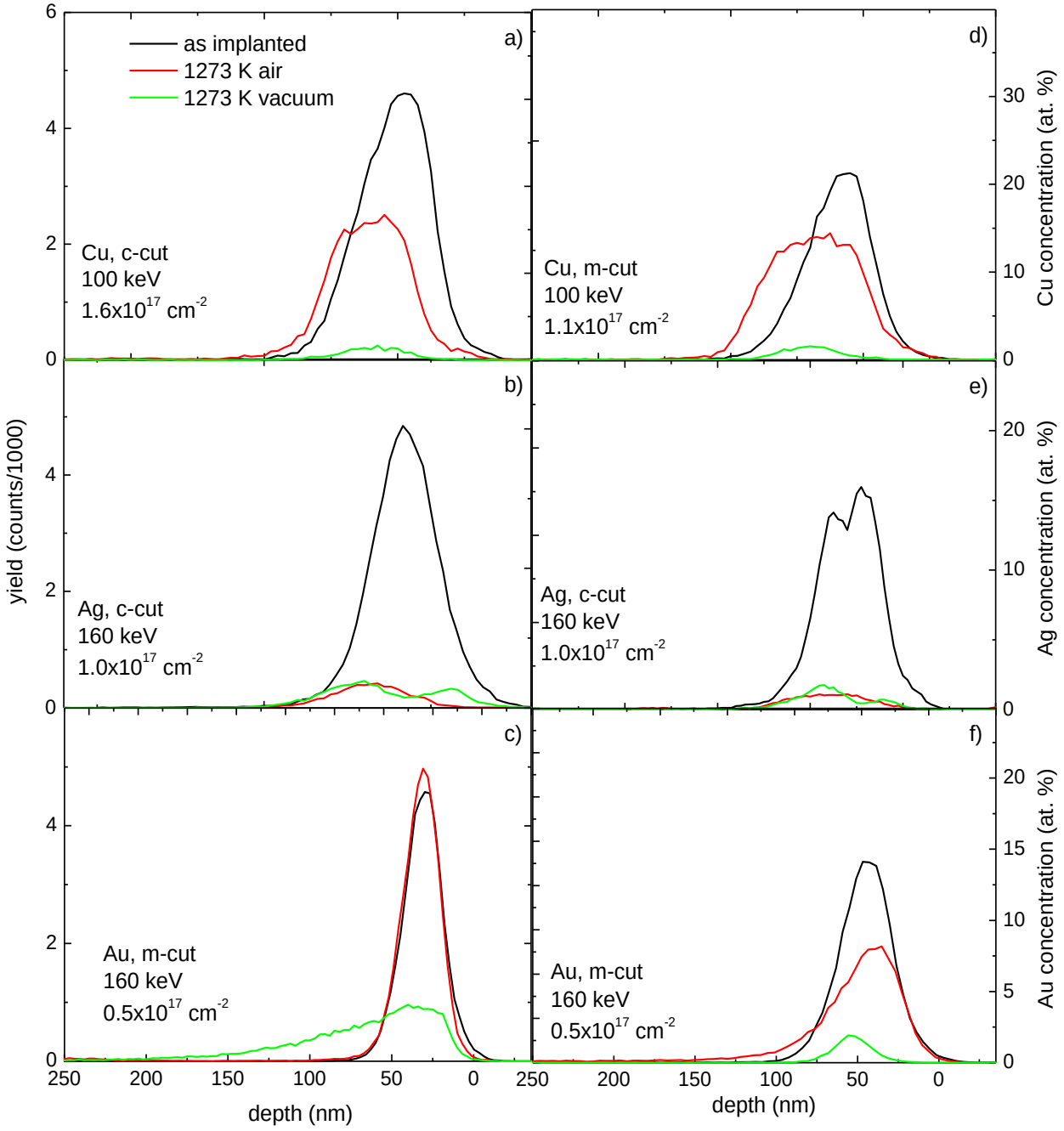

Figure 4.68 – RBS spectra of the implanted species profile for NM.

In the case of silver, its stability upon annealing in air is about 1073 K in c-cut samples, while Au is kept up to 1273 K. In vacuum conditions this limit drops 1073 K in both cases.

This behaviour is correlated with the matrix crystalline recovery, as shown in *Figure 4.69*. C-cut samples show always better deep channelling, a result of the better crystalline quality of the topmost layers, be it in a lower damage density or smaller damage extension.

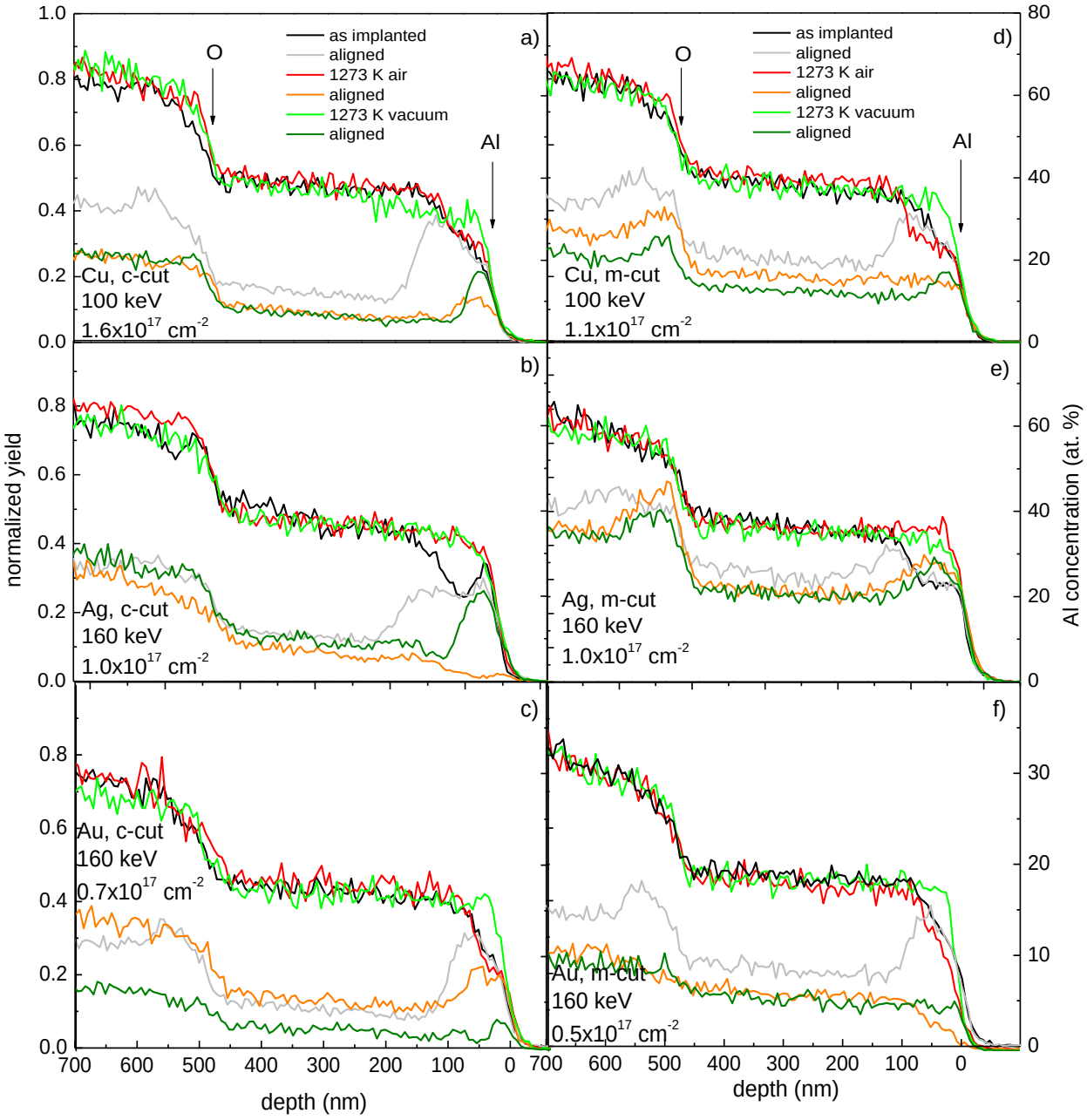

Figure 4.69 – Matrix evolution for NM ions implantations upon annealing at 1273 K in air or vacuum (the depth scale is valid only for the Al sublattice).

The fluence loss is particular visible in the case of the NM as compared to TM, as shown in *Figure 4.70*. By annealing in air, Cu and Ag show the higher fluence losses. Au, on the other hand, keeps most of the implanted fluence but in a surface and removable film. In vacuum conditions, the NM group again show higher losses. It is also important to notice that the crystalline orientation is important. It is clear that m-cut samples tend to facilitate the out-diffusion of the implanted species and hence favour its evaporation.

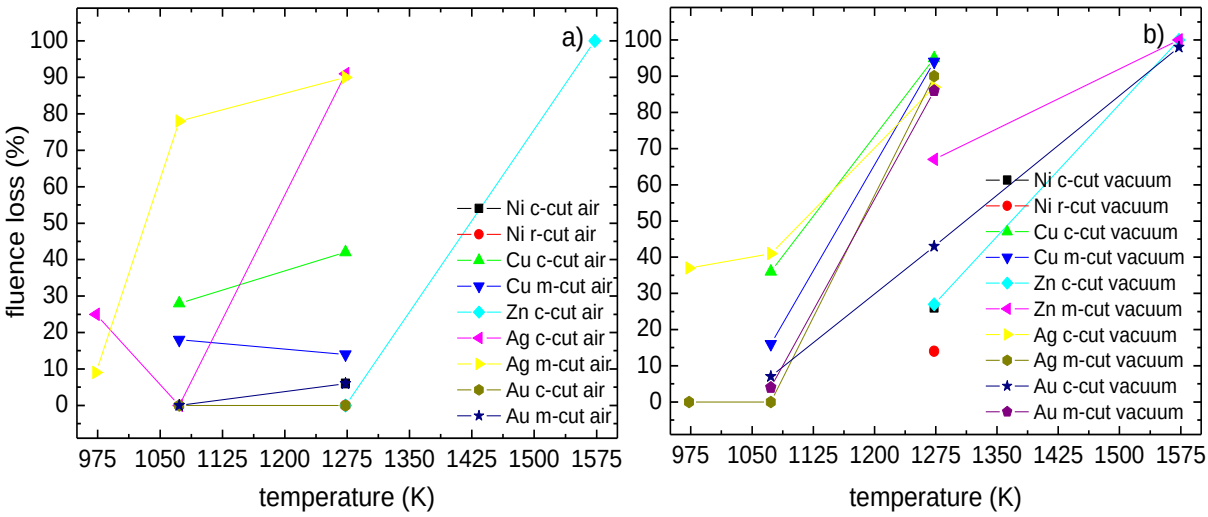

Figure 4.70 – Fluence loss vs. annealing temperature for TM and NM systems for: a) air and b) vacuum atmospheres.

Regarding the optical behaviour of annealed samples, in the case of silver the SPR band is extinguished after annealing in air in all cases. In vacuum, there is a minor red shift at 1073 K (+2 nm) and a blue shift (-32 nm) at 1273 K for c-cut samples, the latter accompanied by a decrease on the intensity of this band. On the other hand, m-cut samples a continuous red shift is observed: +33 nm and + 8 nm at 1073 K and 1273 K, respectively.

The annealing in air at 1073 K of gold implanted samples produces blue-shift (-16 nm) on c-cut samples, while a red shift of +40 nm is observed on m-cut samples. Further annealing at 1273 K result in similar red shifts: +54 nm and +51 nm for c- and m-cut samples, respectively.

When the annealing is performed under vacuum conditions, at 1073 K there are also red shifts: +31 nm and +82 nm for c- and m-cut samples, respectively. Further annealing at 1273 K destroyed SPR absorption.

SCOUT code fits of the experimental spectra allowed determining the dielectric constants of the composite material. The model used (Bergman representation) implies a modification of the bulk dielectric constants of the metallic phase of the composite material. *Figure 4.71*a shows the dielectric constants calculated by SCOUT code for the NM ions. These modifications are expected due to the size of the precipitates, which affects the behaviour of the electrons. Moreover, the model used has to include features related to defect centres in order to fit the full spectra. *Figure 4.71*b shows the dielectric constants of the composite material. There are steep increases in both constants near the resonance regions.

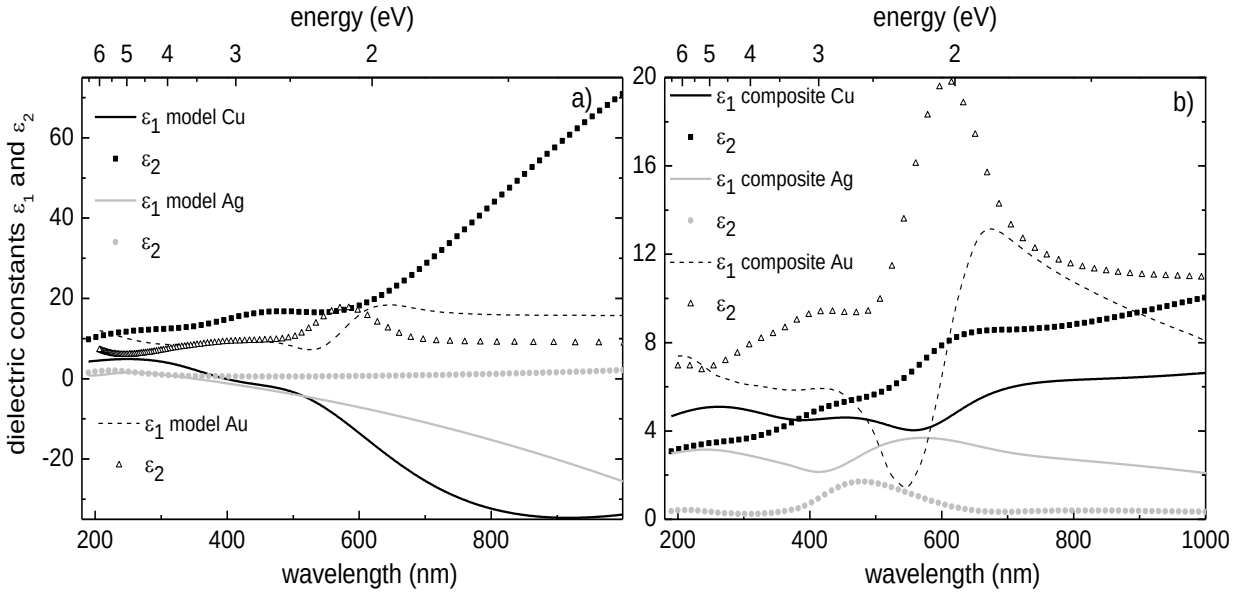

Figure 4.71 – SCOUT code calculation of the dielectric constants of: a) NM and b) composite material.

Table 4.49 summarizes the annealing behaviour of the TM and NM systems upon annealing up to 1273 K.

Table 4.49 – Evolution of the TM and NM systems implanted with the highest fluences upon annealing in air or vacuum up to 1273 K.

as implanted (~RT)	γ-Al_2O_3, Me^0, O_2, possibly some amorphous Me_xO_y	
temperature	annealing in air	annealing in vacuum
1073 K	O_2, γ-Al_2O_3, Me_xO_y Unstable oxides (CuO, AgO) partially decompose with some loss of the implanted species	γ-Al_2O_3, Me^0 Unstable oxides (CuO, AgO) partially decompose with some loss of the implanted species
1273 K	O_2, and γ to α-Al_2O_3 complete TM: cation counter diffusion and formation of aligned $MeAl_2O_4$ (> 10 nm) Ag and Au: Me^0 (>10 nm) at the top layers	partial γ to α-Al_2O_3, aligned Me^0 (>10 nm) low melting point elements near the surface evaporate (Zn) or unstable oxides (CuO, AgO) decompose with major loss of the implanted species

4.5 Rare-earth implantations

4.5.1 Introduction

The optical properties of sapphire can be tailored by the incorporation of optical active ions like rare-earths. We chose Eu and Yb due to its characteristic emission which can be probed with our new IBIL setup, being also, at this initial stage, a benchmark of the performance status of this experimental apparatus.

In this study sapphire single crystals were implanted at RT with 100 keV Eu^{+} or 300 keV Yb^{2+} to promote red (Eu^{3+}) and NIR (Yb^{3+}) emission. Low fluences were used aiming at minimizing the radiation damage which hinders the optical activity of the systems formed. Subsequent thermal annealings were carried up to 1573 K in air or vacuum. These are necessary to activate the emission of these ions, both by decreasing the number non-radiative de-excitation paths created by the radiation damage and by promoting the diffusion of the implanted ions to regular lattice sites were the desired trivalent state is preferred.

Table 4.50 presents the most relevant information regarding the implantation of Eu and Yb, as well as bulk properties of these RE elements, to be used in the interpretation of the experimental results.

Table 4.50 – Pertinent quantities associated to each implantation or element and to the analysis of the experimental results [Oma93, Lid02 and W4].

	Eu	Yb
energy (keV)	100	300
current density ($\mu A\ cm^{-2}$)	2	< 2
samples	c, OSP, 0.4 mm	c, BSP, 0.5 mm
fluence (cm^{-2})	$1\times10^{15} – 1\times10^{16}$	1.6×10^{15}
SRIM R_p (nm)	29	61
SRIM straggling (nm)	6	13
SRIM FWHM (nm)	14	30
SRIM vacancies per ion	932	3721
SRIM sputtering yield (at. per ion)	8.98	10.91
n_{dpa}	6 – 65	12
electronic and nuclear dE/dx (eV nm^{-1})	5.5 and 42.6	11.4 and 50.0
Ionic radii (pm)	Eu^{3+}: 108.7 (6-coor.) Eu^{3+}: 120.6 (8-coor.) Eu^{2+}:139.0 (8-coor.)	Yb^{3+}: 100.8 (6-coor.) Yb^{3+}: 112.5 (8-coor.) Yb^{2+}: 128.0 (8-coor.)
atomic density (cm^{-3})	2.08×10^{22}	2.43×10^{22}
melting point (K)	1099	1097
boiling point (K)	1800	1469
space group, structure and lattice parameters	Im-3m; bcc; 0.46 nm	Fm-3m; bcc; 0.55 nm
compounds and thermal stability	Eu_2O_3 stable up to 2623 K	Yb_2O_3 stable up to 2708 K
ground state electronic configuration	$[Xe].4f^7.6s^2$	$[Xe].4f^{14}.6s^2$

It is worth noting the low melting point of both elements, as well as the low boiling point of Yb (the lowest amongst RE). Moreover, Yb^{3+} is the smallest of the RE ions and both ions are of the few rare-earths (along with Sm and Tm) that may be found in the 2+ oxidation state (besides the common 3+ or more exotic 4+ states) and thus form stable monoxide or spinel phases.

4.5.2 Eu implantation

Sapphire c-cut samples were implanted at RT with 100 keV $^{153}Eu^{+}$ ions with three different fluences: 1×10^{15} cm^{-2}, 5×10^{15} cm^{-2} and 1×10^{16} cm^{-2}. These samples were subsequently annealed at 1073 K, 1273 K and 1573 K for one hour either in vacuum or ambient atmosphere. The low fluences were used to minimize radiation damage and avoid Eu clustering and concentration quenching of the luminescence while high annealing temperature was needed to maximize the recovery of crystalline quality of sapphire and of the structures produced. RBS, RBS-C, XRD, OA and IBIL measurements were used to characterize the systems formed at each stage. In fact, the performance of the IBIL setup assembled in the framework of this thesis was first tested in this particular system.

4.5.2.1 Results and discussion

4.5.2.1.1 Structural studies

The RBS-C measurements presented in Figure 4.72 were performed after implantation of all fluences to probe the distribution of the implanted ion as well as to measure the radiation damage produced in the sapphire lattice, in particular in the Al sublattice.

After implantation of 1×10^{15} cm^{-2} (Figure 4.72a) the samples show a shallow (~60 nm) uniformly damaged layer, where χ_{min} = 20 %. E_D is about 1.7×10^{22} keV cm^{-3}. The dechanneling in deeper regions in the Al sublattice (E < 1100 keV), is very low: χ_{min} = 5 %. The comparison with the Cu:Al_2O_3 system implanted with similar fluence and energy (cf. *Figure 4.13*), shows that in the case of Eu implantation there is much better channelling (χ_{min} = 5 % and χ_{min} = 30 % for Eu and Cu, respectively). This is due to the characteristics of the damaged layer in the case of Eu, which not only has a lower defect concentration but it is also thinner (60 nm vs. 80 nm). The combination of these factors results in a layer that does not produce significant deviation in the trajectories of the probe ions, which channel nearly unperturbedly into the inner defect free region.

The Eu profile is essentially Gaussian with FWHM of 15 nm and peaking at 15 nm and displays some channelling, with χ_{min} = 70 %. This is in excellent agreement with SRIM prediction for the FWHM (14 nm) but is half of the predicted R_p (29 nm, cf. Table 4.50). The average concentration reaches 0.5 at %, as simulated with NDF code.

As the implantation fluence increases to 5×10^{15} cm^{-2} the damaged layer enlarges to approximately 70 nm and χ_{min} raises to 75 %, as seen Figure 4.72b. E_D is about 7.0×10^{22} keV cm^{-3} at this stage. The top most 20 nm seem completely amorphized, according to RBS-C, as the aligned RBS yield from this region equals that of the random (off-alignment direction). The deep regions remain with low χ_{min} (~10 %).

Amorphization at RT at such energies and low fluences (E_D being smaller than the amorphization threshold found by Mouritz and co-workers [Mou87]) is observed for chemically reactive elements (such as titanium [Mar02]) and agrees with the fact that Eu is the most reactive of the RE elements.

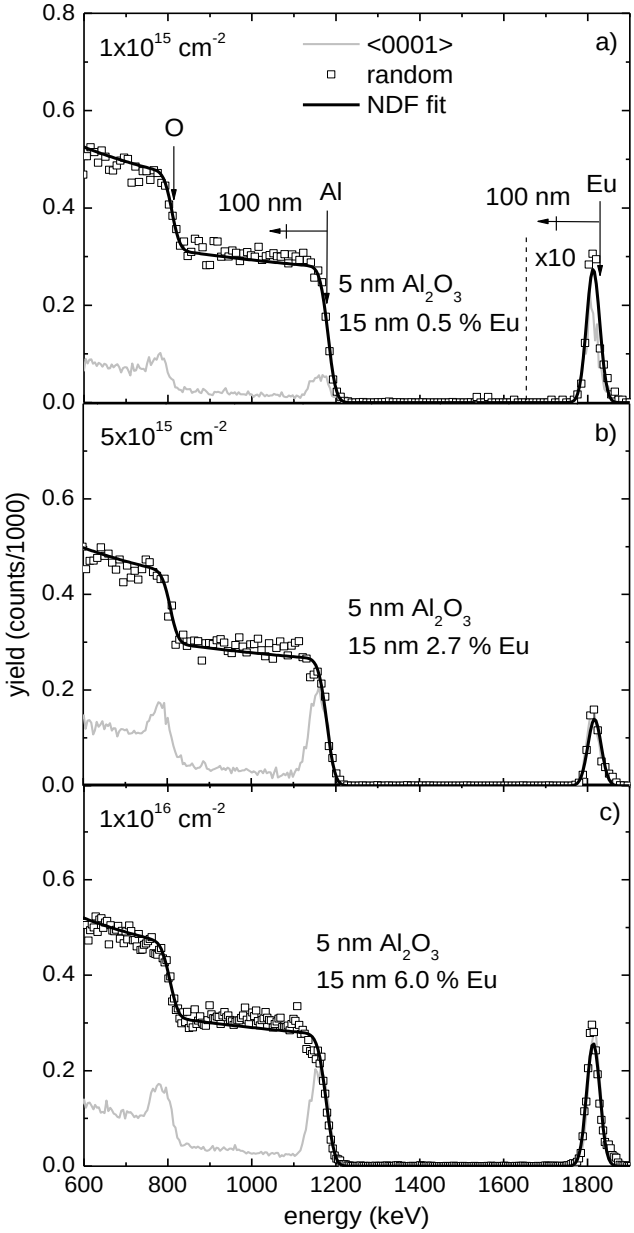

The Eu profile remains Gaussian shaped but showing no channelling. As in the lower implantation fluence, its FWHM is 15 nm and peaks around 15 nm. The measured average concentration reaches about 2.7 at. % in this case.

Further increase in implantation fluence to 1×10^{16} cm^{-2} (Figure 4.72c) rises E_D to about 1.4×10^{23} keV cm^{-3} but the profile of the Al lattice remains similar to 5×10^{15} cm^{-2} implantation. The Eu profile remains nearly Gaussian, peaking at 15 nm depth, being fit with NDF code by a 15 nm layer with 6.0 at. %.

Table 4.51 summarizes the RBS-C results of the as implanted samples.

Figure 4.72 – RBS-C spectra and NDF code composition fit of c-cut α-Al_2O_3 as implanted at RT with 100 keV europium: a) 1×10^{15} cm^{-2}, b) 5×10^{15} cm^{-2} and c) 1×10^{16} cm^{-2}.

Table 4.51 – RBS-C results of c-cut sapphire samples as implanted with Eu ions.

sample	1×10^{15} cm^{-2}	5×10^{15} cm^{-2}	1×10^{16} cm^{-2}
host matrix			
max. damage depth (nm)	0 – 60	0 – 70	0 – 70
χ_{min} (%)	20	75	85
damage extension (nm)	60	100	100
E_D (10^{22} keV cm^{-3})	1.7	7	14
deep region χ_{min} (%)	5	10	10
implanted profile			
max. conc. depth (nm)	15	15	15
χ_{min} (%)	70	100	100
FWHM (nm)	15	15	15
max. conc. (at. %)	0.5	2.7	6.0

All samples were annealed at 1073 K, 1273 K and 1573 K in air or vacuum. Up to 1273 K all samples keep the as implanted random and aligned profiles unchanged irrespective of the annealing atmosphere. Indeed, for all fluences, in all but the annealing at 1573 K no significant matrix recovery is observed and, concomitantly, no channelling effects are observed in the Eu profile allowing concluding that the Eu ions are randomly distributed in the host material at T ≤ 1273 K. This is shown in *Figure 4.73*a and *Figure 4.73*c for the highest implantation fluence where the results obtained after annealing at 1273 K are presented. There is no diffusion or loss of Eu, despite its low melting point. Can and co-workers also did not observe any noticeable diffusion as a result of either thermal (up to 1473 K) or laser annealing of sapphire implanted with 400 keV Eu ions [Can94]. This may also be related to the reactivity of Eu or to the extreme size difference between Al and Eu atoms (0.182 nm and 0.256 nm respectively) which hinder the mobility of Eu.

The annealing atmosphere plays an important role in the system evolution only at T > 1273 K, for all fluences. The RBS-C spectra of the samples implanted with the highest fluence after annealing at 1573 K in air or vacuum are shown in *Figure 4.73*b and *Figure 4.73*d, respectively. Even at this temperature no loss of Eu was observed, an indication of the formation of a more stable Eu compound.

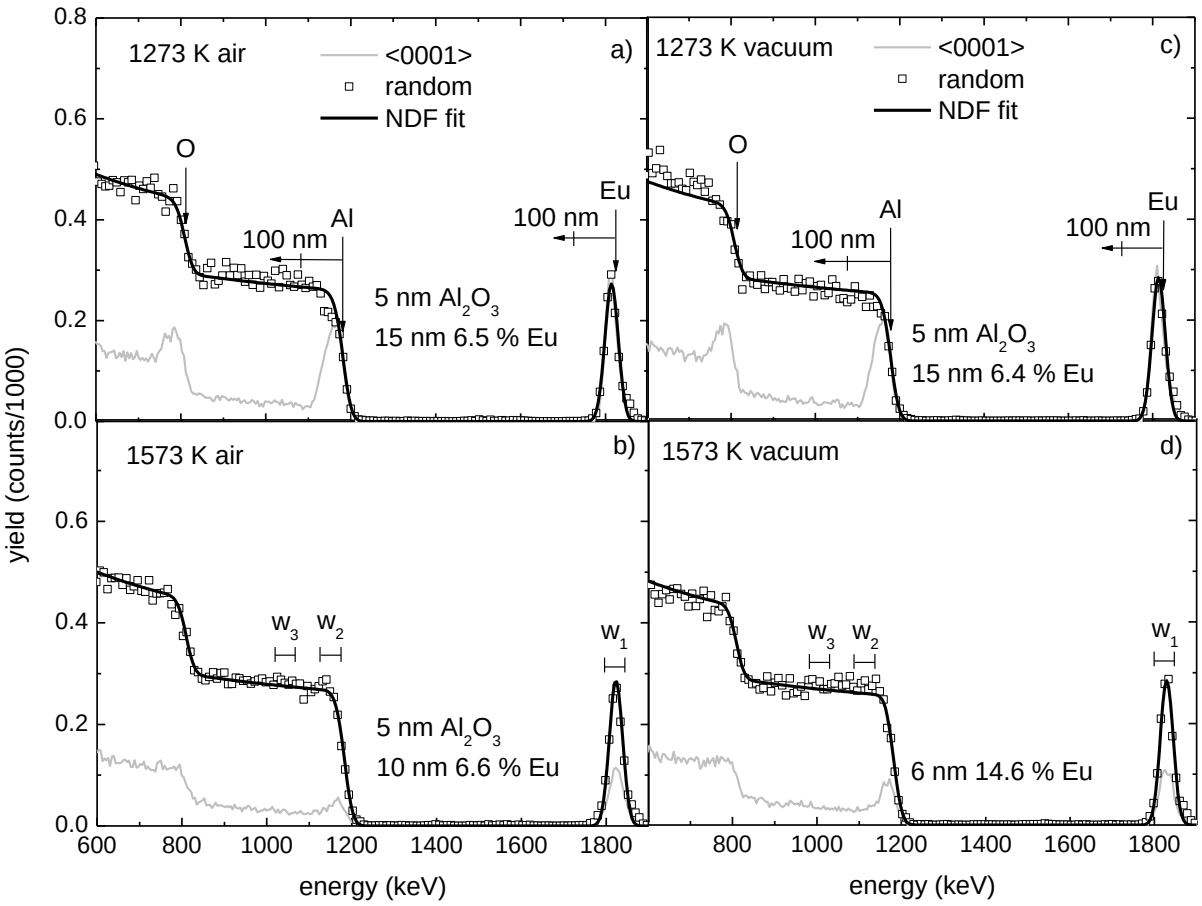

Figure 4.73 – RBS-C spectra of sapphire implanted with 1×10^{16} cm^{-2} Eu ions and annealed for 1 hour at 1273 K and 1573 K in: a) and b) air and c) and d) vacuum (also represented the windows used for the detailed angular scans of Figure 4.74), with NDF code composition fit.

Annealing at 1573 K promotes the crystalline recovery of sapphire, which is more evident in the annealing in air than in the annealing performed in vacuum. In fact, after annealing in air the surface damaged layer is characterized, in the Al lattice (1150 keV – 1200 keV), by only 18 % dechanneling (*Figure 4.73*b) against the 36 % found when the annealing is performed in vacuum (*Figure 4.73*d). The O sublattice shows also lower surface damage. The χ_{min} in deeper regions is also different, with 10 % and 15 % after annealing in air and vacuum, respectively, as a result of the different damage concentration and extension of the surface layer.

As also shown in *Figure 4.73*b and *Figure 4.73*d, after the 1573 K annealing the Eu profile presents a noticeable channelling effect along the c-axis (χ_{min} = 45 %), irrespective of the annealing atmosphere, suggesting the distribution of a large fraction of the ions into regular lattice sites. These results indicate the dispersion of Eu in regular lattice sites (e.g. in a solid solution) or even the presence of some Eu phase with crystalline coherence with the sapphire matrix after this annealing. The Eu profile remains Gaussian shaped in both cases, with FWHM of 10 nm and 6 nm after annealing in air and vacuum, respectively.

Given the existence of dechanneling in the Eu profile after 1573 K annealing, detailed angular scans were performed to determine the site location of Eu in the sapphire lattice. Detailed angular scans performed along the $< 0001 >$, $< 1\bar{2}13 >$ and $< 1\bar{1}01 >$ directions are displayed in Figure 4.74 after annealing at 1573 K in air (top figures) and in vacuum (bottom) for one hour. Three regions were chosen, one corresponding to the Eu profile and two pertaining aluminium: close to the surface in the implanted region, and in a deeper region (i.e. corresponding to the unperturbed matrix), as shown in *Figure 4.73*b. These scans show that a fraction of Eu ions must occupy interstitial sites of the sapphire lattice.

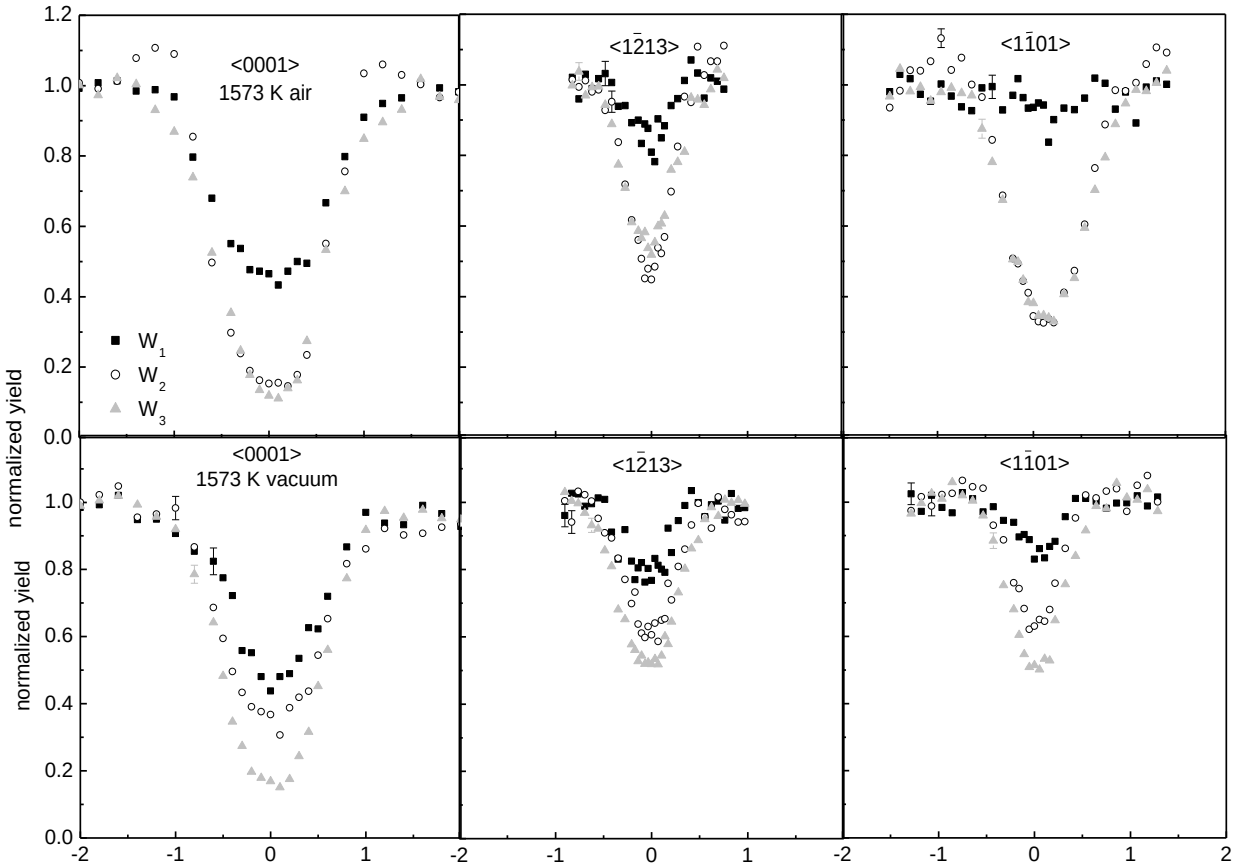

Figure 4.74 – Detailed angular scans along $< 0001 >$, $< 1\bar{2}13 >$ and $< 1\bar{1}01 >$ directions on sapphire implanted with 1×10[16] cm[-2] after annealing at 1573 K in air (top) and vacuum (bottom).

The Eu behaviour is different for both annealing atmospheres, particularly in the $< 1\bar{1}01 >$ direction. In fact, while for the $< 0001 >$ and $< 1\bar{2}13 >$ directions the substitutional fractions of the Eu impurity atoms in matrix sites, calculated through equation 3.28, are 65 % and 45 % after annealing in air and 85 % and 55 % after annealing in vacuum, along the $< 1\bar{1}01 >$ direction these values are about 15 % for the sample annealed in air and 40 % after the annealing in vacuum. The difference in the regular fraction along the three axial directions reveals the presence of Eu in different sites along the c-axis. A possibility is the occupation of the empty sites located on the c-direction. The surface crystallinity, as measured by RBS-C, after annealing in vacuum is consistently worse than after annealing in air, which, given the similar yields of the Eu profiles in both annealing atmospheres, leads to an higher fraction of substitutionality in the case of annealing in vacuum. The reactiveness of Eu may be responsible for the persistence of amorphization even at low fluences as well as the annealing behaviour of the samples up to 1273 K, irrespective of the annealing atmosphere. This reactiveness can also explain the lower recrystallization observed in vacuum where Eu would compete with Al for the oxygen necessary to reconstruct the matrix. We propose that Eu reacts during implantation becoming randomly distributed. The structure formed doesn't change up to 1273 K. After annealing at 1573 K some redistribution occurs, possibly accompanying the γ to α transition of sapphire (normally occurring between 1273 K and 1573 K), retarded by the presence of the impurity, with Eu occupying now preferential sites, perhaps partially substituting Al in the 3+ oxidation state in an oxide phase with some degree of coherence with the matrix. Ozuna and co-workers also observed that the presence of the europium ions retards the reconstruction of the α-phase of alumina to temperatures above 1473 K [Ozu04]. Table 4.52 aggregates the RBS-C results of the annealed samples.

Table 4.52 – RBS-C results of sapphire samples implanted with Eu and annealed up to 1573 K.

sample	1273 K air	1573 K air	1273 K vac.	1573 K vac.
host matrix				
max. damage depth (nm)	0 – 70	0	0 – 70	0
χ_{min} (%)	85	18	85	36
damage extension (nm)	100	40	100	60
deep region χ_{min}	12.5	12.5	15	15
implanted profile				
max. conc. depth (nm)	20	10	15	6
χ_{min} (%)	100	45	100	45
retained fluence (10^{15} cm^{-2})	10	10	10	10
fluence loss (%)	0	0	0	0
FWHM (nm)	15	10	15	6
max. conc. (at. %)	6.5	6.6	6.4	14.5
$f_{sub.}$	-	15	-	40

These samples were analysed with XRD in order to identify crystalline phases present. Figure 4.75 displays the results obtained. After implantation only sapphire reflections are visible, which means that if europium phases do form it must be in amorphous phase or in small or extremely diluted precipitates. The annealing in air promotes the formation Eu_2O_3 precipitates. The RE sesquioxides may be divided into three main polymorphic types, which form depending on the radius of the RE element. Each RE element has only one truly stable polymorph. Europium, being an average sized RE element, may form a metastable C-type (with a cubic Mn_2O_3 type structure of space

group $Ia\bar{3}$) at temperatures below 1348 K (at which the monotropic C – B transformation occurs), after which has a stable B-type (a monoclinic distortion of the C-type), while A-type is typical of large RE (with a hexagonal La_2O_3 type structure of space group $P\bar{3}m1$) [Pet07]. The stability relations of the A, B and C polymorphic forms or the RE sesquioxides are shown in *Figure 4.76*. At 1573 K Eu is expected to form B type. However, in this case, it is competing with Al for oxygen. Moreover, the C-type may still be present at 1573 K due to the crystallographic arrangement (defect rich) in these particular conditions of ion implantation processing. The C - B transformation is proportional to the crystallinity of the C polymorph [Rot60]. In fact, the reflection of sapphire has, on its left side, a peak that may be ascribed to gamma alumina (PDF card 00-010-0425). This peak develops after the annealings but is more intense in the case of vacuum annealing. In addition, another metastable phase of aluminium oxide, delta alumina (PDF card 00-046-1215), is also visible after this annealing, with about 15 nm average dimensions, as the result of incomplete recrystallization of the matrix. We ascribe the reflections obtained after this annealing to {111} and {100} families of planes of C-type sesquioxides, in precipitates with about 15 nm dimension. This texture may result from the reactiveness of Eu which may have formed this phase already on top of metastable cubic forms of alumina present as a result of the destruction of the sapphire lattice. If so, the lattice mismatch to sapphire is about 3.5 % while for γ-alumina it is about 8 %. A small amount of oxides is also evident with reflections from Eu_2O_3 (222) plane as well as (040) plane of Eu_3O_4, with 20 nm and 9 nm, respectively. The sizes determined with the Scherrer formula are compatible with the RBS-C measurements of thicknesses. Table 4.53 shows the results obtained with XRD measurements.

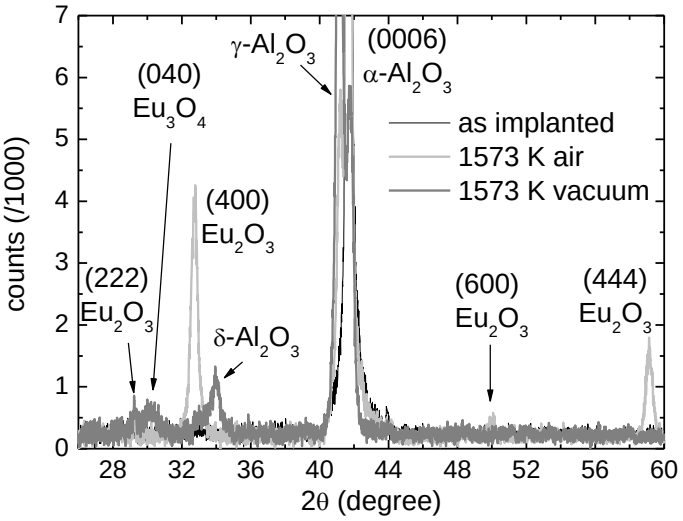

Figure 4.75 – XRD spectra of c-cut sapphire obtained after implantation of 1×10^{16} cm^{-2} Eu^+ and after annealing at 1573 K in air or vacuum for one hour.

Table 4.53 – XRD results of Eu implanted samples.

sample	2θ	phases	size (nm)	calculated and tabulated lattice dimensions (nm)	PDF card
as implanted	-	-	-	-	-
1573 K air	59.11 32.73	Eu_2O_3 (444) Eu_2O_3 (400)	16 15	1.082 / 1.087 1.094 / 1.087	00-034-0392
1573 K vacuum	29.20 30.18	Eu_2O_3 (222) Eu_3O_4 (040)	20 9	1.059 / 1.087 1.183 / 1.205 (b)	00-034-0392 01-071-2188

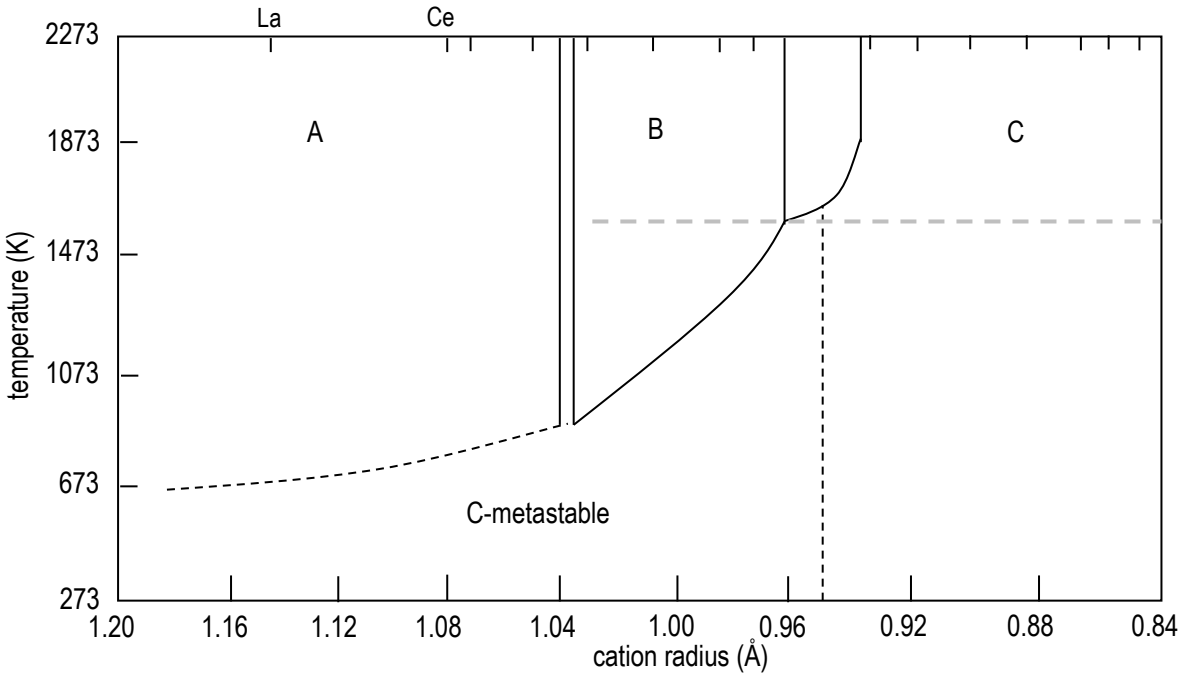

Figure 4.76 – Stability relations of the A, B and C polymorphic forms or the RE sesquioxides [Rot60].

According to the calculated phase diagram of *Figure 4.77*, at low (6 at. %) Eu concentrations (and enough oxygen) and 1573 K the phases present are expected to be Eu_2O_3 mixed with alumina, reaching the empirical formula of Eu_4Al_2O9 only for 33 % of Eu_2O_3.

.

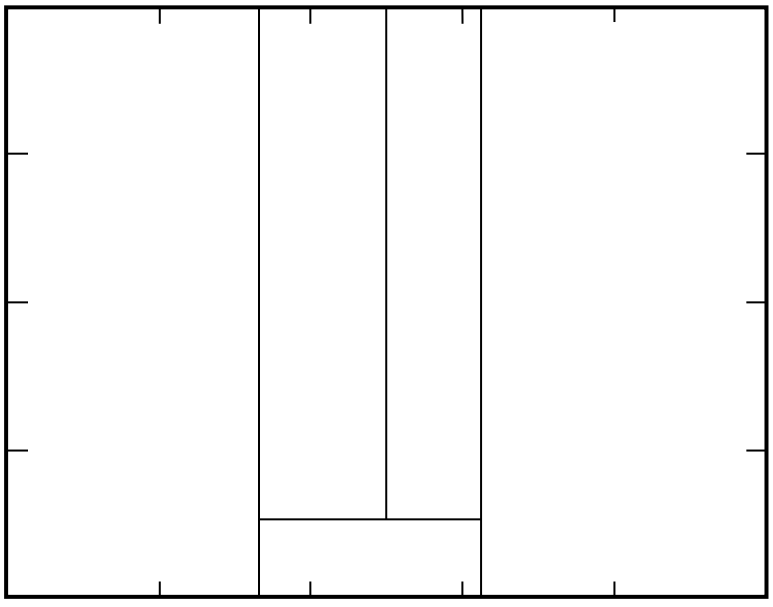

Figure 4.77 – Calculated phase diagram of the Al_2O_3 – Eu_2O_3 system [Wu92].

4.5.2.1.2 Optical studies

4.5.2.1.2.1 Optical absorption

Optical absorption measurements were performed in the 190 nm to 1100 nm wavelength range to investigate both the defects in the O lattice and the possible characteristic absorption related to Eu. No significant absorption was present in the 500 nm to 1100 nm range and thus this region is omitted in the displayed spectra. The main features occur thus in the 190 nm to 500 nm wavelength region and are shown in Figure 4.78 for all implantations.

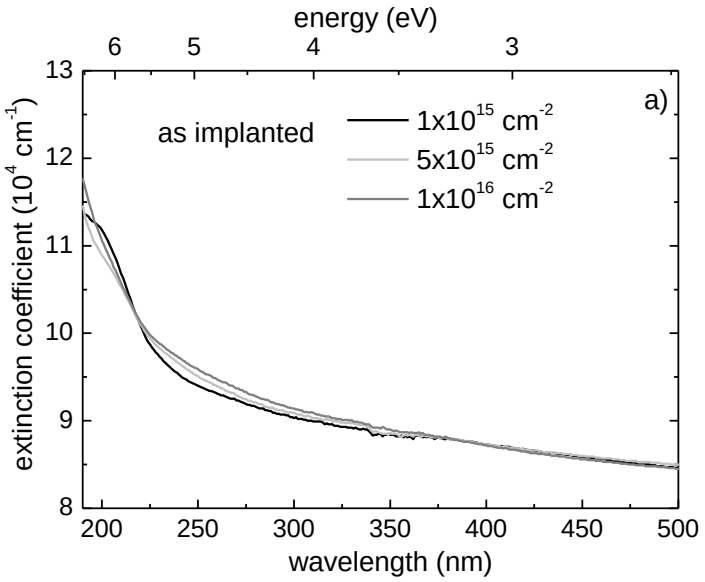

Figure 4.78 – Optical absorption spectra of sapphire implanted with 100 keV Eu^+, as implanted with 1×10^{15} cm^{-2}, 5×10^{15} cm^{-2} and 1×10^{16} cm^{-2}.

After implantation the defect related bands in the UV region (F centres at 205 nm and F^+ centres at 203 nm, 225 nm and 258 nm, cf. Table 2.3) dominate the spectra, the individual wide bands overlapping in an increasing absorption band towards the UV.

The optical spectra of the samples implanted with the highest fluence after annealing in air up to 1573 K are shown in *Figure 4.79*a. At 1073 K there is a general decrease of absorption intensity. This trend continues up to 1273 K, where minimum absorption is observed (except in the high energy side, λ < 225 nm). However, at 1573 K two absorption bands develop at 240 nm and at 265 nm and the overall UV absorption increases. The 265 nm band is known to be associated with the presence of Eu oxides in silica and silica-alumina glasses [Nog96].

Annealing in vacuum shows similar behaviour, *Figure 4.79*b, a general decrease of damage-related F type centres bands, mainly that at 205 nm up to 1273 K. At 1573 K the bands at 240 nm and 265 nm develop again, while at 310 nm a large and weak band also appears.

These results are in agreement with the structural findings, indicating the formation of a small quantity of Eu oxide already after implantation, stable up to 1273 K.

Annealing at higher temperatures, 1573 K, in air leads to the formation of more oxide, absorbing around 265 nm, leaving fewer defects than in vacuum. The enthalpy of formation of Eu_2O_3 makes this compound thermodynamically nearly as favoured as Al_2O_3 (-1651 kJ mol^{-1} vs. -1676 kJ mol^{-1} at RT) and this process may leave Al in the metallic state. These structures are encapsulated in crystalline mixture of Al_2O_3 and Eu_2O_3 and may thus maintain its metallic state. Aluminium nanoprecipitates with radius up to 25 nm would absorb in the wavelength

region between 220 nm and 350 nm, as shown in the MiePlot simulations in Figure 4.36a. The dipole SPR band has maximum intensity for r = 7 nm, peaking at 250 nm. Further increase in the particles average dimensions results in less intense but broader band. Quadrupole SPR band starts to develop for r > 9 nm, centred around 220 nm. It is then plausible that the absorption at 240 nm be related to SPR of nanoparticles of metallic aluminium, with about 7 nm radius. This is consistent with the RBS-C spectra of the annealed samples of

Figure 4.73 where the O lattice reveals significant order while the Al lattice retains some disorder, which may be due to the above mentioned process: O taken in the formation of aligned Eu sesquioxide and Al dispersed in metallic precipitates.

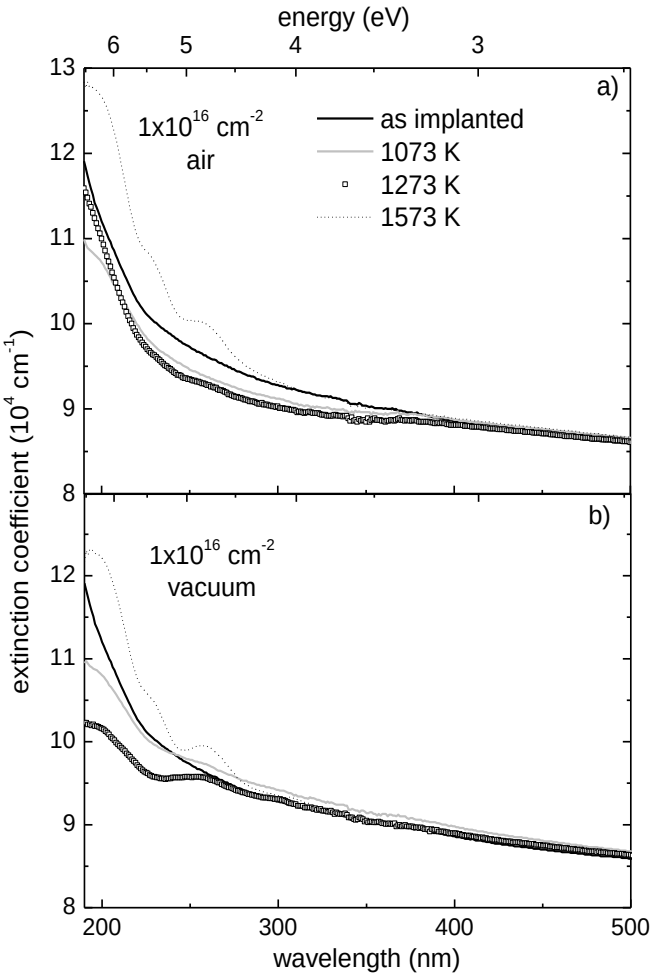

Figure 4.79 – Optical absorption spectra of sapphire implanted with 1×10^{16} cm^{-2} 100 keV Eu^{+} annealed in a) air and b) vacuum for one hour at 1573 K.

The optical analysis may be further developed by drawing the Tauc plot of the samples annealed at 1573 K, as shown in *Figure 4.80*. The band-gap of Eu_2O_3 may be estimated to be 4.0 eV, while the 3.0 eV may be ascribed to defects. Using Smakula formula it is possible to quantify the amount of F type centres present in each sample. Table 4.54 shows the results obtained for the as implanted samples. These suggest F-centres are initially created and subsequent implantation oxidises these centres, eventually promoting the formation of defect complexes.

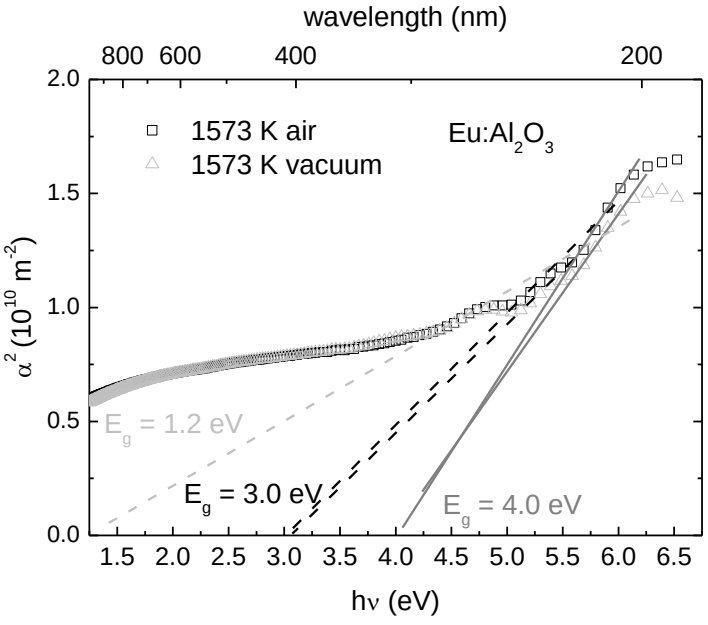

Figure 4.80 – Tauc plot to determine the energy levels associated with each transition.

Table 4.54 – F-type centre concentration determined with Smakula formula after implantation of Eu.

sample	experimental data				F-centre concentration	
	λ (nm)	$\Delta\lambda$ (nm)	U (eV)	u (cm^{-1})	N_0 ($\times 10^{16}$ cm^{-3})	$N_{0,imp}$ ($\times 10^{19}$ cm^{-3})
1×10^{15} cm^{-2}	201.56	24.92	0.76	4.43	1.36	9.07
	224.10	33.11	0.82	1.61	1.05	7.00
	257.18	43.85	0.83	0.82	0.54	3.61
5×10^{15} cm^{-2}	200.38	27.07	0.84	3.81	1.29	5.16
	224.72	35.16	0.87	1.71	1.18	4.72
	256.42	45.00	0.86	0.99	0.68	2.71
1×10^{16} cm^{-2}	201.56	25.21	0.77	4.04	1.26	5.04
	224.72	37.82	0.94	2.15	1.61	6.44
	258.07	46.98	0.88	1.40	0.98	3.92

Similar calculations were performed for the annealed samples, considering all the measured absorption as related to defects. The F centre concentration results are summarized in Table 4.55 for the annealed samples. The general trend is a decrease on the F-type centres after annealing up to 1273 K. However, the annealing at 1573 K seems to increase the concentration of these defects. This further supports the possibility of these bands being related to Al precipitates that grow with the annealing temperature.

Table 4.55 – F-type centre concentration determined with Smakula formula after implantation of 1×10^{16} cm^{-2} Eu ions and after each annealing stage.

sample	experimental data				F-centre concentration	
	λ (nm)	$\Delta\lambda$ (nm)	U (eV)	u (cm^{-1})	N_0 ($\times 10^{16}$ cm^{-3})	$N_{0,imp}$ ($\times 10^{19}$ cm^{-3})
as implanted	201.56	25.21	0.77	4.04	1.26	5.04
	224.72	37.82	0.94	2.15	1.61	6.44
	258.07	46.98	0.88	1.40	0.98	3.92
1073 K air	204.15	26.32	0.79	2.58	0.86	3.44
	223.86	40.38	1.01	1.20	1.02	4.10
	257.10	45.64	0.86	0.68	0.49	1.96
1273 K air	204.15	20.78	0.62	2.92	0.78	3.10
	224.08	32.90	0.82	1.37	0.95	3.80
	257.30	39.22	0.74	0.55	0.34	1.35
1573 K air	204.15	19.07	0.57	6.67	1.62	16.2
	224.10	28.38	0.70	3.75	2.18	21.8
	256.62	40.32	0.76	2.15	1.36	13.6
1073 K vacuum	204.15	23.85	0.71	2.72	0.82	3.28
	224.72	31.60	0.78	1.22	0.79	3.16
	254.52	49.21	0.95	1.12	0.89	3.56
1273 K vacuum	203.71	25.97	0.78	1.72	0.57	2.28
	224.72	33.76	0.83	0.65	0.45	1.80
	257.23	41.35	0.78	1.04	0.74	2.96
1573 K vacuum	204.15	19.45	0.58	6.22	1.54	10.2
	224.72	26.40	0.65	3.17	1.74	11.6
	258.07	34.94	0.65	2.05	1.12	7.5

4.5.2.1.2.2 IBIL

Ionoluminescence measurements were conducted on these systems in order to further develop the characterization of their optical properties. Moreover, europium is known to have a richness of emission bands which provide the appropriate initial benchmark for the IBIL setup installed in the course of this work. This setup allows probing the radiation damage produced in sapphire (F-centres at 420 nm and F^+-centre at 325 nm, cf. Table 2.3) and the emission spectrum of Eu^{3+} which extends from 500 nm to 750 nm with a relatively simple energy level structure.

As was the case in other experimental techniques, the initial results concern the characterization of pristine samples. These present essentially two defect bands at 329 nm (F^+-centre emission) and 415 nm (F-centre emission), with extrinsic substitutional impurities emitting at ~692 nm and ~694 nm (Cr^{3+}) and 750 nm (Ti^{3+}), as presented in Table 2.3. The IBIL spectra containing these bands are present in *Figure 4.81*. These spectra are in excellent agreement with the literature values obtained with other techniques: the Gaussian shape of F^+ emission with FWHM of 29 nm is comparable to that of literature (30 nm in [Pez06]), as it is the asymmetrical shape of F emission, as observed in CL experiments [Giu06]. In fact, this band may be decomposed in three Gaussian curves, centred at 405 nm, 431 nm and 447 nm. The spectrum is not continuous but taken in (3) separate wavelength regions, the low energy side with a filter cutting below 630 nm.

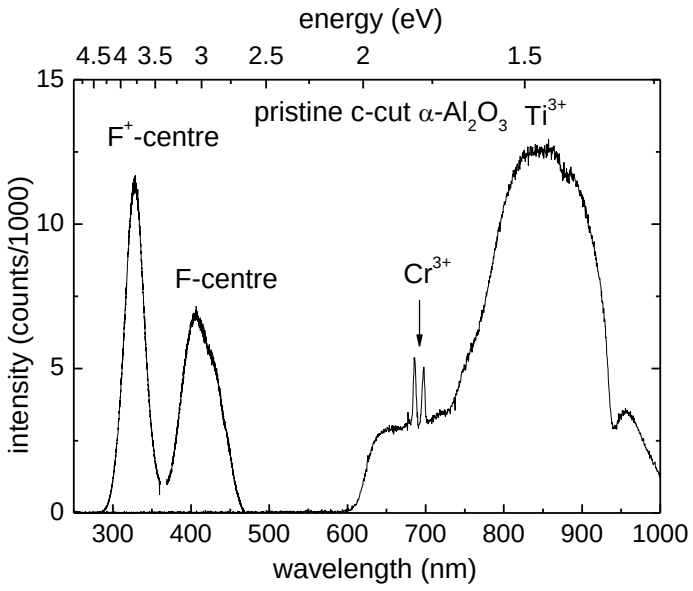

Figure 4.81 – IBIL spectrum of the characteristic features of pristine sapphire samples: F-centres and Cr^{3+} and Ti^{3+} emission.

Moreover, at this initial stage we sought the optimization the beam characteristics, namely the beam particle, since H or He was available. The energy was chosen as to minimize the impact on the samples and provide a stable beam. The main characteristics of these beams in sapphire, calculated with SRIM code, are listed in Table 4.56. It is clear that He^+ is expected to produce more damage and ionization. For these reasons we chose to use proton beams for this type of analysis.

Table 4.56 – Calculated characteristics of 1.0 MeV H^+ and He^+ beams in sapphire.

beam	$(dE/dx)_e$ (eV nm^{-1})	$(dE/dx)_n$ (eV nm^{-1})	vacancies per ion	R_P (μm)	energy loss via ionization in the first 200 nm (eV nm^{-1})
H^+	75	0.05	13.7	8.92	105
He^+	569	0.75	95.6	2.04	810

The intensity of the emission band is known to change with the irradiation time. To measure the rate of production of the defects, the intensity of these bands was plotted against the irradiation time, in what is called a F-colouring curve. In this context, *Figure 4.82* shows the evolution of F^+-centres emission as a function of irradiation time for 1.0 MeV H^+ or He^+ beams. Each point represents a 10 s collection at a given time. The dispersion of the data is due to the fluctuation of beam current. It is clear that F^+-centre emission is stronger in the case of H^+, a fact also observed in PIXE experiments. These bands develop slowly with irradiation time, eventually saturating in the time scale studied.

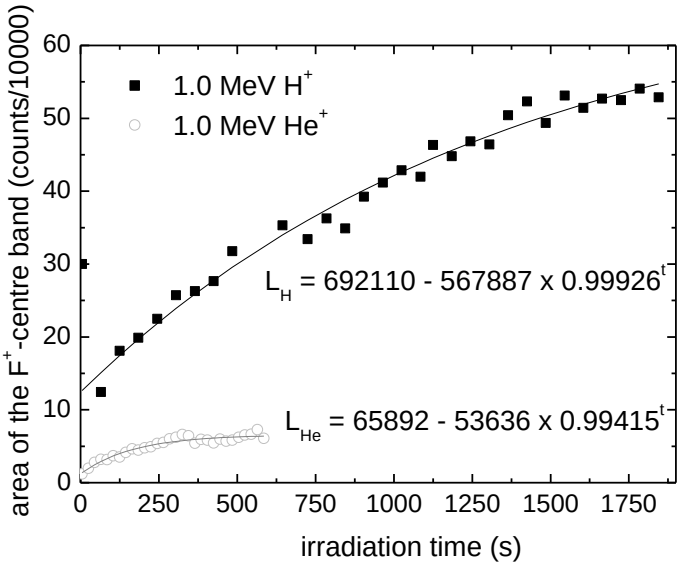

Figure 4.82 – F^+-centre evolution with irradiation time in pristine sapphire samples: a) 1.0 MeV H^+ and b) 1.0 MeV He^+.

The F-colouring curves obtained with H^+ ion are shown in *Figure 4.83*a and *Figure 4.83*b for F^+ and F centres, respectively. F^+-centre emission is present at the beginning of irradiation. This is explained by the ionization of pre-existing F-centres. For F^+-centres an asymptotic model was chosen to fit the data. Moreover, if one considers the presence of V-centres, as Vallayer and co-workers [Val01], another explanation involves the migration of electrons from F-centres to V-centres, and hence increasing F^+ emission. The evolution of the height of the F^+ emission band follows that of the area, a direct consequence of the constant FWHM of this band (about 29 nm).

From these spectra it is obvious that F-type centre damage increases with irradiation time in this irradiation regime, even if these irradiation conditions are unlikely to displace O ions. This increase of F centre emission can be explained by the existence of non radiative or inactive state of an oxygen vacancy that is activated during the irradiation. In fact, simulations from Lagerlöf and co-workers estimated that the most common defect in sapphire should be interstitial oxygen [Lag98]. It is possible that upon irradiation these defects become optically active.

On the other hand, the evolution of F-centres was adjusted with the model presented in chapter 2. Regarding the components used to fit the evolution of the F-centres, the extreme bands have two components while the central band evolves almost linearly. Using this model and from the F-colouring curves fit, the estimated lifetime of F-centres in trap 1 is about 400 s, in accordance with data from Moroño and co-workers [Mor02] in sapphire irradiated with 1.8 MeV electron beam.

Table 4.57 presents the fitting parameters, from which the lifetime of the defect centres for each fitting component (type of defect trap) is very different. The trap type 1 show similar parameters but the second component is very different in the case of the 431 nm emission.

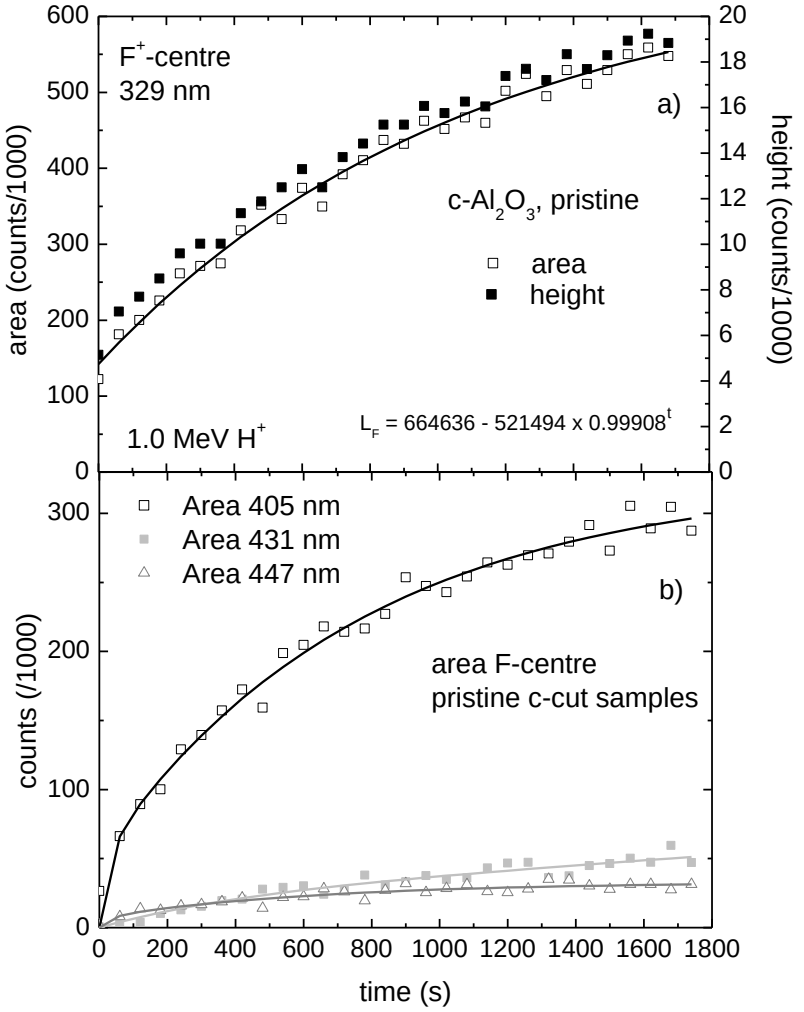

Figure 4.83 – F-colouring curve of pristine sapphire as a function of irradiation time with 1.0 MeV H^+: a) F^+-centre and b) F-centre.

Temperature dependent studies are necessary to definitely ascribe these bands. Their growth with irradiation time dismisses the possibility of being related to impurities.

The dimension of the F centre can also be estimated, in a simple model of a particle in a box system, to be around 0.19 nm, thus justifying, as far as these defect centres are concerned, the absence of scattering effects in the optical absorption analysis.

Table 4.57 – Parameters used to fit the development of F-centre in pristine sapphire samples.

band	A_1	a_1 (10^{-3} s^{-1})	τ_1 (s)	A_2	a_2 (10^{-3} s^{-1})	τ_2 (s)
405 nm	274344	2.30	435	50427	38.04	26
431 nm	22335	2.43	412	10449325	0.0016056	one week...
447 nm	25678	1.56	641	7286	33.07	30

Regarding Eu implanted samples,

Figure *4.84* shows the spectra recorded in this region for the highest fluence and annealing temperature (1573 K) in air and vacuum as well as the energy diagram of Eu^{3+}. This spectrum reveals the presence of Cr^{3+} signal, in all samples. The signal strength of Cr^{3+} emission increases upon annealing since the radiationless deexcitation paths provided by defects decrease. The IBIL signal is time integrated but due to beam current fluctuation it is not possible to directly compare different spectra intensities. Moreover, the 60º tilt of the sample is due to technical limitations and to intensify the signal originating from the implanted layer.

The intensity increase of Eu lines after annealing is an indication of the decrease of radiationless de-excitation paths (e.g. defects), which is more evident on samples annealed in air, in accordance with RBS-C measurements. These bands are fewer (only visible those centred at 590 nm, 616 nm, 632 nm and 658 nm) and

weaker after implantation. Up conversion at 612 nm [Pet08] was not evident. The presence of Eu^{2+} is excluded since its broad *d* - *f* transition emission around 450 nm was not observed. The assignment of emission bands is difficult because besides purely electronic transitions the spectra contain vibronic and satellite lines, lines due to Eu^{3+} in lattice sites with different local symmetry. In fact, the transitions to $^7F_2$ and $^7F_4$ states are sensitive to the local electric environment and the abundance of bands at their standard values is an indication of the presence of Eu^{3+} in a variety of crystalline symmetries [Ozu04]. This is particularly possible when polymorphic phases are

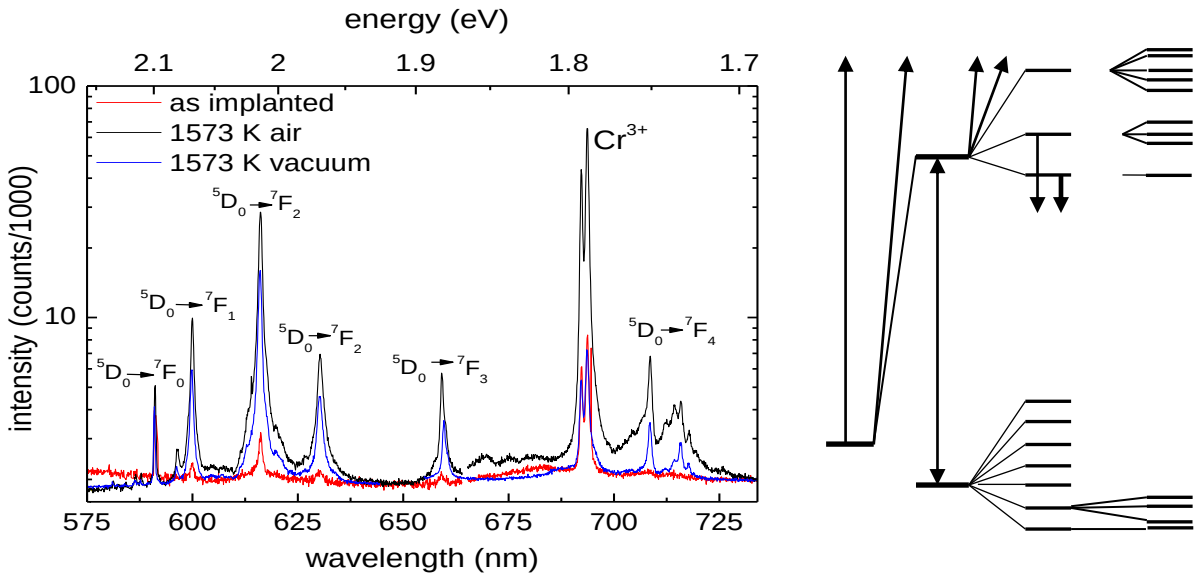

present, which is the case, with some C-type Eu_2O_3 probably mixed with B-type form.

Figure 4.84 – IBIL spectra measured at 60º of sapphire implanted with 1×10^{16} cm^{-2} Eu^+, as implanted and after annealing at 1573 K for one hour in air and vacuum. On the right side is represented the energy diagram of Eu^{3+}.

At this stage it was interesting to compare IBIL data with standard PL measurements. *Figure 4.85* shows the spectra obtained with IBIL and PL on a sample implanted with Eu. The PL spectrum was taken below RT and that is the reason for the Fe-related lines to be so well resolved (in the RT spectrum their intensity is hugely reduced). The spectra are very similar, despite the different nature of the excitation source.

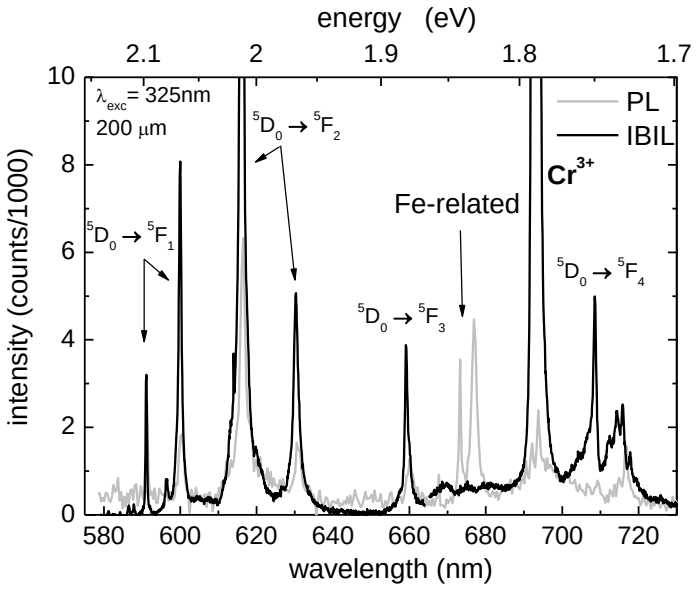

Figure 4.85 – Comparison between IBIL and PL data of Eu implanted sapphire.

Using the definition of Ozuna and co-workers of the asymmetry ratio –

it is the quotient between the intensity of the electric dipole allowed transition $^5D_0$ - $^7F_2$ and magnetic dipole allowed transition $^5D_0$ - $^7F_1$ (which is insensitive to the local field) – it is possible to ascertain the degree of symmetry of the location of the Eu^{3+} ion [Ozu04]. For the as implanted samples this is a low ratio (1.3), an indication of the high symmetry and weak electric fields present around europium ions. This ratio increases to 2.7 after annealing in vacuum and reaches 2.9 after annealing in air. This is a consequence of the movement of the Eu ions to lower symmetry sites after annealing, which, in accordance with RBS-C results, is more efficient when the annealing is carried in air. Time dependent measurements would allow determining the lifetime of these centres, necessary to ascribe definite positions to the ions.

In principle, it should be possible to relate this asymmetry ratio to the minimum normalized yield measured with RBS-C. Figure 4.86 shows the evolution of these quantities as a function of the annealing temperature (for the highest fluence). There is a coherent trend in the two parameters, both decreasing with annealing temperature. The precise measurement of the beam current may provide more precise values and possibly allow to directly estimating the implanted fluence.

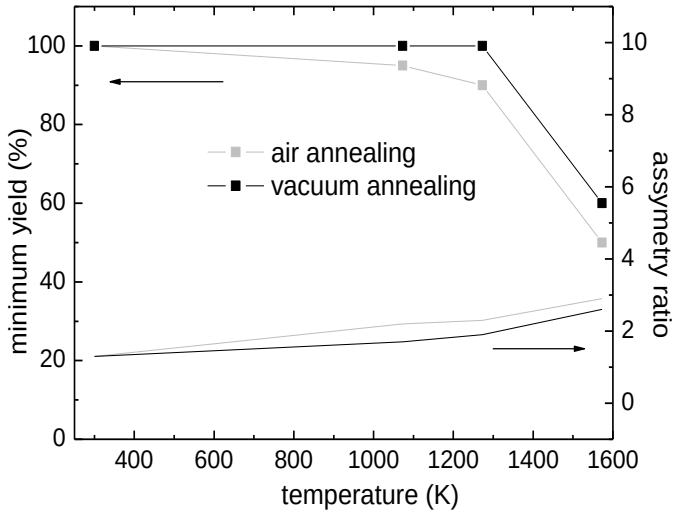

Figure 4.86 – Comparison of the experimental damage parameters minimum yield (measured with RBS-C) and asymmetry ratio (measured via IBIL), as a function of the annealing temperature for the sample implanted with 1×10¹⁶ cm⁻² Eu⁺.

In the scope of the tentative analysis with IBIL conducted at this initial stage, grazing incidence measurements were also performed, aiming at minimizing the signal from the host sapphire and maximizing the path of the ions inside the implanted layer. The spectra taken at 45º, 60º and close to 90º are shown in Figure 4.87.

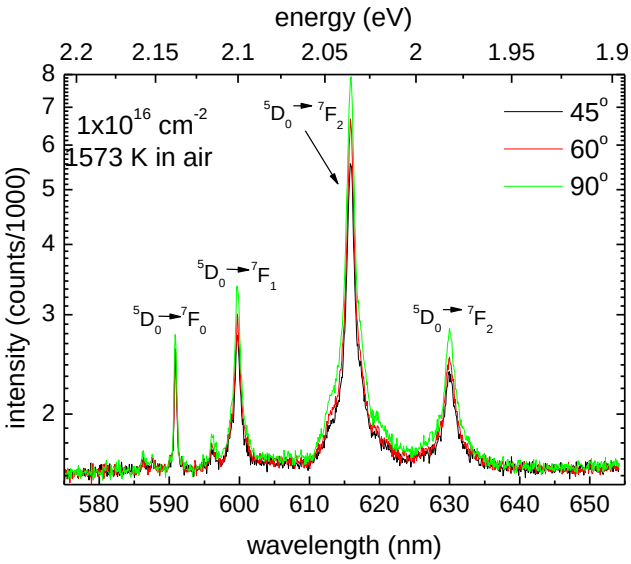

Figure 4.87 – Comparison of IBIL spectra collected at 45º, 60º and close to 90º (grazing incidence) of c-cut sapphire implanted with 1×10¹⁶ cm⁻² Eu⁺ and annealed in air at 1273 K.

The intensity of the Eu related lines increases slightly with the tilt angle. It should be noted that by tilting the sample the beam spot also increases and thus the luminescence gain is due to both the increased path of the

beam in the implanted region as well as to its broadening to an ellipsoidal cross section. These effects allow for better resolution.

During analysis it was possible to see that the luminescence of these samples changed from red to blue with the irradiation time. To ascertain this, spectra were taken in the Eu related emission range (Figure 4.88) as a function of the irradiation time. The samples are continuously irradiated and 10 s acquisitions are recorded at the specified times.

Regarding the Eu signal, the spectra intensity decays with irradiation time, as can be seen in Figure 4.88 for the 616 nm emission. This feature was attributed to thermal quenching by Castillo and co-workers [Cas08], using proton beam currents of 20 nA, at normal incidence. In our case, less than 1 nA was used in a tilted direction (larger volume irradiated) and so the loss of intensity may also be related to defect production during irradiation. These defects would, as previously mentioned for Cr^{3+}, provide non radiative paths for deexcitation. In fact, as previously stated, the emission of these samples changes from red to blue as the irradiation time increases. The decrease in the Eu signal with the irradiation time is similar to that of impurities such as Cr or Ga [Mor02].

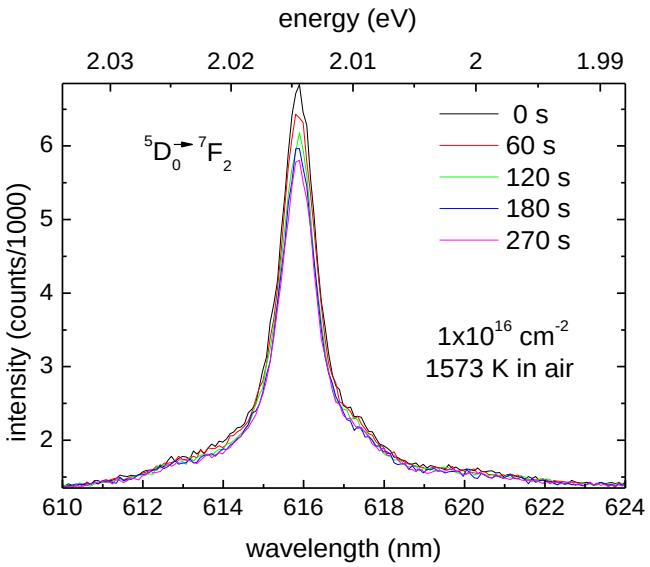

Figure 4.88 – IBIL spectra of c-cut sapphire implanted at RT with 1×10^{16} cm^{-2} Eu^+ and annealed in air at 1573 K in the 616 nm range as a function of the irradiation time.

4.5.3 Yb implantation

Sapphire c-cut samples were implanted at RT with 1.6×10^{15} cm^{-2} 300 keV $^{174}Yb^{2+}$ ions, and annealed at 1573 K for one hour either in vacuum (2×10^{-4} Pa) or air (ambient atmosphere). The low fluence was used to avoid Yb clustering and concentration quenching of the luminescence and limit the radiation damage, while high annealing temperature was needed to maximize the recovery of the crystalline quality of sapphire, providing a defect free environment for the new structures created. RBS, RBS-C, XRD, OA and IBIL experiments were used to characterize the systems formed after implantation and after each annealing stage.

4.5.3.1 Results and discussion

4.5.3.1.1 Structural studies

The RBS-C measurements presented in *Figure 4.89* were performed after implantation to measure the distribution of the implanted species as well as that of the radiation damage produced during implantation in the host lattice, particularly in the Al sublattice. *Figure 4.89*a shows the RBS-C spectra of the as implanted sample. Regarding the damage profiles, after implantation of this low fluence, 1.6×10^{15} cm^{-2}, a large amount of defects is already visible in the Al (and O) sublattice, in a double peak feature, with maxima at the surface and around 100 nm and extending up to 130 nm. The first peak (with χ_{min} = 20 %) is the usual surface damage peak while the latter (χ_{min} = 25 %) is assigned to lattice atoms displaced near the end of range of the implanted ions. E_D is 3.7×10^{22} keV cm^{-3}, well below the amorphization threshold of sapphire suggested by Mouritz and co-workers [Mou87]. In deeper regions χ_{min} = 15 %.

The double peak behaviour differs from that of the Eu implantation (cf. Figure 4.72), and, in fact, from all other ions implantations studied in this thesis, where only one damage peak is observed after implantation. This is explained by the higher implantation energy (300 keV) used in this case, which leads to a larger separation between the surface damage peak and the maximum lattice displacements peak. Indeed, due to the higher energy of the incoming ions the displaced ions are projected to a higher depth. In the energy range used with TM ions this effect accounts for the shallow highly crystalline surface layer. This double peak feature in the Al lattice on the aligned spectra was also observed by Alves and co-workers after implantation of 4.0×10^{15} cm^{-2} Er^+ ions with 200 keV at RT in sapphire [Alv95]. Similar features would occur for very low fluences (10^{14} cm^{-2}), where the surface defects and end of range disorder are low enough not to overlap, as in the work of Mouritz and co-workers with 10^{15} cm^{-2} 100 keV In^+ implantation at RT in sapphire [Mou87].

The Yb profile is asymmetric being properly fit with NDF code by two layers of Yb:Al_2O_3, with maximum concentration (0.5 at. %) at 65 nm, in good agreement with SRIM prediction of a nearly Gaussian distribution (Kurtosis = 0.25 and skewness = 3.00) centred at 61 nm (cf. Table 4.50). The corrected FWHM of the implanted profile is about 20 nm, far from the code prediction of 30 nm. Some dechanneling (χ_{min} = 50 %) is observed in the Yb profile, an indication of the non-random distribution of Yb after implantation. This is better channelling than that obtained in the case of Eu implantation of a similar fluence and average concentration, where χ_{min} = 70 %, which may be related to a somewhat higher affinity of Yb for oxygen. This is also ascribed to the larger spatial distribution due to the higher implantation energy. Moreover, E_D is also larger (0.37×10^{23} keV cm^{-3} vs. 0.17×10^{23} keV cm^{-3}), providing the damage and thermal input for faster diffusion.

Given the existence of significant channelling in the Yb profile after implantation, detailed angular scans were performed in order to assess the site location of this ion in the sapphire matrix. These scans are presented in *Figure 4.89*b, and were obtained for the regions marked in the corresponding RBS-C spectra, clearly showing the existence of alignment of the Yb ions with sapphire after implantation in the <0001> and <$02\bar{2}1$> directions.

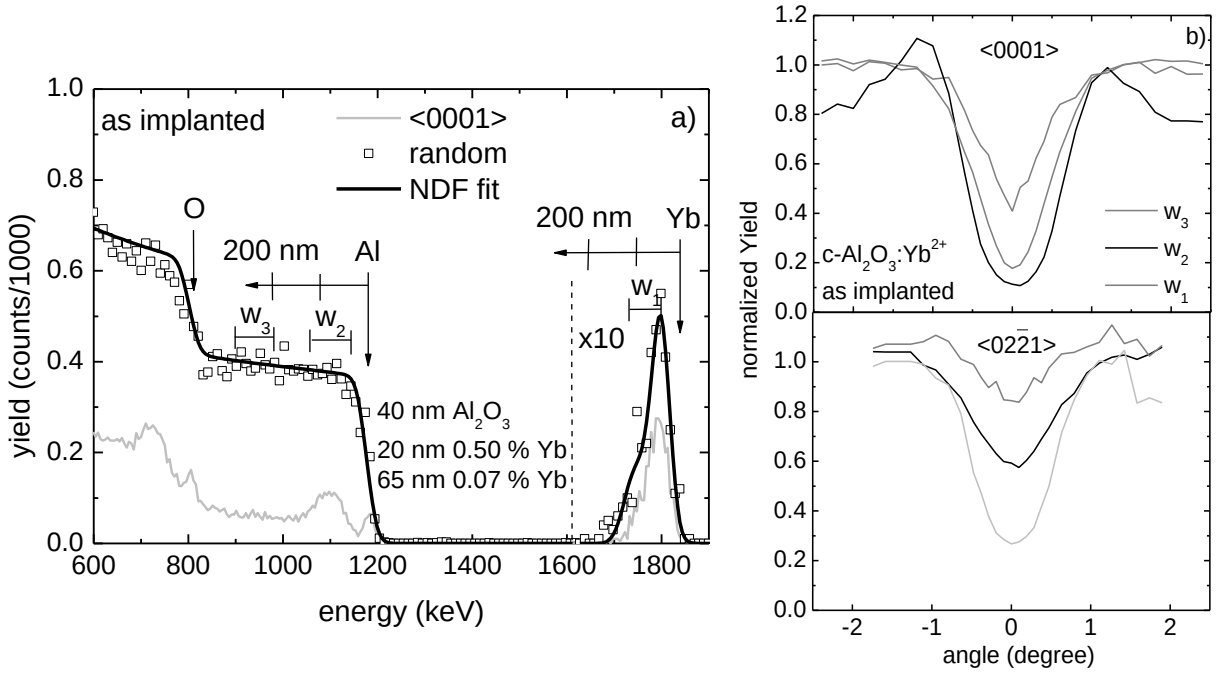

Figure 4.89 – Sapphire c-cut samples as implanted at RT with 300 keV 1.6×10^{15} cm^{-2} Yb^{2+} ions: a) RBS-C spectra and b) detailed angular scans through <0001> (top) and <02$\bar{2}$1> (bottom) axes.

That is, after implantation a fraction of the Yb ions are already found in regular sites of the matrix. Using equation 3.28, the apparent substitutional fraction is about 40 %, i.e. 40 % of the implanted ions occupy lattice sites, probably Yb^{3+} substituting Al^{3+} along the c-axis.

To promote the recrystallization of sapphire and also to achieve a higher degree of substitutionality of Al by Yb, where the latter is optically active, thermal annealings were carried at 1573 K for one hour in air or vacuum. *Figure 4.90*a shows the RBS-C spectra obtained after the annealing in air.

After the annealing there is a major crystalline recovery of the host matrix, with a minimum yield of 5 % in the first 100 nm. The double peak feature observed in each sublattice after implantation is still visible but considerably attenuated. The Al surface region shows a higher improvement than that obtained with Eu implanted samples subjected to the same annealing (cf. Figure 4.73), which is related with both the higher concentration of Eu present in that region and also to the higher damage density produced upon implantation of those samples. Moreover, Eu is larger and more reactive than Yb and may thus have lower mobility and form compounds, respectively, which may delay crystalline recovery and ion diffusion. The minimum yield drops to 10 % in deeper regions.

Regarding the Yb profile, we observe a redistribution of the ions, now in a nearly rectangular shaped profile still centred at 65 nm but wider (FWHM of 95 nm), with the maximum concentration dropping to 0.12 at. %, as simulated by NDF code. A fluence loss of about 18 % is observed. Using the expression for the out diffusion processes, the diffusivity of Yb was about 10^{-22} m^2 s^{-1}, in accordance with the values obtained for the diffusion of this ion in apatite [Che00] or zircon [Che97]. The aligned spectrum in this region shows χ_{min} = 40 %, as in the as

implanted state. The mobility of Yb derives from its low size, the smallest of the RE elements. This has been observed in diffusion studies in other materials doped with several RE [Che97, Che00].

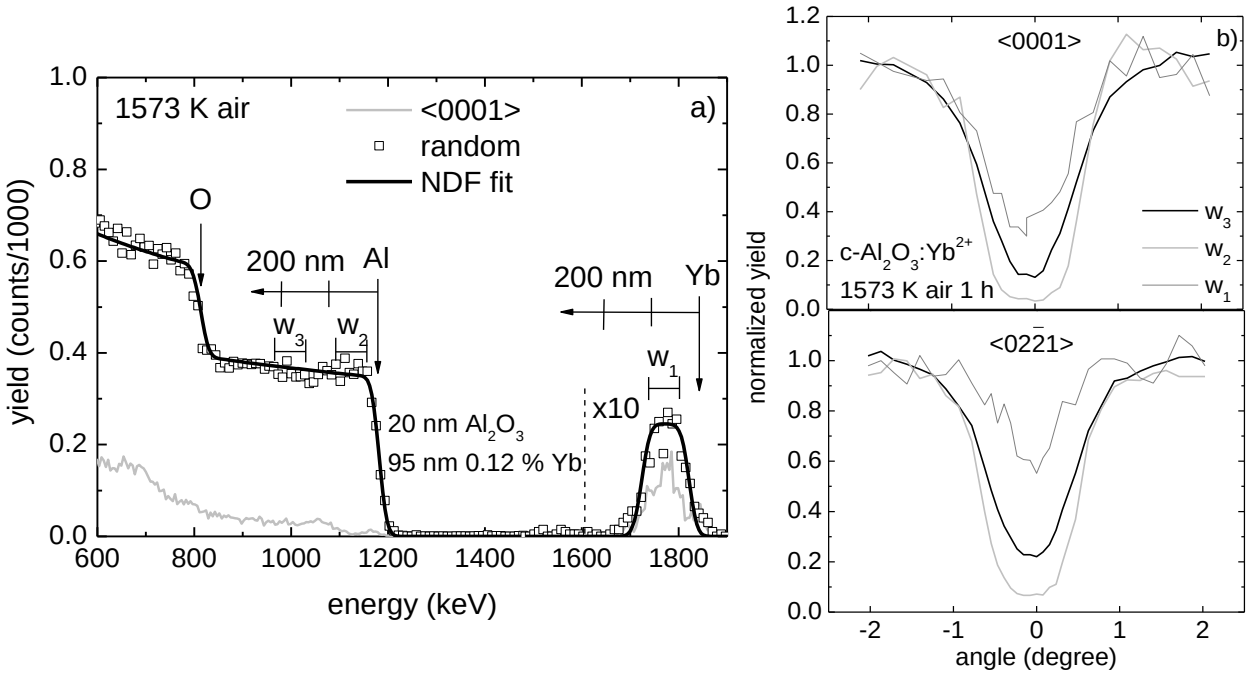

Figure 4.90 – Sapphire c-cut samples implanted with 1.6×10[15] cm[-2] Yb[2+] ions and annealed at 1573 K for one hour in air: a) RBS-C spectra and b) detailed angular scans through <0001> (top) and <$02\bar{2}1$> (bottom) axes.

The angular scans performed in the surface region for Al and Yb signals are shown in *Figure 4.90*b. The damage decrease in the host lattice is visible by the wider and deeper scans obtained in this region. The Yb curve is also deeper and wider, in particular in the <$02\bar{2}1$> direction, an indication of a higher degree of substitutionality after this annealing, which is now estimated to be of 50 %.

Similar heat treatment was carried out in vacuum. The RBS-C results are shown in *Figure 4.91*a. Again, a major crystalline recovery of sapphire is detected. Yet, a slightly higher amount of defects in the Al and O sublattices remain (χ_{min} = 15 %) as compared to the air annealed samples (χ_{min} = 5 %). This is reflected also in deeper regions, where χ_{min} = 13 %.

Regarding the Yb profile, there is a redistribution leading again to a nearly rectangular profile, with FWHM of 85 nm, with the maximum concentration of 0.12 at. % reached around 70 nm depth. There is a higher fluence loss (24 %) as compared to the annealing in air. Moreover, Yb dechanneling remains close to that found after implantation.

Detailed angular scans performed in the regions marked in the corresponding RBS-C spectra confirm the recovery of the crystalline quality of sapphire and the minor effect on Yb substitutionality (*Figure 4.91*b). In fact, the substitutional fraction at this stage is about 40 %, similar to the value obtained after implantation. Table 4.58 summarizes all RBS-C results for Yb implanted samples.

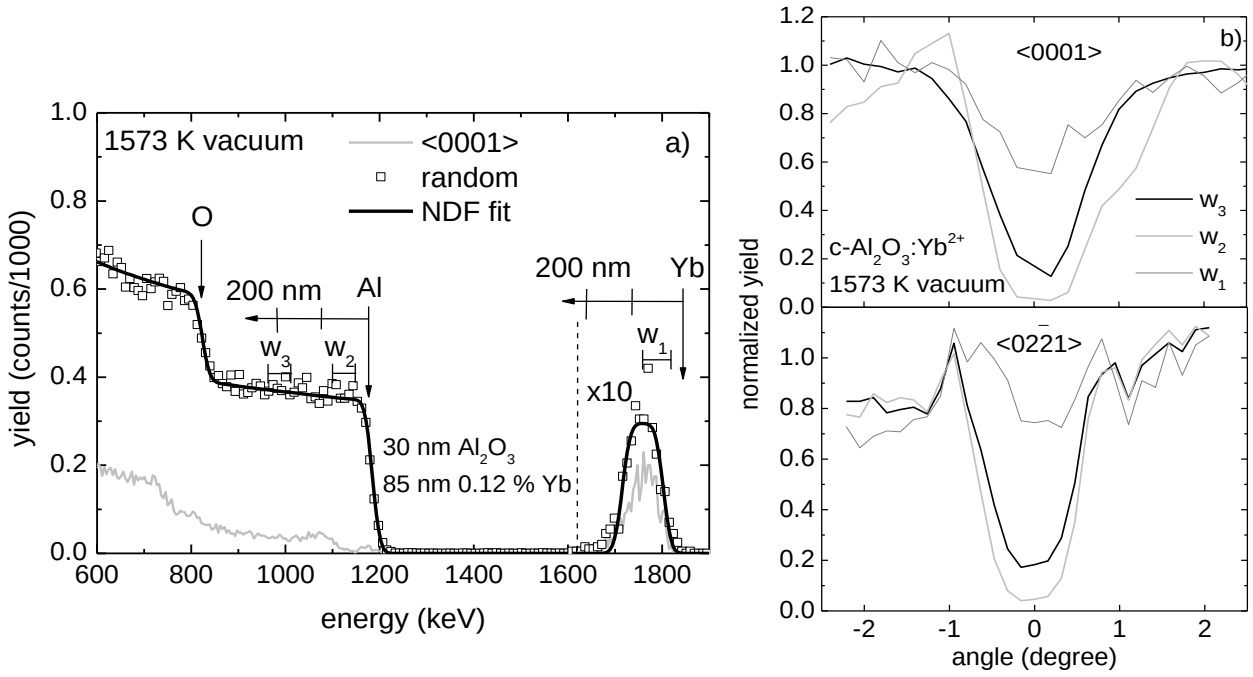

Figure 4.91 – Sapphire c-cut samples implanted at RT with 300 keV 1.6×10^{15} cm^{-2} Yb^{2+} ions and annealed at 1573 K for one hour in vacuum a) RBS-C spectra and b) detailed angular scans through <0001> (top) and <02$\bar{2}$1> (bottom) axis.

Table 4.58 – RBS-C results of sapphire c-cut samples implanted with Yb and annealed at 1573 K in air or vacuum.

sample	as implanted	1573 K air	1573 K vacuum
host matrix			
max. damage depth (nm)	0/90	120	130
χ_{min} (%)	20/25	5	15
damage extension (nm)	130	130	130
E_D (10^{22} keV cm^{-3})	3.7	-	-
deep region χ_{min}	15	10	13
implanted profile			
max. conc. depth (nm)	50	65	70
χ_{min} (%)	50	40	50
retained fluence (10^{15} cm^{-2})	-	1.32	1.21
fluence loss (%)	-	18	24
FWHM (nm)	20	95	85
max. conc. (at. %)	0.50	0.12	0.12
f_{sub}	40	50	40

These samples were analysed with XRD in order to identify the crystalline phases present. *Figure 4.92* displays the results obtained after implantation and after the annealing stages at 1573 K. The data from the annealed samples is translated vertically for clarity. After implantation already a small reflection from Yb_2O_3 is observed, with its <222> axis parallel to c-axis of sapphire, while the radiation damage produced in the host lattice is visible by the broadening of the (0001) reflection of sapphire. These precipitates are estimated to have around 35 nm. The annealing in air promoted the small growth of the oxide phase, with precipitates having average dimension of 38 nm, again with its <222> axis parallel to c-axis of sapphire, consistent with the thickness of the Yb layer and channelling measured

by RBS-C. This indicates that Yb_2O_3 is in C-type polymorph, with a cubic (bcc) Mn_2O_3 type structure of space group $Ia\bar{3}$, typical of sesquioxides of the heavy lanthanides, as previously discussed in the Eu:Al_2O_3 system (cf. *Figure 4.76*). The calculated lattice constant is *a* = 1.060 nm. Using equation 4.3 this implies a lattice mismatch of about 5 %.

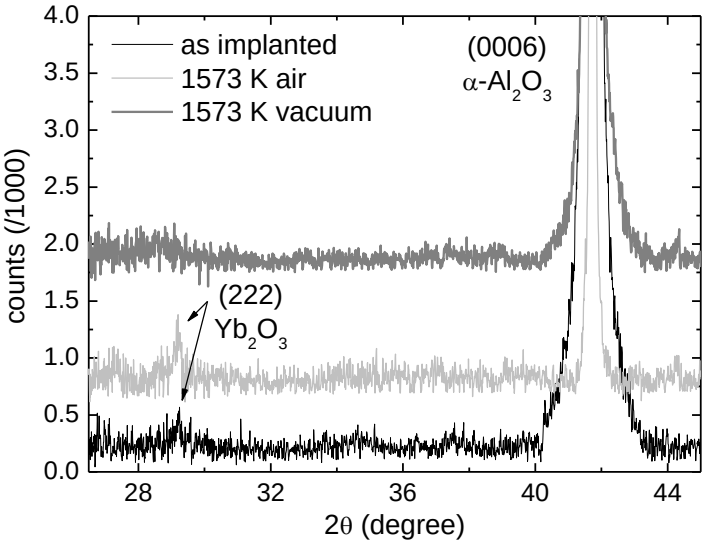

After this annealing step the reflection of the c-axis of sapphire narrows as a result of the recrystallization process already observed with RBS-C.

Figure 4.92 – XRD spectra of c-cut sapphire after implantation of 1.6×10^{15} cm^{-2} Yb^{2+} and after annealing at 1573 K in air or vacuum for one hour.

On the other hand, after the annealing in vacuum the oxide phase is essentially absent or diluted in very small and randomly oriented precipitates. The relative width of the (0001) reflection of sapphire at this stage reveals the existence of more defects than after annealing in air. The XRD results are summarized in *Table 4.59*.

Table 4.59 – XRD results of Yb implanted samples.

sample	2θ	phases	size (nm)	calculated and tabulated lattice dimensions (nm)	PDF card
as implanted	29.19	Yb_2O_3 (222)	35	1.060 / 1.043	00-041-1106
1573 K air	29.19	Yb_2O_3 (222)	38	1.060 / 1.043	00-041-1106
1573 K vacuum	-	-	-	-	-

The annealing in air provided enough oxygen to allow both the recovery of the host matrix and the formation of Yb oxides, which would otherwise be competing processes. In vacuum, recrystallization also occurs but to a lower extent due to the limited availability of oxygen, justifying the small difference on the substrate remaining defects. The low amount of oxygen available is essentially used in the formation of Yb oxide which is thermodynamically favoured over Al oxide at RT (-1814 kJ mol^{-1} vs. -1676 kJ mol^{-1}, respectively). However, Yb oxide grows in a still very disordered lattice and this may limit its growth and coherence with matrix host.

Figure 4.93 shows the calculated phase diagram of Yb_2O_3 – Al_2O_3 system, without O restrictions and thus better suited for the annealing in air case. For the lower concentration used in this work (0.5 at. %), the sesquioxide phase is expectable.

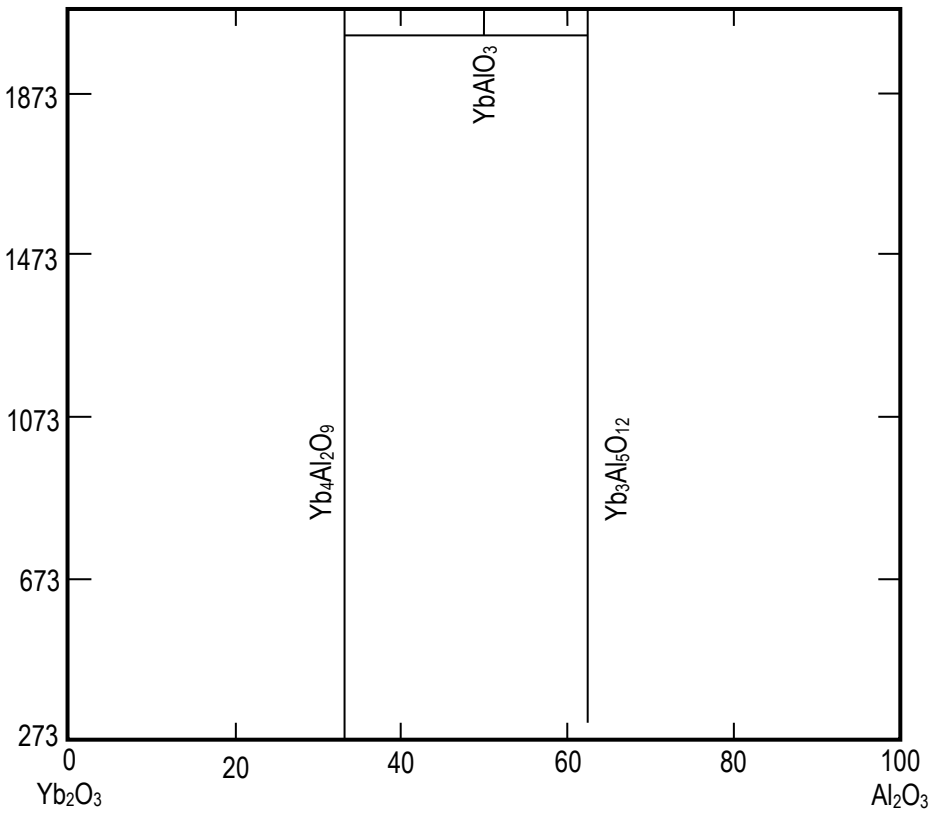

Figure 4.93 – Calculated phase diagram of Yb_2O_3 – Al_2O_3 system [Wu92].

4.5.3.1.2 Optical studies

4.5.3.1.2.1 Optical absorption

Optical extinction measurements were carried out in the wavelength range of 190 nm to 1100 nm mainly to inspect the defect related absorption region (cf. Table 2.3) and possible Yb phases. No significant absorption was present in the 650 nm to 1100 nm range in any case (and thus this range will not be displayed), despite Yb^{3+} absorbing in the 900 nm to 1000 nm region, as revealed by the work of Krebs and co-workers, who observed sharp absorption peaks from Yb^{3+} in sapphire doped with Yb, processed using the sol-gel method [Kre01]. However, even if their samples have comparable concentrations of Yb, this element is homogeneously dispersed in a thicker layer, which results in more intense absorption. The OA results in the 190 nm – 650 nm region are shown in Figure 4.94 for all samples. These spectra were corrected by subtracting reflections and thus the absorption coefficient concern exclusively to the implanted region.

The main feature observed after implantation is the development of an intense absorption band, centred at about 200 nm, which is assigned to the convolution of absorption by F and F^+ centres (at 205 nm and 203 nm, respectively), the latter being responsible also for the smaller bands at 225 nm and 258 nm (dashed lines).

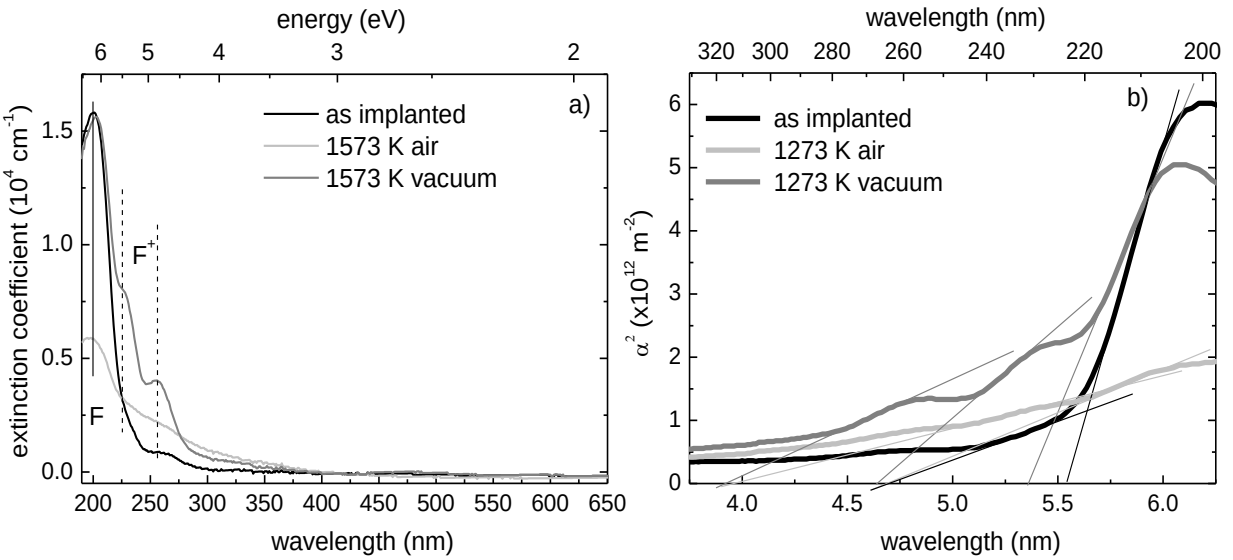

Figure 4.94 – a) optical absorption spectra of c-cut sapphire as implanted with 1.6×10^{15} cm^{-2} Yb^{2+} ions and annealed at 1573 K for one hour in air or vacuum and b) Tauc plot to determine the energy levels associated with each transition.

Upon annealing in air at 1573 K the 200 nm band decreases, coherently with the smaller amount of lattice defects observed in the corresponding RBS-C spectra. However, a large band centred at 260 nm develops, encompassing the F^+ bands at 225 nm and 258 nm. If this band is related to F^+ centres its increase implies the oxidation of the F centres, thus justifying the decrease observed in the F-band. Moreover, Yb^{2+} is also oxidised in this process to form Yb_2O_3, substituting aluminium with its 3+ oxidation state. An effective drain of all these extra electrons would be the reduction of the unbound aluminium ions (displaced during implantation) to metallic precipitates. The increase in absorption around 350 nm may be due to more complex F centres, e.g. F_2^+ (cf. Table 2.3). According to the literature, absorption related to Yb_2O_3 is not expected at these wavelengths.

Annealing in vacuum produces little change in the 200 nm band but a remarkable increase in the absorption at 225 nm and 258 nm, very similar to what was observed with Eu. Such an increase may, again, be due to the formation of Al precipitates or to the oxidation of F centres. In fact, as was the case with Eu, the Yb_2O_3 phase has a very low enthalpy of formation, being thermodynamically favoured over Al_2O_3 (-1814 kJ mol^{-1} vs. -1676 kJ mol^{-1} at RT), leading to consumption of the limited supply of oxygen and allowing for the formation of metallic aluminium precipitates. These may be responsible for the absorption in the 220 nm to 270 nm range, as shown in

*Figure 4.36*a. The estimative of this absorption feature was calculated with MiePlot code, with a 7 nm sphere of Al embedded in sapphire.

Table 4.60 displays the concentration of F-type centres at each stage, obtained by applying Smakula formula, assuming the optical features of the spectra of Figure 4.94 as being due to F-type centres only. A large amount of defects (even if in the 0.1 at. % range) is detected after implantation. The annealing procedure tends to reduce its concentration, more efficiently when performed in air than in vacuum.

Qualitatively the results are coherent for F-centres, with a decrease of F-centre concentration upon either annealing, as expected due to the crystalline recovery observed in the corresponding RBS-C and XRD spectra.

The increase in F^+ centre concentration indicates that the oxidation of F-centres may also be responsible for the decrease of the F-centre absorption. Moreover, the annealing in vacuum seems to promote a higher oxidation rate, presenting an overall stronger absorption in this range. Nevertheless, the RBS-C spectra show that major crystalline recovery was also obtained after annealing in vacuum. Again, as in the case of Eu implantation, we propose that not only the oxidation of F-centre occurs via the formation of metallic Al precipitates, but that these Al precipitates present a SPR band which coincides with the F^+ centre transitions and thus leads to the overestimation of defect concentration. The annealing in vacuum favours the Al precipitation and thus justifies the marked increase in the absorption, as compared to the samples annealed in air.

Table 4.60 – F-type centre concentration on Yb implanted samples, after implantation and after annealing for one hour at 1573 K in air or vacuum.

sample	experimental data				F-centre concentration	
	λ (nm)	$\Delta\lambda$ (nm)	U (eV)	u (cm^{-1})	N_0 ($\times10^{16}$ cm^{-3})	$N_{0,imp}$ ($\times10^{19}$ cm^{-3})
as implanted	201.97	24.98	0.76	4.91	1.51	5.81
	224.72	25.96	0.64	0.89	0.45	1.74
	257.10	45.42	0.86	0.57	0.39	1.50
1573 K air	201.56	26.03	0.80	1.82	0.59	2.26
	224.72	33.26	0.82	1.16	0.76	2.91
	258.07	46.34	0.87	0.96	0.66	2.55
1573 K vacuum	204.10	23.99	0.72	4.29	1.25	4.81
	227.81	23.82	0.51	1.61	0.73	2.81
	255.72	41.78	0.80	1.40	0.89	3.43

The Tauc plot of all samples is presented in *Figure 4.94*b. A common gap at 3.9 eV occurs for the annealed samples, which we ascribe to the energy gap of Yb_2O_3. The higher energy gaps are from F-centre transitions while the gap at 4.6 eV, common to all samples, might be due to the SPR absorption of Al precipitates. The band gap found for Yb_2O_3 is similar to that of Eu_2O_3 (4.0 eV).

4.5.3.1.2.2 IBIL

The optical response of these systems was also monitored with IBIL, which spectra are shown in *Figure 4.95*. In the blue region of the spectra (*Figure 4.95*a), the main feature is a large band centred around 420 nm, the characteristic emission of F centres. However, this band is better explained, and fitted, by considering three Gaussian shaped bands centred at 412 nm, 429 nm and 451 nm, as represented in the figure. This type of convolution was also observed in the pristine and Eu emission spectra. Regarding the red and IR region of the spectrum (*Figure 4.95*b), it is again visible, as in the case of Eu, the strong emission line at 694 nm due to native Cr^{3+} emission in the sapphire substrate. Also similarly to the Eu implantation, there are more emission bands from Yb after annealing in air than after annealing in vacuum. This observation favours the existence in a larger extent of Yb^{3+}, and thus Yb_2O_3, in the air annealed samples, which also has a lower concentration of defects, which may act as non-radiative decay paths.

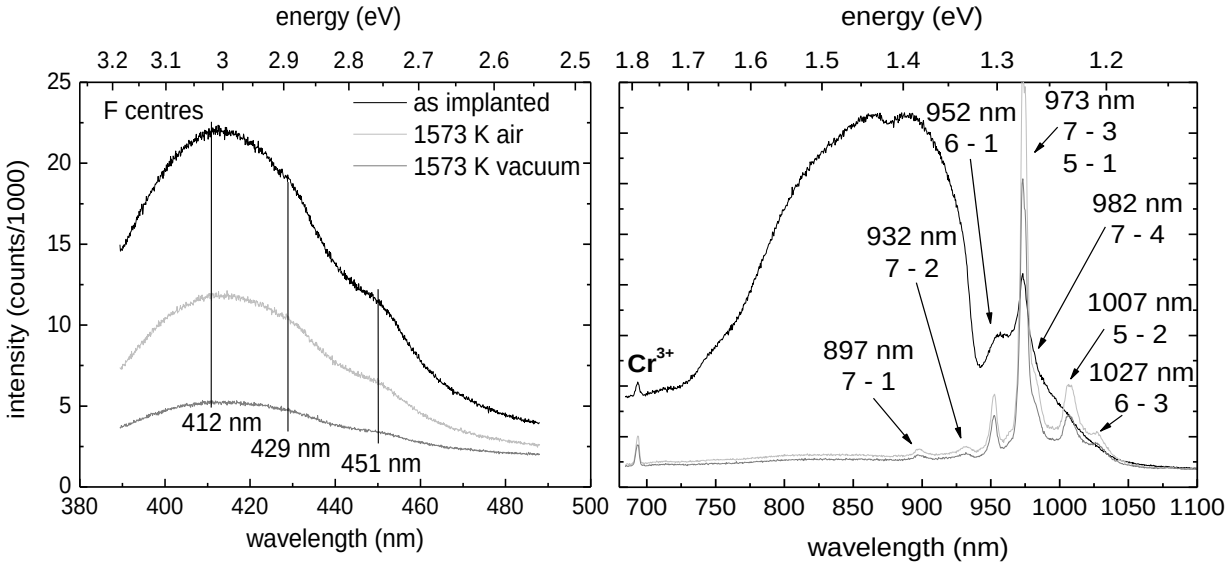

Figure 4.95 – IBIL spectra recorded at 60º of c-cut sapphire as implanted at RT with 300 keV 1.6×10^{15} cm^{-2} Yb^{2+} ions and annealed at 1573 K for one hour in air or in vacuum: a) F-centre region and b) Yb^{3+} emission region.

Using this spectrum it is possible to associate the energy level diagram presented in Figure 4.96 for Yb^{3+} in sapphire, which is similar to that presented by Krebs and co-workers in Yb doped sapphire fibres [Kre01]. It's worth noting that excited states populated at RT may limit the accuracy of this scheme, which must be verified by other techniques, such as Raman spectroscopy or low temperature optical absorption. Moreover, the FWHM of these RT transitions may hide the possible diversity of site symmetries of Yb in this system.

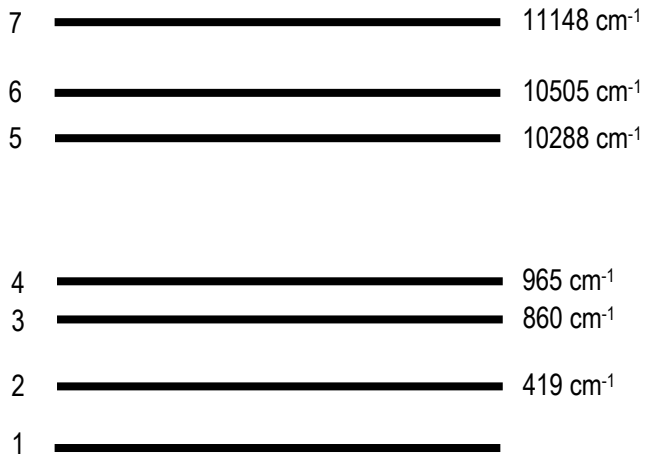

Figure 4.96 – Schematic energy level diagram of Yb^{3+} on sapphire.

No significant emissions were recorded in the 490 nm – 690 nm range. In particular cooperative or pair luminescence at ~500 nm [Nak70] was not observed, probably due to the low concentration and dispersion of Yb ions since this phenomenon is expected when the Yb pair is separated by 0.6 nm or less [Auz94]. The broad emission band in the 750 nm to 950 nm is attributed to Ti (cf. Table 2.3), and is in fact the emission responsible for the tunability of Ti:sapphire lasers.

4.5.4 Discussion

Sapphire c-cut crystals were implanted at RT with 100 keV europium or 300 keV ytterbium ions with fluences up to 1×10^{16} cm^{-2}, and subsequently annealed up to 1573 K in air or vacuum for one hour.

In the case of Eu, intensive surface damage is observed through RBS-C for the 5×10^{15} cm^{-2} implantation, χ_{min} reaching 75 %. This effect is well above the typical values for these implantation conditions, $E_D = 7\times10^{22}$ keV cm^{-3}, being an order of magnitude smaller than the amorphization threshold found by Mouritz and co-workers [Mou87]. This is only observed for heavy or chemically reactive elements (such as titanium [Mar02]) and agrees with the fact that Eu is the most reactive of the RE elements.

In the case of Yb implantation, the increased damage extension resulting from higher implantation energy prevents a significant damage energy and χ_{min} is about 25 %.

Figure 4.97 compares the evolution of the minimum yield measured in the Al sublattice (full marks) and on the implanted profile (open marks) for TM, NM and RE ions. Clearly the Eu implantation produces the higher dechanneling ratio in both regions of the spectra at the lowest energy deposited: 5.0×10^{22} keV cm^{-3}, demonstrating the strong chemical effect, induced by the highly reactive Eu.

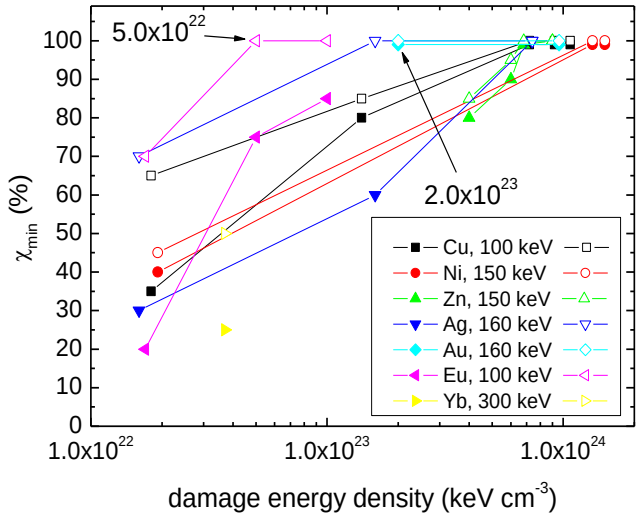

Figure 4.97 – Damage energy deposition for RE, NM and TM ions implanted in sapphire at RT.

The predictions of SRIM regarding FWHM and R_p of the as implanted profiles were systematically different from the experimental measurements, namely for the higher fluences. Figure 4.98 shows the difference between the experimental values and the code predictions as a function of the implanted fluence.

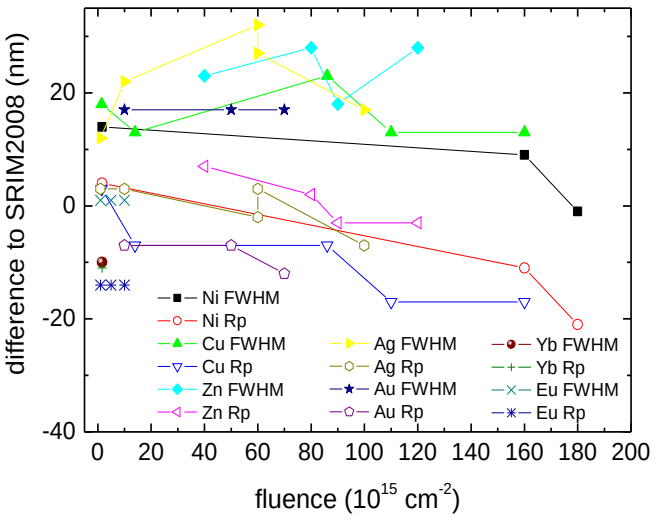

Figure 4.98 – FWHM and R_p difference between the experimental values and SRIM prediction for TM, NM and RE systems.

In the case of RE ions, implanted only in the low fluence regime, the FWHM is correctly predicted in the case of Eu while the Yb implantation is the only case where SRIM underestimates this value. The calculated

projected range is also overestimated, even more than in the case of most TM and NM implantations. The reactiveness of Eu may justify these differences. As the fluence increases and the material is damaged the FWHM converges to the SRIM value while R_p diverges, due to the densification of the material.

The radiation damage produced was measured by RBS but also via OA measurements. *Figure 4.99* compares the F- and F^+-centre formation as a function of the implanted fluence for TM, NM and RE implantations. It is clear that for the heavier elements at the lower fluences the F-centre (open marks) dominates. As the fluence increases the values tend to be similar and for F = 1.0×10^{16} cm^{-2} the F^+-centres dominate. TM always show a higher concentration of F-centres, even for F = 1.4×10^{16} cm^{-2}.

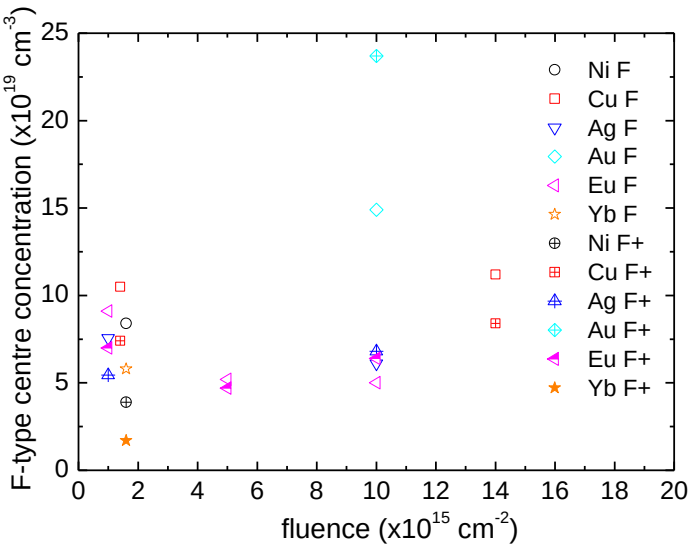

Figure 4.99 – Defect evolution with the implanted fluence for TM, NM and RE ions.

The samples were subsequently annealed up to 1573 K in air or vacuum. In the case of Eu, the samples keep the as implanted profiles unchanged irrespective of the implantation fluence and annealing atmosphere up to 1273 K. We propose that europium reacts already during implantation where it is found randomly distributed, a state which is kept unchanged up to 1273 K annealings. The structure only recrystalizes by annealing at 1573 K where some redistribution occurs with a fraction of Eu occupying regular sites, possibly with partial substitution of the Al sites in the 3+ oxidation state, in an oxide phase (Eu_2O_3) with some coherence with the host matrix. This oxide phase may be present after annealing in air and also after annealing in vacuum, but in the latter case formed in competition with the reconstruction process of the matrix for the available oxygen. This competition concurrently retards the crystalline recovery, as corroborated by optical absorption and ionoluminescence measurements. No loss of Eu was observed, despite its low melting point (and hence enhanced mobility at the temperatures used), another indication of its stabilization in a compound. XRD measurements reveal the presence of 16 nm sized Eu_2O_3 precipitates after annealing in air, aligned with (100) or (111) plane parallel to the c-plane of the host matrix. On the other hand, annealing in vacuum produces a mixture of Eu_2O_3 and Eu_3O_4 precipitates (20 nm and 7 nm, respectively) due to the limited amount of oxygen.

In the case of Yb implantation, Yb_2O_3 is already observed after implantation. At 1573 K there is some out-diffusion and evaporation, with about 15 % loss after annealing in air and 25 % loss in vacuum. The host structure recrystalizes with some Yb moving to regular sites, possibly with partial substitution of the Al sites in the 3+ oxidation state, on an oxide phase with some coherence with the host matrix. Yb_2O_3 is again detected after annealing in air, in large precipitates (38 nm). In the case of the annealing in vacuum it is possible that the competition with the reconstruction process of the matrix for the available oxygen may limit the full crystallization of Yb sesquioxide,

which was not observed in XRD. This competition, as in the case of Eu implantation, concurrently retards the crystalline recovery, but also promotes Yb redistribution, out diffusion and eventually evaporation due to its low melting and boiling temperatures. The redistribution of the RE ions by annealing is accompanied by the optical activation of these ions, more evident after annealing in air than in vacuum.

The optical properties of these systems improved after annealing by the annihilation of radiation defects that act as non radiative de-excitation paths and by the distribution of some of the implanted ions into regular lattice sites. This process is enhanced in oxygen rich atmosphere. This recovery is higher upon annealing in air since there is enough oxygen for both matrix recovery and RE oxide formation. In vacuum these are competing processes therefore leading to lower recrystallization of sapphire and formation rate of RE oxide phases. Table 4.61 list the enthalpy of formation of RE and Al oxides.

Table 4.61 – Formation enthalpy of Al and RE oxides ($-\Delta H^0_{298}$), kJ mol^{-1}.

Al_2O_3	Eu_2O_3	Eu_3O_4	Yb_2O_3
1676	1651	2271	1814

Regarding the thermal evolution of RE:Al_2O_3 systems, the process in air may be modelled as follows:

$$20\ Al + 30\ O + 0.02\ RE + n\ O_2 \rightarrow 10\ \gamma\text{-}Al_2O_3 + 0.01\ RE_2O_3 \rightarrow 10\ \alpha\text{-}Al_2O_3 + 0.01\ RE_2O_3 \quad [4.10]$$

On the other hand, in vacuum:

$$20\ Al + 30\ O + 0.02\ RE \rightarrow \sim 10\ \gamma\text{-}Al_2O_3 + 0.01\ RE_2O_3 + 0.03\ Al \rightarrow \sim 5\ \alpha\text{-}Al_2O_3 + \sim 5\ \gamma\text{-}Al_2O_3 + 0.01\ RE_2O_3 + 0.03\ Al \quad [4.11]$$

The stoichiometric coefficients simply reflect the estimated atomic fraction of each element. The annealing in vacuum would therefore free aluminium which would eventually precipitate in nanometre sized precipitates, as suggested by the OA measurements in the UV region, which we attribute to the SPR band of aluminium in spherical precipitates (r = 7 nm), and by the high dechanneling yield in the Al sublattice (as compared to the O sublattice) measured with RBS-C.

The first experimental results with the IBIL technique were quite successful, allowing characterizing the emission from Eu and Yb ions embedded in sapphire, as well as the defects of the host matrix, namely F-centres and some impurities. Moreover, by playing with beam direction as well as with the irradiation time the most advantageous conditions for analysis were established: the more tilted the best resolution while irradiation time must be minimized in order not to produce extra defect centres and avoid quenching of the luminescence centres. These processes may in fact be correlated, as the measured increase of the defect signal is accompanied by a decrease in the Eu emission. From the F-colouring curves measured on this system, the lifetime of F^+-centre traps in sapphire was estimated to be around 400 s.

It was not possible to achieve a strong correlation between the asymmetry ratio of Eu emission and the minimum yield measured with RBS-C, partially due to the major uncertainty on this later measurement, which depends strongly on the region of analysis.

Regarding Yb, an energy level diagram was sketched, namely from the emission measured after annealing in air.

The loss of RE, as compared with the TM and NM systems, as a function of the annealing temperature for each atmosphere (air and vacuum) is shown in Figure 4.100.

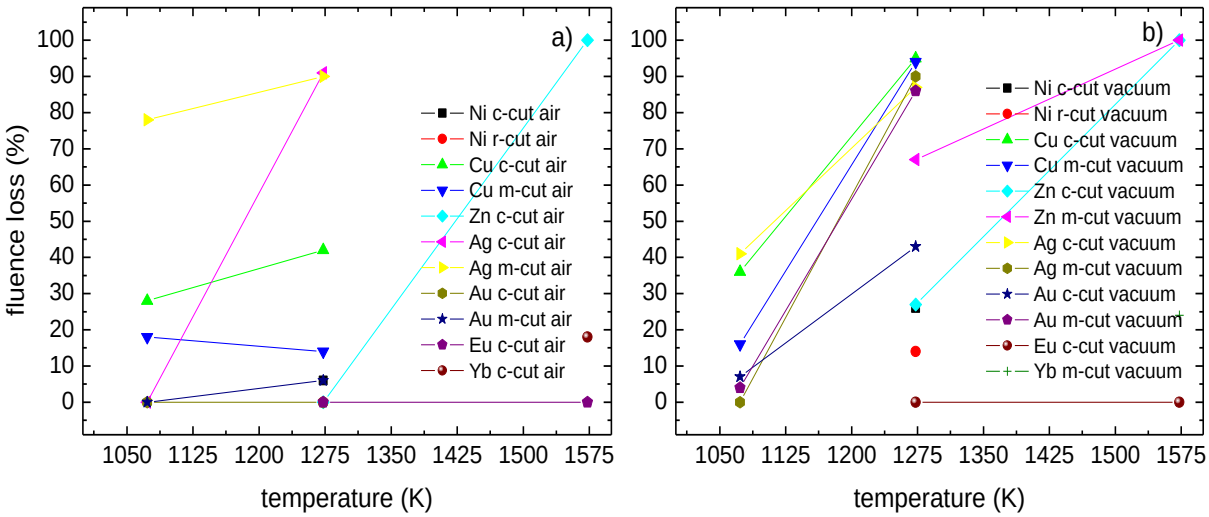

Figure 4.100 – Fluence loss vs. annealing temperature for TM, NM and RE systems: a) air and b) vacuum atmosphere.

It is clear that the RE are amongst the most stable elements, regarding volatilization, since no loss of Eu is observed at all while minor losses of Yb occur only at 1573 K.

Table 4.62 summarizes the annealing behaviour of the systems upon annealing up to 1573 K.

Table 4.62 – Evolution of the TM, NM and RE systems implanted with the highest fluences upon annealing.

temperature	annealing in air	annealing in vacuum	extreme cases
as implanted (~RT)	O_2, γ-Al_2O_3, Me^0, possibly some amorphous Me_xO_y	γ-Al_2O_3, Me^0, O_2, possibly some amorphous Me_xO_y	Yb forms crystalline Yb_2O_3
1073 K	O_2, γ-Al_2O_3, Me_xO_y Unstable oxides decompose	γ-Al_2O_3, Me^0 Unstable oxides decompose	
1273 K	O_2, cation counter diffusion and formation of $MeAl_2O_4$, γ to α-Al_2O_3 complete, Ag^0 and Au^0	partial γ to α-Al_2O_3, Me^0 low melting point elements near the surface evaporate	Yb retards alumina transition
1573 K	some loss of Yb, no loss of Eu Eu_2O_3 and Yb_2O_3 form	some loss of Yb, no loss of Eu	

5 Final conclusions

The results obtained by this work clearly set the implantation conditions and annealing parameters of relevance for the development of the systems sought. A set of important conclusions is summarized in what follows.

For low fluences (below 5×10^{15} cm^{-2}) the implanted ions occupy mostly regular sites in the sapphire lattice and low levels of damage are produced. Total dechanneling in the profile of the implanted species occurs for concentrations in the range of 0.20 at. % to 0.75 at. %, limiting the possibility of site location studies.

As the fluence increases the damage concentration and extent increases and the distribution of the implanted ions among the available lattice sites is no longer well defined and it becomes essentially random.

Amorphization is eventually reached for fluences that strongly depend on the nature of the implanted species. For small ions (TM Ni, Cu and Zn) this occurs near 1.0×10^{17} cm^{-2}. For larger, heavier ions (NM and RE) amorphization is found for lower fluences (e.g. 1.0×10^{16} cm^{-2} in the cases of Au and Eu).

The amount of defects created during implantation and the nature and atomic concentration of the implanted species determine also the resulting system at a given temperature. After implantation TM and RE form oxides which react with polycrystalline alumina. As the fluence increases the metallic state dominates in TM and NM systems. The extension and output of the thermally activated reactions depends on these initial conditions as well as on the temperature and atmosphere of annealing.

In all cases it was found that the formation of new phases demands the implantation of a threshold atomic concentration. TM and NM ions in atomic concentrations exceeding 10 at. % will lead to the formation of optically metallic active precipitates after implantation which will develop or transform in mixed oxide phases, depending on the annealing parameters. Below this value either phase is too diluted or small to be observed by the experimental techniques used. RE ions are exceptions due to its remarkable reactivity with oxygen, comparable to that of Al, which results in the formation of sizeable phases even at 6 at. %.

Ion implantation of high fluences of Ni, Cu, Zn, Ag and Au promoted the formation of metallic nanoparticles already during implantation, XRD revealing average diameters of the order of 10 nm, with alignment with the matrix, despite the amorphized or polycrystalline nature of the surrounding medium. The metallic precipitates are firstly detectable through the development of SPR bands, which also helped estimating their dimensions. The peak position of these SPR bands may be tuned with the implanted fluence.

Annealing in vacuum promoted essentially the formation of metallic phases of TM and NM ions, with a reduction from Me^{+} to Me^{0}. Vacuum acted as a reducing atmosphere. Apparently, after the annealing in vacuum pure metallic compositions are preferred, these metals competing less effectively with Al for the unbound O. However, small amounts of ZnO and $ZnAl_2O_4$ or $NiAl_2O_4$ spinels do form in samples implanted with Zn or Ni, possibly due to incomplete reduction. In the case of Zn, the type of oxide seems to depend on the amount of Al displaced during implantation: it is lower in m-cut samples where the formation of ZnO is observed; it is higher in c-cut samples where a spinel phase is obtained. The presence of stable oxides (NiO and ZnO) formed in the initial moments of annealing may concurrently explain the incomplete reduction of mixed oxides. The phases formed are present around the implantation mean depths R_p with nanometre sizes. The crystalline recovery of the host matrix occurs in a limited extent, in these high fluence implantations. In spite of the tendency for the formation of metallic

nanoaggregates, the annealing in vacuum also facilitated the evaporation of low melting point ions, such as Zn, or the decomposition of unstable oxides (in the case of Ag or Cu), resulting in partial loss of the material through the surface.

Increasing the annealing temperature essentially increases the size and crystalline quality of the precipitates, in close correlation with the crystalline recovery of the matrix. As temperature increases the radiation damage decreases as the displaced ions tend to regain their lattice sites.

These changes are reflected in large variations on the SPR band peak position.

On the contrary, annealing in air allowed the formation of stable oxides of the implanted species and also mixed oxide phases, namely spinels ($NiAl_2O_4$, $CuAl_2O_4$ and $ZnAl_2O_4$) and RE sesquioxides, usually accompanied by major crystalline recovery of the implantation damage in the host matrix, as compared to annealing in vacuum. In the case of the NM ions this recovery process promoted its out-diffusion already at 1073 K, and proceeds to temperatures up to 1273 K.

Again, the size and crystalline quality of the particles increased with the annealing temperature, the extension of the new phases resulting from the competition process with the crystalline recovery of the matrix. Furthermore, the size and site preference of the ions of the implanted species affects its mobility in the crystal lattice and hence may retard the formation of new phases, sapphire included, limiting their extension and crystallinity.

The band gap of these spinels is 4.7 eV, 3.5 eV and 3.8 eV, respectively.

The crystalline orientation of the sample to be implanted is very important since it influences the diffusion process at high temperatures and dictates the orientation of the new phases formed. The orientation of the fast mobility c-plane in respect to the sample surface is a key factor. For samples where this plane is directed to the surface (as in r- and m-cut crystals) a high loss of implanted ions is generally observed, as compared to c-cut samples which have the c-plane parallel to the surface. An important conclusion of this work is that the use of r- and m-cut sapphire is to be avoided if implanted ions loss should be prevented. The implantation energy plays also an important role. The use of high energy implantation allows sandwiching the implanted species between bulk crystalline material and a surface polycristaline or amorphous layer. Upon annealing this top most layer recrystallizes and acts as a diffusion barrier. This is of great importance and to take into account when planning implantations if out diffusion and loss of material is to be avoided, especially with low melting point elements.

Furthermore, the morphology of the precipitates depends on the crystalline environment where they grow. The fast diffusion c-plane allows the coalescence process in this direction and hence particles grow with oblong or tabular features along this plane. Thus the crystal host orientation will determine the crystalline orientation of the new phases formed by solid state epitaxial reaction. Cubic phases, like metallic Cu and Ni or spinels will grow with its <111> axis parallel to the c-axis of sapphire. This alignment is found after implantation and develops upon annealing.

Analysis of the SPR bands allowed determining the threshold fluences for the precipitation of optically active precipitates. Moreover, it was possible to establish and explore the correlation between the SPR band and the implanted fluence providing a simpler means (other than RBS) to measure the fluences implanted above the threshold limit, as long as the parameters pertaining the pair implanted ion and host (as well as the implantation

conditions) are known. The optical absorption properties of metallic nanoparticles embedded in sapphire due to SPR effects may be used as optical filters and other optical components.

From the technical point of view, i.e. concerning new analytical equipment and associated techniques, the installation of the IBIL setup was successful and it is now starting to be used by other research groups. As an example, it has been applied to semiconductor AlN doped with the RE Eu, and the first results obtained are similar to PL measurements at cryogenic temperatures. Moreover, this setup may be used together with the external beam facility providing complementary measurements in the analysis of μg/g impurities like Cr or Mn, along with RBS and PIXE measurements. The potential of this technique and equipment was presented to the scientific community at the conference Física 2008 held in Lisbon in September 2008.

5.1 Future work

On the materials research scope, future work will centre in the production of ZnO. To produce embedded ZnO, co-implantation of Zn and O is a promising path to potentiate the formation of ZnO soon after implantation. Alternatively, O implantation can be carried after annealing in vacuum of Zn implanted samples, with the implantation R_p estimated as to match the region rich in Zn precipitates.

To avoid evaporation and loss of the implanted species at high temperatures, annealing treatments in pressurized inert atmospheres should be investigated as this may allow retaining the implanted species while maximizing the crystalline recovery of the matrix.

Complementary experimental techniques are also important to refine the data gathered so far. The definite and direct measurement of the size and morphology of metallic precipitates is also desirable and contacts have been established to achieve TEM measurements, despite the extreme difficulty presented by the preparation of sapphire samples for TEM.

Ellipsometric measurements are necessary to evaluate the refraction index of the implanted region, an important input for a precise optical analysis, particularly in the case of Zn:Al_2O_3 system where the use of standard bulk optical constants in Mie theory does not even provide a qualitative explanation of the features observed in the optical extinction spectra. A trial experiment is being carried. The full understanding of the optical properties of the implanted samples needs other analysis techniques, namely reflectivity measurements in order to accurately determine the optical coefficients.

XRD measurements as a function of temperature are also foreseen aiming at pinpointing phase transitions in the various systems studied, from matrix evolution to the development of the new phases, clearing if at the initial stages of high temperature annealing in vacuum some metallic oxide forms and if it's eventually reduced after one hour to the metallic state.

Regarding the further development of the IBIL setup, future work encompasses the acquisition of a photomultiplier or an InGaAs detector to extend the analytical capability to the IR region, taking advantage of the existing diffraction gratings which already operate in the IR (up to 4000 nm). Furthermore, a charge integrator is necessary if more quantitative measurements are to be made, e.g. a precise comparison between samples by measuring the intensity of the emission peaks for a given charge accumulation. However, to achieve more precise results the beam current control must be optimized to avoid possible effects arising from beam intensity fluctuations.

A sample holder with a cold finger will allow IBIL measurements to be performed as a function of temperature, as often the structure in a luminescence spectrum can only be resolved when the sample is sufficiently cooled.

A lock-in amplifier will allow probing the time behaviour of the luminescence spectra and thus allow for a better characterization of the emission centres. The development of time integration capacity needs a beam shutter or deflector in order to confine the irradiation in time. IBIL imaging may eventually be pursued by detailed surface scanning but this implies a major modification of the experimental chamber.

Moreover, the use of the setup in the RBS-C line would allow using lower energy densities and perform IBIL measurements combined with RBS-C. Trial experiments were conducted from which resulted the need to acquire and install a vacuum proof camera, allowing focussing the mirror based light collector on the irradiated spot and, principally, it is necessary to identify the nature and distribution of the radiation around the experimental chamber during the analysis since the CCD was flooded by very intense and sharp peaks that degraded considerably the acquired spectra.

6 References

1. [Abe04] O. Abe, Y. Ohwa, Solid State Ionics 172 (2004) 553.
2. [Agn92] P. Agnew, Nucl. Instr. and Meth. B 65 (1992) 305.
3. [Alv95] E. Alves, M.F. da Silva, G.N. van den Hoven, A. Polman, A.A. Melo, J.C. Soares, Nucl. Instr. and Meth. B 106 (1995) 429.
4. [Alv99] E. Alves, R.C. da Silva, O. Conde, M.F. da Silva, J.C. Soares, Nucl. Instr. and Meth. B 148 (1999) 1049.
5. [Alv00] E. Alves et al., Surf. and Coat. Tech. 128-129 (2000) 434.
6. [Ame04] H. Amekura, N. Umeda, Y. Takeda, J. Lu, N. Kishimoto, Appl. Phys. Lett. 85(01) (2004) 1015.
7. [Ame05] H. Amekura, N. Umeda, Y. Sakuma, N. Kishimoto, C. Buchal, Appl. Phys. Lett. 87(01) (2005) 3109.
8. [Ame07] H. Amekura, Y. Sakuma, M. Yoshitake, Y. Takeda, N. Kishimoto, C. Buchal, Nucl. Instr. and Meth. B 257 (2007) 64.
9. [And77] H.H. Andersen, J.F. Ziegler, Hydrogen - stopping powers and ranges in all elements, Pergamon, New York 1977.
10. [Aon98] K. Aono, M. Iwaki, Nucl. Instr. and Meth. B 141 (1998) 518.
11. [App67] B.R. Appleton, C. Erginsoy, W.M. Gibson, Phys. Rev. 161 (1967) 330.
12. [Arm69] J.S. Armijo, Oxidation of Metals 1 (1969) 171.
13. [Arn96] G.W. Arnold et al., Nucl. Instr. and Meth. B 116 (1996) 507.
14. [Ata96] B.M. Ataev, A.M. Bagamadova, V.V. Mamedov, Thin Solid Films 283 (1996) 5.
15. [Atw05] H.A. Atwater, S.A. Maier, A. Polman, J.A. Dionne, L.A. Sweatlock, MRS Bull. 30 (2005) 385.
16. [Auz94] F. Auzel, D. Meichenin, F. Pellé, P. Goldner, Optical Materials 4 (1994) 35.
17. [Bal97] C. Ballesteros, Yi Chen, Y. Chen, R. González, M.R. Kokta, X.F. Zong, Phil. Mag. 76(2) (1997) 357.
18. [Bar71] J.H. Barrett, Phys. Rev. B 3 (1971) 1527.
19. [Bar97] N.P. Barradas, C. Jeynes, R.P. Webb, Appl. Phys. Lett. 71 (1997) 291.
20. [Bar03] W.L. Barnes, A. Dereux, T. Ebbesen, Nature 424 (2003) 824.
21. [Bet94] A.A. Bettiol, D.N. Jamieson, S. Prawer, M.G. Allen, Nucl. Instr. and Meth. B 85 (1994) 775.
22. [Bla07] M.G. Blaber, M.D. Arnold, N. Harris, M.J. Ford, M.B. Cortie, Physica B 394 (2007) 184.
23. [Bod08] M. Bodaghi, A.R. Mirhabibi, H. Zolfonun, M. Tahriri, M. Karimi, Phase Trans. 81(6) 571.
24. [Boh98] C.F. Bohren, D.R. Huffman, Absorption and Scattering of Light by Small Particles, Wiley Science Paperback Series, Ed. John Wiley & Sons, 1998.
25. [Bol93] P.H. Bolt, S.F. Lobner, T.P. van den Bout, J.W. Geus, F.H.P.M. Habraken, App. Surf. Sci. 70 (1993) 196.
26. [Bol94] W. Bolse, Mat. Sci. Eng. R 12 (1994) 53.
27. [Bol95] P.H. Bolt, S.F. Lobner, J.W. Geus, F.H.P.M. Habraken, App. Surf. Sci. 89 (1995) 339.
28. [Bol98] P.H. Bolt, F.H.P.M. Habraken, J.W. Geus, J. of Solid State Chem. 135 (1998) 59.
29. [Bou03] G. Boulon, L. Laversenne, C. Goutaudier, Y. Guyot, M.T. Cohen-Adad, J. Luminescence 102 (2003) 417.
30. [Bro00] M.L. Brongersma, J.W. Hartman, H.A. Atwater, Phys. Rev. B 62 (2000) 16356.
31. [Bro02] R.J. Brooks, D.E. Hole, P.D. Townsend, Nucl. Instr. and Meth. B 190 (2002) 136.
32. [Can94] N. Can, P.D. Townsend, D.E. Hole, C.N. Afonso, Appl. Phys. Lett. 65 (15) (1994) 1871.
33. [Can96] N. Can et al., Nucl. Instr. and Meth. B 113 (1996) 248.
34. [Car68a] W.T. Carnall, P.R. Fields, K. Rajnak, J. of Chem. Phys. 49(10) (1968) 4424.
35. [Car68b] W.T. Carnall, P.R. Fields, K. Rajnak, J. of Chem. Phys. 49(10) (1968) 4443.
36. [Car68c] W.T. Carnall, P.R. Fields, K. Rajnak, J. of Chem. Phys. 49(10) (1968) 4447.
37. [Car68d] W.T. Carnall, P.R. Fields, K. Rajnak, J. of Chem. Phys. 49(10) (1968) 4450.
38. [Cas06] C. Cascales et al., Phys. Rev. B 74 (2006) 174114.
39. [Cas08] H. C. del Castillo et al., J. Luminescence 128 (2008) 735.

40. [Cau93] K.J. Caulfield, R. Cooper, J.F. Boas, Phys. Rev. B 47 (1993) 55.
41. [Che90] O. Cheshnovsky, K.J. Taylor, J. Conceição, R.E. Smalley, Phys. Rev. Lett. 64 (1990) 1785.
42. [Che97] D.J. Cherniak, J.M. Hanchar, E.B. Watson, Chem. Geol. 143 (1997) 289.
43. [Che98] J. Chen et al., J. Vac. Sci. Technol. A 16(3) (1998) 1409.
44. [Che99] D.J. Cherniak, J.M. Hanchar, E.B. Watson, Chemical Geology 134 (1997) 289.
45. [Che00] D. J. Cherniak, Geochimica et Cosmochimica Acta 64(22) (2000) 3871.
46. [Chi06a] K.-F. Chiu, C.C Dai, Thin Solid Films 513 (2006) 374.
47. [Chi06b] S. Chi et al., J. of Cryst. Growth 293 (2006) 344.
48. [Cho99] S. Choopun et al., Appl. Phys. Lett. 75 (1999) 3947.
49. [Chu78] W.K. Chu, J.W. Meyer, M.A. Nicolet, Backscattering Spectrometry, Academic Press, New York, 1978.
50. [Col94] J.M.F. Colinas, C.O. Aréan, J. of. Sol. State Chem. 109 (1994) 43.
51. [Con90] M.R. Conseil, Les alumines et leurs applications, édition Nathan, Paris, 1990.
52. [Cor03] E.A. Coronado, G.C. Schatz, J. Chem. Phys. 119 (2003) 3926.
53. [Cor07] A. G. Cortés et al., IEEE J. of Quantum Electronics 43(9) (2007) 758.
54. [Cra84] J.H. Crawford, Nucl. Instr. and Meth. B 1 (1984) 159.
55. [Cul72] B.D. Cullity, X-ray diffraction, Addison-Wesley, New York, 1972.
56. [Dan04] M.C. Daniel, D. Astruc, Chem. Rev. 104 (2004) 293.
57. [Dex56] D.L. Dexter, Phys. Rev. 101 (1956) 48.
58. [Die75] G.J. Dienes, D.O. Welch, Phys. Rev. B 11 (1975) 3060.
59. [Din05] J. Dintinger, A. Degiron, T.W. Ebbesen, MRS Bull. 30 (2005) 381.
60. [Dio05] J.A. Dionne, L.A. Sweatlock, H.A. Atwater, A. Polman, Phys. Rev. B 72 (2005) 075405.
61. [Doo85] L.R. Doolitlle, Nucl. Instr. and Meth. B 9 (1985) 344.
62. [Dyg94a] A. Dygo, W.N. Lennard, I.V. Mitchell, P.J.M. Smulders, Nucl. Instr. and Meth. B 84 (1994) 23.
63. [Dyg94b] A. Dygo, W.N. Lennard, I.V. Mitchell, P.J.M. Smulders, Nucl. Instr. and Meth. B 90 (1994) 161.
64. [Ebb98] T.W. Ebbesen, H.J. Lezec, H.F. Ghaemi, T.Thio, P.A. Wolff, Nature 391 (1998) 667.
65. [Eil95] H. Eilers, B.M. Tissue, Mater. Lett. 24 (1995) 261.
66. [Eil96] H. Eilers, B.M. Tissue, Chem. Phys. Lett. 251 (1996) 74.
67. [Elr81] F.A. Elrefaie, W.W. Smeltzer, J. Electrochem. Soc. 128 (1981) 2237.
68. [Esp02] A.E. Esparza-García, M. García-Hipólito, M.A. Aguilar-Frutis, C. Falcony, Phys. Stat. Sol. A 193(1) (2002) 117.
69. [Eva78] B.D. Evans, M. Stapelbroek, Phys. Rev. B 18 (1978) 7089.
70. [Eva94] B.D. Evans, G.J. Pogatshnik, Y. Chen, Nucl. Instr. and Meth. B 91 (1994) 258.
71. [Fal98] M. Falconieri et al. Appl. Phys. Lett. 73(3) (1998) 288.
72. [Far90] G.C. Farlow, P.S. Sklad, C.W. White, C.J. McHargue, J. Mater. Res. 5(7) (1990) 1502.
73. [Fel82] L.C. Feldman, J.W. Mayer, S.T. Picraux, Materials analysis by ion channelling (Academic Press, New York, 1982).
74. [Fic57] E. Fick, G. Joos. Handbuch der Physik 28. Springer-Verlag, Berlin, 1957.
75. [Fox04] M. Fox, Optical properties of solids, Oxford University Press, 2004.
76. [Fuj97] T. Fujimura, S. Tanaka, Acta Mater. 12 (1997) 4917.
77. [Fuj98] T. Fujimura, S. Tanaka, Acta Mater. 46(9) (1998) 3057.
78. [Fuj03] J.G. Fujimoto, Nat. Biotechnol. 21 (2003) 1361.
79. [Fuj06] K. Fujiwaka, H. Watarai, H. Itoh, E. Nakahama, N. Ogawa, Anal. Bioanal. Chem. 386 (2006) 639.
80. [Fut94] T. Futagami, Y. Aoki, O. Yoda, S. Nagai, Nucl. Instr. Meth. B 88 (1994) 261.
81. [Gad64] A.M.M. Gadalla, J. White, Trans. Br. Ceram. Soc. 63 (1964) 39.
82. [Gan05] R.A. Ganeev et al., Optics Communications 253 (2005) 205.
83. [Gan06] R.A. Ganeev et al., Optics and Spectroscopy 101 (2006) 615.
84. [Gar02] N.Y. Garces et al., Appl. Phys. Lett. 81 (2002) 622.
85. [Ged00] A. Gedanken et al., Appl. Phys. Lett. 77(7) (2000) 945.
86. [Gem74] D.S. Gemmell, Rev. Mod. Phys. 46 (1974) 129.

87. [Gol97] P. Goldner, F. Pellé, D. Meichenin, F. Auzel, J. Lumin. 71 (1997) 137.
88. [Gon99] O. Cíntora-González, C. Estourès, D. Muller, J. Guille, J.J. Grob, Nucl. Instr. and Meth. B 147 (1999) 422.
89. [Gos60] B.R. Gossick, J. Appl. Phys. 31(4) (1960) 650.
90. [Got96] W. Gotschy, K. Vonmetz, A. Leitner, F.R. Aussenegg, Appl. Phys. B 63 (1996) 381.
91. [Hal02] I. Halevy, D. Dragoi, E. Ustundag, A. Yue, E. Arredondo, J. Hu, M. Somayazulu, J. Physics-Cond. Matt. 14(44) (2002) 10511.
92. [Hay99] T. Hayakawa, S.T. Selvan, M. Nogami, Appl. Phys. Lett. 74(11) (1999) 1513.
93. [Hei99] A. Heilman, A. Kiesow, M. Gruner, U. Kreibig, Thin Solid Films 343 (1999) 175.
94. [Hio86] T. Hioki, A. Itoh, M. Ohkubo, S. Noda, H. Doi, J. Kawamoto, J. of Mater. Sci. 21 (1986) 1321.
95. [Hir06] L.R. Hirsch et al., Ann. of Biomed. Eng. 34 (2006) 15.
96. [Hof91] H. Hofsäss, G. Lindner, Phys. Rep. 201 (1991) 121.
97. [Hof96] H. Hofsäss, Hyperfine Interactions 97 (1996) 247.
98. [Hof03] H. Hofmeister, M. Dubiel, H. Graener, J.-C. Pivin, Rad. Eff. Defects in Sol. 158 (2003) 49.
99. [Hom94a] N.P. O Homman, C. Yang, K.G. Malmqvist, Nucl. Instr. and Meth. A 352(1-3) (1994) 610.
100. [Hom94b] P. Homman. "Trace element analysis in geochemistry using a nuclear microprobe" PhD thesis, Department of Nuclear Physics, Lund Institute of Technology, Lund, Sweden, 1994.
101. [Hud07] J.R. Huddle, P.G. Grant, A.R. Ludington, R.L. Foster, Nucl. Instr. and Meth. B 261 (2007) 475.
102. [Hui04] M.A. van Huis et al., Nucl. Instr. and Meth. B 216 (2004) 390.
103. [Hul81] H.C. van de Hulst, Light Scattering by Small Particles, Dover, New York, 1981.
104. [Hun97] E.M. Hunt, J.M. Hampikian, J. Mater. Sci. 32 (1997) 3393.
105. [Iso95] T. Isobe, S.Y. Park, R.A. Weeks, R.A. Zuhr, J. Non-cryst. Sol. 189 (1995) 173.
106. [Iso07] T. Isobe, K. Daimon, K. Ito, T. Matsubara, Y. Hikichi, T. Ota, Ceram. Int. 33 (2007) 1211.
107. [Jac98] J.D Jackson, Classical electrodynamics, 3rd Ed., John Wiley & Sons, New York 1998.
108. [Jad01] W.M. Jadwisienczak, H.J. Lozykowski, J. Appl. Phys. 89(8) (2001) 4384.
109. [Jad03] W.M. Jadwisienczak, H.J. Lozykowski, Opt. Mat. 23 (2003) 175.
110. [Jin01] R. Jin, Y. Cao, C.A. Mirkin, K.L. Kelly, G.C. Schatz, J.G. Zheng, Science 294 (2001) 1901.
111. [Joh72] P.B. Johnson, R.W. Christy, Phys. Rev. B 6 (1972) 4370.
112. [Jun99] K.S. Jung, B. Coh, H. Lee, Bull. Korean Chem. Soc. 20 (1999) 89.
113. [Kar05] T. Karali et al., Physica B 363 (2005) 88.
114. [Kel03] K.L. Kelly, E. Coronado, L.L. Zhao, G.C. Schatz, J. Phys. Chem. B 107 (2003) 668.
115. [Kim03] Y. Kim, P. Kim, C. Kim, J. Yi, J. of Mat. Chem. 13 (2003) 2353.
116. [Kin55] G.H. Kinchin, R.S. Pease, Rep. Prog. Phys. 18 (1955) 1.
117. [Kir02] A.V. Kir'yanov et al., Optics Express 10(16) (2002) 832.
118. [Kis02] N. Kishimoto, N. Okubo, N. Umeda, Y. Takeda, Nucl. Instr. and Meth. B 191 (2002) 115.
119. [Kis03] N. Kishimoto, Y. Takeda, N. Umeda, N. Okubo, R.G. Faulkner, Nucl. Instr. and Meth. B 206 (2003) 634.
120. [Kle92] K.M. Klein, C. Park, A.F. Tasch, IEEE T. Electron. Dev. 39 (1992) 1614.
121. [Kli01] A. Kling et al., Nucl. Instr. and Meth. B 175 (2001) 331.
122. [Kli03] A. Kling et al., Nucl. Instr. and Meth. B 206 (2003) 653.
123. [Kob96] T. Kobayashi, T. Terai, T. Yoneoka, S. Tanaka, Nucl. Instr. Meth. B 116 (1996) 187.
124. [Kre95] U. Kreibig, M. Vollmer, Optical properties of metal clusters, Springer, Berlin, 1995.
125. [Kre01] J.K. Krebs, U. Happek, J. Luminescence 94 (2001) 65.
126. [Kum06] K. Kumar, K. Ramamoorthy, R. Chandramohan, K. Sankaranarayanan, Crys. Res. Technol. 41 (2006) 217.
127. [Kur00] E.Z. Kurmaev, A. Moewes, V.R. Galakhov, D.L.Ederer, T. Kobayashi, Nucl. Instr. Meth. B 168 (2000) 395.
128. [Kuz07] Y. Kuzminykh, H. Scheife, S. Bär, K. Petermann, G. Huber, J. Phys. Conf. Series 59 (2007) 462.
129. [Lag98] K.P.D. Lagerlöf, R.W. Grimes, Acta Mater. 46 (1998) 5689.
130. [Lee78] K.H. Lee, J.H. Crawford Jr., Appl. Phys. Lett. 33 (1978) 273.

131.[Lee99] W.W. Lee, D.B. Lee, M.H. Kim, S.C. Ur, Intermetallics 7 (1999) 1361.
132.[Lee02] C.G. Lee, Y. Takeda, N. Kishimoto, Nucl. Instr. and Meth. B 191 (2002) 591.
133.[Lee05] J.K. Lee et al., Appl. Phys. Lett. 86 (2005) 183111.
134.[Leu07] L.C. Leu, D.P. Norton, G.E. Jellison Jr, V. Selvamanickam, X. Xiong, Thin Solid Films 515 (2007) 6938.
135.[Lid02] D.R. Lide, editor, CRC Handbook of Chemistry and Physics, CRC Press, Boca Raton, 85th ed. 2002.
136.[Lin65] J. Lindhard, K. Dan. Vidensk. Selsk. Mat. Fys. Medd. (1965) 34.
137.[Lin00] S. Link, M.A. El-Sayed, Int. Rev. in Phys. Chem. 19(3) (2000) 409.
138.[Lin05] L. Yin et al., Nano Lett. 5 (2005) 1399.
139.[Liu98] Z. Liu, H. Wang, H. Li, X. Wang, Appl. Phys. Lett. 72(15) (1998) 1823.
140.[Liu02] X. Liu, W. Cai, H. Bi, J. Mater. Res. 17 5 (2002) 1125.
141.[Mal95] K.G. Malmqvist, Nucl. Instr. and Meth. B 104(1) (1995) 138.
142.[Mal96] K.G. Malmqvist, M. Elfman, G. Remond, C. Yang, Nucl. Instr. and Meth. B 109 (1996) 227.
143.[Mai07] S.A. Maier, Plasmonics: Fundamentals and Applications, Springer, New York 2007.
144.[Man97a] C. Manfredotti et al., Nucl. Instr. and Meth. B 130(1) (1997) 491.
145.[Man97b] C. Manfredotti et al., Diamond and Related Materials, 7(6) (1997) 742.
146.[Man98] C. Manfredotti et al., Nucl. Instr. and Meth. B 136 (1998) 1333.
147.[Mar00] M. Martinelli, L. Gomes, R.J. Harowicz, Appl. Opt. 39 (2000) 6193.
148.[Mar02] C. Marques et al., Nucl. Instr. and Meth. B 191 (2002) 644.
149.[Mar06] C. Marques, N. Franco, A. Kozanecki, R.C. da Silva, E. Alves, Nucl. Instr. and Meth. B 250 (2006) 90.
150.[Mar07] J. Margueritat et al., Appl. Phys. A 89 (2007) 369.
151.[Mat04] A.R.J.M. Mattos, S.H. Probst, J.C. Afonso, M. Schmal, J. Braz. Chem. Soc. 15 (2004) 760.
152.[McD02] F.D. McDaniel et al., Nucl. Instr. and Meth. B 190 (2002) 1.
153.[McF03] A.D. McFarland, R.P. Van Duyne, Nano Lett. 3 (2003) 1057.
154.[McH89] C.J. McHargue, M.E. O'Hern, C.W. White, M.B. Lewis, Mater. Sci. Eng. A 115 (1989) 361.
155.[McH93] C.J. McHargue, W.B. Snyder, Jr, Proceedings SPIE, 2018 (1993) 135.
156.[Mck00] J. McKittrick, C.F. Bacalski, G.A. Hirata, J. Am. Ceram. Soc. 83(5) (2000) 1241.
157.[Men97] M. Menning, M. Schmitt, H. Schmitt, J. Sol Gel Sci. Tech. 8 (1997) 1035.
158.[Mer04] H. Mertens, J. Verhoeven, A. Polman, F.D. Tichelaar, Appl. Phys. Lett. 85 (2004) 1317.
159.[Mey95] J.D. Meyer, R.W. Michelmann, F. Ditrói, K. Bethge, Nucl. Instr. and Meth. B 99 (1995) 440.
160.[Mir07] D.Kh. Mirkarimov, T.D. Radjabov, A.I. Kamardin, Z.T. Khakimov, IEEE (2007).
161.[Mit06] M. Mitsushio, K. Miyashita, M. Higo, Sensors and Actuators A 125 (2006) 296.
162.[Moh03] T. Mohanty, N.C. Mishra, F. Singh, S.V. Baht, D. Kanjilal, Rad. Measur. 36 (2003) 723.
163.[Mor97] A. Moroño, E.R. Hodgson, J. of Nucl. Mater. 249 (1997) 128.
164.[Mor02] A. Moroño, E.R. Hodgson, J. of Nucl. Mater. 307 (2002) 1246.
165.[Mot86] C. Moty, in Defects in Solids, A.V. Chadwick, M. Terezi editors, Plenum, New York, 1986.
166.[Mou87] A.P. Mouritz, D.K. Sood, D.H. St John, M.V. Swain, J.S. Williams, Nucl. Instr. and Meth. B 19 (1987) 805.
167.[Mül66] R. Müller, H.H. Günthard, J. Chem. Phys. 44 (1966) 365.
168.[Mur05] T.E. Murphy, D.Y. Chen, E. Cagin, J.D. Phillips, J. Vac. Sci. Technol. B 23(3) (2005) 1277.
169.[Nak70] E. Nakamura, S. Shionoya, Phys. Rev. Lett. 25(25) (1970) 1710.
170.[Nak02] S. Nakao, Y. Miyagawa, S. Miyagawa, M. Tazawa, M. Ikeyama, Nucl. Instr. and Meth. B 190 (2002) 528.
171.[Nak03] Y. Nakanishi et al., Nucl. Instr. and Meth. B 206 (2003) 1033.
172.[Nar83] H. Naramoto et al., J. Appl. Phys. 54 2 (1983) 683.
173.[Nog96] M. Nogami, Y. Abe, Appl. Phys. Lett. 69(25) (1996) 3776.
174.[Nol98] H. Nolte, W. Assmann, H. Huber, S.A. Karamian, H.D. Mieskes, Nucl. Instr. and Meth. B 136 (1998) 587.

175.[Ohk88] M. Ohkubo, N. Suzuki, Phil. Magazine Lett. 57(5) (1988) 261.
176.[Oma93] M.A. Omar, Elementary Solid State Physics, Ed. Benjamin Cummings, 1993.
177.[Ozu04] O. Ozuna, G.A. Hirata, J. McKittrick, Appl. Phys. Lett. 84(8) (2004) 1296.
178.[Pal97] J. Pallon et al., Nucl. Instr. and Meth. B 130(1) (1997) 199.
179.[Pal98] E.D. Palik, editor Handbook of Optical Constants of Solids III, Academic Press, 1998.
180.[Par00] H.H. Paradies, M. Thies, U. Hinze, The Rigaku Journal 17 (2000) 9.
181.[Pel79a] G.P. Pells, AERE Report, AERE R - 9359 (1979).
182.[Pel79b] G.P. Pells, D.C. Philips, J. of Nucl. Mater. 80 (1979) 207.
183.[Pel79c] G.P. Pells, D.C. Philips, J. of Nucl. Mater. 80 (1979) 215.
184.[Per93] S. Perkowitz, Optical Characterization of Semiconductors, Academic Press, 1993.
185.[Per06] M. Peres et al., Supperlatt. and Microstruct. 40 (2006) 537.
186.[Pet07] L. Petit, A. Svane, Z. Szotic, W.M. Temmerman, Top. Appl. Phys. 106 (2007) 331.
187.[Pet08] R. Peters, C. Kränkel, K. Petermann, G. Huber, J. of Crys. Growth 310 (2008) 1934.
188.[Pez06] G. Pezzotti, K. Wan, M.C. Munisso, W. Zhu, J. Appl. Phys. 89 (2006) 041908.
189.[Pic08] A. Piccioto et al., Rad. Eff. & Defects in Solids 163 (2008) 513.
190.[Piv02] J.C. Pivin, M. Sendova-Vassileva, M. Nikolaeva, D. Dimova-Malinovska, A. Martucci, Appl. Phys. A 75 (2002) 401.
191.[Pok94] P. Pokorny, A. Ibarra, J. Appl. Phys. 75 (1994) 1088.
192.[Pri04] J. Prikulis, F. Svedberg, M. Kall, Nanoletters 4 (2004) 115.
193.[Pro07] I. Prosicevas, J. Puiso, A. Guobiene, S. Tamulevicius, R. Naujokaitis, Mater. Sci. 13 (2007) 188.
194.[Pru99] L.M.V. Prudêncio, *Modificação e caracterização de superfícies de alumínio implantadas com crómio*, PhD. thesis, Instituto Superior Técnico, Universidade Técnica de Lisboa, 1999.
195.[Qu02] S.C. Qu et al., Appl. Phys. Lett. 80 (19) (2002) 3605.
196.[Qua05] A. Quaranta, Nucl. Instr. and Meth. B 240 (2005) 117.
197.[Qua06] A. Quaranta et al. J. of Physics: Conference Series 41 (2006) 543.
198.[Qua07] A. Quaranta, J. Salomon, J.C. Dran, M. Tonezzer, G.D. Mea, Nucl. Instr. and Meth. B 254 (2007) 289.
199.[Qui98] M. Quinten, A. Leitner, J.R. Krenn, F.R. Aussenegg, Opt. Lett. 23 (1998) 1331.
200.[Ras94] F.B. Rasmussen, B.B. Nielsen, Phys. Rev. B 49 (1994) 16353.
201.[Ren95] S. Ren, Ph. D. Dissertation, University of Tennessee, 1995.
202.[Rob63] M.T. Robinson, O.S. Oen, Phys. Rev. 132 (1963) 2385.
203.[Rot60] R.S. Roth, S.J. Schneider, J. of Research of the National Bureau of Standards A 64 (1960) 309.
204.[Ruv08] J. L. Ruvalcaba-Sil, L. Manzanilla,E. Melgar, R.L.S. Cruz, X-Ray Spectrom. 37 (2008) 96.
205.[Rya95] C.G. Ryan, Nucl. Instr. and Meth. B 104 (1995) 377.
206.[Sai03] Y. Saito, Y. Imamura, A. Kitahara, Nucl. Instr. and Meth. B 206 (2003) 272.
207.[Sal04] P. Saltykov, O. Fabrichnaya, J. Golczewski, F. Aldinger, J. of Alloys and Compounds 381 (2004) 99.
208.[Sam98] S.K. Sampath, J.F. Cordaro, J. Am. Ceram. Soc. 81(3) (1998) 649.
209.[Sar98] S.S. Sarkisov et al., Nucl. Instr. and Meth. B 141 (1998) 294.
210.[Saw05] J. Sawahata, H. Bang, J. Seo, K. Akimoto, Sci. and Technol. of Adv. Mater. 6 (2005) 644.
211.[Sch94] T. Schenkel, H. Hebert, J.D. Meyer, R.W. Michelmann, K. Bethge, Nucl. Instr. and Meth. B 89 (1994) 79.
212.[Ser01] R. Serna, J. Gonzalo, C.N. Afonso, J.C.G de Sande, Appl. Phys. B 73 (2001) 339.
213.[Sha05] A. El-Shaer, A. Che Mofor, A. Bakin, M. Kreye, A. Waag, Superlatt. and Microstruct. 38 (2005) 265.
214.[Sin07] S.C. Singh, R. Gopal, Bull. Mater. Sci. 30 (2007) 291.
215.[Sku96] V.A. Skuratov, V.A. Altynov, S.M. Abu AlAzm, Nucl. Instr. and Meth. B 107 (1996) 263.
216.[Sku06] A.V. Skuratov, K.J. Gun. J. Stano, D.L. Zagorski, Nucl. Instr. and Meth. B 245 (2006) 194.
217.[Smi47] A.D. Smigelskas, E.O. Kirkendall, Trans. AIME 171 (1947) 130.
218.[Spe92] E.D. Specht, C.J. Sparks, C.J. McHargue, Appl. Phys. Lett. 60 (1992) 2216.

219.[Spi66] W.E. Spicer, J. of Appl. Phys. 37 (1966) 947.
220.[Sta83] A.Y. Stathopoulous, G.P. Pells, Phil. Mag., 47 (1983) 381.
221.[Ste02] A.L. Stepanov, V.N. Popok, D.E. Hole, I.B. Khaibullin, Appl. Phys. A 74 (2002) 441.
222.[Ste05a] A.L. Stepanov et al., Technical Phys. Lett 31 (2005) 702.
223.[Ste05b] A.L. Stepanov, I.B. Khaibullin, Rev. Adv. Mater. Sci. 9 (2005) 109.
224.[Suc97] M. Suchanska, Progress in Surface Science, 54(2) (1997) 165.
225.[Sue95] S. Sueno, European Journal of Mineralogy, 7(6) (1995) 1273.
226.[Sur01] A.I. Surdo, V.S. Kortov, V.A. Pustovarov, Rad. Measurements 33 (2001) 587.
227.[Tak99] K. Takahiro et al., Nucl. Instr. and Meth. B 152 (1999) 314.
228.[Tak02] Y. Takeda, C.G. Lee, N. Kishimoto, Nucl. Instr. and Meth. B 191 (2002) 422.
229.[Tak06] Y. Takeda et al., Optical Rev. 13 (2006) 231.
230.[Tat02] T.A. Taton, Trends in Biotechnology, 20(7) (2002) 277.
231.[Tow87] P.D. Townsend, Reports on the Progress of Physics, 50 (1987) 501.
232.[Tow94] P.D. Townsend, P.J. Chandler, L. Zhang, Optical effects of ion implantation, Cambridge University Press, 1994.
233.[Tow01] P.D. Townsend, D.E. Hole, Vacuum 63 (2001) 641.
234.[Tow07] P.D. Townsend, M. Khanlary, D.E. Hole, Surface and Coatings Tech. 201 (2007) 8160.
235.[Tro98] W.J. Tropf, M.E. Thomas, Handbook of Optical Constants of Solids III, Academic Press, 1998.
236.[Tru90] K.P. Trumble, M. Rühle, Acta Metallur. Mater. 39 (1990) 1915.
237.[Ull03] K. Ullrich, S. Locmelis, M. Binnewies, K.D. Becker, Phase Transitions 76 (2003) 103.
238.[Ust00] E. Ustundag, B. Clausen, M.A.M. Bourke, App. Phys. Lett. 76 (2000) 694.
239.[Val91] J. Valbis, N. Itoh, Rad. Eff. Def. Sol. 116 (1991) 171.
240.[Val01] J. Vallayer, C. Jardin, D. Tréheux, Optical Mater. 16 (2001) 329.
241.[Vil02] M.G. Vilarigues, *Caracterização de superfícies de Ti e Mg modificadas por implantação de Cr*, MSc. Thesis, Fac. de Ciências, Universidade de Lisboa, 2002.
242.[Vir92] D. Viry, N. Tercier, J.P. Denis, B. Blanzat, F. Pellé, J. Chem. Phys. 97(4) (1992) 2263.
243.[Voo92] V. van der Voort, A. Imhof, G. Blasse, J. of Sol. Sta. Chem. 96 (1992) 311.
244.[Wef87] K. Weffers, C. Misra, Oxides and Hydroxides of Aluminium, ALCOA Technical Paper, 1987.
245.[Whi81] E.J.W. Whittaker, Crystallography. An introduction for earth science (and other solid state) students , Pergamon Press, Oxford, 1981.
246.[Whi05] A.V. Whitney et al., J. Phys. Chem. B 109 (2005) 20522.
247.[Wil99] E.K. Williams et al., Nucl. Instr. and Meth. B 148 (1999) 1074.
248.[Wil05] B. Wiley et al., MRS Bull. 30 (2005) 356.
249.[Woo93] R.A. Wood, P.D. Townsend, N.D. Skelland, D.E. Hole, J. Barton, C.N. Afonso, J. Appl. Phys. 74(9) (1993) 5754.
250.[Wrz02] J. Wrzyszcz et al., J. of Alloys and Compounds 341 (2002) 358.
251.[Wu92] P. Wu, A.D. Pelton, J. of Alloys and Compounds 179 (1992) 259.
252.[Wu02] Z. Wu et al., Nucl. Instr. and Meth. B 191 (2002) 121.
253.[Xia04a] H.B. Xiao et al., App. Surf. Science 222 (2004) 180.
254.[Xia04b] X. Xiang, X.T. Zu, S. Zhu, L.M. Wang, App. Phys. Lett. 84 (2004) 52.
255.[Xia05] X. Xiang, X.T. Zu, S. Zhu, L.M. Wang, Physica B 368 (2005) 88.
256.[Xia06a] X. Xiang et al., Nanotechnology, 17 (2006) 2636.
257.[Xia06b] X. Xiang, X.T. Zu, S. Zhu, C.F. Zhang, L.M. Wang, Nucl. Instr. and Meth. B 250 (2006) 192.
258.[Xu00] H. Xu, J. Aizpurua, M. Käll, P. Apell, Phys. Rev. E 62 (2000) 4318.
259.[Xu02] H. Xu, M. Käll, Sensors and Actuators B 87 (2002) 244.
260.[Yal99] T.N. Yalovets, P.A. Gurjiyants, V.N. Kurlov, F. Theodore, J. Delepine, Crys. Res. Technol. 34(7) (1999) 821.
261.[Yan94] C. Yang, N.P. O Homman, L. Johansson, K.G. Malmqvist. Nucl. Instr. and Meth. B 85 (1994) 808.
262.[Yan95] C. Yang, N.P. O. Homman, K.G. Malmqvist, L. Johansson, N.M. Halden, V. Barbin, Scanning Microscopy, 9 (1995) 43.

263.[Yan96] C. Yang. “Ionoluminescence techniques for geological applications” PhD thesis, Department of Nuclear Physics, Lund Institute of Technology, Lund, Sweden, 1996.
264.[Yan97a] C. Yang et al., AIP Conference Proceedings, 392 (1997) 735.
265.[Yan97b] C. Yang et al. Nucl. Instr. and Meth. B 130 (1997) 746.
266.[Yes07] O.A. Yeshchenko, I.M. Dmitruk, A.M. Dmytrukb, A.A. Alexeenko, Mater. Sci. and Eng. B 137 (2007) 247.
267.[Yoo02] M.H. Yoon, S.H. Lee, H.L. Park, H.K. Kim, M.S. Jang, J. of Mat. Sci. Lett. 21 (2002) 1703.
268.[Yos03] A. Yoshikawa et al., J. Appl. Phys. 94(9) (2003) 5479.
269.[You02] J.H. Youk et al., Langmuir 18 (2002) 2455.
270. [Zha04] Q. Zhao, L. Hou, C. Zhao, S. Gu, R. Huang, S. Ren, Laser Phys. Lett. 1(3) (2004) 115.
271.[Zha09] D. Zhang, E. Cherkaev, J. of Comput. Phys. 228 (2009) 5390.
272.[Zho91] R.S. Zhou, R.L. Snyder, Acta Cryst. B – Struct. Sci. 47 (1991) 617.
273.[Zho06] G. Zhou, Y. Dong, J. Xu, H. Li, J. Si, X. Qian, X. Li, Materials Lett. 60 (2006) 901.
274.[Zie77] J.F. Ziegler, Helium – stopping powers and ranges, Pergamon, New York 1977.
275.[Zie09] J. F. Ziegler, J. P. Biersak, U. Littmark, The Stopping and Range of Ions in Solids Pergamon Press, New York, 2009, available at www.SRIM.org.
276.[Zin97] S.J. Zinkle, C. Kinoshita, J. of Nucl. Mater. 251 (1997) 200.
277.[Ziv76a] M. Zivitz, E.W. Thomas, Phys. Rev. B - Solid State Physics, 13 (1976) 2747.
278.[Ziv76b] M. Zivitz, E.W. Thomas, Nucl. Instr. and Meth. 132 (1976) 411.
279.W1 http://www.kyburz-sapphire.ch/Sapphire_Characteristics_en.pdf
280.W2 http://www.korth.de/eng/503728952d091450d/503728952d09d151e.htm
281.W3 http://www.philiplaven.com/mieplot.htm
282.W4 http://www.webelements.com/